Analyse et contrôle de sillages turbulents tridimensionnels : des cas axisymétriques aux automobiles

Mathieu Grandemange

École Polytechnique — ENSTA ParisTech

PhD Thesis

Defended by

Mathieu Grandemange

To obtain the title of

Docteur de l'ENSTA ParisTech

Speciality: Fluid Mechanics

Analysis and Control of Three-dimensional Turbulent Wakes: from Axisymmetric Bodies to Road Vehicles

Defended on December 2nd, 2013

Jury

President:	Pr. Jean-Marc Chomaz	École Polytechnique (LadHyX)
Reviewers:	Pr. Jacques Borée	ENSMA (LEA)
	Pr. Thomas Leweke	IRPHE
Examinator:	Pr. Jacques Magnaudet	IMFT
Advisors:	Pr. Olivier Cadot	ENSTA ParisTech (UME)
	Dr. Marc Gohlke	PSA Peugeot Citroën

Remerciements

La qualité d'une thèse est liée à celle de l'entourage du doctorant ; je tiens donc à remercier les personnes qui ont contribué à ces travaux.

Tout d'abord, Olivier, tu es certainement celui qui a le plus travaillé avec moi sur ce projet. Tu t'es énormément investi, avec une pédagogie et un enthousiasme exceptionnels. Ta réactivité a été exemplaire, le summum correspondant sans doute à ta mission en Inde au cours de laquelle le décalage horaire nous faisait travailler presque en continu. Si l'on ajoute à cela les expériences inoubliables de nos différents séjours à l'étranger, je crois que notre collaboration n'aurait tout simplement pas pu mieux fonctionner. Pour toutes ces raisons, je te remercie profondément.

Marc, tu as veillé au bon fonctionnement de cette thèse et aux intérêts industriels de nos actions. Malgré tes nombreuses autres responsabilités et ton éloignement géographique, tu as toujours été disponible, impliqué, en proposant régulièrement de nouvelles perspectives à nos travaux ; je t'en suis très reconnaissant. Tu as été pour moi un hiérarchique irréprochable mais avant tout un collègue avec qui j'ai toujours apprécié travailler et discuter.

J'ai passé la majorité de ma thèse à l'Unité de Mécanique de l'ENSTA ParisTech. Thierry, Nicolas et surtout Lahcene, je tiens à vous remercier pour votre aide précieuse lors de la mise en place des dispositifs expérimentaux. Un grand merci également à Régine car tu m'as toujours aidé avec le sourire pour les démarches administratives. De manière générale, je remercie toute l'équipe de l'UME pour les bons moments passés au quotidien.

Du côté de PSA Peugeot Citroën, Vincent, je tiens à te remercier pour ta confiance accordée dès mon arrivée. Fabien, merci pour ta disponibilité et ta bonne humeur jour après jour. Merci Axel pour ta conduite des essais à la Ferte Vidame ; et bien sûr, un grand merci à toute l'équipe SFTA pour les discussions, scientifiques ou non, que nous avons eu autour d'un café.

Par ailleurs, de nombreux essais de ce travail ont été réalisés dans le cadre du CNRT R2A, association des principaux acteurs français de la recherche sur les thématiques de l'aérodynamique et de l'aéroacoustique du transport terrestre. Ce partenariat fonctionne grâce à l'implication de chacun de ses membres que je remercie sincèrement ; Jean et Denis, je tiens à saluer votre investissement lors de nos essais.

Je souhaite également remercier le jury pour le temps passé à l'étude du manuscrit ainsi que l'attention et la reconnaissance qu'il a eu pour ce travail. Plus généralement, merci à la communauté de l'aérodynamique automobile pour les discussions et les échanges au cours des différents congrès et rassemblements.

Enfin, merci à mes proches pour leur soutien.

Merci à vous !

Contents

The present work results from a CIFRE agreement between the mechanical department (UME) of École Nationale Supérieure de Techniques Avancées (ENSTA ParisTech) at Palaiseau and the research and innovation department of fluid mechanics of PSA Peugeot Citroën at Vélizy-Villacoublay.

These experimental studies aim at improving the comprehension of the flow over road vehicles. The objective is to identify the dominant drag sources; based on this diagnostic, flow control strategies are suggested and implemented to improve the aerodynamic performances.

Chapter 1

Introduction

This chapter introduces the industrial context. Then, it gives some bibliographical elements on bluff body wakes in order to present the academical motivations and the originality of the study.

In parallel, the notations and some general notions of fluid mechanics are presented in appendix A.

Abstract

Car manufacturers are intensively working on the reduction of the pollutant emissions of their new vehicle fleets. As the resisting force induced by the air flow over a car is the dominant contributor to power consumption at high speeds, an important effort is devoted to drag reduction. The development of efficient flow control strategies relies on the comprehension of the drag sources which must first be studied past basic bluff bodies. While the flow control strategies for drag reduction are relatively clear over bidimensional geometries due to the presence of the von Kármán dynamics, it appears that the drag sources are not trivial even for simple three-dimensional geometries such as spheres or disks. When it comes to real vehicle shape, it is admitted that the wake induces low pressure levels on the afterbody but the corresponding physics remain open issues. In this context, this work aims at improving the comprehension of three-dimensional wakes by increasing the complexity of the geometry and by exploring the sensitivity of the flow to local disturbances.

Contents

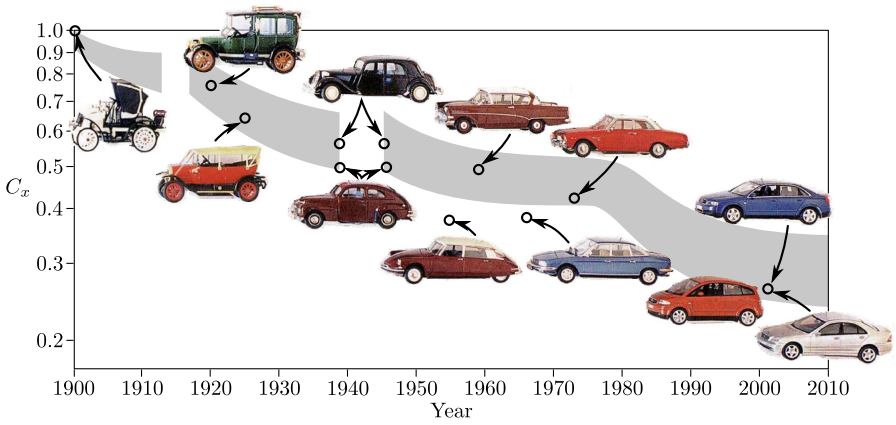

Figure 1.1. History of the drag of road vehicles from Hucho (1998).

1.1 Industrial context

Growing economical and environmental considerations on fuel consumption are motivating car manufacturers to improve the energetic efficiency of their vehicles. In particular, the European Union is introducing thresholds of CO_2 emissions with significant financial penalties for over-pollution. The manufacturers have to ensure that their new car fleets do not emit more than an average of 130 grams of CO_2 per kilometer by 2015 and 95 g(CO_2)/km by 2020.

To reach these objectives of CO_2 emissions, different levers are identified such as engine optimization, mass diminution and drag reduction. Indeed, the resisting force applied by the air stream on the vehicle, *i.e.* the drag, is responsible for the dominant power consumption for high speeds, typically over 70 km/h. To give some figures, for a median vehicle emitting 130 g(CO_2)/km, roughly 30 g(CO_2)/km are ascribed to aerodynamic effects.

The drag force relies on the shape of vehicles; it is quantified using a normalized coefficient, denoted C_x, allowing the comparison of the vehicles shapes. The history of the drag of road vehicles is presented in figure 1.1. One can first see the decreasing trend: the drag coefficient has been reduced from 1.0 in the begining of the 20^{th} century to an average of 0.3 in 2010. The interesting period is the sharp decrease of C_x that begins from the end of the 70's as a response to the energy crises and goes on in the 80's with the benefits of the increasing use of wind tunnels during the vehicle conception. However, the drag coefficient seems to have reached a limit as no significant drag reduction has been observed over the last decade.

Currently, the car manufacturers face different concerns on automotive drag reduction. First, the shape of the vehicle is strongly affected by some functional aspects such as space of the passenger compartment, crash safety, engine cooling and style design. These constraints limit the use of more streamlined shapes that could easily provide better drag performances.

Furthermore, the drag reduction strategies gradually lead to a standardization of the vehicles shapes because all the manufacturers have similar constraints and consequently similar optima. This leaves less and less liberties to the design department: the inclination of the roof, the presence of a spoiler and its orientation, the use of sharp edges on the afterbody... All these parameters are set to reach the best aerodynamic performances.

Finally, any drag reduction obtained using an additional device has a significant cost,

both in terms of development and integration on the vehicle. Nevertheless, for commercial reasons, it may not be added to the selling price. The penalties for over-pollution introduced by the European Union should alter this balance and encourage innovation.

Therefore, the role of the research departments in car aerodynamics is to provide new levers of drag reduction as well as alternative technologies allowing more design liberties.

In this industrial context, the present work aims at improving the comprehension of drag sources in the wakes past road vehicles. It addresses different open issues such as the presence of global mode activity and its impact on drag. Based on this drag diagnostic, the objective is to provide a drag reduction strategy that can be achieved through flow control.

Now that the industrial motivations are defined, some bibliographical notes on bluff body wakes and their control are given in section 1.2 increasing the complexity of the geometries progressively.

1.2 Bluff body wakes and strategies of flow control

This section presents the general characteristics of bluff body wakes with some strategies of flow control for drag reduction that are reported in the literature. First, section 1.2.1 is devoted to the behavior of a plane mixing layer. Then, bidimensional geometries are studied in section 1.2.2. Finally, section 1.2.3 depicts the flow over basic three-dimensional bodies and some elements on road vehicle wakes are provided in section 1.2.4.

1.2.1 Planar mixing layers

The common characteristic of bluff body wakes is the presence of flow separations on the geometry. The boundary layer detachments introduce concentrated vorticity in the wake and forms mixing layers between the flows of different velocities: $U \sim U_0$ in potential flow while $U \ll U_0$ in the separated region. Thus, the dynamics of the mixing between two fluids of different velocities are the starting ingredients of bluff body wakes.

Features of the natural flow

The behavior of a planar mixing layer between a high velocity flow ($\vec{U} = U_0\vec{e_x}$) and a fluid at rest is depicted from studies present in the literature (Champagne *et al.*, 1976; Bell & Mehta, 1990; Pope, 2000). This configuration is a general organization of a shear flow considered in the reference frame of the low velocity flow; a sketch is given in figure 1.2(a). The coordinate system is chosen so that the mean vorticity in the shear layer is oriented in the z direction. For a given streamwise position x, the position y_α is defined as

$$U(y_\alpha) = \alpha U_0, \tag{1.1}$$

with $\alpha \in [0, 1]$. The characteristic thickness δ_m of the mixing layer is evaluated by

$$\delta_m(x) = |y_{0.9}(x) - y_{0.1}(x)|. \tag{1.2}$$

The characteristic lengths δ_1 and δ_2, displacement and momentum thicknesses respectively, defined for wall boundary layers in equations (A.12) and (A.13) can be extended to mixing layers: they are denoted by δ_{m1} and δ_{m2} respectively.

Moving downstream, the momentum of the high velocity flow is transfered to the fluid at rest by viscous or turbulent diffusion depending on the flow regime. This phenomenon results in a mixing layer growth at a rate of $\mathrm{d}\delta_m/\mathrm{d}x \sim {\mathrm{Re}_{\delta_m}}^{-0.5}$ in the laminar regime and $\mathrm{d}\delta_m/\mathrm{d}x \in [0.1, 0.2]$ in the turbulent regime[1]. Hence, the growth rate is generally much smaller in the laminar regime than in the turbulent one. Furthermore, for a turbulent mixing layer, it is observed that the contours y_α are straight lines and the growth is measured toward the domain of the fluid at rest. One can interpret such a spatial growth as fluid entrainment by the mixing layer.

Now, the time-averaged momentum conservation expressed in equation (A.8), considered in the y direction at large Reynold numbers ($\mathrm{Re}_{\delta_m} = U_0\delta_m/\nu \gg 1$) and under mixing layer assumptions ($U_x \gg U_y \sim U_z$ and $\partial/\partial y \gg \partial/\partial x \sim \partial/\partial z$), gives the equilibrium between the dominant terms

$$\frac{\partial C_p}{\partial y^*} + 2\frac{\partial \langle {u'_y}^{*2} \rangle}{\partial y} = 0. \tag{1.3}$$

[1] Experiments show that the exact value of the growth rate relies on the initial conditions of the shear layer.

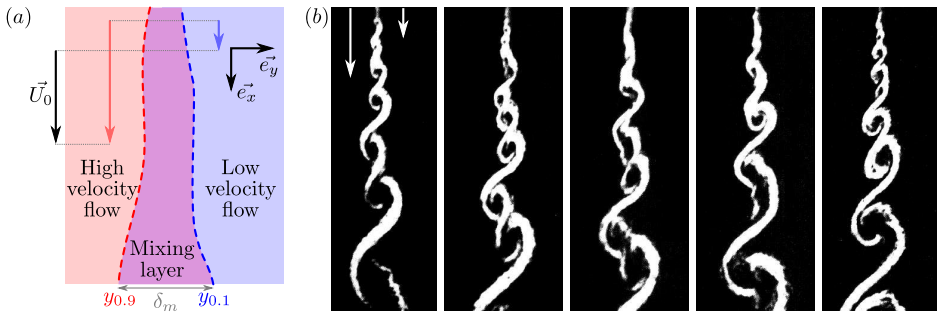

Figure 1.2. Sketch of a mixing layer configuration (a) and characteristic dynamics at $\mathrm{Re}_{\delta_m} = 8.5\ 10^5$ (b); the time sequence is from Roshko (1976).

Thus, after integration in the y direction, equation (1.3) shows that $C_p + 2\langle {u'_y}^{*2} \rangle$ is constant across the mixing layer: at first order, the pressure of the fluid at rest is equal to the static pressure of the high momentum flow.

The fluctuations of velocity in the mixing layer are ascribed to turbulent behaviors but also to proper vorticity dynamics. Indeed, a planar shear layer is unstable (Kelvin-Helmholtz instability) which results in the development of rollings of the shear surface at $\mathrm{St}_{\delta_{m2}} \approx 0.02$ (Michalke, 1965; Ho & Huerre, 1984). In particular, the time sequence in figure 1.2(b) shows pairings of vortices which is one of the basic ingredients of the mixing layer growth. The size of the vortices clearly relies on the streamwise position in the flow; so in the spectral domain, the frequency $f_{LS/I}$, separating the large-scale structures (related to the rollings) and the inertial range of turbulence, decreases with the streamwise position (Hussain & Zaman, 1985).

Flow control strategies

In terms of flow control, an interesting approach is the modification of the growth rate $\mathrm{d}\delta_m/\mathrm{d}x$, *i.e.* the quantity of fluid incorporated by the mixing layer. This growth rate may easily be increased by enhancing the turbulent activity or exciting the natural rollings as evidenced in figures 1.3(a)–(c). On the contrary, the reduction of $\mathrm{d}\delta_m/\mathrm{d}x$ is a real challenge for shear flows at high Reynolds numbers. The main technique consists in postponing the transition to turbulence and the development of the instabilities.

First, one can refer to the work of Greenblatt & Wygnanski (2000) as well as the experiments of Parezanović *et al.* (2013) using active control methods in transitional mixing layers. In particular, Parezanović *et al.* (2013) show that a high frequency actuation prevents the formation of the large-scale structures which results in a reduction of the Reynolds stresses and a diminution of the growth rate (compare figures 1.3b and 1.3d).

Moreover, perturbations forming optimal streaks are proved to delay the transition to turbulence in boundary layers (Fransson *et al.*, 2006). Consequently, they may provide an interesting approach in a mixing layer configuration given similitudes between these two shear flows.

The mixing layer dynamics are part of the basic ingredients of separated flows but many wake properties result from the interactions between several shear layers, especially for bidimensional geometries.

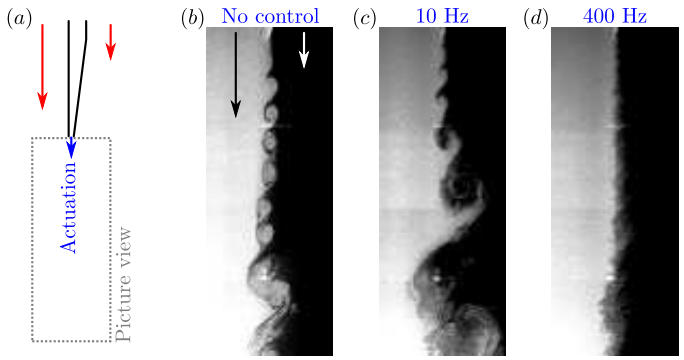

Figure 1.3. Smoke visualizations of the effect of micro-jet actuators on a mixing layer at $\mathrm{Re}_{\delta_{m2}} = 500$ from Parezanović *et al.* (2013): experimental setup (a); natural flow (b) with a characteristic frequency around 30 Hz, *i.e.* $\mathrm{St}_{\delta_{m2}} = 0.02$, and controlled flows with actuations at 10 Hz (c) and 400 Hz (d).

1.2.2 Bidimensional geometries

The presence of boundary layer separations on cylinders[2] leads to configurations of two shear layers of opposite sign in the flow. Now, this vorticity distribution has a strong impact on the wake behavior.

Features of the natural flow

Over a certain Reynolds number ($\mathrm{Re}_D = 47$ for a circular cylinder), the interaction of the two shear layers of opposite vorticity results in an antisymmetric instability. A global mode consisting in a periodic shedding of vortices, known as the von Kármán vortex street, is observed in the wake (see figures 1.4*a*–*b*). The shedding frequency is $\mathrm{St}_{D_r} \approx 0.2$ with D_r the thickness of mean wake as defined in figure 1.5(a) (Roshko, 1954). A flourishing literature can be found on the different regimes of this vortex shedding (see Roshko, 1993; Williamson, 1996; Zdravkovich, 1997, and references therein).

These intense von Kármán vortices are sources of low pressure in the wake. As a consequence, their formation and dynamics significantly affect both the drag and the instantaneous lift. For example, the periodic motion of the vortex shedding is responsible for a dominant part of the velocity fluctuations: in the turbulent wake of a circular cylinder at $\mathrm{Re}_D \sim 10^5$, Cantwell & Coles (1983) reports that 35% to 55% of the Reynolds stresses are ascribed to the coherent activity. So it is clear that the von Kármán street plays a first order role in the mean wake properties, even at large Reynolds numbers.

Two general trends between the mean flow and the base pressure can be stated from experimental results.

- First, the thicker the wake in comparison to the geometry, the lower the base pressure, the larger the drag.

  This rule may be ascribed to the bluffness effect where the bluffness is defined as the ratio between the wake width and the cross-flow size of the cylinder, *i.e.* D_r/D in figure 1.5(a) (Roshko, 1954; Apelt & West, 1975; Roshko, 1993). Note that the

[2] The term *cylinder* refers to bodies of constant geometry in the spanwise direction. The circular cylinder is the particular case with a circular profile.

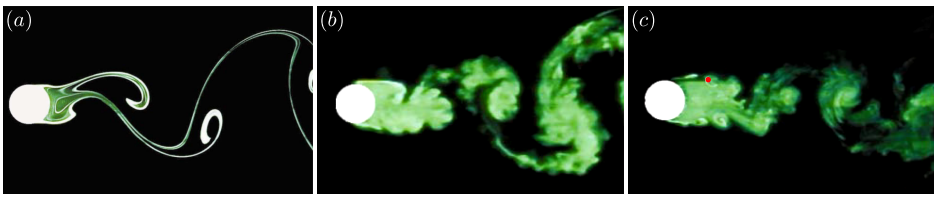

Figure 1.4. Von Kármán street past a circular cylinder in laminar regime at $\mathrm{Re}_D = 10^3$ (a), in turbulent regime at $\mathrm{Re}_D = 3\ 10^3$ (b) and its control at $\mathrm{Re}_D = 3\ 10^3$ (c) using a small disturbing cylinder displayed in red (from Dalton *et al.*, 2001).

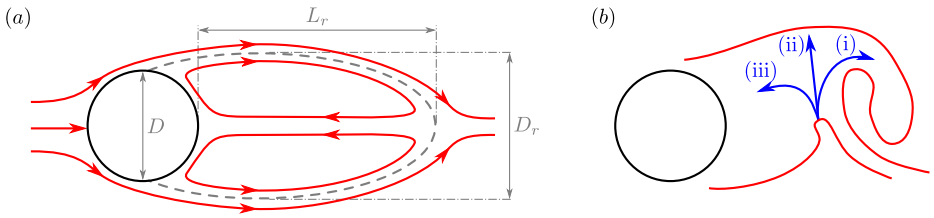

Figure 1.5. Mean flow (a) and instantaneous flow dynamics (b) around a circular cylinder: (i) and (ii), entrainment flows; (iii), reverse flow. The sketch (b) is from Gerrard (1966).

orientation of the flow at separation has a fundamental impact on this ratio; for example, the drag coefficient of a flat plate is larger than the drag of a circular cylinder (Tropea *et al.*, 2007). Another example of this dependence between bluffness and drag is the transition that occurs at $\mathrm{Re}_D \sim 2\ 10^5$ over a circular cylinder. The point of massive separation moves downstream due to an early transition to turbulence which results in a thinner wake; meanwhile, the drag coefficient approximatively decreases from 1.2 to 0.4 (Zdravkovich, 1997).

Besides, the experiments of Apelt & West (1975) prove that this bluffness rule remains valid after the suppression of the von Kármán street using a splitter plate.

- Second, for a given bluffness, the larger the recirculation length, the higher the base pressure, the lower the drag (Roshko, 1993; Zdravkovich, 1997; Parezanović & Cadot, 2012).

  It is worth mentioning that this rule is equally obtained from potential flow theory combined with cavity models (Riabouchinsky, 1921; Wu, 1972).

The model presented by Gerrard (1966) introduces an interesting interpretation of the mean recirculation length: the recirculation region results from an equilibrium between the reverse flow and the flow entrained by the mixing layers (see figure 1.5b). Note that the entrainment of a laminar mixing layer is negligible in front of a turbulent one, this equilibrium strongly depends on the streamwise position of the transition to turbulence. Now, an increase in entrainment flows (i) and (ii) cannot be compensated by an increase in reverse flow (iii) which results in a vortex formation closer to the base and a shorter recirculation bubble in average. This interpretation introduces a strong correlation between the mixing layer activity, the position of the formation of the von Kármán vortices, the recirculation length and the drag.

The identification of the mechanisms responsible for the selection of the base pressure paves the way to the implementation of efficient flow control strategies for drag reduction that are now presented.

Flow control strategies

Different strategies naturally come out from the two dominant drag trends. The first one consists in decreasing the bluffness of the cylinders. The experiments of Munshi *et al.* (1997) show that the use of rotating elements at the edges of a rectangular cylinder injects momentum in the fluid which results in a thinner wake and drag reduction. Another technique consists in implementing plasma actuators in proximity of a circular cylinder. It delays the massive separation on the geometry which limits the wake width (Artana *et al.*, 2003; Hyun & Chun, 2003).

A second drag reduction strategy lies in the increase of the recirculation length by altering the formation of the von Kármán street. The simplest method is the suppression of the antisymmetric instability using the mirror effect of a splitter plate[3] in the plane of symmetry (Apelt *et al.*, 1973; Unal & Rockwell, 1988; Nakamura, 1996).

The base bleed equally provides interesting drag reduction even for low momentum injection as presented by Arcas & Redekopp (2004); the mechanism may be directly connected to the model of Gerrard (1966) as the flow injection in the recirculation region is a direct compensation of the flow entrained by the shear layers. The vortex formation is moved further downstream which delays the closure of the recirculation region.

Furthermore, one can mention techniques which break the synchronization of the opposed shear layers in order to prevent the development of the von Kármán street. This effect may be achieved through three-dimensional modulations in the shear layers (Park *et al.*, 2006) or active actuation (Pastoor *et al.*, 2008); both methods postpone the vortex formation region and attenuate the global mode activity.

Now, one more interesting strategy is related to the use of the natural sensitivity of the global mode: a slight perturbation of the flow can result in significant modifications of the near wake dynamics. The precursory experiments of Strykowski & Sreenivasan (1985, 1990) prove that the vortex shedding past a circular cylinder at $\mathrm{Re}_D = 80$ can be suppressed by placing a small control cylinder in one of the mixing layers. This work has been followed by various experiments in the turbulent regime past different shapes of cylinders (Sakamoto *et al.*, 1991; Sakamoto & Haniu, 1994; Dalton *et al.*, 2001; Cadot *et al.*, 2009; Parezanović & Cadot, 2009; Parezanović & Cadot, 2012). All these experiments confirm the high sensitivity of the global mode dynamics to local disturbances: the control cylinder delays the vortex formation and attenuates the shedding activity (see figure 1.4*c*). The modifications induced by the perturbation are related to the introduction of a stagnation point in the main wake. Due to viscosity, this generates vorticity in the flow, whose interaction with the main flow vorticity is at the origin of the sensitivity (Parezanović & Cadot, 2009).

A systematic study varying the position of the small control cylinder leads to the construction of sensitivity maps of global properties of the wake such as the shedding frequency or the base pressure. In parallel, theoretical work gives access the structural sensitivity of global mode wakes (Hill, 1992; Marquet *et al.*, 2008; Luchini *et al.*, 2009). Although the theory usually remains limited to the laminar regime, the latest developments of Meliga

[3] In the inviscid theory, a splitter plate or a flat wall is equivalent to a steady straight streamline with a symmetric flow on the other side.

et al. (2012) extend the approach to the turbulent flow around a D-shaped cylinder at $\mathrm{Re}_D = 1.3\ 10^4$. The presented sensitivity map of the global mode frequency is in good agreement with the experimental results of Parezanović & Cadot (2012), both in terms of spatial distribution and amplitude.

This approach provides a useful tool in the framework of control strategy since it predicts where a disturbance efficiently affects global properties of the flow.

Now that the dominant features and control strategies of the flow around bidimensional bluff bodies are presented, the wakes past basic three-dimensional geometries are considered in section 1.2.3.

1.2.3 Basic three-dimensional bodies

This section depicts some academical studies to introduce general wake properties and perspectives on drag reduction for basic three-dimensional geometries.

Features of the natural flow

In the simplest case of a sphere of diameter D in a uniform flow, non-trivial bifurcations are reported in the wake as the Reynolds number increases (Sakamoto & Haniu, 1990).

First evidenced by Magarvey & Bishop (1961), the laminar wake loses its axisymmetry at $\mathrm{Re}_D \approx 210$: the steady axisymmetric wake selects one cross-flow direction which leads to a steady solution with only one azimuthal plane of symmetry (see figures 1.6*a*–*b*); the wake orientation is denoted by θ_W .

A second bifurcation is reported at $\mathrm{Re}_D \approx 280$: the wake becomes unsteady but preserves the reflectional symmetry and the azimuthal orientation of the first bifurcation. A periodic shedding of parallel vortex loops is reported (Achenbach, 1974; Ormières & Provansal, 1999) as presented in figures 1.6(*c*). Then, the flow presents an increase in complexity as the Reynolds number is raised. The azimuthal orientation θ_W of the wake starts oscillating (Mittal, 1999; Chrust *et al.*, 2013), typically for Reynolds numbers larger than 400. Turbulent scales appear in the wake for $\mathrm{Re}_D > 800$ in addition to the periodic dynamics. The wake gradually loses its preference towards the reflectional plane of symmetry defined at the first steady bifurcation (Mittal *et al.*, 2002) and the axisymmetry of the mean flow is finally restored from $\mathrm{Re}_D \sim 10^3$. At moderate Reynolds numbers, the high frequency instabilities of the mixing layers in the near wake degenerate into large-scale vortex loops developing from the end of the recirculation bubble; the wake oscillates randomly (Taneda, 1978; Sakamoto & Haniu, 1990) and may get a helical organization highly coherent in space (Pao & Kao, 1977; Berger *et al.*, 1990; Yun *et al.*, 2006); the Strouhal number of this oscillating global mode ranges in $\mathrm{St}_D \in [0.12, 0.19]$. One can have a global view of the instantaneous turbulent flow from the sketch and visualizations given in figure 1.7; in the cavitation experiments in figures 1.7(*b*)–(*c*), the interface between liquid and vapor locate the low pressure regions in the instantaneous flow (see Beaudoin *et al.*, 2004, and references therein for details on the visualization technique).

Eventually, as for the circular cylinder, an early transition to turbulence can delay the massive separation on the afterbody which leads to significant drag decreases at $\mathrm{Re}_D \sim 4\ 10^5$ (Hoerner, 1965; Taneda, 1978). The Reynolds number for which the drag crisis is reported strongly depends on the roughness of the surface. This point is evidenced by the well-known example of the gulf ball: in spite of the insufficient Reynolds number reached after a swing, the wake of the ball is in a low drag configuration due to the

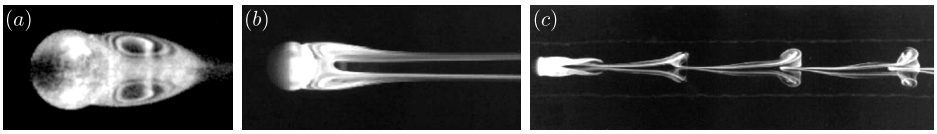

Figure 1.6. Regimes of the laminar wake past a sphere (from Nakamura, 1976; Thompson *et al.*, 2001): steady axisymmetric for $\mathrm{Re}_D < 210$, (*a*); steady planar symmetric for $210 < \mathrm{Re}_D < 280$, (*b*); unsteady planar symmetric for $280 < \mathrm{Re}_D \lesssim 400$, (*c*).

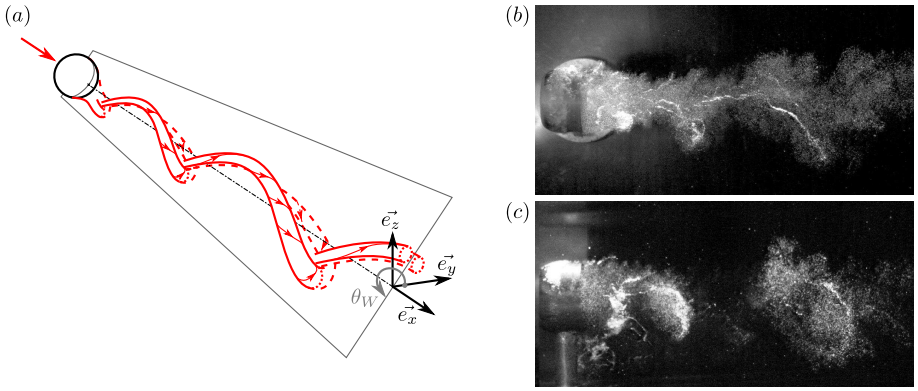

Figure 1.7. Sketch of the large-scale structures in the turbulent wake of a sphere (*a*) from Vilaplana *et al.* (2013). Side view (*b*) and top view (*c*) of the instantaneous wake past an axisymmetric blunt body at $\mathrm{Re}_D \approx 10^5$ using cavitation techniques.

turbulent activity introduced by the asperities.

The axisymmetry breaking at $\mathrm{Re}_D \approx 210$ is associated with the development of two vortex threads in the streamwise direction as visible in figure 1.8 (Thompson *et al.*, 2001; Schouveiler & Provansal, 2002; Fabre *et al.*, 2008). A steady side force also appears on the sphere in the direction of the reflectional plane of symmetry as shown by Pier (2008) in figure 1.9. After the unsteady transition at $\mathrm{Re}_D \approx 280$, the vortex shedding generates oscillations of this side force but its intensity remains significant. The statistical axisymmetry of the mean flow in the turbulent regime results in a nil cross-flow force in average (Yun *et al.*, 2006); nonetheless, an instantaneous side force is always present on the geometry. A fundamental interest is ascribed to the dynamics of this unsteady cross-flow force as it is responsible for part of the drag: approximately 10% of the total drag at $\mathrm{Re}_D = 350$ (Pier, 2008).

The additional drag related to such a cross-flow force is reminiscent of the notions of induced drag commonly used in aeronautics (Batchelor, 2002): for a lifting airfoil, the induced drag coefficient is proportional to the square of the lift coefficient, the proportional factor being a geometrical parameter dependent on the distribution of the lift along the span of the wing. This induced drag is strongly connected to the formation of a pair of counter-rotating streamwise vortices downstream of the wingtips.

The sphere wake is massively studied because it is a prototypical axisymmetric wake: similar behaviors are found in the flow around other axisymmetric geometries. For example,

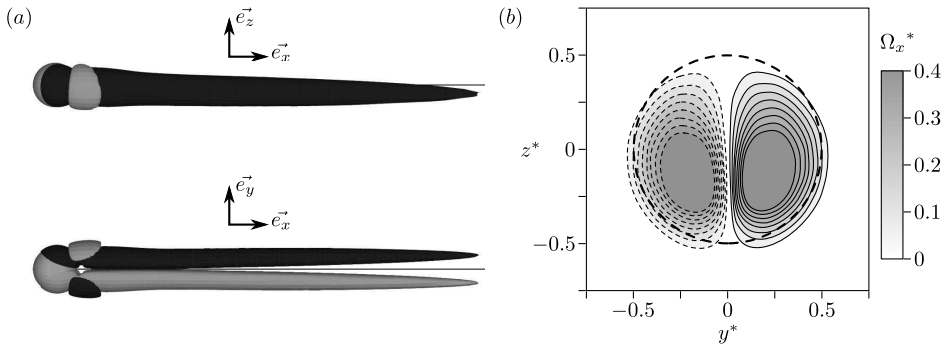

Figure 1.8. Pair of streamwise counter-rotating vorticies of the steady planar symmetric regime past a sphere at $\mathrm{Re}_D = 250$ for $\theta_W = 3\pi/2$ (from Fabre *et al.*, 2008; Thompson *et al.*, 2001): iso-surfaces of streamwise vorticity (a) and contours of streamwise vorticity in the cross-flow plane $x^* = 1$ (b). The continuous and dashed lines are positive and negatives values respectively; the contour interval is 0.05; the contour 0 is not plotted; the dashed circle locates the sphere.

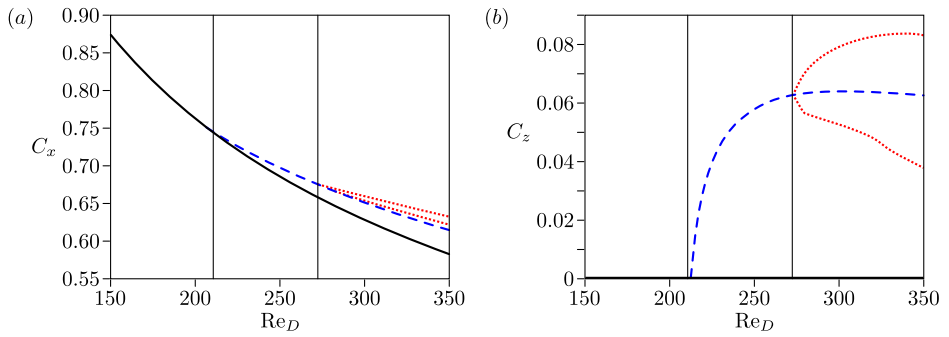

Figure 1.9. Drag (a) and lift (b) of a sphere at low Reynolds numbers from Pier (2008) depending on the wake regime ($\theta_W = 3\pi/2$ for $\mathrm{Re}_D > 210$): steady axisymmetric (continuous black line), steady planar symmetric (dashed blue line) and unsteady planar symmetric (dotted red lines delimiting maxima and minima).

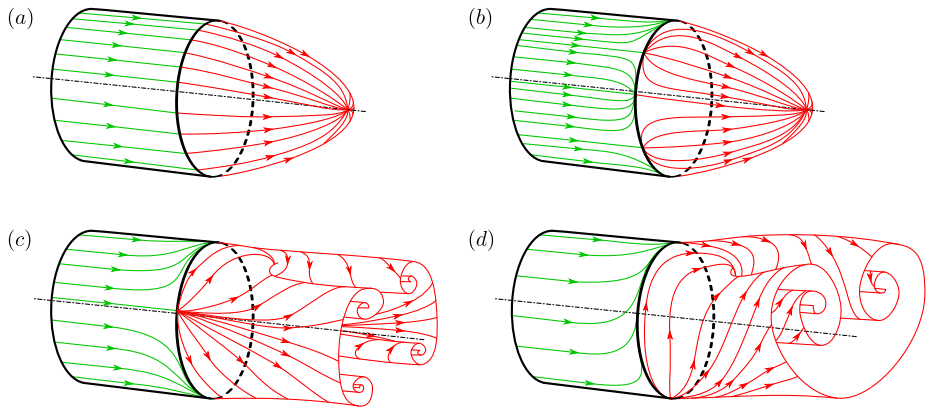

Figure 1.10. Wake topologies past axisymmetric blunt geometries from Délery (2013): optimal case, (a); cell organization, (b); organization with two pairs of counter-rotating vortices, (c); imperfect case, (d).

the wake past a disk presents a comparable behavior. Literature depicts a steady bifurcation at $\mathrm{Re}_D \approx 115$ and an unsteady one at $\mathrm{Re}_D \approx 121$ even if Fabre *et al.* (2008) report slight differences: the unsteady bifurcation first leads to a regime that slightly breaks the reflectional symmetry. Besides, as in bidimensional wakes, the Strouhal number of the periodic oscillations relies rather on the distance between the opposed shears than on the size of the geometry. The vortex shedding past a disk is reported at $\mathrm{St}_D = 0.135 \pm 0.005$ for $\mathrm{Re}_D \in [10^3, 10^5]$ (Miau *et al.*, 1997; Ruiz *et al.*, 2009), *i.e.* $\mathrm{St}_{D_r} \approx 0.20$ as $D_r \approx 1.5D$ (see appendix C), whereas past the sphere, a value of $\mathrm{St}_{D_r} \approx \mathrm{St}_D = 0.19$ is measured at equivalent Reynolds numbers (Sakamoto & Haniu, 1990).

The dependence between the Strouhal number and the gap separating the shear layers is confirmed by the experiments of Kiya & Abe (1999) depicting the impact of the aspect ratio on the vortex shedding in the wake of elliptical and rectangular cross-flow plates. Two peaks of energy are observed in the power spectra of velocity signals, at Strouhal numbers between 0.05 and 0.15 depending on the aspect ratio. They correspond to periodic oscillations of the wake in the two cross-flow directions; the phenomenon at the higher frequency is usually more energetic and is associated with the interactions of the closer shear layers.

Independently of these bifurcation scenarii and periodic dynamics, a classification of the flow topologies past axisymmetric afterbodies at high Reynolds numbers is provided by Délery (2013) from topology analyses and singular point theory. The simplest admissible flows are the ideal case of an axisymmetric organization of the recirculation bubble (see figure 1.10a) or an organization comprised of a finite number of cells (see figure 1.10b). However, these two topologies are unlikely to be observed experimentally due to slight imperfections of the axisymmetry. The topology with two pairs of counter-rotating vortices presented in figure 1.10(c) is mentioned as the most probable organization preserving a nil cross-flow force but a slight amplification of the imperfection of the axisymmetry is very likely to result in a single pair of counter-rotating vortices shown in figure 1.10(d). One can see that this latter topology, associated with a non-nil mean side force, is similar to the wake after the first steady bifurcation past a sphere at $\mathrm{Re}_D \approx 210$ (see figures 1.6b and 1.8).

In the experimental framework, the study of the turbulent wake past axisymmetric geometries is a challenge because of the fixing system. Indeed, apart from the unusual magnetically supported body presented by Higuchi *et al.* (2006), the fixation method is necessarily intrusive. The problem is that, as soon as the axisymmetry of the setup is lost, the axisymmetry of the turbulent wake is altered. For example, the experiments of Vilaplana *et al.* (2013) show that the introduction of an asymmetry in the setup fixes the orientation θ_W of the vortex shedding. In the theoretical framework, such an azimuthal lock is equally proven by Meliga *et al.* (2009*a*) using global stability analysis in the case of a disk: the azimuth of the global mode is necessarily equal or opposed to that of the disturbance. Furthermore, the common method consisting in holding a sphere with four thin wires leads to a $m = 4$ azimuthal periodicity of the mean flow (Vilaplana *et al.*, 2013). On the other hand, in the widespread system of a sphere mounted on a streamwise axis held from downstream, the support disturbs the center of the recirculation region; so, such a setup is very likely to generate a controlled wake as a reference flow.

Flow control strategies

The drag reduction strategies in the wake of basic three-dimensional geometries are similar to the bidimensional cases: decrease of the wake width, *i.e.* of the bluffness, and increase of the recirculation region for a fixed flow separation.

The wake width can be controlled by orienting the flow at the trailing edge (see Abramson *et al.*, 2011, and references therein).

On the contrary, the global mode activity being far less coherent than past cylinders, the control techniques that shall be implemented to delay the closure of the recirculation region are still open issues. Most of the work on passive and active control of axisymmetric turbulent wakes focuses on the unsteady global mode dynamics (Mair, 1965; Berger *et al.*, 1990; Weickgenannt & Monkewitz, 2000; Sevilla & Martinez-Bazan, 2004; Higuchi, 2005; Morrison & Qubain, 2009; Weiss & Deck, 2011). It shows connections between the parameters of the control setup, the drag and the intensity of the oscillating global mode. In particular, Berger *et al.* (1990) prove that a disk forced to oscillate near the helical mode frequency stabilizes the structure of this global mode in space and time at a coherence level close to 1. On the other hand, Weickgenannt & Monkewitz (2000) performed experiments displacing a control disk in the recirculation bubble pointing out different flow regimes depending on the disk position associated with important evolutions of drag and Strouhal number.

In parallel, the recent work of Meliga *et al.* (2009*b*, 2010) extends the theoretical sensitivity analyses to the wake past axisymmetric blunt bodies in the laminar regime. The results show zones of high sensitivity in the recirculating bubble. The receptivity of the oscillating global mode is located around the separatrix at the end of the recirculation region while the receptivity of the steady antisymmetric mode is close the center of the recirculation region. Nevertheless, the comparison to experimental work is difficult as the control techniques previously mentioned are too intrusive to be considered as perturbations. One can still refer to the experiments of Vilaplana *et al.* (2013) disturbing a sphere wake with a small control sphere; the results evidence modifications of the oscillating global mode both in terms of frequency and structure. For example, when the control sphere is off-centered, a subharmonic at half the natural frequency appears and the azimuthal phase becomes imposed by the control sphere. Then, when the control sphere reaches the separated shear, a pure subharmonic mode is observed suggesting a shedding of alternative vortex loops from both sides of the wake.

As a consequence, contrary to the bidimensional cases, the mechanisms responsible for

the closure of the recirculation region are not well-defined in three-dimensional wakes and hence, the control strategies aiming at increasing the recirculation length are still to be clarified.

Now, in addition to the three-dimensional aspect of the flow, road vehicle wakes are related to complex geometries in ground proximity. These configurations are presented in section 1.2.4.

1.2.4 Road vehicles

General properties of the turbulent flow past road vehicle and their control are presented in this section with a particular focus on blunt geometries.

Features of the natural flow

First, as a transition from the academical studies described in the previous section, it is worth noting that the high sensitivity of the flow to residual asymmetries is equally observed over more complex geometries. In the study of the separated flow past a three-dimensional backward facing step, Herry *et al.* (2011) depict a strong sensitivity of the wake to the symmetry of the setup. A residual yaw angle is proved to fix the wake out of the reflectional plane of symmetry and for a perfectly symmetric configuration, the flow is bistable with two preferred reflectional symmetry breaking positions; the equiprobability of the two states restores a statistical symmetry at long time-scales. Similar bistable properties may be responsible for the asymmetric results obtained by Lawson *et al.* (2007) in the recirculation bulb on the rear window of a car. In parallel, high degrees of asymmetry are measured in both experiments and numerical simulations (Lee *et al.*, 2009; Wassen *et al.*, 2010). These phenomena are reminiscent of the symmetry breaking regimes found in closed-cell flows (Ravelet *et al.*, 2004) and may be a general property of turbulent flows.

In the framework of car aerodynamics, the work of Ahmed *et al.* (1984) significantly improved the comprehension of the flow around different shapes of road vehicles: it characterizes the critical influence of the afterbody configuration (see figure 1.11).

For slant angles below 10° or larger than 30°, the topology is characterized by a massive recirculation bubble on the afterbody. This region is associated with low levels of base pressure and is the major contributor to the aerodynamic drag (see figure 1.11*a*). The autopower spectra of the base pressure signals, mixing layer velocities or force measurements show characteristic frequencies in the natural wake. The following analyses are reported in the literature but the spatial organization of these structures and their interactions still need to be clarified.

- A low frequency behavior at $\mathrm{St}_H \approx 0.07$ is measured experimentally (Duell & George, 1999; Khalighi *et al.*, 2001, 2012) and interpreted as a periodic interaction between the upper and lower part of the trapped toric vortex in the near wake; a shedding of pairs of vortices from the trailing edge with a lateral oscillation is also hypothesized (Khalighi *et al.*, 2001).

- The numerical simulations of Bayraktar *et al.* (2001) report two frequencies at Strouhal numbers 0.106 and 0.086 in the unsteady measurements of the lift and side forces respectively but the organization of the corresponding global modes is not discussed.

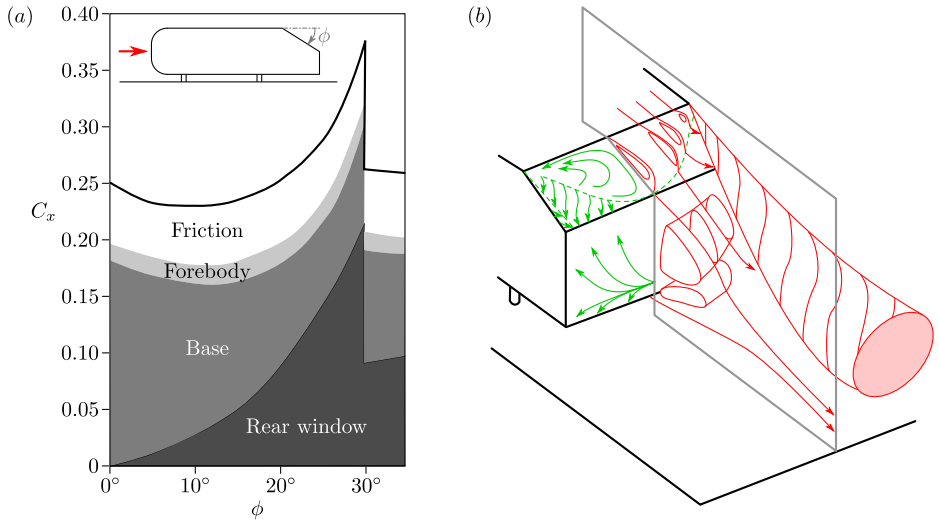

Figure 1.11. (*a*) Drag contribution of the Ahmed geometry depending on the angle of the rear window ϕ. (*b*) Wake topology in the $\phi = 25°$ configuration. The results are from Ahmed *et al.* (1984).

- The work of Khalighi *et al.* (2012) presents a coherent motion at $\mathrm{St}_H = 0.17$ downstream of the recirculation region with a peak of energy particularly clear when the probe is in the plane of symmetry.
- High frequency dynamics are observed by Duell & George (1999) at $\mathrm{St}_H = 1.157$ and interpreted as a shedding of vortices from the mixing layers with a pseudo-helical structure.

In addition, such coherent wake motions are likely to be affected by wall proximity. For example, the work of Ruiz *et al.* (2009), studying the unsteady near wake of a disk normal to a wall, shows an increase in the complexity of the flow as the gap ratio decreases. The vertical wake oscillation is progressively attenuated and combined with a slight increase in the shedding frequency. Eventually, a critical gap ratio is found under which the vertical oscillation of the disk wake is suppressed and a separation occurs on the ground, this latter phenomenon being associated with low frequency evolutions at $\mathrm{St}_D \sim 0.03$. In parallel, past a simplified squareback vehicle, a change in the wake topology is also observed through the base pressure distribution when the gap ratio becomes small in presence of a fixed ground (Duell & George, 1993).

On the other hand, for moderate slant angles, *i.e.* $10° < \phi < 30°$, a pair of intense counter-rotating vortices develops in the wake of the model reducing the pressure on the afterbody (see figures 1.11*b* and 1.12). In the worst drag configuration of a slant angle close to 30°, these structures induce up to 50% increase in drag in comparison to the 0° case. These intense flow structures and their control are source of much interest in the literature as similar streamwise vortices persist over real vehicles, especially in the wakes of sedan and fastback shapes (see figure 1.13) or even pick-up trucks (Al-Garni & Bernal, 2010).

In the case of real vehicles having a blunt shape, the topology is associated with a massive recirculation region on the afterbody without intense streamwise vortices (see figure 1.13*a*). However, the absence of top – bottom symmetry of the geometry alters the

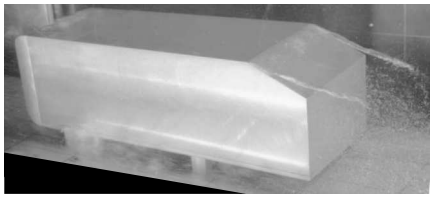

Figure 1.12. Cavitation visualization of the pair of counter-rotating vortices past the 25° Ahmed geometry from Beaudoin *et al.* (2004).

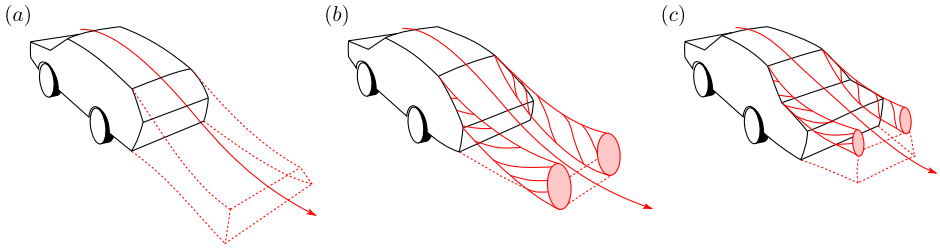

Figure 1.13. Wake topologies past road vehicles depending on the afterbody: square-back (a), fastback (b) and sedan (c). The sketches are from Hucho (1998).

organization of the recirculation region: a residual pair of counter-rotating vortices is very likely to be present as a signature of the non-nil lift force. A common flow topology from Depardon (2006) is presented in figure 1.14.

The topologies shown in figures 1.13 correspond to very different force intensities and the presence or absence of a pair of intense counter-rotating vortices often lies in geometry details. There is a high sensitivity of the wake to the shape of the edges, especially at the end of the roof. There, the use of a sharp edge forcing the flow separation allows to switch from a high lift – high drag configuration of a fastback flow to a low lift – low drag case of the squareback topology. This point is evidenced in figure 1.15 with the implementation of a spoiler on a Citroën C4 model. Figures 1.15(a)–(b) present the case without spoiler, the potential flow follows the shape of the afterbody in the plane of symmetry which results in the formation of an intense pair of counter-rotating vortices. On the contrary, the use of a spoiler leads to a massive recirculation region and the strong attenuation streamwise vortices as visible in figures 1.15(c)–(d); the obtained topology is similar to the one given

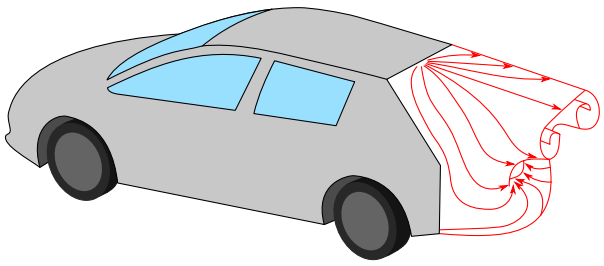

Figure 1.14. Wake topology past a blunt vehicle model from Depardon (2006).

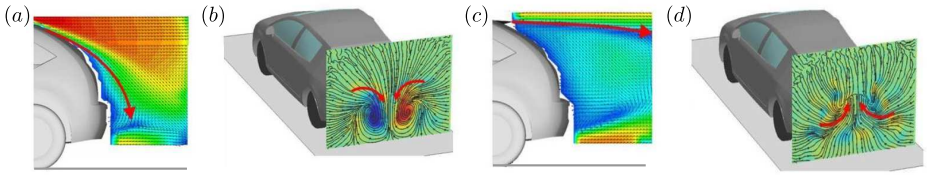

Figure 1.15. Wake topologies past a Citroën C4 model without spoiler (*a*)–(*b*) and with a spoiler at the end of the roof (*c*)–(*d*): qualitative modulus of the velocity in the plane of symmetry and streamwise vorticity in a cross-flow plane.

in figure 1.14. Such a crucial influence of the spoiler explains its systematic use in the conception of recent vehicles even if it alters the style design. Note that the orientation of the spoiler is accurately set to reach a drag minimum.

Finally, the presence of wheels on the geometries may induce significant differences in the afterbody flow. Some intense vortices are locally generated by the wheel, especially by the front ones (Wäschle, 2007). The proper wake structures present important differences depending on the setup: rotating or fixed wheel, tire width, permeability of the rim...

Flow control strategies

As previously mentioned, an important work is devoted to the control of fastback flows through various passive and active strategies such as splitter plates (Gilliéron & Kourta, 2010), flaps (Beaudoin & Aider, 2008; Fourrié *et al.*, 2011), vortex generators (Aider *et al.*, 2010), boundary layer streaks (Pujals *et al.*, 2010) or even pulsed jets (Bruneau *et al.*, 2011). The efficiency of a control device relies on its ability to alter the formation of the pair of streamwise vortices or its capacity to reduce the wake width by limiting the bulb of separated flow on the slanted face without amplifying the streamwise vortices.

On the other hand, the control strategies for drag reduction for squareback vehicles rely on similar mechanisms than the wakes past basic three-dimensional bodies (see section 1.2.3). Thus, by modifying the bluffness or by increasing the recirculation length, diverse strategies provide interesting base pressure recovery. One can refer to the use of afterbody flaps with and without cavity (Cooper, 1985), splitter plates (Duell & George, 1993; Khalighi *et al.*, 2001) and active control (Rouméas *et al.*, 2009; Littlewood & Passmore, 2012).

The experiments of Littlewood & Passmore (2010) depict the effect of a small chamfer at the upper trailing edge of a squareback geometry similar to the $\phi = 0°$ Ahmed configuration. Despite the small size of the chamfer in the streamwise direction of 15% of the body height[4], an optimal drag reduction of 4.4% is obtained for a chamfer angle of 12°. The parabolic-like dependence between the chamfer angle and the drag is reminiscent of the results of Ahmed *et al.* (1984) for moderate slant angles where an optimal 8% drag reduction is obtained for $\phi = 12.5°$. Thus, the significant drag gain obtained by Littlewood & Passmore (2010) with a small chamfer confirms the high impact of the orientation of the trailing edge on aerodynamic forces. This approach using chamfered shapes is particularly interesting since it corresponds to the method applied by the car manufacturers on real vehicles to limit the drag. Indeed, the angles of the spoiler and of the diffuser (when one is present) are set empirically in order to reach the optimal drag point given the vehicle

[4]For comparison, the length of the slanted face in the Ahmed geometry is 77% of the body height.

parameters (global shape, ground clearance...), while the characteristic length of these devices remains small in front of the vehicle size.

Eventually, literature reports some experiments of flow control for drag reduction on real vehicles. For example, Irving Brown *et al.* (2010) proves that the use of passive base bleed and the implementation of cavity on the base achieve drag reduction. In parallel, the numerical simulations of Inchul *et al.* (2008) presents innovating spoiler shapes to optimize the fluid forces.

In this academical context, the originality of the approach of the present work is now detailed in section 1.3.

1.3 Approach of the present work

The bibliographical elements presented in section 1.2 highlight three main levers of drag reduction:

- the reduction of the bluffness;
- for a given bluffness, the increase of the recirculation length;
- the attenuation of the streamwise vortices related to three-dimensional effects.

As mentioned in section 1.1, the vehicle shapes are already highly constrained so the reduction of the bluffness may appear unappropriated. Consequently, the interest of orienting the flow at the trailing edge of the vehicle is quantified in this work but most of the following experiments focus on the analysis and control of the separated flow with fixed separation. Because of the strong differences between bidimensional and three-dimensional flows, these studies consider three-dimensional configurations only. The objective is to clarify the physical mechanism responsible for the closure of the recirculation bubble (mixing layer growth, global modes...). In addition, the exploration of the flow sensitivity of global properties of the wake to perturbations helps identify efficient control strategies for drag reduction.

The work is structured as a function of the geometries by increasing their complexity step by step. Part I is devoted to axisymmetric bodies with the cases of a sphere in chapter 2 and an axisymmetric bullet-shaped body in chapter 3.

Then, part II details the wake past parallelepiped geometries based on the square-back Ahmed configuration: bifurcations of the laminar wake in chapter 4, natural flow at $\mathrm{Re}_H = 9.2\ 10^4$ in chapter 5 with a focus on the influence on the aspect ratio of the base in chapter 6. Chapters 7 and 8 present experiments of flow control based on a sensitivity analysis and on the orientation of the flow at the base separation respectively. Finally, chapter 9 explores the relevance of the previous results at industrial scales, *i.e.* at $\mathrm{Re}_H = 2.5\ 10^6$.

The wakes of real vehicle are considered in part III with a characterization of the wake dynamics through full-scale studies in chapter 10. Then, chapter 11 extends the phenomena studied in parts I and II to real vehicles.

Finally, a comprehensive synthesis is provided in chapter 12.

In parallel, the fluid notations and some general notions of fluid mechanics are depicted in appendix A. Besides, visualisations of the flow structures aroud different vehicle shapes are given in appendix B using cavitation techniques. Some details on the turbulent wake of a disk are given in appendix C as a complement to chapter 2. Finally, analytical results of a bistable turbulent signals are provided in appendix D.

Given the large number of geometries and of wind or water tunnels used in the following, no detailed presentation of the facilities is provided. For each chapter, the main features of the setup are depicted with the measurement systems; when available, references providing additional information are also given.

Part I

Axisymmetric geometries

Chapter 2

Axisymmetry of the turbulent sphere wake

This chapter is devoted to the turbulent sphere wake. The objectives are to clarify the statistics that lead to the axisymmetry of the wake and to detail the instantaneous topology of the flow. In particular, these experiments quantify the wake asymmetry related to imperfections of the setup.

In parallel, a similar study in a disk configuration is provided in appendix C.

Abstract

As a starting point of the study past three-dimensional bodies; the prototypical case of the turbulent sphere wake is considered at $\mathrm{Re}_D = 1.9\ 10^4$. It is found axisymmetric in average with an unsteady global mode at $\mathrm{St}_D = 0.19$. PIV snapshots in a cross-flow plane show that the axisymmetry of the mean flow is due to the equal exploration of all the azimuths by the instantaneous wake. Conditional averaging enables to extract the flow topology associated with one azimuthal direction; the obtained wake shows strong similarities with the unsteady planar symmetric flow observed in the laminar regime. In addition, the use of perturbations of the axisymmetry leads to modifications of the azimuthal statistics: the periodicity of the perturbation is recovered in the wake since one or several preferred orientations are identified. Hence, such statistics pave the way to multi-stable behaviors in three-dimensional wakes.

Contents

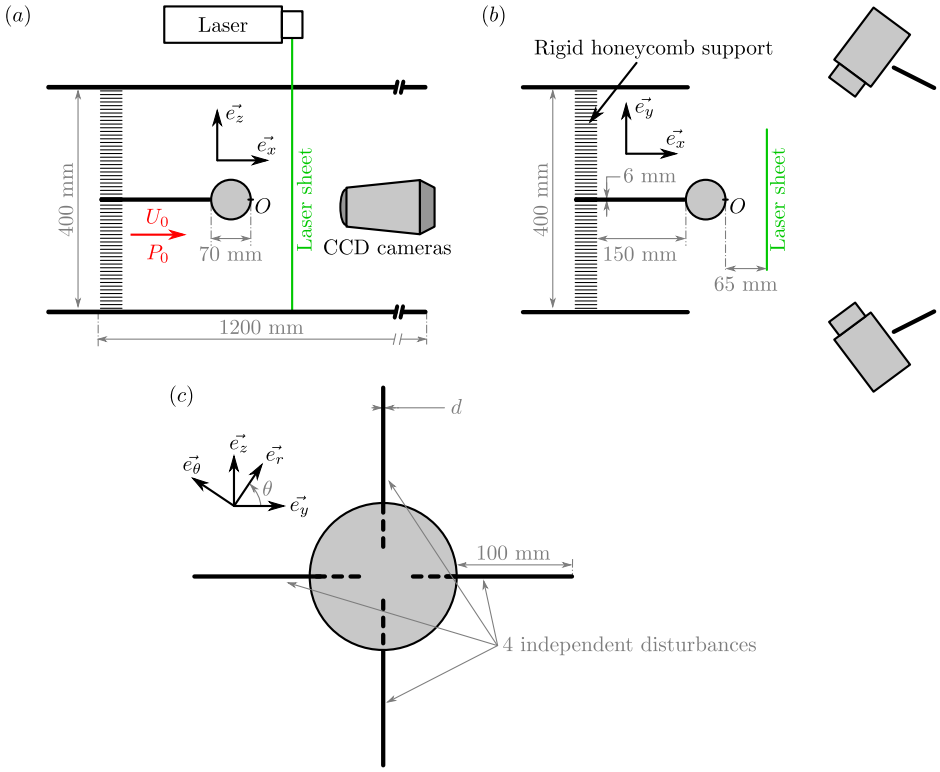

Figure 2.1. Side view (a) and top view (b) of the experimental setup with the stereoscopic PIV system; back view of the sphere with the disturbance apparatus (c).

2.1 Experimental setup

This section present successively the main characteristics of the setup and of the velocity measurements.

Geometry

As mentioned in section 1.2.3, one of the main challenges of experimental studies of the wake past axisymmetric bluff bodies lies in the system fixing the geometry in the flow. The present experiments use an Eiffel-type wind tunnel; the sphere is held using an axis fixed upstream of the test section on a rigid honeycomb support so that the setup is as axisymmetric as possible (see figures 2.1a–b); the residual asymmetries come from the alveoli of the honeycomb. In turn for providing a sphere support, the presence of the honeycomb alters the quality of the flow: when the sphere is removed from the test section, the homogeneity of the flow at 200 mm downstream of the honeycomb is raised to 2.2% and the turbulent intensity reaches 3.4%.

The free-flow velocity is set at $U_0 = 4.3$ m s^{-1} and the sphere diameter is $D = 70$ mm so the Reynolds number of the wake is $\mathrm{Re}_D = U_0 D/\nu = 1.9\ 10^4$. The origin O of the coordinate system is at the maximal downstream location of the sphere (see figure 2.1). For practical interest, a polar coordinate (x, r, θ) is also used, the plane $\theta = 0$ being defined to match the plane (xOy) in the domain $y^* > 0$.

In addition, the setup is designed to study the influence of perturbations of the axisymmetry. Four independent cylinders can be fixed on the sphere in the cross-flow directions as shown in figure 2.1(c). The length of a disturbance is 100 mm, *i.e.* $1.4D$; its diameter is denoted by d. The effects on the wake are considered for one, two (diametrically opposed) or four cylinders of diameter $d^* = d/D = 0.029$ on the sphere; the corresponding results are referred by $m = 1$, $m = 2$ or $m = 4$ disturbed wakes, m being the azimuthal periodicity.

For $m = 1$, additional configurations detail the effects of the size of the disturbance for $d^* \in \{0.017, 0.029, 0.057, 0.086\}$.

Velocity measurements

In this chapter, the wake analyses are made from particle image velocimetry (PIV) and hot-wire anemometry exclusively.

The PIV system is a dual pulse laser (Nd:YAG, 2×135 mJ, 4 ns) combined with two Dantec CCD cameras (FlowSense EO, 4 Mpx). The setup acquires image pairs at a rate of 10 Hz; each acquisition records 2000 image pairs. The measurement system gives access to u_x and u_z in the plane $y^* = 0$. In addition, the three components of the velocity are obtained in the plane $x^* = 0.93$ through stereoscopic PIV. The interrogation window of 32 px $\times$ 32 px corresponds to physical sizes of 1.3 mm $\times$ 1.3 mm in the plane $y^* = 0$ and 1.9 mm $\times$ 1.9 mm in the plane $x^* = 0.93$.

The mean velocities and the Reynolds stresses are measured from the valid vectors of the instantaneous velocity fields; these statistics are taken into account only when more than 1500 valid vectors are obtained from the 2000 measurements.

To get time-resolved velocities in the flow, a hot-wire probe is used; it is oriented to measure u_{xz}. The probe is from Dantec (hot-wire type 55P15, support type 55H22) and uses an overheat ratio of 1.5; it is connected to a DISA55 hot-wire anemometry measurement unit. Mounted on a displacement system, this probe records the velocity in the wake at a sampling frequency of 1 kHz.

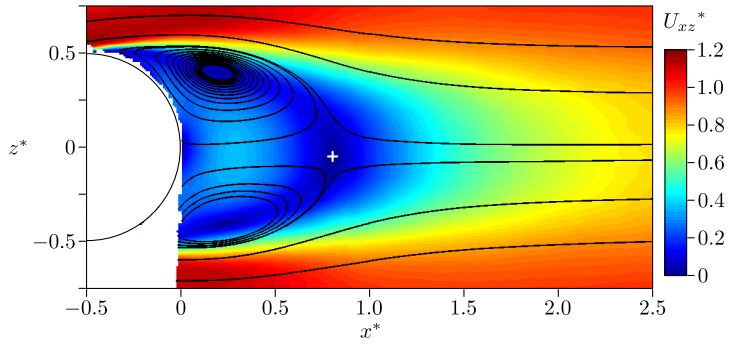

Figure 2.2. Intensity of ${U_{xz}}^*$ in the plane $y^* = 0$; the white cross locates the saddle point.

RS	max (RS)	x^* (max (RS))	r^* (max (RS))
$\langle {u'_x}^{*2} \rangle$	0.105 ± 0.005	0.45 ± 0.01	0.47 ± 0.01
$\langle {u'_r}^{*2} \rangle$	0.090 ± 0.005	0.80 ± 0.01	0.01 ± 0.01
$-\langle {u'_x}^* {u'_r}^* \rangle$	0.045 ± 0.005	0.59 ± 0.01	0.41 ± 0.01

Table 2.1. Maxima of the Reynolds stresses (RS) in the wake and their corresponding locations; the data are reported from PIV in the plane $y^* = 0$ where $u'_r = \pm u'_z$.

2.2 Mean natural flow

The objective of this section is to validate the experimental setup as a relevant method to produce the axisymmetric turbulent wake past a sphere. The mean velocities and the Reynolds stresses are analyzed in the plane $y^* = 0$ and in the cross-flow plane $x^* = 0.93$ in section 2.2.1 and 2.2.2 respectively. Section 2.2.3 is devoted to the periodic dynamics of the wake.

2.2.1 Velocities in the plane $y^* = 0$

The mean velocity field in the plane $y^* = 0$ is presented in figure 2.2. The PIV measurements evidence a recirculation region in the wake that extends up to $x^* = 0.80$. Even if it cannot be directly measured from the velocity field, it seems that the boundary layer separation occurs on the sphere close to the apex as expected for such Reynolds numbers (Yun *et al.*, 2006). Besides, the flow presents a relatively good symmetry referring to the plane $z^* = 0$ without any trace of flow inhomogeneity in the sphere proximity.

The measurements of the Reynolds stresses are plotted in figure 2.3. As for the mean velocity map, the symmetry of the normal stresses and the antisymmetry of the shear stress referring to the plane $z^* = 0$ are satisfactory. The stress intensities are measured maximal on the separatrix; the extrema and their corresponding locations are listed in table 2.1. The spatial distribution of the Reynolds stresses and their intensities are in agreement with the results in the literature (see Jang & Lee, 2008, and references therein).

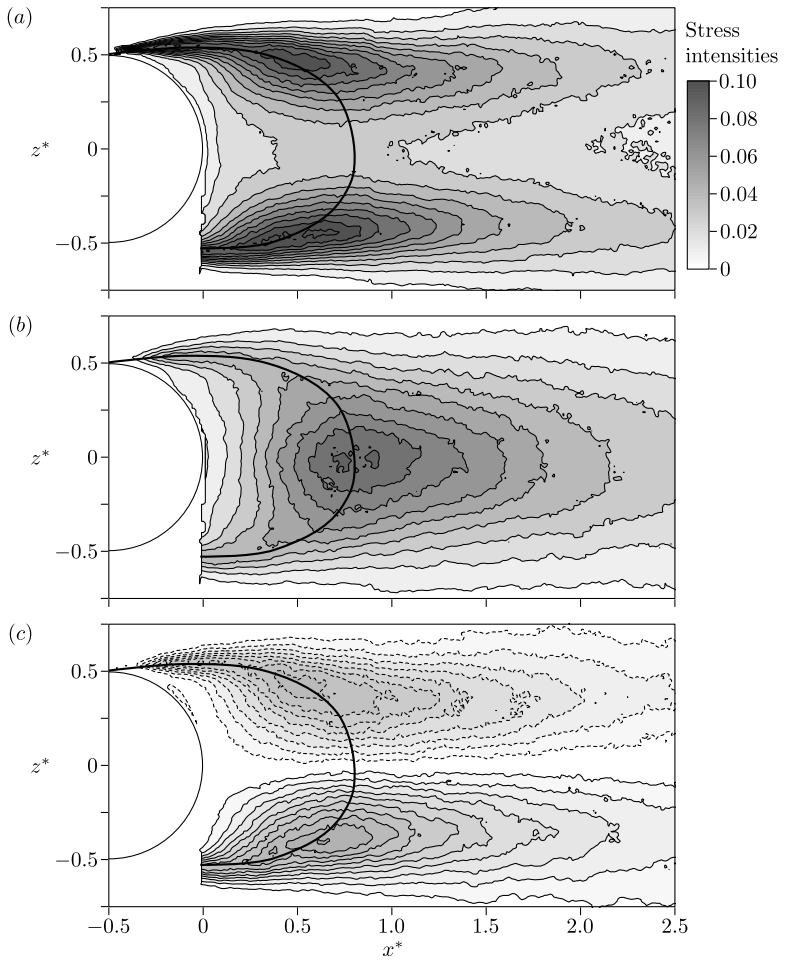

Figure 2.3. Reynolds stresses in the plane $y^* = 0$: $\langle {u'_x}^{*2} \rangle$ (a), $\langle {u'_z}^{*2} \rangle = \langle {u'_r}^{*2} \rangle$ (b) and $\langle u'^*_x u'^*_z \rangle$ (c). The continuous and dashed lines are positive and negative values respectively; the contour intervals are 0.010 in (a)–(b) and 0.005 in (c), the contour 0 is not plotted. The thick black line is the separatrix of the mean recirculation bubble.

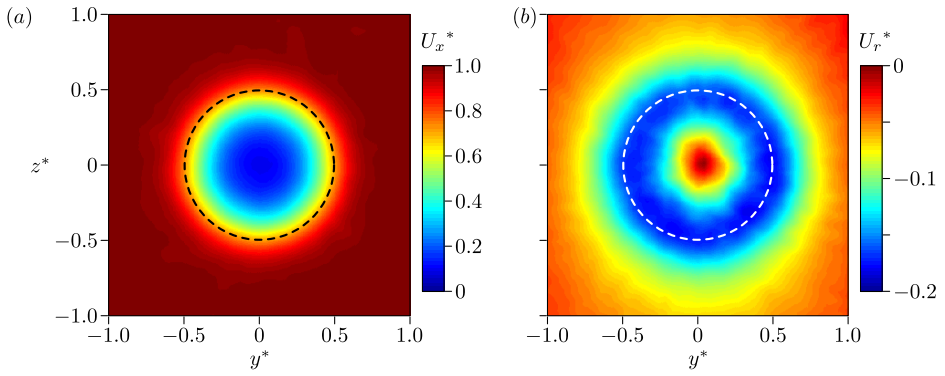

Figure 2.4. Intensities of $U_x{}^*$ (a) and $U_r{}^*$ (b) in the plane $x^* = 0.93$; the dashed circle locates the sphere.

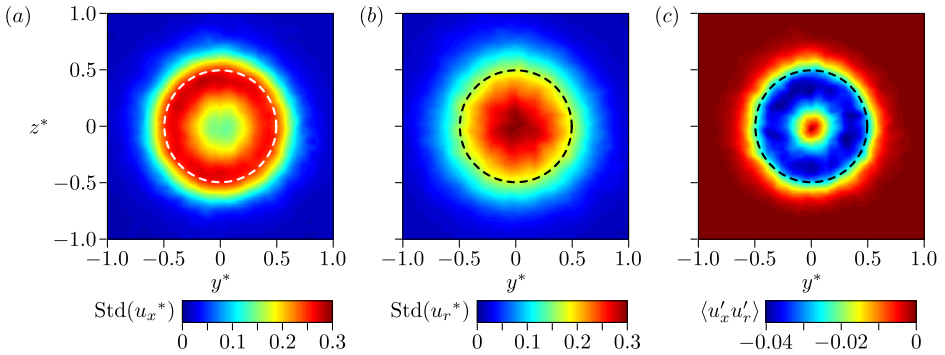

Figure 2.5. Intensities of $\mathrm{Std}(u_x{}^*)$ (a) and $\mathrm{Std}(u_r{}^*)$ (b) and $\langle u_x'{}^* u_r'{}^* \rangle$ (c) in the plane $x^* = 0.93$; the dashed circle locates the sphere.

2.2.2 Velocities in the plane $x^* = 0.93$

The stereoscopic PIV system gives access to the three components of the velocity in the plane $x^* = 0.93$. The results of the mean velocities are presented in figure 2.4. The axisymmetry of the flow is confirmed by both the streamwise and radial velocities. As expected from the measurements presented in figure 2.2, the cross-flow plane at $x^* = 0.93$ is located just downstream of the end of the recirculation bubble: $U_x{}^*$ ranges from 0.10 to 1.01.

The maps of the fluctuating velocities in the plane $x^* = 0.93$ are given in figure 2.5. The results validate the axisymmetry in the distribution of the Reynolds stresses and their spatial organizations are consistent with the maps in the plane $y^* = 0$ plotted in figure 2.3.

Using equations (A.27) and (A.28), the momentum conservation of the fluid in a volume containing the geometry gives the force coefficients on the sphere from the cross-flow measurements. Here, there is no pressure information but the pressure terms may be neglected at this streamwise position[1]. The drag force is estimated at $C_x = 0.49$ and the cross-flow force at 0.01. The low value of the cross-flow force is consistent with the

[1]This point is evidenced in chapter 5 in figures 5.6(a)–(b): the mean pressure just downstream of the end of the recirculation bubble is close to the free-flow pressure for three-dimensional wakes.

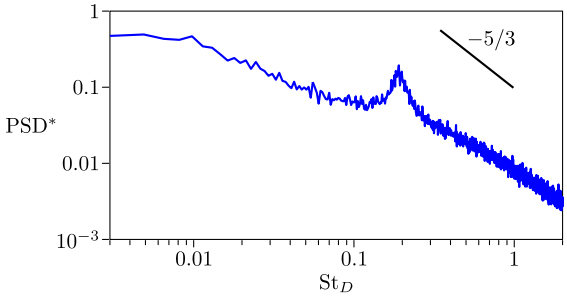

Figure 2.6. Autopower spectrum of a hot-wire signal at $x^* = 1.00$, $y^* = 0$ and $z^* = 0.40$.

axisymmetry of the flow and the drag coefficient is in agreement with the data reported in the literature.

As a consequence, the experimental setup enables to generate a turbulent sphere wake which is axisymmetric in average; the obtained statistics of the velocities are consistent with previous studies. This indicates that the presence of the honeycomb support does not significantly affect the mean properties of the flow. To complete the validation of the setup, the dynamics of the flow is analyzed in section 2.2.3.

2.2.3 Periodic dynamics of the wake

The presence of the honeycomb support does not change the mean flow features but the previous experiments of Tyagi *et al.* (2006) show that the raise of inhomogeneity and of turbulence intensity of the flow may alter the global mode dynamics of the wake.

In order to verify the presence of a coherent wake motion, a hot-wire probe signal is analyzed. Figure 2.6 presents the autopower spectrum of the velocity signal recorded at $x^* = 1.00$, $y^* = 0$ and $z^* = 0.40$. The power spectral density (PSD) characterizes the energy of the different scales in the wake at this probe location. The low values of Strouhal number ($\mathrm{St}_D \lesssim 0.2$) correspond to the large-scale structures of turbulence in the wake. The peak at $\mathrm{St}_D = 0.19$ indicates a significant contribution of the periodic oscillations at this Strouhal number which is consistent with the frequencies of vortex shedding reported in literature at this Reynolds number (Sakamoto & Haniu, 1990; Yun *et al.*, 2006). Furthermore, the smaller scales, *i.e.* the larger frequencies (for $\mathrm{St}_D \gtrsim 0.3$), are related to the inertial range of turbulence. It is worth mentioning that, for the inertial range, the Kolmogorov theory predicts a power-law distribution of energy of coefficient $-5/3$ in the case of an homogeneous and isotropic turbulence.

In order to describe the envelops of the global mode, the PSD of the hot-wire signals are considered for different probe positions. The probe is moved in the plane $y^* = 0$ from $z^* = -0.71$ to $z^* = 0.71$ by steps of 0.07 for $x^* = 0.5$, 1.0, 1.5 and 2.0. The obtained spectra are presented in figure 2.7. One can see that the characteristic frequency at $\mathrm{St}_D = 0.19$ is a global property of the flow but it is only measured downstream of the mixing layers, at $z^* \approx \pm 0.4$. As x increases, the energy of the coherent process gradually emerges from the one of the large-scale structures of turbulence. Hence, the hot-wire probe clearly evidences the unsteady global mode in the wake but principally downstream of the end of the recirculation bubble. Such results are reminiscent of the observations of Berger *et al.* (1990): a large-scale antisymmetric structure dominates the near wake while the

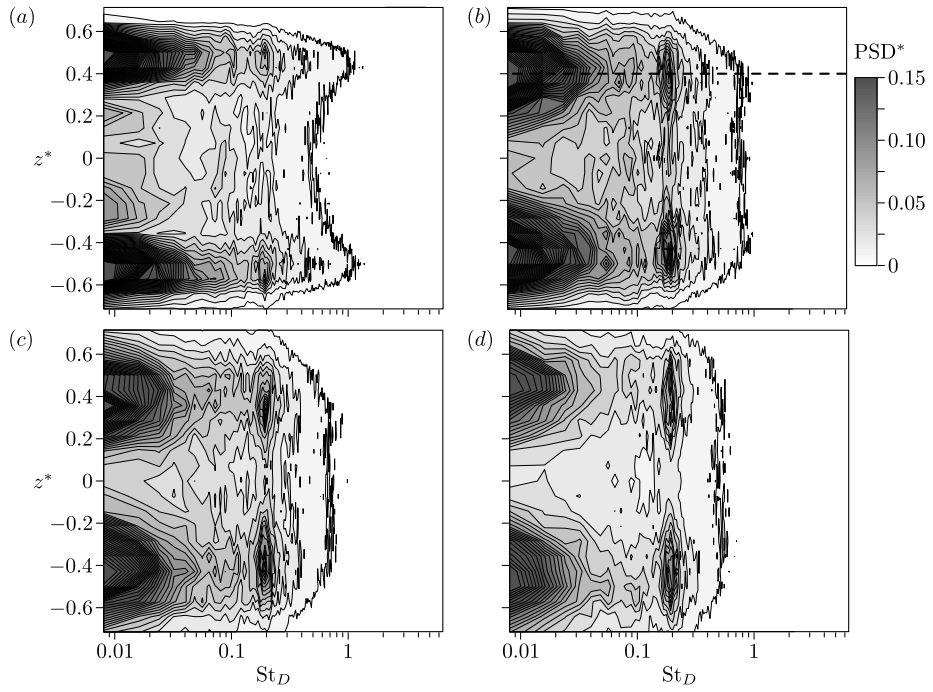

Figure 2.7. Autopower spectra from hot-wire measurements in the plane $y^* = 0$ depending on z^* at $x^* = 0.5$ (a), $x^* = 1.0$ (b), $x^* = 1.5$ (c) and $x^* = 2.0$ (d). The contour interval is 0.01. The dashed line in (b) corresponds to the spectrum plotted in figure 2.6.

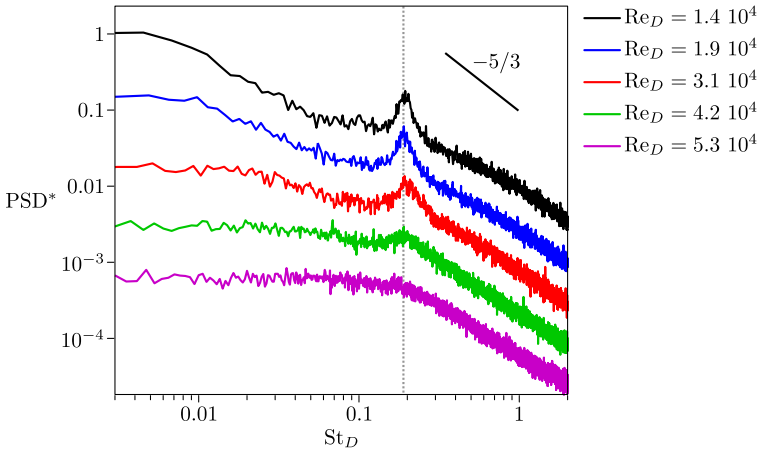

Figure 2.8. Autopower spectrum of a hot-wire signal at $x^* = 1.00$, $y^* = 0$ and $z^* = 0.40$ for different Reynolds numbers. The spectra are offset after successive divisions by $10^{0.5}$ as Re_D increases. The dashed line locates $\mathrm{St}_D = 0.19$.

velocity fluctuations in the immediate wake region are rather related to high frequency shear layer instabilities.

This spectral analysis is completed by the exploration of the effects of the Reynolds number on the energy of the oscillating global mode. The autopower spectra obtained by the hot-wire probe at $x^* = 1.00$, $y^* = 0$ and $z^* = 0.40$ are presented in figure 2.8 for various free-flow velocities. There is a clear attenuation of the global mode activity in front of the one of the large-scale structures of turbulence as the Reynolds number increases: the peak of energy at $\mathrm{St}_D = 0.19$ is well defined for $\mathrm{Re}_D < 4\ 10^4$ but over this value, there is no more peak in the PSD of the velocity signal. This observation tends to indicate that the higher the Reynolds number, the less energetic the coherent structures in front of the incoherent ones.

As a consequence, the experimental setup allows the study of the axisymmetric wake past a sphere at $\mathrm{Re}_D = 1.9\ 10^4$. Even if the presence of a rigid honeycomb support upstream of the geometry increases the inhomogeneity and the turbulence intensity of the free-stream flow, the main features of the sphere wake at this Reynolds number are close to other studies presented in the literature.

The statistics of the wake symmetries are now detailed in section 2.3.

2.3 Statistics of the axisymmetry

First, the results associated with the natural flow are considered in section 2.3.1 studying the azimuthal orientation of the instantaneous flow; then, the effects of disturbances of the axisymmetry of the setup are presented in section 2.3.2.

2.3.1 Instantaneous topology of the natural flow

The instantaneous topology of the natural flow is successively studied in the cross-flow plane $x^* = 0.93$ and in the plane $y^* = 0$.

Topology in the plane $x^* = 0.93$

In order to obtain details on the flow dynamics, the instantaneous snapshots of the wake in the plane $x^* = 0.93$ are used. The barycenter of the momentum deficiency is an indicator of the position of the instantaneous wake in the cross-flow direction. From the stereoscopic PIV snapshots, the corresponding positions y_W and z_W are calculated as

$$y_W{}^* = \frac{\iint y^* \cdot (1 - u_x{}^*)\,\mathrm{d}s}{\iint (1 - u_x{}^*)\,\mathrm{d}s}, \tag{2.1}$$

and

$$z_W{}^* = \frac{\iint z^* \cdot (1 - u_x{}^*)\,\mathrm{d}s}{\iint (1 - u_x{}^*)\,\mathrm{d}s}, \tag{2.2}$$

with a domain of integration limited[2] to $u_x{}^* < 0.5$ in the plane $x^* = 0.93$. The associated positions in the cylindrical coordinate system are denoted by r_W and θ_W.

A sample snapshot is shown in figure 2.9(a); its barycenter of momentum deficiency is measured at $r_W{}^* = 0.21$ and $\theta_W = 197°$. By analyzing the 2000 instantaneous measurements, the probability distributions of r_W and of θ_W can be evaluated. The corresponding probability density functions (PDF) are presented in figures 2.9(b)–(c); the results show that $r_W{}^*$ ranges in the interval [0,0.35] with a most probable value of 0.12 ± 0.01; this latter quantity is an indicator of the instantaneous wake asymmetry. In parallel, the constant value of PDF(θ_W) indicates that all the azimuths are identically explored by the wake as expected from the axisymmetry of the mean flow.

Consequently, the statistics prove that the axisymmetry of the mean flow is due to the exploration of all the azimuths.

The topology of the instantaneous flow for a given azimuth can now be detailed from conditional averaging: the 2000 snapshots are treated as follows. First, the instantaneous orientation of the wake θ_W is obtained. Then, a rotation of $-\theta_W$ is applied to the velocity fields so that the barycenter of momentum deficiency becomes centered on $\theta = 0$. Finally the 2000 rotated velocity fields are averaged to obtain the mean flow associated with the orientation $\theta_W = 0$. Given the axisymmetry of the setup, this approach is strictly equivalent to a conditional averaging performed after selection of the wakes for which $\theta_W = 0$. The main interest of this method in comparison to a direct conditional averaging is the consideration of all of the 2000 snapshots instead of the few snapshots verifying $\theta_W \approx 0$. In particular, it allows the calculation of both the mean velocities and their fluctuations.

The corresponding maps of the streamwise velocity $\Omega_x{}^*$ and of the fluctuations of streamwise velocity Std($u_x{}^*$) are presented in figure 2.10. Obviously, such a conditional averaging

[2]The domain of integration is limited to get rid of the proper wake of the disturbances that are added in section 2.3.2.

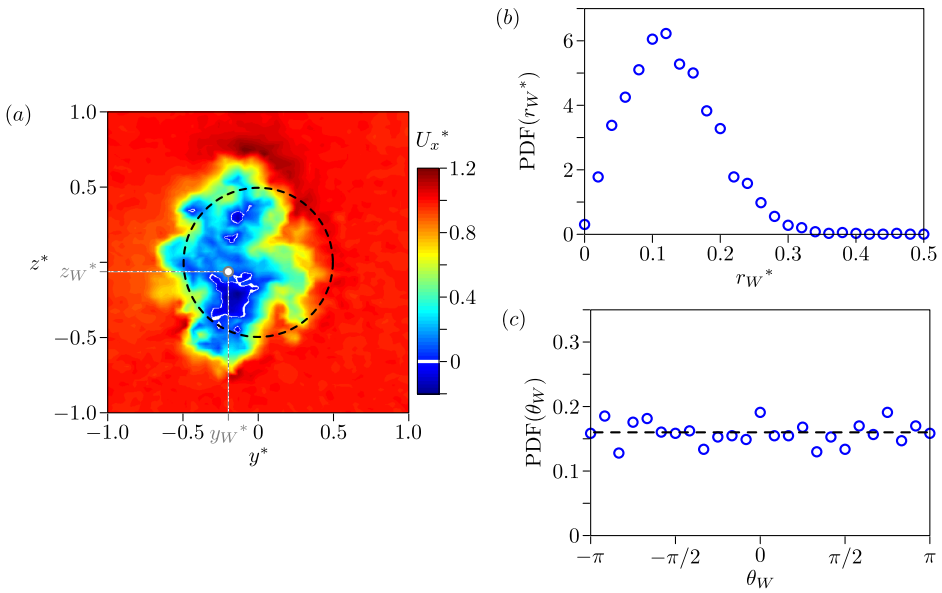

Figure 2.9. Barycenter of momentum deficiency of a sample snapshot in the plane $x^* = 0.93$ (a) and probability distributions of $r_W{}^*$ (b) and of θ_W (c).

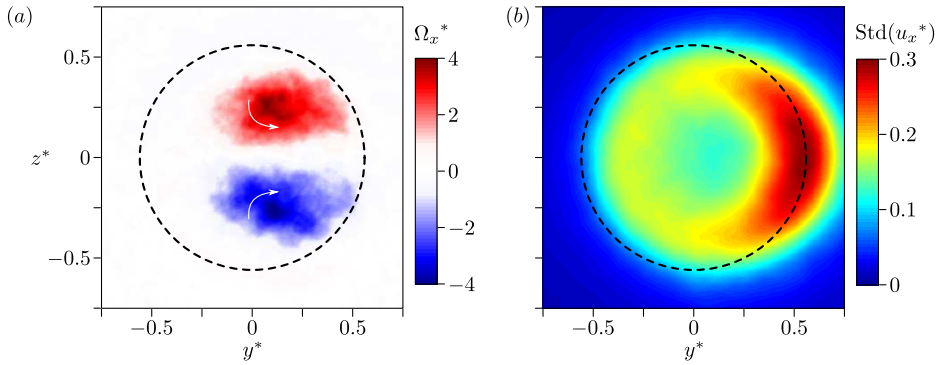

Figure 2.10. Mean streamwise vorticity $\Omega_x{}^*$ (a) and fluctuations of streamwise velocity Std($u_x{}^*$) (b) in the plane $x^* = 0.93$ for the natural flow when $\theta_W = 0$.

leads to an off-centered wake, oriented in the direction $\theta = 0$. However, the results evidence a non-trivial pair of counter-rotating vortices developing downstream of the sphere. This flow structure is reminiscent of the two thread vortices observed in the laminar regime (compare with figure 1.8*b*). It is a signature of the instantaneous cross-flow force that is present on the sphere at this Reynolds number but that cancels out in average due to its random orientation. The force estimation using equation (A.28) gives $C_y = -0.08$. On the other hand, it is observed in figure 2.10(*b*) that the fluctuations of streamwise velocity are concentrated on the side of the wake, *i.e.* at $\theta \approx 0$ and $r^* \approx 0.5$.

As a result, figure 2.10 depicts the mean structure of the flow for $\theta_W = 0$; one can recognize the signature of the unsteady planar symmetric regime that appears after the second bifurcation of the laminar wake at $\mathrm{Re}_D \approx 280$ (see section 1.2.3). The distributions of ${\Omega_x}^*$ and of $\mathrm{Std}({u_x}^*)$ are consistent with the shedding of parallel vortex loops oriented in the direction $\theta = 0$ (imagine figure 1.7 with $\theta_W = 0$).

Since all the azimuthal directions explored by the wake are equiprobable, the axisymmetric mean flow visible in figures 2.4 and 2.5 corresponds to an azimuthal averaging of the flow presented in figure 2.10. It is worth mentioning that the intensities of $\mathrm{Std}({u_x}^*)$ are of similar amplitude in figures 2.5(*a*) and 2.10(*b*). This results from the construction of the fluctuations of velocity of the axisymmetric mean flow visible in figure 2.5(*a*). It is a superposition of two terms: $\langle \mathrm{Std}\left(u_x(\theta_W = 0)\right)\rangle_\theta$ and $\mathrm{Std}(U_x(\theta_W = 0))_\theta$, where $\langle ... \rangle_\theta$ and $\mathrm{Std}(...)_\theta$ refer to the mean and the standard deviation of the azimuthal statistic respectively.

Now that the flow topology in a cross-flow plane is detailed for a given value of θ_W, the confrontation with the instantaneous PIV measurements in the plane $y^* = 0$ enables to have a three-dimensional view of this asymmetric topology.

Topology in the plane $y^* = 0$

The construction of the asymmetric flow for a given wake orientation is based on conditional averaging of the snapshots. Hence, an indicator of the wake direction, similar to the barycenter of momentum deficiency, is needed in the plane $y^* = 0$. A characteristic parameter of the instantaneous flow asymmetry is the orientation of the recirculating flow; for each snapshot, the space-averaged value of ${u_z}^*$ in the recirculation bubble, denoted ${u_{zr}}^*$ and defined in equation (2.3), is considered as a discriminating parameter.

$$ {u_{zr}}^* = \frac{1}{0.36} \int_{x^*=0.1}^{0.7} \int_{z^*=-0.3}^{0.3} {u_z}^*(x^*, y^* = 0, z^*)\, \mathrm{d}x^* \mathrm{d}z^*. \tag{2.3} $$

Conditional averaging is performed to obtain the states of the flow when the wake is oriented in one azimuthal direction. All the difficulty lies in the determination of the thresholds used in the conditional averaging, the objective being to extract the instantaneous snapshots associated with the orientations $\theta_W = 0$ (or π) and $\pm\pi/2$. Here, the thresholds are optimized to present the best correspondence with the distribution of mean streamwise velocity measured by stereoscopic PIV for $\theta_W = 0$ in the plane $x^* = 0.93$.

The probability distribution of ${u_{zr}}^*$ is given in figure 2.11 with the thresholds used for the conditional averaging. One can see a residual asymmetry in the PDF which corresponds to the slightly negative value of ${U_z}^*$ in the recirculation bubble of the flow presented in figure 2.2.

The comparison of the velocity profiles between the stereoscopic PIV data in the plane $x^* = 0.93$ (see figure 2.10) and the measurements in the plane $y^* = 0$ is given in figure 2.12 for $\theta_W = \pm\pi/2$ and in figure 2.13 for $\theta_W \in \{0, \pm\pi\}$.

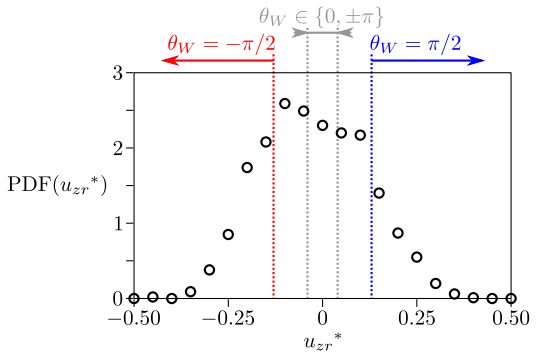

Figure 2.11. Probability density functions of $u_{zr}{}^*$ and thresholds used to obtain the flow topologies for $\theta_W \in \{0, \pm\pi\}$ and $\theta_W = \pm\pi/2$ from conditional averaging.

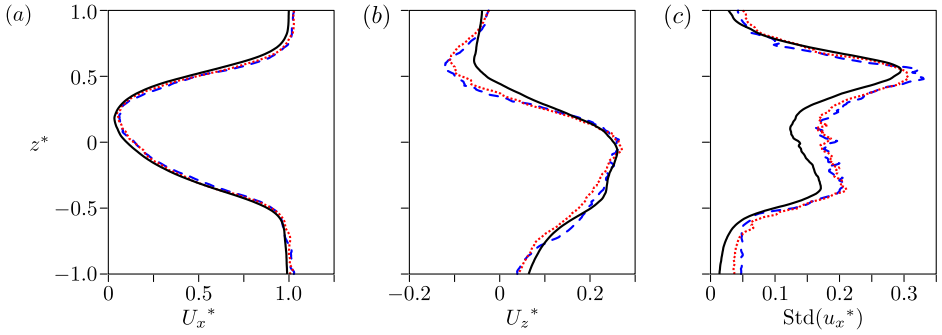

Figure 2.12. Profiles of $U_x{}^*$ (a), $U_z{}^*$ (b) and Std($u_x{}^*$) (c) at $x^* = 0.93$ and $y^* = 0$ for $\theta_W = \pi/2$: —, stereoscopic PIV (see section 2.3.1); - - -, PIV in the plane $y^* = 0$ for $\theta_W = \pi/2$; $\cdots$, PIV in the plane $y^* = 0$ for $\theta_W = -\pi/2$. The data for $\theta_W = -\pi/2$ are plotted against $-z^*$ to facilitate comparison.

In figure 2.12(a), the correspondence between the streamwise momentum deficiencies is clear which is expected since it defines the thresholds presented in figure 2.11. The interesting point is the concordance between the levels of $U_z{}^*$ and Std($u_x{}^*$) in figures 2.12(b)–(c) even if the levels of Std($u_x{}^*$) suffers from the limited number of snapshots verifying the thresholds on $u_{zr}{}^*$.

In parallel, the comparison between the conditional averaging for the wake orientation $\theta_W \in \{0, \pm\pi\}$ is presented in figure 2.13. The similarity between the streamwise velocity profiles is clear but expected by construction. Besides, the trends on $U_z{}^*$ and on Std($u_x{}^*$) show a reasonable correspondence even if the fluctuations of streamwise velocity are slightly overestimated using the data in the plane $y^* = 0$.

As a result, the conditional averaging using the thresholds on the quantity $u_{zr}{}^*$ may allow to recover quantitatively the flow field in the plane $y^* = 0$ for the cases $\theta_W \in \{0, \pm\pi/2, \pm\pi\}$.

The velocity fields in the plane $y^* = 0$ for the wake orientations $\theta_W = \pi/2$, $\theta_W = -\pi/2$ and $\theta_W \in \{0, \pm\pi\}$ are presented in figure 2.14. First of all, it is clear that the flows for $\theta_W = \pm\pi/2$ present a symmetrical dependence on each other referring to the plane $z^* = 0$. Second, a circulation around the sphere related to the cross-flow force on the sphere for the

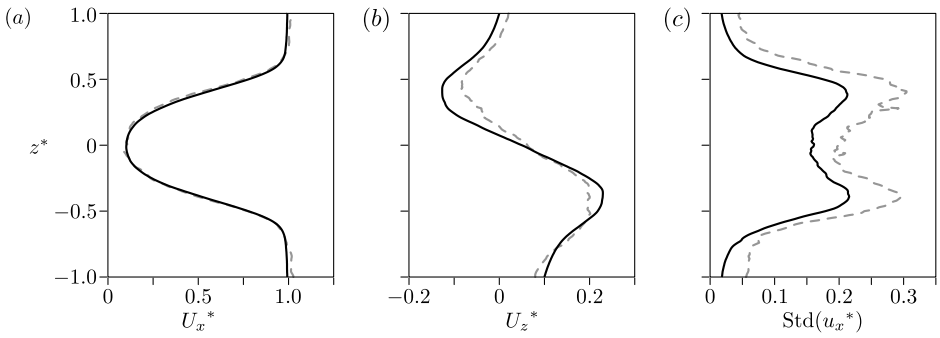

Figure 2.13. Profiles of $U_x{}^*$ (a), $U_z{}^*$ (b) and Std($u_x{}^*$) (c) at $x^* = 0.93$ and $y^* = 0$ for $\theta_W \in \{0, \pm\pi\}$: —, stereoscopic PIV in the plane $x^* = 0.93$ (see section 2.3.1); - - -, PIV in the plane $y^* = 0$.

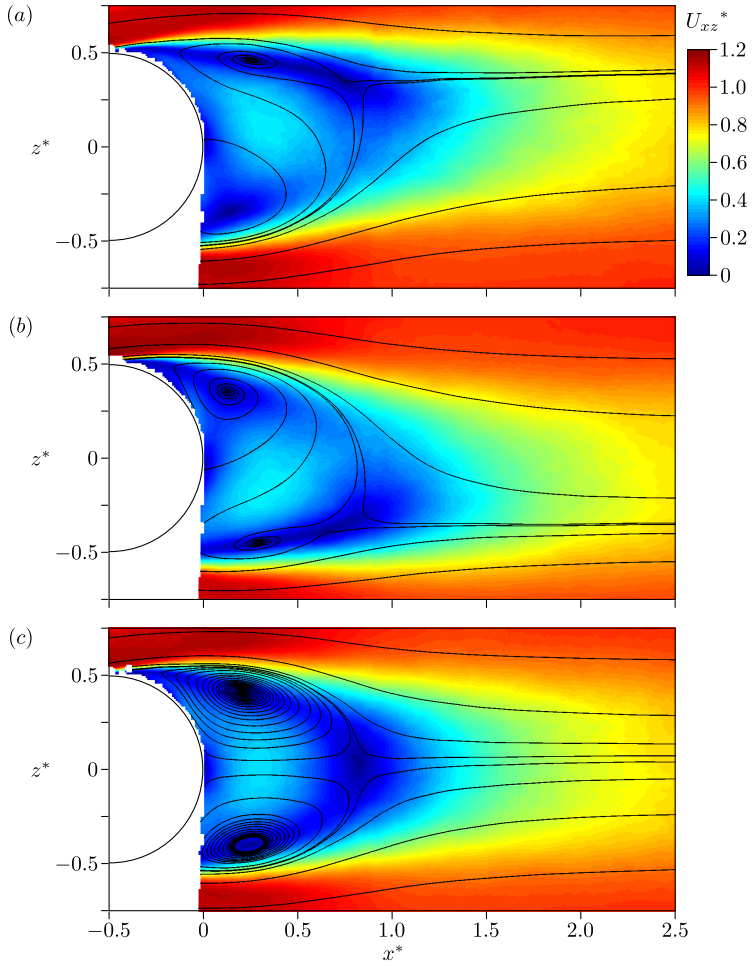

Figure 2.14. Intensity of $U_{xz}{}^*$ in the plane $y^* = 0$ for $\theta_W = \pi/2$ (a), $\theta_W = -\pi/2$ (b) and $\theta_W \in \{0, \pm\pi\}$ (c) obtained from conditional averaging.

cases $\theta_W = \pm\pi/2$ (see figures 2.14*a*–*b*) seems visible; it is also associated with the pair of counter-rotating vortices evidenced in figure 2.10(*a*).

The principal interest of these velocity maps is to build a complete three-dimensional view of the asymmetric flow topology for a given wake orientation. Furthermore, it is observed that the flows are strongly different not only in the recirculation region but also in the potential flow. Hence, there is a concordance between the topology of the recirculation region and of the potential flow. In other words, the information of the circulation around the geometry related to the cross-flow force is equally present in the organization of the recirculating flow.

When slight asymmetries are introduced in the setup such as crossing wires to fix the sphere, the main features of the flow may remain identical (global mode dynamics, mixing layer activity...) but the axisymmetry of the mean flow is altered. The effects of disturbances of the axisymmetry are considered in section 2.3.2.

2.3.2 Azimuthally disturbed flows

The effects of azimuthal disturbances are presented varying the periodicity and the size successively.

Effect of the periodicity of the disturbance

Three different configurations are tested using perturbations of diameter $d^* = 0.029$ (see figure 2.1*c*) with the azimuthal periodicities $m = 1$, 2 and 4. The corresponding intensities of fluctuating streamwise velocity in the plane $x^* = 0.93$ are presented in figure 2.15. In spite of the small size of the rods, the azimuthal periodicity of the setup is visible in the velocity statistics, especially for the cases $m = 2$ and $m = 4$.

Autopower spectra in the wake of the disturbed flows can be confronted to the natural case in order to study the influence of the disturbances on the global mode dynamics. The spectra obtained with a hot-wire probe at $x^* = 1.00$ and $r^* = 0.40$ are presented in figure 2.16; for each configuration, the azimuthal position of the probe is adapted to avoid the proper wakes of the disturbances. The hot-wire allows to measure the PSD of the velocity fluctuations near their maximum intensity visible in figure 2.15. The spectra show that the global mode is measured in the wake for all the azimuthal disturbances at $\mathrm{St}_D = 0.19$. Nevertheless, the energy of the periodic motion tends to decrease in comparison to the activity of the other large-scale structures as the periodicity is increased: the peak of energy in the spectrum becomes less clear when m is increased.

Now, as for the natural flow, the statistics of the wake orientation θ_W can be studied from the instantaneous velocity measurements. The plane of stereoscopic PIV is at $x^* = 0.93$ which corresponds to $x = 32d$; hence, the proper wake of the disturbing cylinder so far downstream is in the domain ${u_x}^* > 0.5$. Since the domain of integration used to define y_W and z_W in equations (2.1) and (2.2) is limited to ${u_x}^* < 0.5$, the rods do not directly alter the calculation of the barycenter of momentum deficiency.

First, the probability distributions of ${r_W}^*$ for $m = 1$, 2 and 4 are confronted to the reference case in figure 2.17. It is observed that all the PDF presents a similar shape; the main difference lies in the slight variations of the mean value of ${r_W}^*$. It gradually increases from 0.130 for the reference case to 0.154 for $m = 4$ as m is incremented.

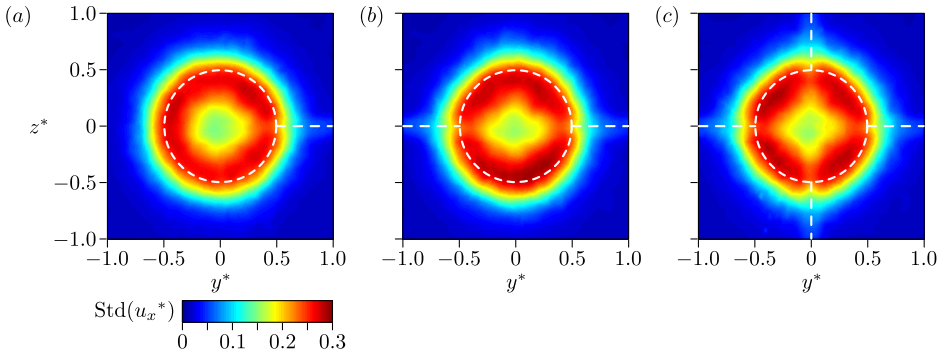

Figure 2.15. Intensities of Std($u_x{}^*$) in the plane $x^* = 0.93$ for azimuthally disturbed flows with perturbations of diameter $d^* = 0.029$: $m = 1$ (a), $m = 2$ (b) and $m = 4$ (c).

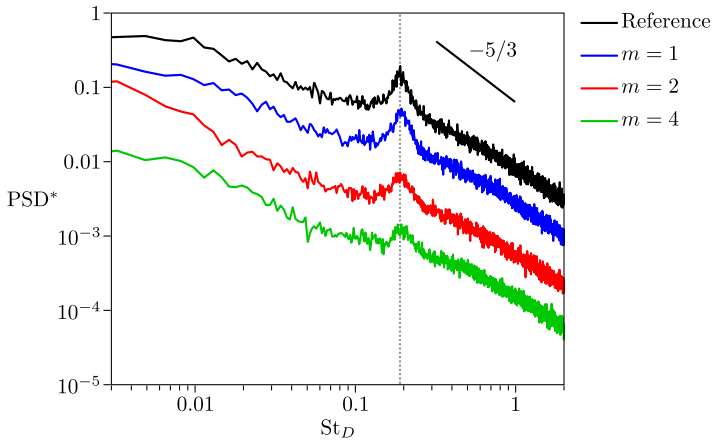

Figure 2.16. Autopower spectrum of a hot-wire signal at $x^* = 1.00$, $r^* = 0.40$ for the reference flow and the azimuthally disturbed flows ($m = 1$, 2 and 4). The azimuth of the hot-wire probe is set to avoid the proper wake of the disturbing cylinders. The data for $m = 1$, 2 and 4 are offset after successive divisions by $10^{0.5}$.

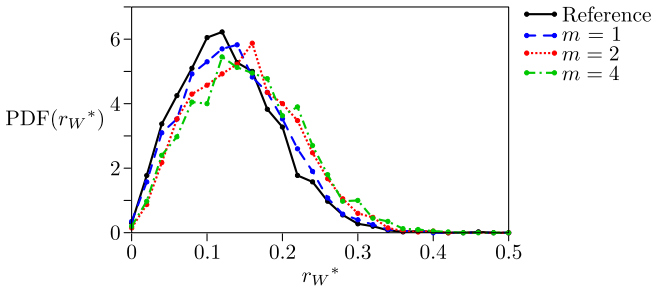

Figure 2.17. Probability density functions of $r_W{}^*$ for the reference flow and the azimuthally disturbed flows ($m = 1$, 2 and 4).

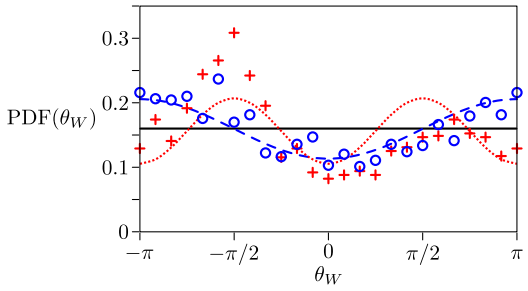

Figure 2.18. Probability density functions of θ_W for the $m = 1$ (◯) and $m = 2$ (+) disturbances. The dashed and dotted lines are the best $m = 1$ and $m = 2$ periodic fits of the experimental data respectively. The continuous line is the uniform distribution.

On the contrary, the probability distributions of θ_W given in figure 2.18 show strong differences depending on the azimuthal periodicity of the disturbance. The experimental results for one cylinder clearly evidence a $m = 1$ azimuthal periodicity in the PDF: the wake has one preferred position at the opposite of the disturbing cylinder. However, there is no clear selection of the wake orientation since the position $\theta_W = \pm\pi$ is only two times more probable than the position $\theta_W = 0$. So the disturbance introduces a slight modulation in the PDF of θ_W; this observation is consistent with the axisymmetry that persists in figure 2.15(a).

Similarly, the configuration with two disturbances leads to a $m = 2$ periodicity of PDF(θ_W) with two maxima at approximately $\pm\pi/2$. Such a probability distribution indicates that the flow presents two preferred orientations. It is worth noting that the experimental PDF presents an asymmetry between $-\pi/2$ and $\pi/2$ which is equally visible in the map of Std($u_x{}^*$). Indeed, in figure 2.15(b), the energy of the velocity fluctuations is stronger for $\theta = -\pi/2$ than for $\theta = \pi/2$. Hence, a residual asymmetry is measured as the wake explores more the azimuth $-\pi/2$ than $\pi/2$.

Finally the data obtained for the configuration $m = 4$ (not presented here) are lacking precision to evidence any $m = 4$ periodicity of PDF(θ_W); this shows the limits of a method based on the barycenter of momentum deficiency in the azimuthal description of the wake dynamics.

As a conclusion, a slight azimuthal perturbation is proved to select one or several preferred wake orientation depending on its periodicity. To terminate this study, one can consider the effect of the diameter of the azimuthal perturbation on the flow statistics.

Effect of the size of the disturbance

Some experimental setups in the literature have a physical connection between the geometry and a recording device located outside of the test section. Such a wire connection, usually through the supports, leads to significant intrusion of the system holding the body, typically with a characteristic size of 0.1 to 0.2D. The following experiments give some quantitative information on the modifications of the wake statistics depending on the size and location of a $m = 1$ azimuthal perturbation.

The probability density functions of θ_W associated with $m = 1$ disturbances of different diameters are presented in figure 2.19. For clarity, the experimental data are not plotted,

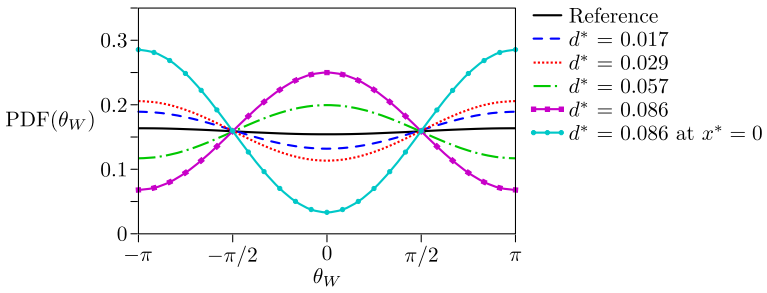

Figure 2.19. Probability density functions of θ_W for the reference case and for the $m = 1$ configurations. The experimental data are not plotted; the curves are their best $m = 1$ fits.

only the best $m = 1$ periodic fits of expression

$$K\cos(\theta_W) + \frac{1}{2\pi} \tag{2.4}$$

are presented. The first intuitive conclusion that can be made is that the larger the disturbance, the less uniform the PDF; in other words, $|K|$ increases with d^*.

The second observation is that the sign of K in equation (2.4) depends on the size of the disturbance. Indeed, the statistics show that the wake is mostly oriented toward the opposite of the disturbance for $d^* = 0.017$ and 0.029 (most probable orientation at $\theta_W = \pm\pi$) while the preferred orientation of the wake is $\theta_W = 0$ for $d^* = 0.057$ and 0.086. However, when the largest disturbance ($d^* = 0.086$) is moved[3] from $x^* = -0.5$ to $x^* = 0$, a change of wake orientation is observed. These results are an indicator of the high sensitivity of the azimuthal phase shift between the wake and the disturbance.

As a consequence, the preference toward one azimuthal direction increases with the disturbance size but the wake can be either oriented toward the perturbation or toward its opposite direction depending on the disturbance size and position. These results are reminiscent of the selection of the phase shift at 0 or π proved theoretically by Meliga *et al.* (2009*a*) using global stability analysis.

[3]For this configuration only, the disturbance is held from the side of the test section.

2.4 Concluding remarks

The alternative system consisting in fixing the sphere on an axis positioned upstream of the body is relevant to produce a turbulent wake with a statistical axisymmetry. The instantaneous wake tends to be off the axis of symmetry and the axisymmetry is restored due to the exploration of all the azimuthal directions.

The flow topology for a given wake orientation can be extracted by conditional averaging in both planes $x^* = 0.93$ and $y^* = 0$. The obtained flow field is reminiscent of the unsteady planar symmetric flow in the laminar regime.

In parallel, it is observed that at large Reynolds numbers, the unsteady global mode may disappear because it becomes less energetic than the large-scale structures of turbulence. On the other hand, traces of the axisymmetry breaking that occurs at $\mathrm{Re}_D \approx 210$ are still reported in the turbulent regime; the associated asymmetric flow is responsible for a permanent lift force and certainly for part of the drag.

Finally, the use of azimuthal perturbations evidences the high sensitivity of the axisymmetry of the wake. Depending on the periodicity of the disturbance, the wake selects one or several preferred orientations; the azimuthal phase shift between the wake and the perturbation is 0 or π and relies on the amplitude and position of the perturbation.

The selection of different preferred orientations may result in multi-stable behaviors. This is the case of the geometry considered in chapter 3.

Chapter 3

Sensitivity analyses of a bistable configuration

Most of the following results are published in Grandemange *et al.* (2012*b*).

This chapter aims at exploring the sensitivity of the wake past a three-dimensional blunt body with a fixed axisymmetric flow separation at $\mathrm{Re}_D = 2.1\ 10^4$. Experiments of passive control using reasonably small devices are performed to disturb the flow. The impact of the control device is reported through sensitivity maps of global mode frequency, pressure on the body and estimation of the drag.

Abstract

The turbulent wake over a three-dimensional blunt body with an axisymmetric trailing edge is investigated at $\mathrm{Re}_D = 2.1\ 10^4$. The flow presents a favored $m = 2$ azimuthal periodicity due to the mounting of the body. It is proved that the wake is bistable with the cohabitation of two asymmetric states. Topology shifts restore the symmetry of the mean flow; the succession of the states is random but, in average, the shifts are reported after a large number of global mode periods. The statistical symmetry is highly sensitive to any antisymmetric disturbance. As a consequence, depending on its position, a small control cylinder in the near wake fixes the flow to one asymmetric topology and it may affect both shedding activity and drag. In particular, the bistable behavior of the flow is altered when the center of the recirculation region is disturbed, these configurations resulting in drag reduction. On the other hand, preserving the mean flow symmetry, a thin control ring has a greater impact on the global mode frequency and the drag. These experiments point out the high sensitivity of three-dimensional wake to perturbations which motivates the studies depicted in part II past parallelepiped bodies.

Contents

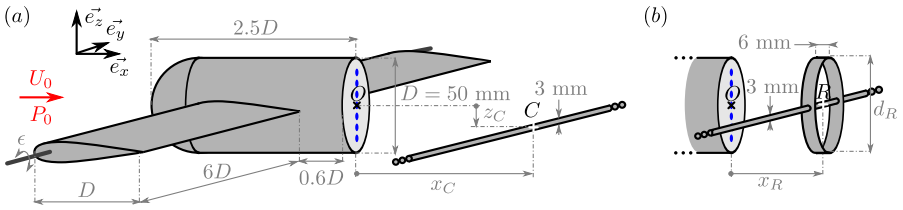

Figure 3.1. Experimental setup of the body controlled by a 3 mm cylinder (a) and a ring (b); O sets the origin of the coordinate system. The blue dots locate the pressure taps on the base.

3.1 Experimental setup

The Eiffel-type wind tunnel is an open-loop air flow facility. The turbulent intensity is less than 0.3% and the homogeneity of the velocity over the 400 mm × 400 mm blowing section is 0.4%. The wake is generated by a three-dimensional symmetric blunt body made up of a streamwise circular cylinder of diameter $D = 50$ mm and a half sphere forebody (see figure 3.1). The total length is $L = 125$ mm. The axisymmetric body is supported by two NACA 0021 profiles[1] fixing the azimuthal planes of symmetry (xOy) and (xOz). Most of the experiments are performed with the body aligned to the incoming flow however, when specified, a small pitching angle ϵ is set to induce an antisymmetric disturbance. The main flow velocity is $U_0 = 6.5$ m s^{-1} and the Reynolds number is $\mathrm{Re}_D = U_0 D/\nu = 2.1\ 10^4$.

The separated flow is first controlled by a cylinder of 3 mm diameter; it is oriented in the y direction and moved in the wake using a motion controller. x_C and z_C refer to the cylinder position (see figure 3.1a). This control geometry may appear surprising as it is bidimensional while it disturbs a fully three-dimensional flow. Indeed, in bidimensional configurations, the experimental work of Parezanović & Cadot (2009) shows that the sensitivity of the flow to the perturbation results from the interactions between the shear layers of the main wake and the vorticity introduced by the disturbance. However, as mentioned in chapters 1 and 2, the flow over three-dimensional geometries may be highly sensitive to any symmetry breaking. Hence, as a first step in the present study, the control cylinder is used to introduce an asymmetry: except when the cylinder is located on the streamwise axis, it is considered as a steady $m = 1$ disturbance of the flow. On the other hand, when ${z_C}^* = 0$, the control cylinder imposes a stagnation point in the wake; therefore, it consists in a local symmetric forcing of the flow.

The other control devices are flat rings with a length of 6 mm and a thickness of 1 mm mounted on a 3 mm diameter rod (see figure 3.1b). x_R is the gap between the base of the body and the center of the ring (point R) as visible in figure 3.1(b). The point R remains on the streamwise axis so that the symmetry of the body is preserved and the rings are associated with $m = 0$ perturbations. Nine ring diameters d_R between $0.7D$ and $1.1D$ are used to disturb the near wake and, more particularly, the mixing layers. Here, the strategy is to disturb the separated shear layers by introducing vorticity with the rings, it is a direct extension of the control experiments presented in Parezanović & Cadot (2012) over a D-shaped cylinder.

[1]The NACA supports can seem very intrusive at first sight as their thickness is $0.21D$ but the forcing they introduce in the flow is relatively small. For example, circular cylinders with a diameter of $0.02D$ would lead to a similar forcing.

The flow analyses are made from bidimensional PIV and stereoscopic PIV in the planes $y^* = 0$ and $x^* = 1.2$ respectively. Statistics from 2000 instantaneous velocity fields estimate the fluctuating velocities. To get the unsteady characteristics of the flow, a hot-wire probe mounted on a three-dimensional traversing mechanism records the velocity in the wake at a sampling frequency of 2 kHz. So, autopower spectra are calculated up to 1 kHz with a resolution of 0.5 Hz.

In addition, the pressure on the body is measured in the plane $y^* = 0$ using two Scanivalve DSA 3217/16 px devices. Thirteen taps are located on the spheric forebody every 15°; seven others give the pressure distribution on the base, the gap between taps on the base is 6 mm. These taps are connected to the acquisition device using 1 m long vinyl tubes going through the NACA supports. The pressure measurements are performed at 1 Hz over a minimum of 120 s. The sampling frequency is limited to 1 Hz to preserve precision. The measurement at 1 Hz is abusively called *instantaneous pressure measurement*; after normalization, it is denoted by c_p in opposition to the mean pressure coefficient $C_p = \langle c_p \rangle$.

In equation (3.1), the pressure drag is estimated by integration of the interpolated pressure on the surface after projection in the streamwise direction. The pressure distributions in each region $z^* > 0$ and $z^* < 0$ are assumed axisymmetric.

$$\begin{aligned} C_{xp} &= \frac{1}{\frac{1}{2}\rho\pi\frac{D^2}{4}{U_0}^2}\left[\iint_{\text{Body}} -P\,\vec{e_n}\;\mathrm{d}s\right].\vec{e_x} \\ &\approx 4\left[\int_{z^*=-0.5}^{0.5} C_p(y^*=0,z^*)\cdot|z^*|\;\mathrm{d}z^*\right]_{\text{Nose}} \\ &\quad -4\left[\int_{z^*=-0.5}^{0.5} C_p(y^*=0,z^*)\cdot|z^*|\;\mathrm{d}z^*\right]_{\text{Base}}. \end{aligned} \tag{3.1}$$

For the uncontrolled flow, the so-evaluated drag is $C_{xpn} = 0.261 \pm 0.002$. Using the experimental method based on momentum deficiency in the far wake as presented in equation (A.27), a larger value of 0.29 is measured, partially due to friction effects. When the control device is in the wake, its contribution to the total drag is not taken into account.

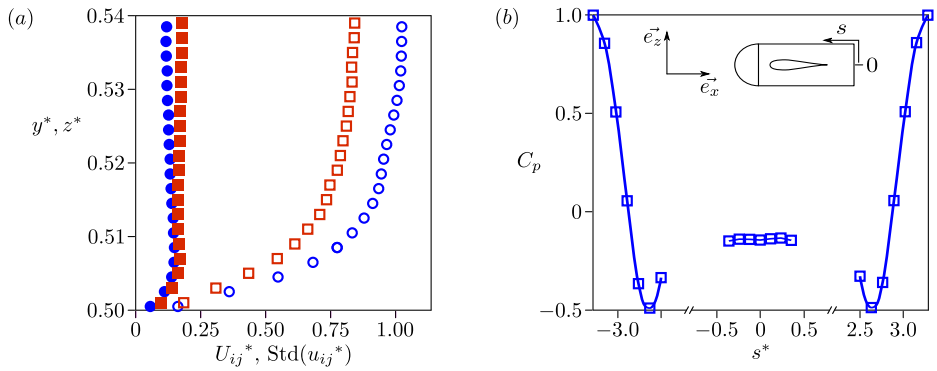

Figure 3.2. (a) Mean and fluctuating velocity profiles (empty and filled symbols respectively) of the boundary layer at the trailing edge: ◯, u_{xz} in the plane $y^* = 0$; □, u_{xy} in the plane $z^* = 0$. (b) Pressure distribution on the body in the plane $y^* = 0$.

	at $y^* = 0$ and $z^* = 0.5$	at $y^* = 0.5$ and $z^* = 0$
$\delta_{0.99}$	1.57 mm $\pm$ 0.05 mm	1.82 mm $\pm$ 0.05 mm
δ_1	0.36 mm $\pm$ 0.02 mm	0.40 mm $\pm$ 0.02 mm
δ_2	0.18 mm $\pm$ 0.02 mm	0.19 mm $\pm$ 0.02 mm
H_{12}	2.0 $\pm$ 0.3	2.1 $\pm$ 0.3

Table 3.1. Boundary layer characteristics at the trailing edge.

3.2 Natural flow

In this section, the mean properties of the flow and its periodic dynamics are first presented. Then, section 3.2.2 focuses on the bistable behavior of the wake.

3.2.1 Mean flow and periodic dynamics

Different flow separations are observed over this body. First, an adverse pressure gradient on the forebody leads to a boundary layer detachment at $s^* \approx \pm 2.5$. The flow then reattaches on the cylindrical part before the massive separation at the trailing edge. The flow characteristics at the trailing edge also depend on the azimuth due to the presence of the NACA supports in the plane $z^* = 0$.

The velocity profiles at the trailing edge in planes $y^* = 0$ and $z^* = 0$ are presented in figure 3.2(a). In the plane $y^* = 0$, the successive detachment and reattachment lead to the mean and fluctuating velocity profiles plotted in figure 3.2(a) by the empty and filled circles respectively. The energy of the fluctuations of velocity diminishes when z^* increases and should slowly tend to the free-flow level of turbulence. This particularly high fluctuation level in the whole boundary layer certainly results from the forebody separations. In the plane $z^* = 0$, the NACA supports introduce additional momentum deficiency and the velocity fluctuations remain large even outside the boundary layer (see empty and filled squares in figure 3.2a). The characteristic lengths obtained from these velocity profiles are listed in table 3.1. The high shape factors point out that the boundary layers at the trailing edge may still be in a transitional stage to turbulence. This interpretation tends to be confirmed by the absence of peak in the velocity fluctuations close to the wall in figure 3.2(a).

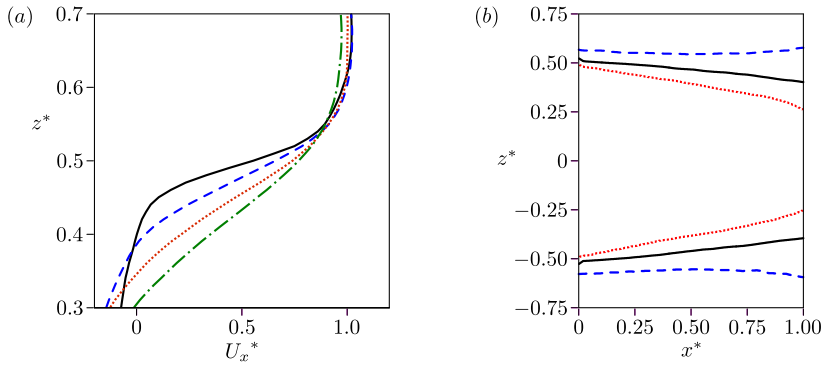

Figure 3.3. (a) Streamwise velocity profiles in the upper mixing layer for different streamwise positions: —, $x^* = 0.2$; ---, $x^* = 0.4$; · · ·, $x^* = 0.6$;-·-, $x^* = 0.8$. (b) Contours of streamwise velocity: · · ·, ${U_x}^* = 0.1$; —, 0.5; ---, 0.9. The data are measured from PIV in the plane $y^* = 0$.

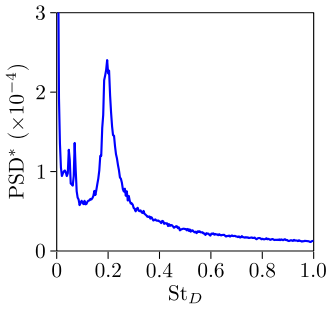

Figure 3.4. Autopower spectrum of a hot-wire probe signal at $x^* = 4.0$, $y^* = 0$ and $z^* = 0.5$.

Downstream of the separation, the mixing layers grow from the trailing edge. Figure 3.3(a) displays the streamwise velocity profiles in plane $y^* = 0$ at different x positions. The size of the mixing layer is defined by $\delta_m(x) = z_{0.9}(x) - z_{0.1}(x)$ with $z_\alpha(x)$ verifying ${U_x}^*(x, z_\alpha(x)) = \alpha$ as in section 1.2.1. The contours of ${U_x}^* = 0.1$, 0.5 and 0.9 (positions of z_α for $\alpha = 0.1$, 0.5 and 0.9) are plotted in figure 3.3(b). The growth of δ_m is approximatively linear between $x^* = 0.1$ and $x^* = 0.7$; $\mathrm{d}{\delta_m}^*/\mathrm{d}x^*$ is measured respectively at 0.17 and 0.18 for the upper and lower mixing layer. The expansion occurs toward the recirculation bubble where ${U_x}^* \sim 0$, the contours ${U_x}^* = 0.9$ being roughly parallel to the streamwise axis. This growth rate is due the proper dynamics of the turbulent shear layers (see section 1.2.1) but also to the oscillations induced by the presence of an unsteady global mode. Indeed, the power spectrum of a hot-wire probe signal at $x^* = 4.0$, $y^* = 0$ and $z^* = 0.5$ reports a wake oscillation at a frequency of 25.8 Hz, *i.e.* $\mathrm{St}_D = 0.199$ (see figure 3.4); the frequency of the global mode is denoted by St_{Dm}. Here, the two peaks at $\mathrm{St}_D \approx 0.05$ and 0.07 correspond to some wind tunnel signatures.

Figure 3.5(a) displays the streamlines and the vorticity field of the mean flow in the plane $y^* = 0$. The natural wake is symmetric referring to the plane $z^* = 0$ with two recirculation structures and two saddle points at $x^* = 0.95$ and $z^* \approx \pm 0.2$ (see figure 3.5b). This topology is consistent with the two pairs of counter-rotating vortices suggested by

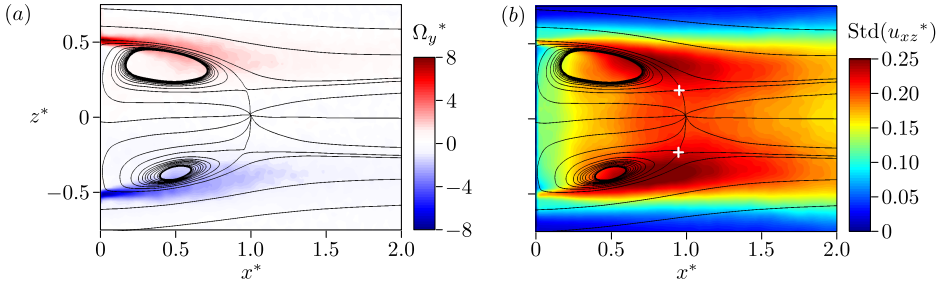

Figure 3.5. Vorticity Ω_y (a) and fluctuating velocities (b) in the plane $y^* = 0$; the white crosses locate the saddle points.

Délery (2013) (see figure 1.10c). The converging streamlines at $z^* \approx \pm 0.2$ for $x^* > 1$ are the signatures of these streamwise vortices in the plane $y^* = 0$: one pair at $z^* \approx 0.2$ and the other at $z^* \approx -0.2$. The vorticity concentrated in the boundary layer vanishes from the detachment to the end of the recirculating bubble. The vorticity is mainly found near the separatrix of the recirculation region and it is clear that the mean recirculation structures do not contain significant vorticity. The maximum fluctuating energy is measured at $z^* \approx \pm 0.4$ and $x^* \approx 0.8$ as visible in figure 3.5(b). These fluctuations are associated with both the turbulent activity of the mixing layers and the development of the unsteady global mode. As expected, the velocity fluctuations are of similar amplitude in the top and bottom of the near wake.

3.2.2 Bistable behavior

In agreement with remarks present in the literature (Délery, 2013; Weickgenannt & Monkewitz, 2000), the symmetry of the wake is highly sensitive to the setup accuracy. A slight incidence ϵ moves the whole wake up or down. Figures 3.6(a)–(b) present the asymmetric wake topology for a slightly nose-up configuration. Measurements in the plane $x^* = 1.2$ show only one pair of counter-rotating vortices at $y^* \approx \pm 0.2$ and $z^* \approx -0.3$ just above a single zone of intense fluctuations; this topology is very similar to the one presented in figure 1.10(d) from Délery (2013). There is also a clear similarity with the topology of the instantaneous wake past the sphere for $\theta_W = -\pi/2$ (see figures 2.10 and 2.14). Therefore, as soon as the symmetry is lost, the unsteady mode develops mostly from the lower part of the wake. It is very likely to correspond to the formation of parallel vortex loops at the end of the recirculation bubble (Achenbach, 1974; Sakamoto & Haniu, 1990; Vilaplana *et al.*, 2013) as visible in figure 1.7. When the symmetry is preserved, these vortex loops must develop statistically from both sides of the wake.

The balanced wake for $\epsilon = 0$ (see figure 3.5) is consistent with an average of two asymmetric topologies, named #1 and #2, each of them being respectively close to the flow presented in figures 3.6(a)–(b) and its symmetric referring to the plane $z^* = 0$. Indeed, averaging the velocity field $\vec{U_\epsilon}$ for state #1 shown in figure 3.6(a) with the expected flow for state #2, an artificial velocity field can be computed as

$$U_x(x^*, z^*) = \frac{1}{2}[U_{\epsilon x}(x^*, z^*) + U_{\epsilon x}(x^*, -z^*)], \tag{3.2}$$

and

$$U_z(x^*, z^*) = \frac{1}{2}[U_{\epsilon z}(x^*, z^*) - U_{\epsilon z}(x^*, -z^*)]. \tag{3.3}$$

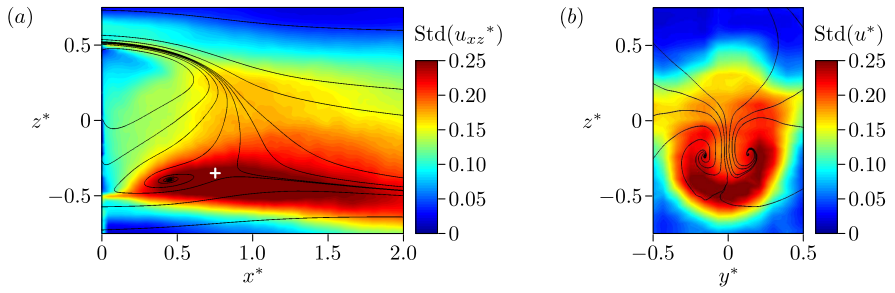

Figure 3.6. Fluctuating velocities in the plane $y^* = 0$ (a) and in the plane $x^* = 1.2$ (b) for slightly nose-up configuration (state #1); the white cross locates the saddle point.

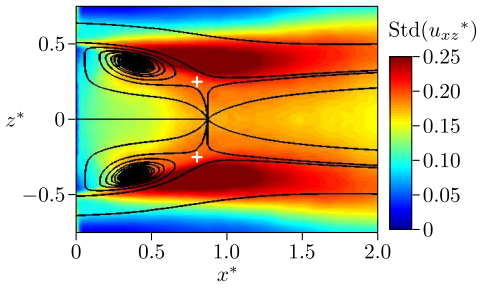

Figure 3.7. Fluctuating velocities in plane $y^* = 0$ for the flow computed from the state #1 (see figure 3.6a) and the expected velocity field for state #2 as defined in equations (3.2) and (3.3). The white crosses locate the saddle points.

This artificial wake presented in figure 3.7 has exactly the same properties as the one measured for a lined-up body in figure 3.5(b): two saddle points are visible, with two zones of intense fluctuations of velocity at $z^* \approx \pm 0.4$.

Hence, two different wake positions are expected for the flow over a perfectly lined-up configuration. When the wake follows the configuration #1, the upper recirculation structure is larger and closer to the base than the lower one. Such an asymmetry of the recirculating flow leads to a non-uniform pressure distribution on the base; the base pressure gradient $\partial C_p/\partial z^*$ is negative in state #1 (see figure 3.8a). The slope of the linear fit of the base pressure distribution gives the pressure gradient and indicates whether the flow mostly follows the state #1 or #2. Thus, the instantaneous measurement of base pressure distribution gives the dominant topology over the second.

The time evolution of the base pressure signal during 5 10^3 s is now considered. A sample evolution of the pressure gradient, *i.e.* the dominant topology, is shown in figure 3.8(b) over 1000 s. Two preferred positions are visible at $\partial c_p/\partial z^* \approx \pm 0.1$ in the probability distribution proving the existence of the two topologies #1 and #2; they are associated with negative and positive gradients respectively. The presence of the minimum between these peaks suggests that the automatic 1 s averaging remains below the mean time of shift estimated at 4.6 s, *i.e.* more than 100 global mode periods. The standard deviation of the base pressure gradient is 0.084. This value is of the order of the absolute values of pressure gradients associated with the asymmetric states (see figure 3.8b); such a high value is then an indicator of the coexistence of the two wake topologies.

Eventually, the spectral analysis of the signal over the 5 10^3 s does not present any

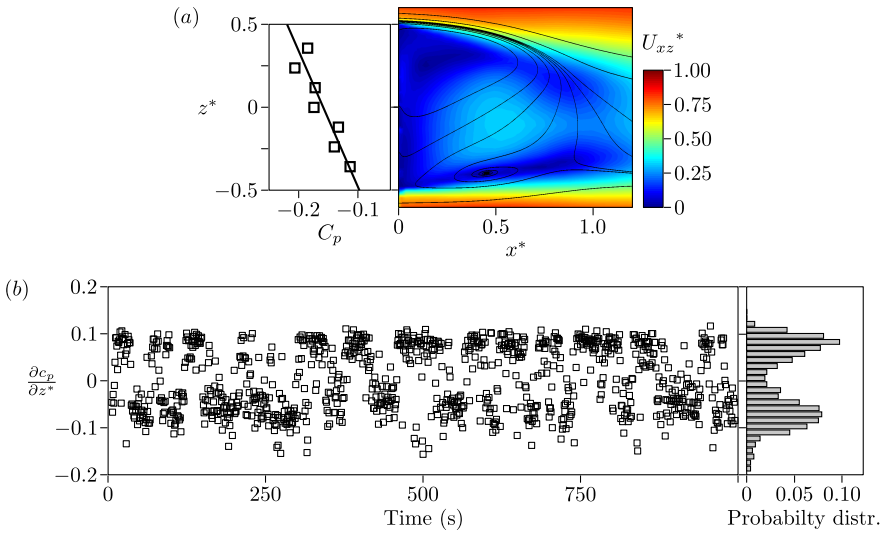

Figure 3.8. (a) Base pressure distribution of the topology #1 characterized by the negative slope of the linear fit (continuous line) with the corresponding velocity field in the near wake from figure 3.6(a). (b) Sample time evolution of the instantaneous base pressure gradient over 1000 s and corresponding probability distribution.

$\mathbb{P}(\mathcal{S}_t = \#1) = 0.53$	$\mathbb{P}(\mathcal{S}_t = \#2) = 0.47$
$\mathbb{P}(\mathcal{S}_t = \#1 \vert \mathcal{S}_{t-1} = \#1) = 0.79$	$\mathbb{P}(\mathcal{S}_t = \#2 \vert \mathcal{S}_{t-1} = \#2) = 0.77$

Table 3.2. Probabilities of states #1 and #2 depending on the previous state for the lined-up uncontrolled flow based on pressure measurements with a sampling frequency at 1 Hz. $\mathbb{P}$(A|B) is the conditional probability of A, given B. The precision is better than 0.02.

characteristic frequency: the shifting process seems random. The two asymmetric topologies are discriminated against the sign of the base pressure gradient. The probability to report the state #1 or #2 at a moment t, denoted $\mathbb{P}(\mathcal{S}_t = \#1)$ or $\mathbb{P}(\mathcal{S}_t = \#2)$ respectively, depends not only on geometrical parameters like incidence but also on the past event (see table 3.2). For $\epsilon = 0$, one expect $\mathbb{P}(\mathcal{S}_t = \#1) = \mathbb{P}(\mathcal{S}_t = \#2) = 0.5$ but a slight incidence strongly affects this equilibrium. Besides, $\mathbb{P}(\mathcal{S}_t = \#1) < \mathbb{P}(\mathcal{S}_t = \#1 \vert \mathcal{S}_{t-1} = \#1)$, which is equally true for the topology #2, $\mathbb{P}$(A|B) referring to the conditional probability of A, given B. Hence, a configuration is more likely to appear at t if it was already there the previous second: this is consistent with the mean time of shift measured at 4.6 s.

As a result, it appears that the $m = 2$ periodicity of the geometry is responsible for a bistable behavior, the topology shifts being long time dynamics. This is in agreement with the PDF of the wake orientation observed for the sphere when the $m = 2$ azimuthal perturbation disturbs the flow (see figure 2.18). One can interpret the slight incidence inducing the asymmetric flow (see figure 3.6) as an superposition of a dominant $m = 1$ perturbation so that the wake has only one preferred position left. The study of an additional $m = 1$ perturbation is now thoroughly studied in section 3.3.1 introducing a control cylinder in the near wake.

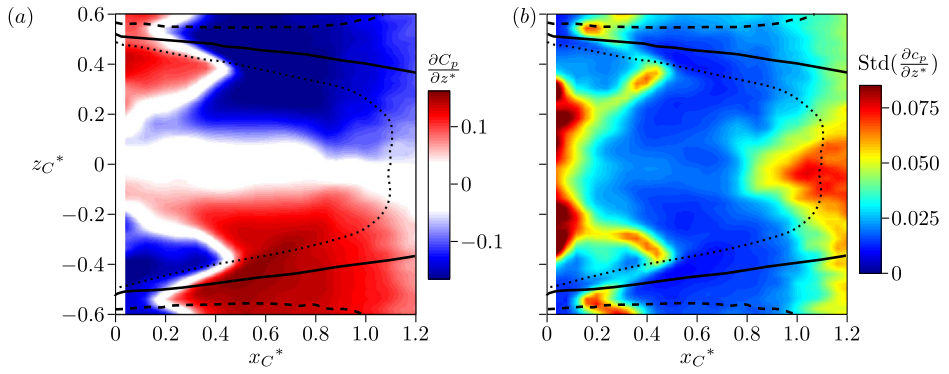

Figure 3.9. Effect of the position of the 3 mm control cylinder on $\partial C_p/\partial z^*$ (a) and on Std($\partial c_p/\partial z^*$) ($b$). The lines locate the mixing layer of the natural flow in the plane $y^* = 0$: $\cdots$, ${U_x}^* = 0.1$; —, 0.5; - - -, 0.9.

3.3 Disturbed wakes

The sensitivity of this flow to $m = 1$ and $m = 0$ azimuthal disturbances, cylinder and rings respectively, is investigated through their effect on global mode activity, velocity field and base pressure.

3.3.1 Control cylinder in the wake

The asymmetric wake presented in figure 3.6 for a slight pitching angle highlights that the wake orientation is sensitive to any tiny asymmetry of the setup. Consequently, the control cylinder, which can be seen as a $m = 1$ steady disturbance for ${z_C}^* \neq 0$, should also have significant impacts on the flow. The base pressure gradient, *i.e.* the dominant topology, as a function of the cylinder position is presented in figure 3.9(a). As expected, this $m = 1$ perturbation is highly efficient in selecting the state #1 or #2. For example, when the cylinder is at ${x_C}^* = 0.2$ and ${z_C}^* = -0.3$, it forces the topology #1 (see figure 3.10a); if it is moved further downstream at constant ${z_C}^* = -0.3$, then the configuration #2 dominates. When ${z_C}^* = 0$, the disturbance is no longer antisymmetric thus the mean wake retrieves the symmetry referring to the plane $z^* = 0$ (see figure 3.10b).

For ${x_C}^* < 0.5$ and ${z_C}^* \neq 0$, there are also positions of control cylinder where no pressure gradient is induced in spite of the asymmetry of the configuration. At these locations, the fluctuation levels of the base pressure gradient are close to the natural value as visible in figure 3.9(b). This points out that both topologies #1 and #2 are still present in the wake.

Further downstream, for ${x_C}^* > 1$, the flow is less influenced by the control cylinder: the effect of the disturbance is not important enough to set a significant base pressure gradient and the fluctuation levels get back to the values of the uncontrolled case. Thus, the receptivity of the flow seems limited to the recirculation bubble.

On the contrary, wherever the cylinder induces high positive or negative base pressure gradient, *i.e.* topology #1 or #2, fluctuation levels of base pressure gradient are much lower than the natural value. Thus, the control cylinder stabilizes the wake in one of the two asymmetric states. As for $m = 1$ disturbed flow over a sphere, the wake can be oriented either toward the disturbance or toward the opposite direction depending on x_C.

Eventually, the fluctuations of base pressure remain quite low when the cylinder is placed in the middle of the recirculation bubble so the wake tends to be stabilized in a

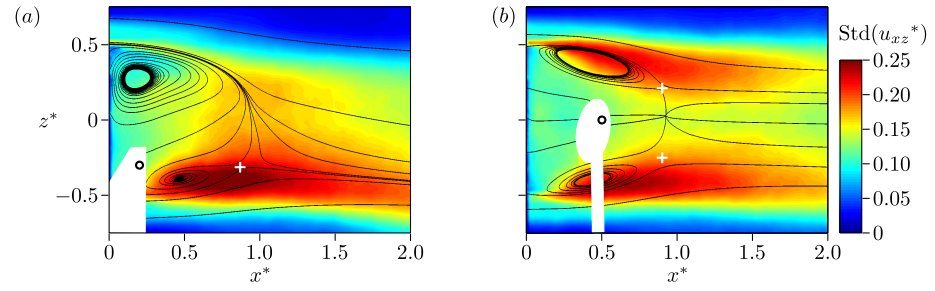

Figure 3.10. Fluctuating velocities in the plane $y^* = 0$ for two controlled cases: ${x_C}^* = 0.2$ and ${z_C}^* = -0.3$, (a); ${x_C}^* = 0.5$ and ${z_C}^* = 0$, (b); the configurations are associated with drag evolutions of $+1\%$ and -9% respectively. The crosses locate the saddle points.

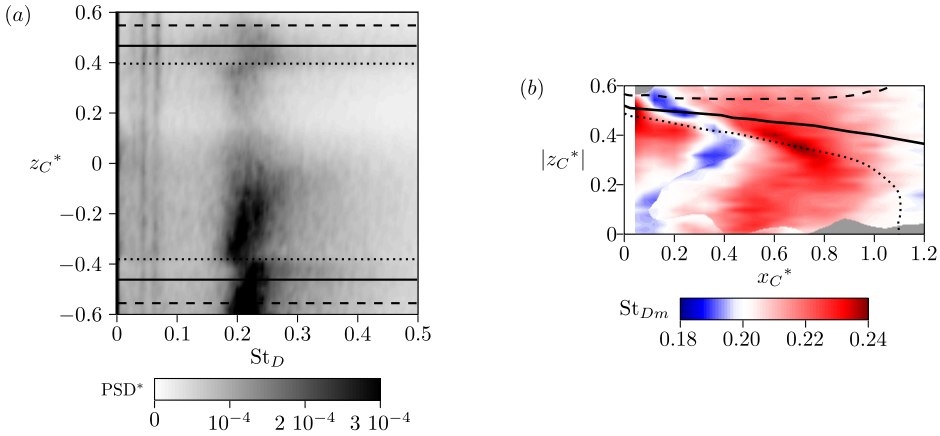

Figure 3.11. (a) Autopower spectra at $x^* = 4.0$, $y^* = 0$ and $z^* = 0.5$ as a function of the position of the control cylinder ${z_C}^*$ for ${x_C}^* = 0.5$. (b) Strouhal of the global mode as a function of the cylinder position. The gray areas correspond to absences of peak in the autopower spectra. The lines locate the mixing layer of the natural flow in the plane $y^* = 0$: $\cdots$, ${U_x}^* = 0.1$; —, 0.5; - - -, 0.9.

topology with a symmetric distribution of base pressure, *i.e.* in a centered state.

The $m = 1$ disturbance equally affects the dynamics of the global mode. The autopower spectrum of the hot-wire probe signal at $x^* = 4.0$, $y^* = 0$ and $z^* = 0.5$ is presented in figure 3.11(a) as a function of the cylinder position ${z_C}^*$ for ${x_C}^* = 0.5$. As the probe is at $z^* = 0.5$, *i.e.* off the streamwise axis, the map of the power spectrum is not symmetric referring to ${z_C}^* = 0$. A higher level energy is measured in the power spectra when the wake is in the state #2, *i.e.* ${z_C}^* < 0$ when ${x_C}^* = 0.5$. Indeed, the fluctuations of velocity are mostly concentrated at the upper part of the recirculation bubble and the turbulent structures are then convected downstream, to the hot-wire probe. On the contrary, when the wake follows the state #1, the fluctuations of velocities are located at the opposite of the probe.

Figure 3.11(b) reports the global mode frequency at positions where a peak of energy is present in the power spectrum. This map is correlated to the map of absolute values of base pressure gradient (see figure 3.9a). The more asymmetric the topology, the higher

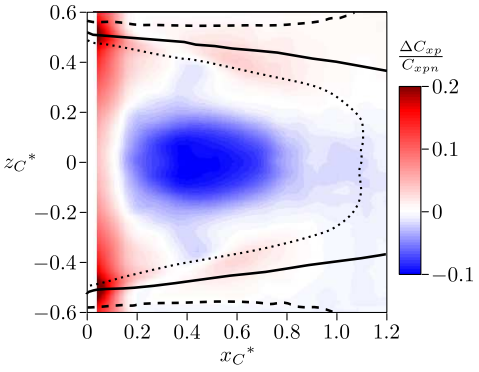

Figure 3.12. Effect of the position of the control cylinder on the drag. The lines locate the position of the mixing layer of the natural flow in the plane $y^* = 0$: $\cdots$, ${U_x}^* = 0.1$; —, 0.5; - - -, 0.9.

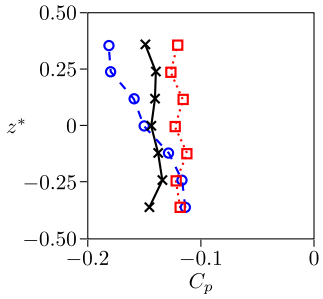

Figure 3.13. Base pressure distribution: — (×), natural flow; - - - (◯), ${x_C}^* = 0.2$ and ${z_C}^* = -0.3$ (see figure 3.10*a*); $\cdots$ (□), ${x_C}^* = 0.5$ and ${z_C}^* = 0$ (see figure 3.10*b*).

the frequency. On the contrary, the shedding frequency tends to be reduced where the control cylinder sets $\partial C_p/\partial z^* \approx 0$. An exception is observed when ${z_C}^* \approx 0$ but the energy associated with the global mode activity is spreading over a large band of frequency so St_{Dm} is poorly defined (see figure 3.11*a*). For theses positions, the total energy of the fluctuations of velocity is slightly lower than the one of the natural flow (compare figures 3.10*b* and 3.5*b*). This observation confirms that the wake tends to be stabilized in a centered state.

In parallel to these different flow modifications, the pressure drag is estimated through the pressure distribution on the body. The largest drag reductions are measured for ${x_C}^* \approx 0.5$ and ${z_C}^* \approx 0$ (see figure 3.12). The optimal position leads to a drag reduction of 9%, exclusively associated with a base pressure recovery (see figure 3.13); the pressure distribution on the forebody is found independent of the cylinder position. When the cylinder induces $\partial C_p/\partial z^* \approx 0$ for $0.2 < {x_C}^* < 0.5$ and ${z_C}^* \neq 0$, there is almost no effect on the drag. At these locations, the flow does not seem disturbed by the cylinder, the only difference is that the global mode frequency is slightly reduced.

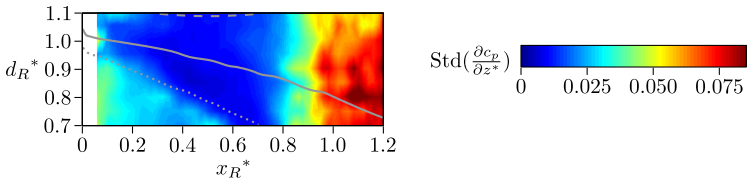

Figure 3.14. Effect of the position of the control rings on Std($\partial c_p/\partial z^*$). The lines locate the mixing layer of the natural flow in the plane $y^* = 0$: $\cdots$, ${U_x}^* = 0.1$; —, 0.5; ---, 0.9.

3.3.2 Control rings in the mixing layers

The sensitivity of the flow to $m = 0$ disturbances is now studied placing the rings in the mixing layers (see figure 3.1*b*). The contribution of the 3 mm support can be estimated through the effect of the control cylinder presented in the previous section for ${z_C}^* = 0$. As the perturbation introduced by the rings is symmetric, the base pressure gradient remains nil but its fluctuation levels are still an indicator of bi-stability. These fluctuations depending on the diameter and position of the rings are presented in figure 3.14. For ${x_R}^* < 0.8$ the fluctuations of the base pressure gradient tend to be attenuated in comparison to the natural flow. In particular, the impact of the control ring on Std($\partial c_p/\partial z^*$) follows the inner frontier of the mixing layer. As for the control cylinder, these low values tend to indicate that the wake is stabilized in a centered state. Then, for ${x_R}^* > 0.8$, the fluctuations of base pressure gradient are close to its natural values.

The modification of the global mode activity due to the presence of the control rings is now considered. Figure 3.15 presents the power spectrum of the hot-wire probe signal at $x^* = 4.0$, $y^* = 0$ and $z^* = 0.5$. For small ring diameters in the near wake, *i.e.* ${d_R}^* < 0.85$ and ${x_R}^* < 0.2$, the disturbance is not in the mixing layers, the global mode frequency and amplitude are close to the natural case (see figure 3.15*c*). As the disturbance reaches the inner part of the mixing layers for ${x_R}^* < 0.4$, the shedding frequency is approximately decreased by 15%. When the ring diameter increases, the perturbation affects the middle of the mixing layers and the global mode is reported far less energetic so it is poorly defined (gray zones in figure 3.15*c*). Reaching the outer part of the mixing layers, the global mode is measured again but at a higher frequency in comparison to the natural value.

Further downstream for $0.4 < {x_R}^* < 0.6$, a different scheme is observed (see figure 3.15*c*). The global mode frequency is reduced for small ring diameters but the peak of energy in the spectra rapidly disappears as ${d_R}^*$ is increased. In the middle of the mixing layer, a new global mode regime is measured with a frequency of $\mathrm{St}_{Dm} \approx 0.1$. Then, for ${d_R}^* > 1$, the disturbance of the outer part of the mixing layer leads to an increase in global mode frequency.

Finally, whatever the value of ${d_R}^*$, for ${x_R}^* > 0.6$ there is no more peak reported in the power spectra. The attenuation of the global mode may be due to the presence of the 3 mm support. Indeed, figure 3.11(*b*) points out that the control cylinder prevents the global mode development when placed on the streamwise axis for ${x_R}^* > 0.7$. So, at these locations, the effect of the support may no longer be negligible.

In parallel, figure 3.16 presents the estimation of the drag depending on the diameter and position of the rings. Like the global mode activity, the effect of the rings approximately follows the position of the mixing layer in the natural flow. The optimal drag reductions are reported when the control device acts on the inner part of the mixing layers.

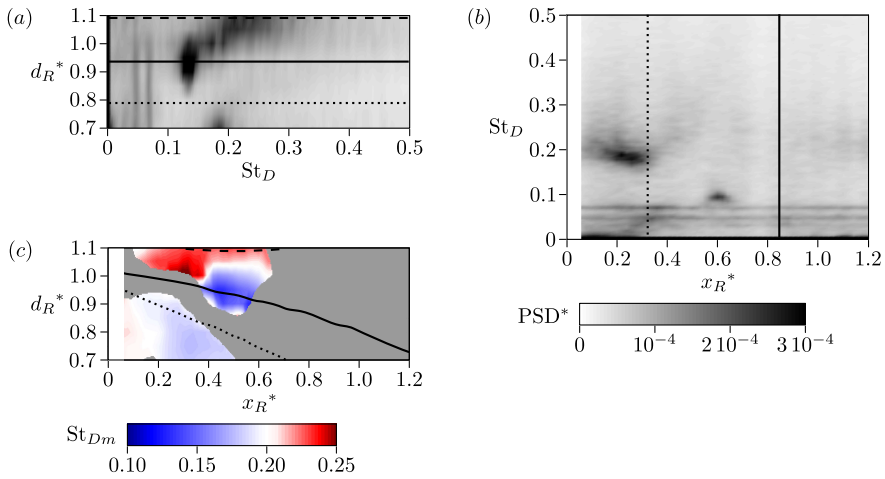

Figure 3.15. Autopower spectra at $x^* = 4.0$, $y^* = 0$ and $z^* = 0.5$ as a function of the ring diameter $d_R{}^*$ for $x_R{}^* = 0.5$ (a) and as a function of the position $x_R{}^*$ for $d_R{}^* = 0.85$ (b). (c) Strouhal number of the global mode depending on the ring position; the gray areas correspond to absences of peak in the autopower spectra. The lines locate the mixing layer of the natural flow in the plane $y^* = 0$: $\cdots$, $U_x{}^* = 0.1$; —, 0.5; - - -, 0.9.

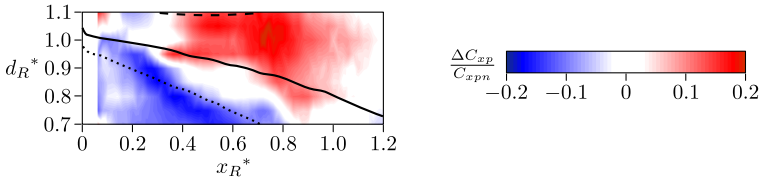

Figure 3.16. Effect of the position of the control ring on the drag. The lines locate the mixing layer of the natural flow in the plane $y^* = 0$: $\cdots$, $U_x{}^* = 0.1$; —, 0.5; - - -, 0.9.

On the contrary, the drag tends to increase when the outer part of the mixing layer is disturbed. An exception is observed for ${x_R}^* \approx 0.2$ where drag is also decreased for the largest ring diameters. Thus, the drag evolutions do not directly correspond to the global mode frequency map presented in figure 3.15(c). Eventually, when ${x_R}^* > 0.9$, the effect is limited on the drag which indicates that the receptivity of the flow is concentrated in the near wake mixing layers.

Different flow topologies correspond to these variations of drag and shedding frequency; three of them are presented in figures 3.17(a)–(c) corresponding to ${x_R}^* = 0.3$, 0.6 and 0.8 for ${d_R}^* = 0.85$. The associated spectra are visible in figure 3.15(b). At ${x_R}^* = 0.3$, a 13% decrease in C_{xp} is measured; the corresponding velocity field is displayed in figure 3.17(a). The mean recirculation structures are moved further downstream in comparison to the uncontrolled flow (compare with figure 3.4) and the length L_r of the recirculation bubble is increased by 7.5%. The pressure recovery induced by the control device is distributed on the whole area of the base (see figure 3.18). This ring position also corresponds to a slight reduction in global mode frequency: St_{Dm} is measured at 0.17 (see figure 3.15b).

Another topology is obtained with ${x_R}^* = 0.6$ and ${d_R}^* = 0.85$. PIV measurements in figure 3.17(b) point out that the mixing layers reattach on the flat ring. The streamlines around $x^* \approx 0.8$ indicate the presence of two stagnation points downstream of the ring but after the recirculation region[2]; they may be associated with the proper wake of the ring. The region where ${U_x}^* < 0$ is strongly shortened, limited to the area between the base and the ring. The mean recirculation structures are close to the body and the curvature of the separatrix increases reducing the base pressure on the periphery. As shown in figure 3.18, a relative high pressure is measured at the center of the body probably due to an intensification of the backward flow in average. However, this high pressure at the center of the base is not sufficient to counterbalance the loss of pressure on the periphery. Indeed, the assumed axisymmetry of the base pressure implies that the area associated with the pressure considered to calculate drag is proportional to $|z^*|$ as presented in equation (3.1). So, the base pressure at $z^* \approx 0$ has a smaller impact on the drag than at the periphery and the drag is measured equal to the uncontrolled case.

A third topology associated with high drag case is presented in figure 3.17(c). The flow reattaches on the rings and the mean recirculation structures are close to the base which implies a shorter recirculation length. The drag is increased due to the loss of pressure reported on the whole base. Finally, it is interesting to note that this high drag configuration is associated with an absence of activity of the unsteady global mode. Hence, contrary to what is usually observed in bidimensional wakes, the suppression of the shedding activity does not necessarily lead to base pressure recovery.

[2]The ring masks the point where ${U_x}^* = 0$ on the streamwise axis.

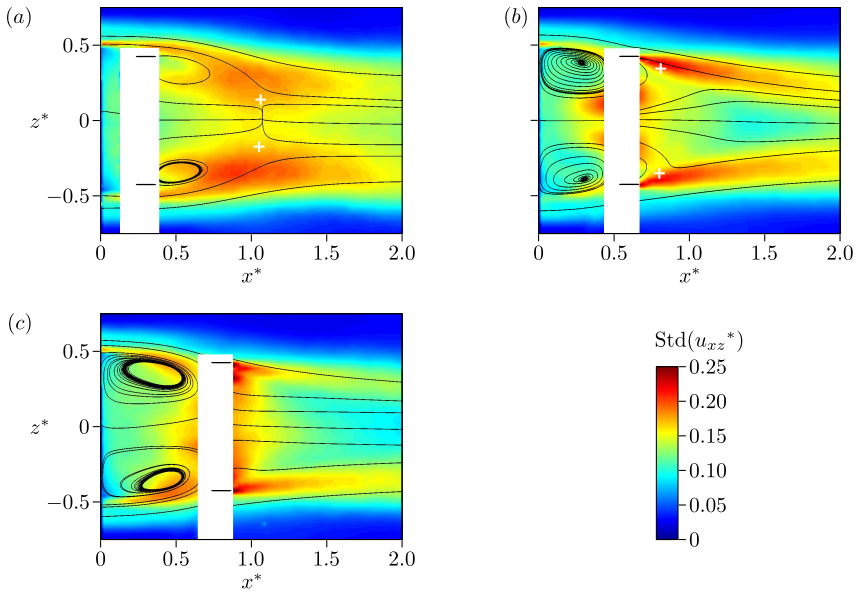

Figure 3.17. Fluctuating velocities in the plane $y^* = 0$ for the controlled flow with the ring of diameter ${d_R}^* = 0.85$ at ${x_R}^* = 0.3$ (a), ${x_R}^* = 0.6$ (b) and ${x_R}^* = 0.6$ (c); the configurations are associated with drag evolutions of -13%, 0% and $+9\%$ respectively. The white crosses locate the saddle points.

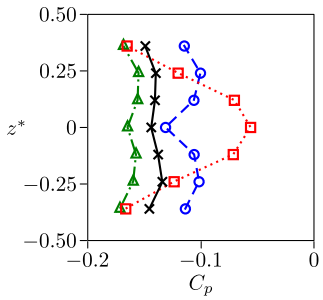

Figure 3.18. Base pressure distributions: — (×), natural flow; - - - (◯), ${x_R}^* = 0.3$ and ${d_R}^* = 0.85$ (see figure 3.17a); ⋯ (□), ${x_R}^* = 0.6$ and ${d_R}^* = 0.85$ (see figure 3.17b); -·- (△), ${x_R}^* = 0.8$ and ${d_R}^* = 0.85$ (see figure 3.17c).

3.4 Concluding remarks

The natural flow over this body with an axisymmetric blunt trailing edge is proved to be a mean of two asymmetric topologies. Due to the presence of the support introducing a $m = 2$ azimuthal periodicity, the wake is not axisymmetric but presents a statistical $m = 2$ symmetry. Instantaneous wake follows a $m = 1$ azimuthal topology and is oriented either above or below the streamwise axis, *i.e.* $\theta_W = \pm\pi/2$, shifting randomly. The unsteady global mode develops from one side of the bubble, depending on the orientation of the instantaneous wake.

A $m = 1$ disturbance, ascribed to a small pitching angle or a control cylinder, sets one of the two asymmetric topologies. This study highlights that the sensitivity of the flow over a body of revolution to an antisymmetric local disturbance may only be observable in the azimuthal plane of the perturbation (Meliga *et al.*, 2009*a*). Any shift in the azimuthal position of the disturbance is very likely to be followed by an equal shift of the azimuthal orientation of the wake. In other words, as for the sphere wake in chapter 2, if θ_P refers to the azimuth of the $m = 1$ perturbation, then θ_W is mostly measured at θ_P or $\theta_P + \pi$, the phase shift depending on the nature and position of the disturbance.

In addition, the use of control rings considered as $m = 0$ disturbances has a strong influence on both the drag and the wake dynamics; the effects follow the position of the mixing layers of the natural flow. In particular, when placed in the inner part of the mixing layer, the rings may delay the development of the shear layer instability. It reduces the global mode frequency and stretches the wake structures in the streamwise direction resulting in drag reductions.

The mean flow symmetry as well as the global mode development are highly sensitive to local perturbations in the recirculation region. These results may be associated with the disturbance of the reminiscent global modes observed in the laminar regime. The development of the steady asymmetric mode after the first bifurcation could contain the wake sensitivity to $m \geq 1$ disturbances. On the other hand, the oscillating mode reported after the second bifurcation (unsteady transition) seems more sensitive to $m = 0$ perturbations due to the modification of the vorticity distribution in the mixing layers.

As a conclusion, chapters 2 and 3 evidence that the instantaneous flow past axisymmetric bodies tends to be off the axis of symmetry. The symmetry of the setup is statistically recovered in the wake but only after long time scales, far larger than D/U_0. In addition, an unsteady coherent motion is reported at $\mathrm{St}_D \approx 0.2$ but the associated energy remains limited. The development of the unsteady global modes may not be responsible for a dominant part of the drag. For example, in section 3.3.2, some control ring positions lead to a total suppression of the shedding process whereas they induce significant drag increases. The mechanisms responsible for the closure of the recirculation region may rather rely on the turbulent activity of the mixing layers and the general trend that seems to dominate from the control experiments presented in section 3.3 is the more energetic the mixing layers and the more asymmetric the wake, the larger the drag.

Finally, such multi-stable behaviors of three-dimensional flows are of critical interest for the understanding of the wake dynamics and they are certainly not limited to axisymmetric bodies. Hence, part II extends similar approaches to the wakes past parallelepiped bodies in ground proximity.

Part II

Parallelepiped geometries in ground proximity

Chapter 4

Reflectional symmetry breaking in the laminar regime

Most of this chapter is published in Grandemange *et al.* (2012*a*).

The experiments depicted in part I evidence strong correlations between the dynamics of the turbulent wake and the bifurcations of the laminar flow. Therefore, it is suitable to start the analyses of the wakes past parallelepiped bodies with an investigation of the bifurcations of the laminar wake.

Abstract

In part I, reminiscences of the bifurcations of the laminar wake past axisymmetric bodies are observed in the turbulent regime. As a consequence, it is pertinent to start the study of the flow past parallelepiped bodies with experiments in the laminar regime. Based on flow visualizations, a permanent reflectional symmetry breaking (RSB) is reported in the wake of the squareback Ahmed geometry (Ahmed *et al.*, 1984). When the ground clearance is large enough to allow a significant underbody flow, a first bifurcation from a trivial steady symmetric state to a steady RSB state is evidenced at $\mathrm{Re}_H = 340$. The RSB state becomes unsteady after a second bifurcation at $\mathrm{Re}_H = 410$. This RSB persists at large Reynolds numbers and it is responsible for the bi-stability of the turbulent wake presented in the next chapter.

Contents

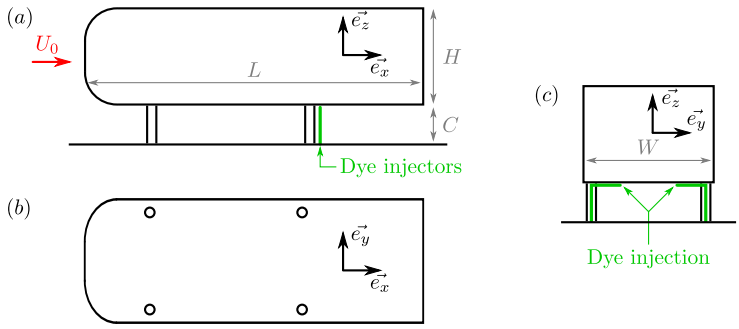

Figure 4.1. Geometry of the model: side view (a), top view (b) and back view (c). Fluorescent dye is injected through two pipes behind the rear supports.

4.1 Experimental setup

The three-dimensional body is described in figure 4.1. The length $L = 94$ mm, the width $W = 35$ mm and the height $H = 26$ mm respect the proportions of the Ahmed geometry (Ahmed *et al.*, 1984). The four supports are cylindrical of diameter 3 mm. The Reynolds number is based on the height of the base $\mathrm{Re}_H = U_0 H/\nu$. The geometry is placed in a low speed water tunnel at different ground clearance $C^* = C/H \in \{0.2, 0.4, 0.6\}$, the reference value in the experiments of Ahmed *et al.* (1984) being $C^* = 0.17$.

Two dye injectors, located behind the rear supports, are used to visualize the wake (see figure 4.1). The Reynolds number varies between 260 and 1300; it is adjusted by the main flow velocity U_0 in the range 1 cm s^{-1} $< U_0 <$ 5 cm s^{-1}; the precision due to the accuracy of the rotameter is $\Delta\mathrm{Re}_H = \pm 10$. The dye is continuously injected with a syringe in such a way that the velocity at the exit of the injector never exceeds 10% of the main velocity. The tunnel has transparent walls; in particular, it is designed to visualize the wake in the streamwise direction (see Thiria *et al.*, 2006, for a description of the tunnel). When the geometry is out of the test section, the boundary layer thickness on the ground at the streamwise position of the base of the geometry is of the order of 1 cm, *i.e.* $\delta \sim 0.4H$. Pictures are taken once the dye has filled the recirculating bubble. In the following, y_W denotes the position of the wake in the y direction and $Y_W = \langle y_W \rangle$. It is measured as the mean position of the dye trail downstream of the recirculation bubble by image analysis of the top view picture; its precision is $0.02W$.

4.2 Topologies of the laminar wake

First, the flow topologies with a moderate ground effect, *i.e.* for a ground clearance of $C^* = 0.6$, are presented. Then, section 4.2.2 depicts the wake configurations for $C^* = 0.2$ and $C^* = 0.4$.

4.2.1 The case $C^* = 0.06$

At the lowest Reynolds numbers, a steady symmetric regime (SS) is observed as shown in figure 4.2(a) for $\mathrm{Re}_H = 310$. The flow preserves the reflectional symmetry of the geometry. The presence of the ground induces a top – bottom asymmetry of the wake but it is clear that there is significant momentum in the underbody flow for this ground clearance. This SS state remains stable up to $\mathrm{Re}_H = 340$.

Past this critical Reynolds number, the wake starts to oscillate periodically in the plane of symmetry as presented in figure 4.2(b). The structure of this unsteady symmetric regime (US) perfectly preserves the reflectional symmetry of the body as it can be stated from the corresponding top and back views. This regime is associated with alternative vortex loops shed from the top and bottom shear layers. In the side view picture, a streamwise evolution of the phase shift between the upper and lower vortices is observed. It is very likely to result from a difference in the convection velocities between the overbody and underbody flows.

The US regime is not observed permanently. Indeed, keeping the Reynolds number constant, this periodic shedding progressively moves off the reflectional plane of symmetry: y_W varies slowly around 0 with a characteristic time evolution of one minute, *i.e.* roughly 10 shedding periods. Then, the wake selects randomly one orientation and stabilizes in an asymmetric position, typically after a duration of ten minutes. There, the oscillations get attenuated and the flow reaches a steady asymmetric regime (SA) denoted SA^+ or SA^- depending on the sign of Y_W. Figure 4.2(c) shows the steady state SA^- that breaks the reflectional symmetry for $\mathrm{Re}_H = 365$. Naturally, both SA^+ and SA^- can be observed repeating the Reynolds number increase from the SS regime without any intervention on the setup. This regime was observed stable over two hours of observation; it is considered steady in the limit of the visualization means and water tunnel stability.

Eventually, increasing the Reynolds number over 410, the SA wake starts to oscillate again (see figure 4.2d) which leads to an unsteady asymmetric regime (UA). The flow preserves its orientation so that SA^+ turns into UA^+ and similarly SA^- becomes UA^-. Hence, figures 4.2(c) and 4.2(d) result from two different experiments of Reynolds number increase. The top view in figure 4.2(d) shows that the oscillations are concentrated on one side of the body but the unsteadiness is associated with oscillations in both the y and z directions. It is then probable that two different frequencies coexist: one may be associated with the interaction of the top – bottom shear layers and the other with the interaction of the lateral ones[1]. However, the setup does not allow a precise measurement of the oscillation amplitudes or frequencies in the cross-flow plane. Eventually, it is worth mentioning that the spontaneous migration between the regimes UA^+ and UA^- was not observed but this shift can be forced by energetic perturbations such as short time suppression of the flow.

After a decrease of Reynolds number, the flow goes from the UA state to the SA one at $\mathrm{Re}_H = 410$ and then directly to the SS state as soon as the Reynolds number becomes smaller than 340: the US regime is not observed. This behavior is summarized through the typical evolution of the wake shift y_W in figure 4.3.

[1] This point is proved in the turbulent regime in chapter 5.

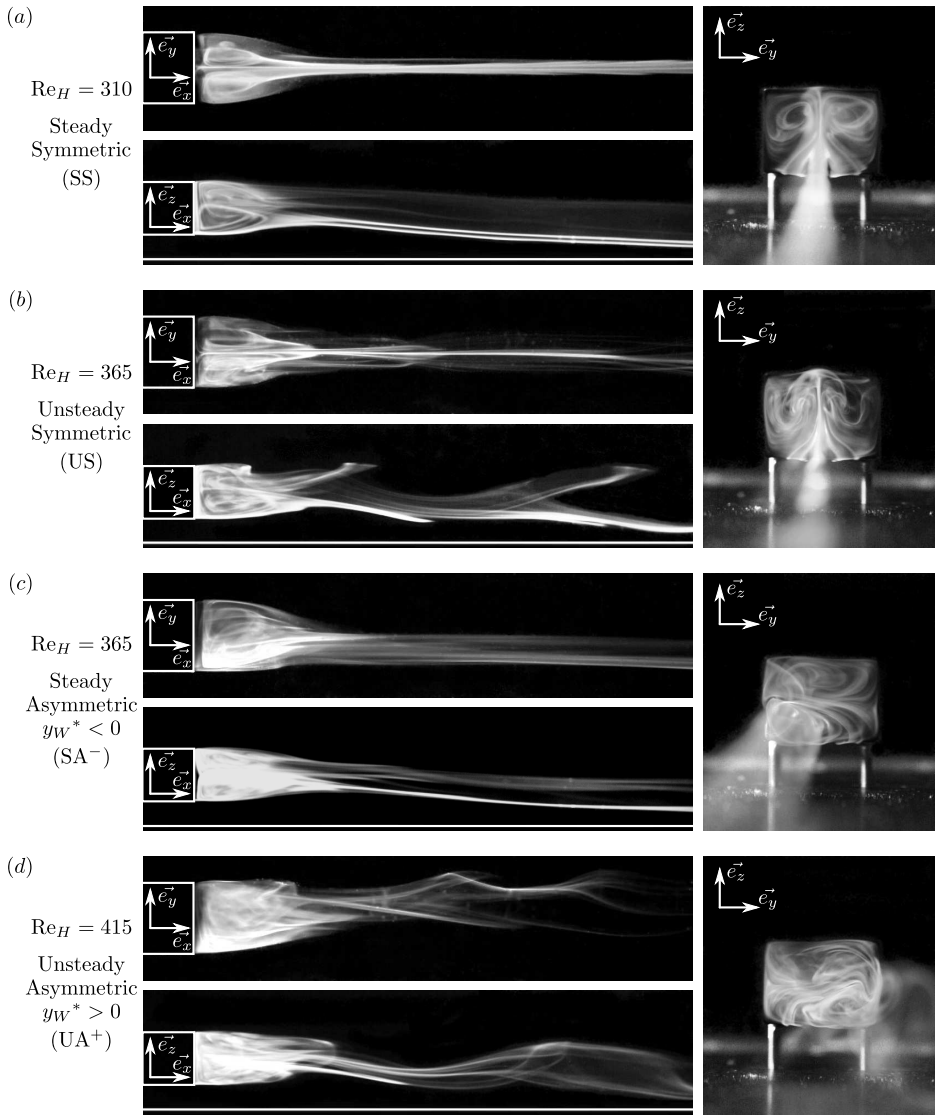

Figure 4.2. Flow visualizations at the Reynolds numbers $\mathrm{Re}_H = 310$ (a), $\mathrm{Re}_H = 365$ (b)–(c) and $\mathrm{Re}_H = 415$ (d). For each Reynolds number: top picture, top view; bottom picture, side view; right picture, back view. The flow comes from the left for both top and side views. The regimes observed in (a), (c) and (d) are permanent states while (b) is a transient state. Observations in (c) and (d) are obtained from different experiments of Re_H increase in order to show both wake orientations ($Y_W{}^* < 0$ and $Y_W{}^* > 0$).

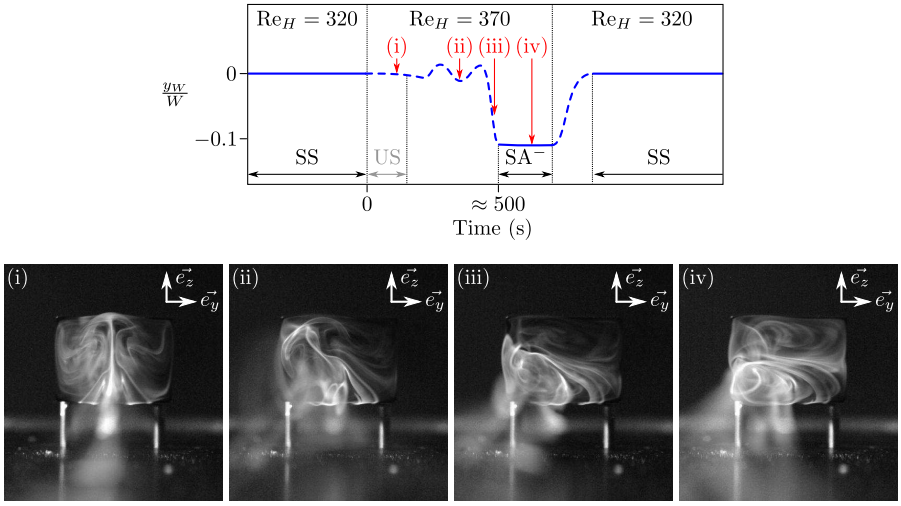

Figure 4.3. Typical evolution of the wake position y_W and corresponding back view visualizations during a Reynolds number increase from 320 to 370 followed by a decrease back to 320: continuous lines, permanent states; dashed lines, transient states.

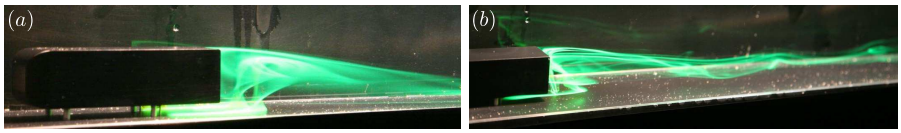

Figure 4.4. Flow visualizations for $C^* = 0.2$ of the SS regime at $\mathrm{Re}_H = 310$ (a) and the US regime at $\mathrm{Re}_H = 600$ (b).

Note that during the transition from SS to SA, the US regime is always reported. This observation indicates that the imperfections of the shedding of the US regime may be needed to initiate slight asymmetries. Then, these asymmetries gradually amplify, moving the wake off the reflectional plane of symmetry, while the periodic oscillations slowly attenuate to eventually reach the SA regime.

As a consequence, the stable regimes for $C^* = 0.6$ are asymmetric for $\mathrm{Re}_H > 340$. The stability of these RSB states is now studied in section 4.2.2 for the two other ground clearances.

4.2.2 The cases $C^* = 0.02$ and $C^* = 0.04$

The viscous effects of the fluid combined with the thick boundary layer on the ground limit the development of the underbody flow. In the case $C^* = 0.2$, there is no momentum in the underbody flow and the recirculation region extends to the ground as visible in figure 4.4. For low Reynolds numbers, the flow is steady and symmetric; an unsteady transition occurs at $\mathrm{Re}_H = 450$ (see figure 4.4b) but the wake preserves the reflectional symmetry in the considered range of Reynolds numbers.

In the configuration $C^* = 0.4$, the ground clearance is of the order of the incoming boundary layer. So, C^* is large enough to allow some underbody flow. A first transition from a SS regime to a US regime is measured at $\mathrm{Re}_H = 380$ (see figures 4.5a–b). Contrary to the case $C^* = 0.6$ presented in section 4.2.1, this US topology is stable at least up to

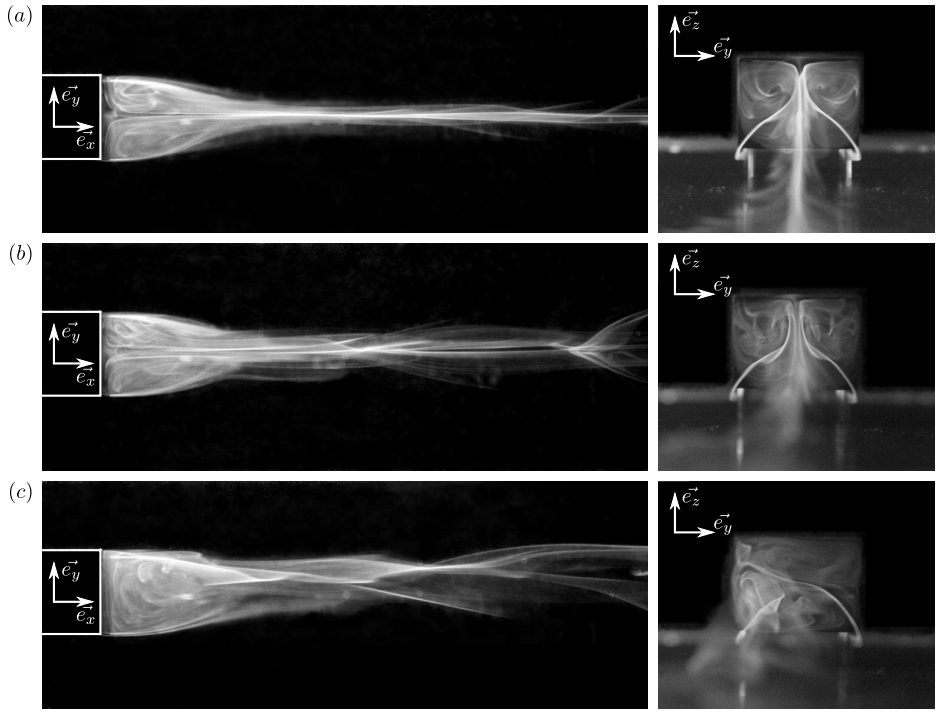

Figure 4.5. Flow visualizations for $C^* = 0.4$ at $\mathrm{Re}_H = 370$ (a), $\mathrm{Re}_H = 420$ (b) and $\mathrm{Re}_H = 470$ (c): left picture, top view; right picture, back view.

$\mathrm{Re}_H = 440$ when a transition to an unsteady asymmetric flow is reported, the asymmetric organization being visible in figure 4.5(c). It is worth noting that, for this value of ground clearance, no steady asymmetric state is observed.

A synthesis of these flow topologies is provided in the next section through the bifurcation scenarii for the different ground clearances.

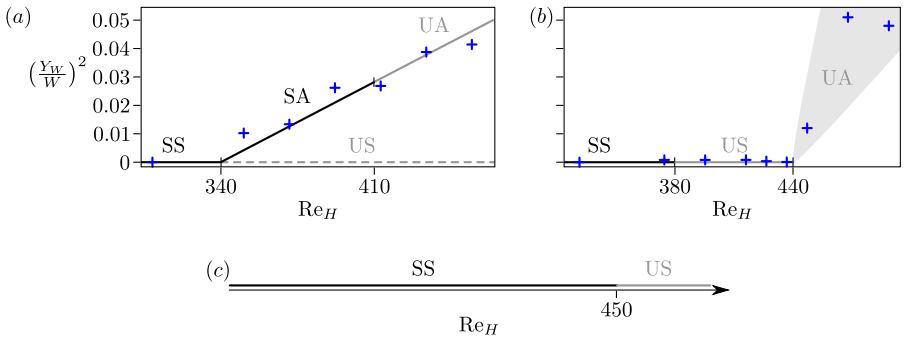

Figure 4.6. Bifurcation scenarii of the wake for $C^* = 0.06$ (a), $C^* = 0.04$ (b) and $C^* = 0.02$ (c): +, experimental data; the black and gray lines are steady and unsteady regimes respectively; the continuous and dashed lines are stable and unstable regimes respectively.

4.3 Bifurcation scenarii

The bifurcation scenario of the configuration $C^* = 0.6$ in figure 4.6(a) is suggested to classify the stable regimes: SS for $\mathrm{Re}_H < 340$, SA for $340 < \mathrm{Re}_H < 410$ and UA for $\mathrm{Re}_H > 410$. The US regime is marked as an unstable state as it is transient and only visible during the transition from SS to SA. The quadratic evolution of Y_W with Re_H confirms the presence of a pitchfork bifurcation at $\mathrm{Re}_H = 340$. Then, the amplitude of the asymmetry, quantified here by Y_W, is very likely to saturate for larger Reynolds numbers.

The bifurcation scenario for $C^* = 0.4$ is given in figure 4.6(b). It reproduces the successive unsteady transition at $\mathrm{Re}_H = 380$ and the reflectional symmetry breaking at $\mathrm{Re}_H = 440$. There are to few measurements in the UA regime to detail the nature of the second bifurcation.

Finally, the basic bifurcation scenario of the case $C^* = 0.2$ is displayed in figure 4.6(c). There is only one unsteady transition at $\mathrm{Re}_H = 450$ between the planar symmetric states.

From the synthesis given in figure 4.6, one can observe the stabilizing effect of the ground: the wall suppresses the y instability or at least delays its development. This is also true for the unsteady bifurcations as all the thresholds of Reynolds numbers increase when the ground clearance is reduced.

4.4 Concluding remarks

As a conclusion, these experiments evidence a reflectional symmetry breaking (RSB) of a three-dimensional wake in the laminar regime: the bifurcation scenarii of the wake for large ground clearances present asymmetric permanent regimes. The SA and UA regimes have equal probability of being shifted toward the $y^* > 0$ or $y^* < 0$ domain. The transient US regime seems to initiate some slight asymmetries in the flow that are needed to reach the permanent asymmetric regimes. Improving the measurement technique, further work could clarify the amplitude and frequencies of the oscillations in the y and z direction. It could also confirm whether both oscillations emerge simultaneously and whether the transition from SA to UA is a Hopf bifurcation.

Besides, it is found that the bifurcation scenario strongly depends on the ground clearance: the steady RSB regime is not reported for $C < 0.4H$ and none of the RSB regimes is observed for $C^* = 0.2$ in the range of Reynolds numbers considered in these experiments.

These results are reminiscent of the loss of axisymmetry observed in the laminar wake past a sphere and the presence of asymmetric stable regimes may be a general characteristic of three-dimensional wakes.

In the turbulent regime, like in the sphere wake, the reminiscences of this asymmetric bifurcation are very likely to lead to a bistable behavior after exploration of the two asymmetric states. As a logical progression, the dynamics of the turbulent wake are now studied in chapter 5.

Chapter 5

Global modes and bi-stability of the turbulent wake

Most of the following results are published in Grandemange *et al.* (2013*b*).

This chapter aims at clarifying the flow past the squareback Ahmed geometry. This body is massively used to develop flow control strategies but the coherent dynamics of the wake are still open issues. In addition, the following results introduce the bases of the sensitivity analyses detailed in chapter 7.

Abstract

After the evidence of a reflectional symmetry breaking state in the laminar regime, experiments at $\mathrm{Re}_H = U_0 H/\nu = 9.2\ 10^4$ investigate the flow around the Ahmed geometry. The massive recirculation on the base, responsible for a dominant part of the drag, is characterized. The analyses of the coherent dynamics of the wake reveal the presence of two very distinctive timescales. At long timescales $T_l \sim 10^3 H/U_0$, the recirculation region shifts between two preferred reflectional symmetry breaking positions. The succession of these asymmetric states is random and the equiprobability of the two states leads to a symmetric mean flow. However, this bistable behavior is reported only over a critical value of ground clearance. At short timescales $T_s \sim 5H/U_0$, the wake presents weak coherent oscillations in the vertical and lateral directions. They are respectively associated with the interaction of the upper – lower and lateral shear layers. When normalized by the height and width of the body respectively, the Strouhal numbers are close to 0.17. In terms of spatial organization, the results suggest an alternate shedding in the vertical oscillation and a parallel vortex shedding in the lateral direction with an orientation linked to the current asymmetric position. More generally, these experiments indicate that flow dynamics, especially the bi-stability, depends on geometrical parameters; these dependences are thoroughly studied in the next chapter.

Contents

5.1 Experimental setup

Geometry

A scheme of the setup is presented in figure 5.1. A ground plate is placed in an Eiffel-type wind tunnel to form a 3/4 open jet facility. The turbulent intensity is less than 0.3% and the homogeneity of the velocity over the 390 mm × 400 mm test section is 0.4%. The wake is generated by a squareback geometry used in the experiments of Ahmed *et al.* (1984). The total length of the body is $L = 261.0$ mm, the height H and width W of the base are 72.0 mm and 97.2 mm respectively. The four supports are cylindrical with a diameter of 7.5 mm and the ground clearance is $C = 12.5$ mm to match the reference experiments. The blockage ratio is less than 5%. The coordinate system is defined as x in the streamwise direction, z normal to the ground and y forming a direct trihedral.

In order to have constant flow conditions, the ground plate is placed at 10 mm over the lower face of the inlet and triggers the turbulent boundary layer 140 mm upstream of the forebody without separation at the leading edge. When the body is not in the test section, the thickness of the ground boundary layer based on 99% of the free-flow velocity at $x = -L$, *i.e.* 140 mm downstream of the leading edge, is $\delta_{0.99} = 6.3$ mm with a precision of 0.1 mm; the displacement and momentum thicknesses are $\delta_1 = 0.89 \pm 0.05$ mm and $\delta_2 = 0.60 \pm 0.02$ mm respectively. The main flow velocity is $U_0 = 20$ m s^{-1} and the Reynolds number is $\mathrm{Re}_H = U_0 H/\nu = 9.2\ 10^4$.

Pressure measurements

The pressure on the body is measured at 62 locations. 21 taps are located on the base of the body; 41 others give the pressure distribution on the forebody and on the sides in the planes $y^* = 0$ and $z^* = 0.67$, this latter plane corresponding to the mid-height of the base. The pressure is obtained using a 64 port HD miniature pressure scanner and a SCANdaq 8000 interface controlled by Labview. The pressure scanner takes 50 pressure samples per second and the measurement is automatically averaged over 1 s. The accuracy of the measurement at 1 Hz is then ±3 Pa; the measurements at 1 Hz are called *instantaneous pressure measurements* in opposition to the mean pressure coefficient $C_p = \langle c_p \rangle$. The pressure scanner is located inside the model so that it is linked to each tap with less than 250 mm of vinyl tube to limit the filtering effect of the tubing. It is connected to the measurement chain by a wire going through a front support of the model so that, apart from the four supports, nothing disturbs the underbody flow.

In addition, the pressure in the wake is measured through the six static ports of a Prandtl tube mounted on a displacement robot and connected to a Scanivalve DSA 3217/16 px device. The pressure is considered without any correction so the result is accurate only when the flow is aligned with the probe. Therefore, it is simply used as a qualitative indicator of pressure in the wake. A three-dimensional mapping of the static pressure is obtained moving the probe in the domain $(x^*, y^*, z^*) \in [0.14; 3.00] \times [-0.83; 0.83] \times [0.07; 1.67]$ by steps of 0.14 in the streamwise direction and of 0.07 in the cross-flow directions.

Force measurements

Drag and lift, respectively F_x and F_z, are obtained using a bidimensional strain balance. The dimensionless coefficient C_i of the aerodynamic force in the i direction is defined according to equation (5.1) using $S = 7.19\ 10^{-3}$ m^2 the projected area of the geometry in

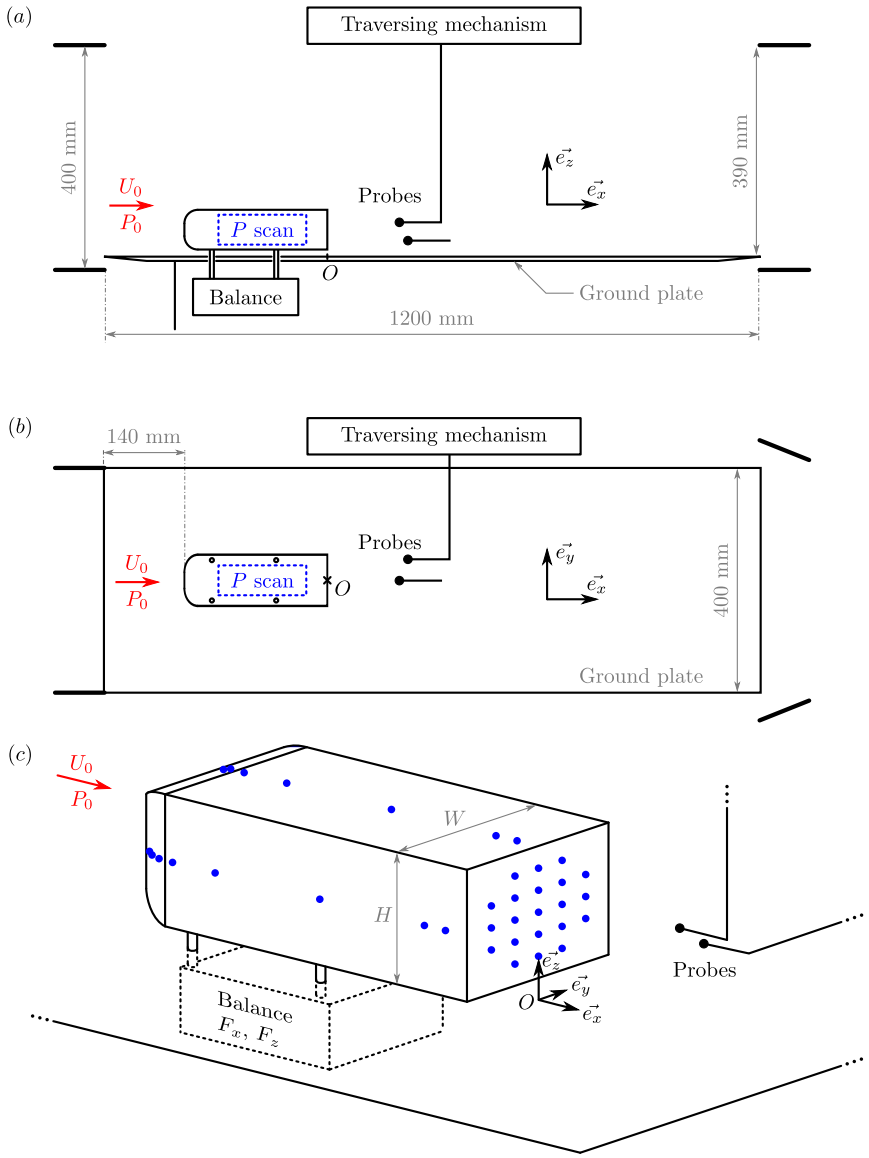

Figure 5.1. Experimental setup: side view (a), top view (b) and perspective view (c); the point O sets the origin of the coordinate system. The blue dots locate the visible pressure taps, they are distributed symmetrically referring to the planes $y^* = 0$ and $z^* = 0.67$ (mid-height of the body); P scan refers to the pressure scanner.

a cross-flow plane.

$$C_i = \frac{F_i}{\frac{1}{2}\rho S {U_0}^2}, \tag{5.1}$$

with $i \in \{x, y, z\}$.

The pressure measurements clarify the origins of the aerodynamic forces. The pressure contribution to the aerodynamic force in the i direction, denoted C_{ip}, is estimated by integration of the pressure after projection in the considered direction as defined in equation (5.2). The precision is limited especially for the measurement of the lift and lateral forces since the pressure distribution is assumed independent of y on the upper and lower faces and independent of z on the lateral faces.

$$C_{ip} = \frac{1}{S} \iint_{\text{Body}} -C_p \, \vec{e_n} \cdot \vec{e_i} \mathrm{d}s, \tag{5.2}$$

with $i \in \{x, y, z\}$.

Particle image velocimetry

Wake analyses are made from particle image velocimetry (PIV). The system is comprised of a dual pulse laser (Nd:YAG, 2×135 mJ, 4 ns) and two Dantec CCD cameras (FlowSense EO, 4 Mpx). The setup acquires image pairs at a rate of 10 Hz; each acquisition records 2000 image pairs. The bidimensional velocity measurements are performed in the planes $y^* = 0$ and $z^* = 0.6$ while stereoscopic PIV measures the three components of the velocity in the planes $x^* = 1.0$ and $x^* = 2.0$. The size of the interrogation window (32 px $\times$ 32 px) corresponds to physical sizes of 2.5 mm $\times$ 2.5 mm in the plane $y^* = 0$, 1.6 mm $\times$ 1.6 mm in the plane $z^* = 0.6$ and 2.4 mm $\times$ 2.4 mm in the planes $x^* = 1.0$ and $x^* = 2.0$.

The mean velocities and the Reynolds stresses are measured from the valid vectors of the instantaneous velocity fields; these statistics are taken into account only when more than 1500 valid vectors are obtained from the 2000 measurements.

Hot-wire probes

To get the unsteady characteristics of the flow, flying hot-wire probes are mounted on three-dimensional displacement systems made up of three Newport (M-)MTM long travel consoles controlled by a Newport Motion Controller ESP301. The precision of the robots is better than 0.1 mm. The probes are from Dantec (hot-wire type 55P15, support type 55H22) and use an overheat ratio of 1.5; they are connected to two DISA55 hot-wire anemometry measurement units. These probes mounted on the displacement systems record the velocity in the wake at a sampling frequency of 1 kHz.

5.2 Mean properties of the flow

The mean flow over this geometry is displayed in figure 5.2; it presents different separations. First, a boundary layer detachment occurs on the four faces at the end of the forebody; visualizations of the separation are visible in figures 5.3(a)–(b). The pressure measurements in the planes $y^* = 0$ and $z^* = 0.67$ (see figures 5.4a–b) evidence the adverse pressure gradient imposed by the geometry in this region; they also locate the separated regions through characteristic plateaus on the body roughly for $-3.5 < x^* < -3.0$ on the four faces. The reattachments, associated with the pressure recovery on the surface, are reported at $x^* \approx -3.0$ on the sides and on the upper faces and slightly sooner on the lower face. This difference between the upper and lower faces is certainly due to the ground: it does not prevent the boundary layer detachment on the lower face of the body but it provokes an early reattachment. These flow separations are also reported in various experiments or numerical simulations (Spohn & Gilliéron, 2002; Krajnović & Davidson, 2005; Franck *et al.*, 2009) and persist at $\mathrm{Re}_H = 2.5\ 10^6$ as they are still observed in the experiments presented chapter 9.

Velocity profiles at the trailing edge are measured to know whether the boundary layers are turbulent or not at the base separation and also to provide their characteristic thickness. The results are presented in figure 5.5; the separations at the end of the forebody induce important losses of momentum beyond the boundary layer at the trailing edge. For the same reason, the levels of fluctuating velocities also remain important far from the geometry except in the case of the lower face (see figure 5.5c) where the ground proximity limits the forebody separation. The peaks of fluctuating velocities near the surface indicate that the boundary layers are turbulent at the trailing edge but the absence of constant velocity far from the surface prevents the use of the usual definitions of characteristic thicknesses. However, considering the size of the region of intense vorticity near the body, the normalized initial thicknesses of the shear layers at separation are 0.026, 0.025 and 0.017, with a precision of 0.003, for the top, side and lower faces respectively.

The blunt trailing edge imposes a massive flow separation at the base. The recirculation region visible in figures 5.2(a)–(c) extends up to $x^* = 1.47$. The cross-flow measurements at $x^* = 1.0$ (see figure 5.2c) show that the recirculation region preserves roughly the rectangular shape of the trailing edge: the geometry of the contour ${U_x}^* = 0$ seems to result from the equal growth of the mixing layers from the separation at $x^* = 0$, at least for the upper and lateral shear layers. The recirculation bubble then closes in the plane $z^* = 0.59$ with two saddle points at $x^* = 1.46$ and $y^* \approx \pm 0.17$. Despite the ground proximity, the mean velocities at the center of the recirculation region remain oriented along the x direction. These PIV measurements emphasize the time-averaged vision of the toric recirculation organization which is also observed through pressure measurements in the wake.

Figures 5.6(a)–(b) show the contours of pressure in the planes $y^* = 0$ and $z^* = 0.67$. The minima of pressure in the wake are reported inside the recirculation region, near the separatrix in the plane $y^* = 0$. These locations correspond to the center of the time-averaged recirculation structures visible in figure 5.2(a)–(b). The three-dimensional mapping of the static pressure reveals the region of the recirculation bubble where the pressure is the lowest, at $x^* \approx 0.6$ (see figure 5.6c). The pressure coefficient is close to 0 at the end of the recirculation bubble and, further downstream, it reaches positive values which can be associated with the change of streamline curvature. The adverse pressure gradient is particularly intense on the ground between $x^* = 1$ and $x^* = 2$. It induces significant losses of momentum close to the ground downstream of the body (see figures 5.2a and 5.2d). Boundary layer separation on the ground in this region is not

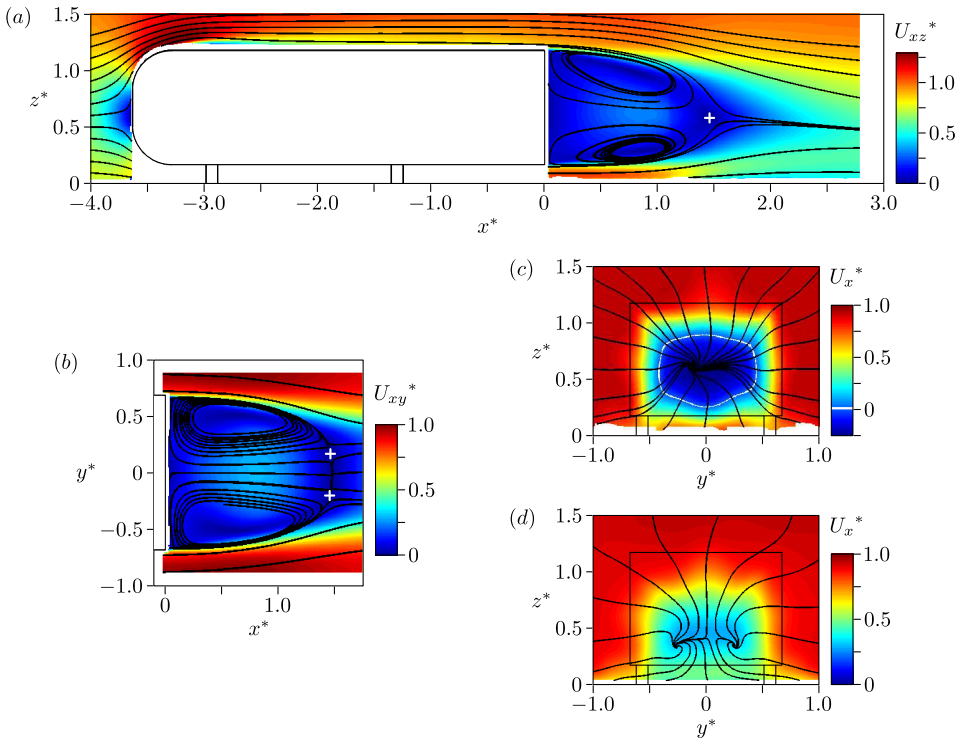

Figure 5.2. Mean velocities in the plane $y^* = 0$ (a), $z^* = 0.6$ (b), $x^* = 1.0$ (c) and $x^* = 2.0$ (d). The crosses locate the saddle points.

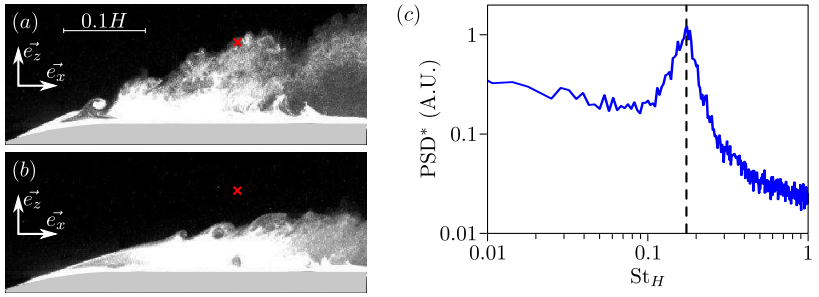

Figure 5.3. Characterization of the forebody detachment on the upper face: visualizations of the turbulent transition at different instants (a)–(b) and autopower spectrum of a hot-wire probe signal in the mixing layer at $x^* = -3.12$, $y^* = 0$ and $z^* = 1.28$ (c). The crosses locate the hot-wire probe; the dashed line locates $\mathrm{St}_H = 0.174$.

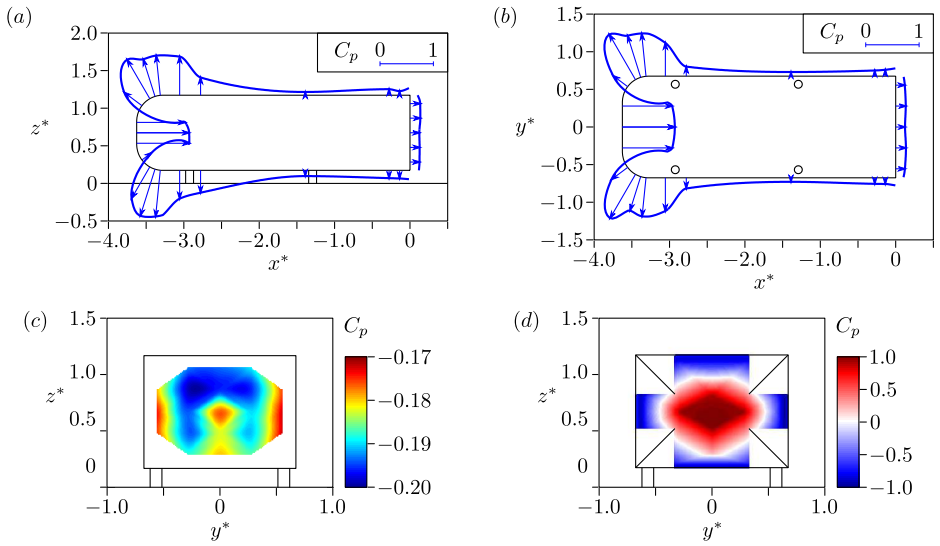

Figure 5.4. Distribution of pressure on the body in the planes $y^* = 0$ (a), $z^* = 0.67$ (b), on the base (c) and on the forebody (d). The arrows locate the pressure taps.

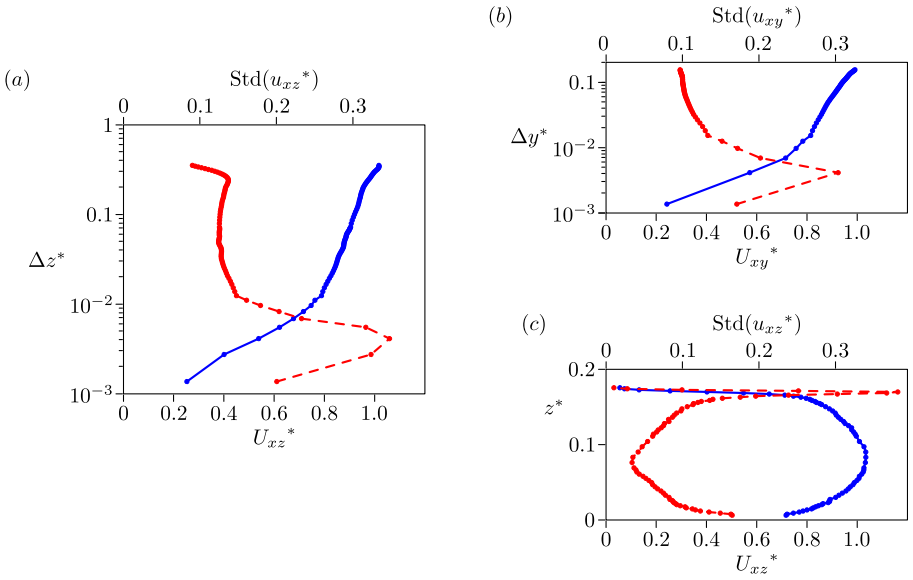

Figure 5.5. Mean (continuous blue line, bottom axis) and fluctuating (dashed red line, top axis) velocity profiles of the boundary layers at $x^* = 0$ from the upper face at $y^* = 0$ (a), the side face at $z^* = 0.67$ (b) and the lower face at $y^* = 0$ (c). Δy^* and Δz^* are the normalized gaps between the hot-wire probe and the surface.

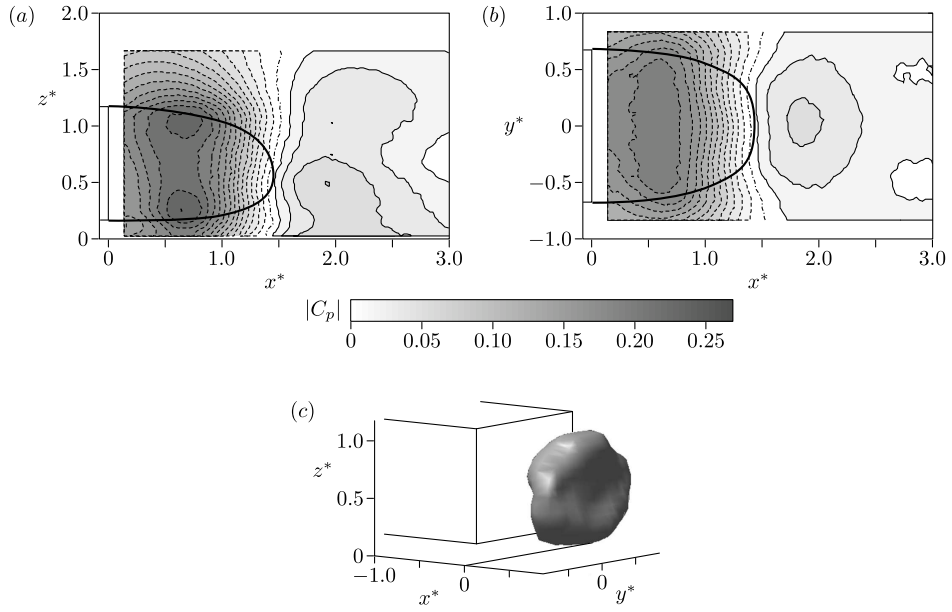

Figure 5.6. Contours of static pressure in the plane $y^* = 0$ (a) and $z^* = 0.67$ (b); the continuous and dashed lines are respectively positive and negative values; the contour 0 is the dotted-dashed line; the contour interval is 0.02. The thick black line locates the separatrix of the mean flow. (c) Iso-surface of pressure $C_p = -0.2$ in the recirculation region.

observed but may occur for smaller ground clearances as suggested by the experiments of Ruiz *et al.* (2009). This point is considered in the next chapter.

The low pressure region in the recirculating flow affects the pressure on the base. It is measured approximately constant around $C_{pb} \approx -0.185$ as visible in figure 5.4(c), the slight variations reflect the impact of the low pressure region in the recirculation bubble (see figure 5.6). The drag measured by the balance is $C_x = 0.274 \pm 0.003$; it is slightly larger than the drag coefficient of 0.250 presented in Ahmed *et al.* (1984) but this value is consistent with the other results reported in literature, usually between 0.26 and 0.32. Considering the distributions of pressure shown in figures 5.4(c)–(d), the pressure contribution to the aerodynamic forces can be estimated using equation (5.2); the different contributions are listed in table 5.1. The dominant part of pressure drag ($C_{xp} \approx 0.75\, C_x$) mostly associated with the low base pressure is also in good agreement with the results of Ahmed *et al.* (1984). In particular, figure 5.4(d) helps understand the limited contribution of the forebody: there is as much over-pressure in the center as under-pressure in the periphery.

The negative sign of C_z is related to the pair of counter-rotating vortices observed through the streamlines in the cross-flow plane at $x^* = 2.0$ (see figure 5.2d). Similarly, the value of $C_{yp} \approx 0$ is coherent with the symmetry of both the geometry and the flow.

The PIV results allow the measurements of the Reynolds stresses in the different planes. Figure 5.7 presents the components $\langle {u'_x}^2 \rangle$, $\langle {u'_z}^2 \rangle$ and $\langle u'_x u'_z \rangle$. They are particularly intense at the forebody separation; the energy of the fluctuations being due to usual shear layer dynamics but also to evolutions of the shear position at $\mathrm{St}_H = 0.174$ (see pictures and autopower spectrum in figure 5.3). The ground induces a slight asymmetry in the z di-

$$\begin{array}{lcrcl} C_x & = & 0.274 & \pm & 0.003 \\ C_z & = & -0.038 & \pm & 0.008 \\ C_{xp} & = & 0.206 & \pm & 0.005 \\ C_{yp} & = & 0.006 & \pm & 0.015 \\ C_{zp} & = & -0.080 & \pm & 0.015 \\ C_{pb} & = & -0.185 & \pm & 0.003 \end{array}$$

Table 5.1. Aerodynamic forces on the body and their pressure components.

RS	$\max_{x^*>0}(\text{RS})$	$x^*\left(\max_{x^*>0}(\text{RS})\right)$	$z^*\left(\max_{x^*>0}(\text{RS})\right)$
$\langle {u'_x}^{*2} \rangle$	0.069	1.18	0.22
$\langle {u'_z}^{*2} \rangle$	0.038	1.67	0.61
$\lvert\langle {u'_x}^* {u'_z}^* \rangle\rvert$	0.027	1.24	1.00

Table 5.2. Maxima of the Reynolds stresses (RS) in the wake and their corresponding locations in the plane $y^* = 0$.

rection. After the massive separation at $x^* = 0$, the mixing layers develop mostly toward the recirculation region and the highest values of normal and shear stresses are measured near the separatrix. The maximal values measured in the wake are detailed in table 5.2; however, it is worth mentioning that the maximum of the streamwise Reynolds stresses is measured in the mixing layer from the forebody detachment: $\langle {u'_x}^{*2} \rangle = 0.23$ at $x^* = -3.06$ and $z^* = 1.24$.

Similar distributions are obtained in the plane $z^* = 0.6$ for the streamwise normal stresses and the shear stresses (see figures 5.8*a* and 5.8*c*). Nevertheless, contrary to the results presented in figure 5.7(*b*), the highest values of $\langle {u'_y}^2 \rangle$ are measured at $y^* = 0$ upstream of the end of the recirculation region (see figure 5.8*b*).

Finally, the values of the Reynolds stresses in the plane $x^* = 1.0$ in figure 5.9 confirm that the dominant component is $\langle {u'_x}^2 \rangle$ and that the shear stresses from the upper and lower faces are more intense than from the lateral ones. The Reynolds stresses from stereoscopic PIV in the plane $x^* = 1.0$ (see figure 5.9) are slightly under-evaluated in comparison to the ones from bidimensional PIV in the planes $y^* = 0$ and $z^* = 0.6$ (see figures 5.7 and 5.8) but their spatial distributions remain consistent[1]. The energy of these velocity fluctuations relies on the turbulent evolution of the flow but also on some coherent fluid motions presented in the next section.

[1]The stereoscopic PIV data are obtained from the correlation between two simultaneous bidimensional PIV measurements so there is an additional step in the calculation; this may slightly improve the estimation of the instantaneous velocities and reduce the average levels of fluctuations.

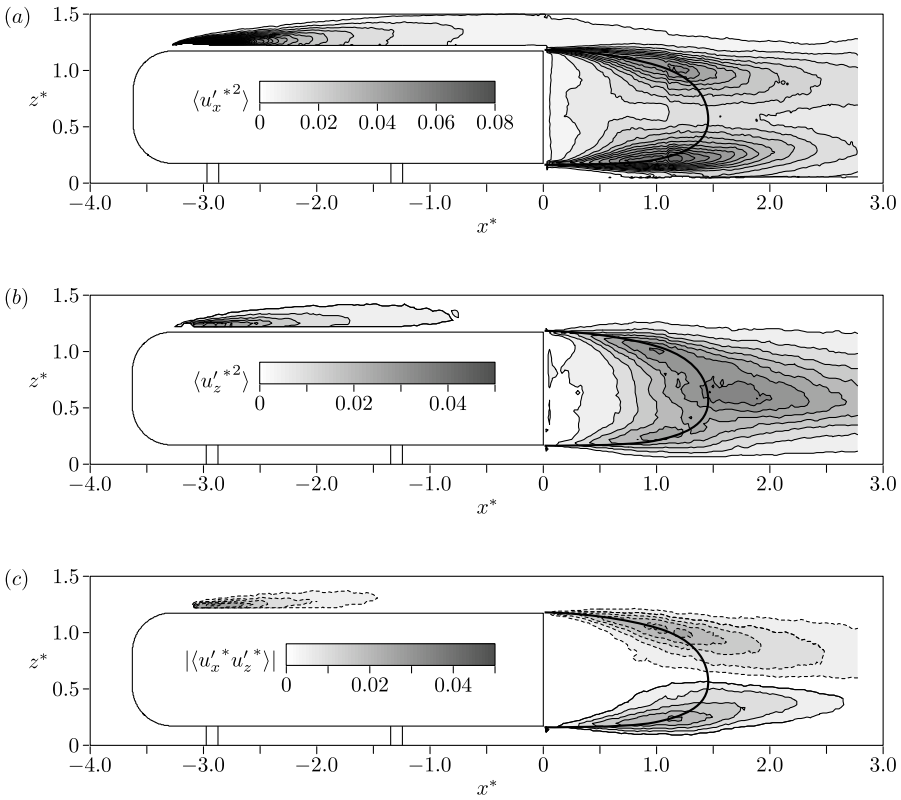

Figure 5.7. Contours of Reynolds stresses in the plane $y^* = 0$: $\langle u_x'^{*2}\rangle$, (a); $\langle u_z'^{*2}\rangle$, (b); $\langle u_x'^{*} u_z'^{*}\rangle$, (c). The continuous and dashed lines are respectively positive and negative values; the contour interval is 0.005; the contour 0 is not plotted. The thick black line locates the separatrix of the mean flow.

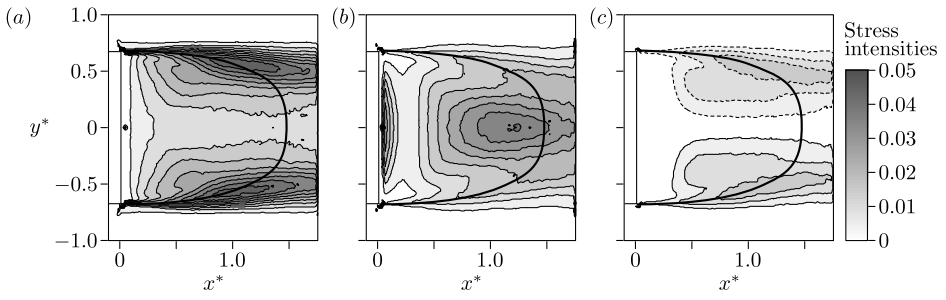

Figure 5.8. Contours of Reynolds stresses in the plane $z^* = 0.6$: $\langle u_x'^{*2}\rangle$, (a); $\langle u_y'^{*2}\rangle$, (b); $\langle u_x'^{*} u_y'^{*}\rangle$, (c). The continuous and dashed lines are respectively positive and negative values; the contour interval is 0.005; the contour 0 is not plotted. The thick black line locates the separatrix of the mean flow.

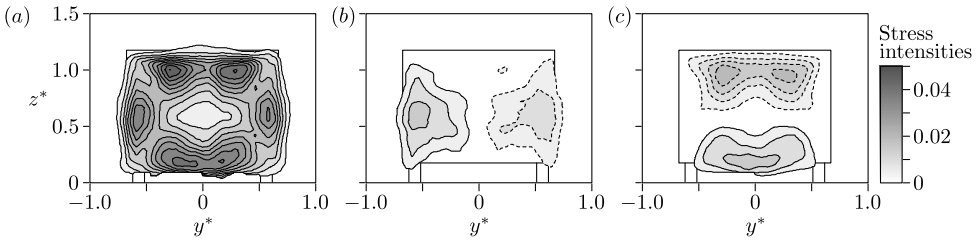

Figure 5.9. Contours of Reynolds stresses in the plane $x^* = 1.0$: $\langle {u'_x}^{*2} \rangle$, (a); $\langle {u'_x}^* {u'_y}^* \rangle$, (b); $\langle {u'_x}^* {u'_z}^* \rangle$, (c). The continuous and dashed lines are respectively positive and negative values; the contour interval is 0.005; the contour 0 is not plotted.

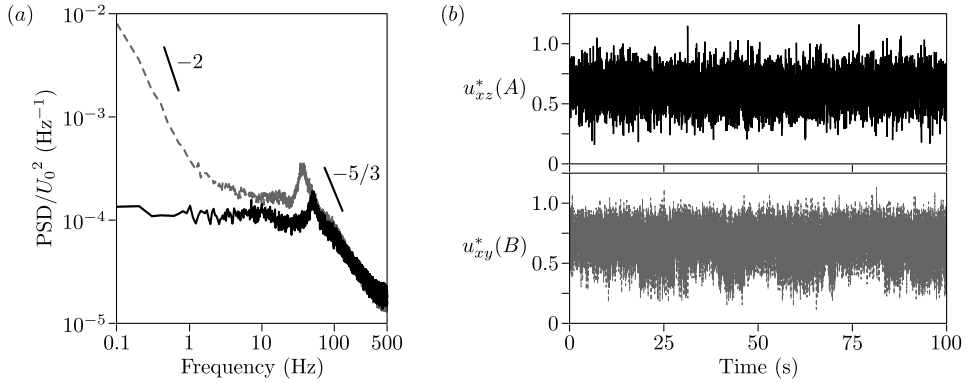

Figure 5.10. Autopower spectra (a) and sample time evolution (b) of the velocity signals recorded at $A(2.5, 0, 0.9)$ (continuous black line) and $B(2.5, 0.5, 0.6)$ (dashed gray line) from hot-wire measurements.

5.3 Wake dynamics

The autopower spectra of hot-wire probe signals in the wake reveal different characteristic frequencies. Figure 5.10(a) shows the autopower spectra at the points A and B respectively located at $x^* = 2.5$, $y^* = 0$, $z^* = 0.9$ and $x^* = 2.5$, $y^* = 0.5$, $z^* = 0.6$, *i.e.* downstream of the upper and lateral mixing layers. Peaks of energy are reported at 35.4 Hz and 48.4 Hz with a precision of 0.2 Hz, the corresponding Strouhal numbers ($\mathrm{St}_H = fH/U_0$) are 0.127 and 0.174 with a precision better than 10^{-3}. In addition, the probe located at B measures an important energy in the low frequency domain. This phenomenon is clear in figure 5.10(b): long time evolutions, over several seconds, are observed on the velocity measurement at B. These two kinds of coherent dynamics, one associated with long time scales, the other at higher frequencies, are analyzed in sections 5.3.1 and 5.3.2 respectively.

5.3.1 Bi-stability of the wake

This section first characterizes the two preferred asymmetric states responsible for the bistable behavior. Then, the corresponding dynamics are studied. Finally, the effects of the free-flow velocity and of the ground clearance are presented successively.

Characterization of the two preferred states

From the local measurements of velocity at B presented in figure 5.10(b), a bistable behavior seems to be detected in the wake, this phenomenon is confirmed using global quantities of the wake. Since it has long time evolutions, it can be analyzed using the PIV measurements at 10 Hz. As for the sphere wake in chapter 2, the barycenter of momentum deficiency in the cross-flow plane $x^* = 1.0$ is considered as an indicator of the wake position. The quantities ${y_W}^*$ and ${z_W}^*$ are defined by

$$ {y_W}^* = \frac{\iint y^* \cdot (1 - {u_x}^*)\,\mathrm{d}s}{\iint (1 - {u_x}^*)\,\mathrm{d}s}, \tag{5.3} $$

and

$$ {z_W}^* = \frac{\iint z^* \cdot (1 - {u_x}^*)\,\mathrm{d}s}{\iint (1 - {u_x}^*)\,\mathrm{d}s}, \tag{5.4} $$

with a domain of integration limited to ${u_x}^* < 1$.

Figure 5.11(a) presents a PIV snapshot of the streamwise velocity in the plane $x^* = 1.0$ and the associated position of the barycenter of the momentum deficiency at ${y_W}^* = 0.043$ and ${z_W}^* = 0.575$. The time evolution of the positions ${y_W}^*$ and ${z_W}^*$ over the 200 s of the PIV measurements[2] are plotted in figure 5.11(b) and 5.11(c) respectively. The associated probability distributions clearly evidence one preferred position in the z direction but two different positions in the y direction centered on ${y_W}^* = \pm 0.06$. The states are denoted by #P for the one associated with a positive value of ${y_W}^*$ and #N for the one with a negative value of ${y_W}^*$. Similar probability distributions with two preferred positions are also obtained from the analyses of the snapshots in the plane $x^* = 2.0$ and $z^* = 0.6$. Therefore, the two preferred states of the wake can be discriminated by the distributions of velocity in the wake. Conditional averaging on the sign of ${y_W}^*$ allows the extraction of the asymmetric topologies from the PIV measurements presented in figure 5.2. The results corresponding to the state #P are displayed in figure 5.12. Figure 5.12(a) presents the asymmetric flow in the plane $z^* = 0.6$. As in chapter 3, there is only one saddle point left, off the streamwise axis, and the mean recirculating flow is diagonal. Figures 5.12(b)–(c) present the flow in the cross-flow planes $x^* = 1.0$ and $x^* = 2.0$ with a clear asymmetry.

Furthermore, this topology #P induces asymmetric distributions of Reynolds stresses in the planes $z^* = 0.6$ and $x^* = 1.0$ (see figures 5.13 and 5.14 respectively). The reflectional symmetry is lost and the activity of the mixing layer is mostly concentrated on the same side as the wake. On the other hand, figure 5.14 shows that the characteristics of the upper and lower mixing layers are almost independent of the state of the wake.

As the two states are associated with a diagonal recirculating flow, they may also be characterized by asymmetric distributions of base pressure (see chapter 3). The states #P and #N can be studied through pressure measurements since the sampling frequency of 1 Hz does not limit the analyses of this behavior. Figure 5.15 presents sample evolutions of the pressure gradients in the y and z directions on the base at $y^* = 0$ with their probability distributions obtained over 10^4 s. Figure 5.15(b) shows that the most probable value of the pressure gradient in the z direction is close to its mean value which is slightly negative as expected from figure 5.4(c). On the contrary, the histogram in figure 5.15(a) is balanced but the two states are clearly visible. The states are associated with $\partial {c_p}/\partial {y^*} = \pm 0.17$; the state #P corresponds to the one with a positive gradient and the state #N to the one with a negative gradient. Approximately 5% of the measurements correspond to $|\partial {c_p}/\partial {y^*}| < 0.1$ but they are likely to be cases of shift from one asymmetric state to another within the second of a pressure measurement; this interpretation is consistent with the equiprobability of the cases $\partial {c_p}/\partial {y^*} \in [-0.1, 0.1]$. Conditional averaging of the pressure is then performed using the sign of $\partial {c_p}/\partial {y^*}$ as a topology indicator.

Figure 5.16(a) shows the asymmetric distributions of pressure on the body in the plane $z^* = 0.67$. The two preferred values of $\partial {c_p}/\partial {y^*}$ at $y^* = 0$ are visible on the base. The coexistence of these two states leads to the mean symmetric distribution of pressure plotted in figure 5.4. These asymmetric distributions are independent of the asymmetric states in the domain $x^* < -1$; for example, the stagnation point on the forebody is measured at the same location. Thus, this bistable behavior results neither from low frequency oscillations of the free-flow direction nor from some wind tunnel modes.

After conditional averaging on the sign of the base pressure gradient in the y direction, the pressure distribution on the base is obtained for the state #P. Figure 5.16(b) show that the asymmetry is a global characteristic of the pressure on the base: it ranges

[2]There are 2000 snapshots recorded at 10 Hz.

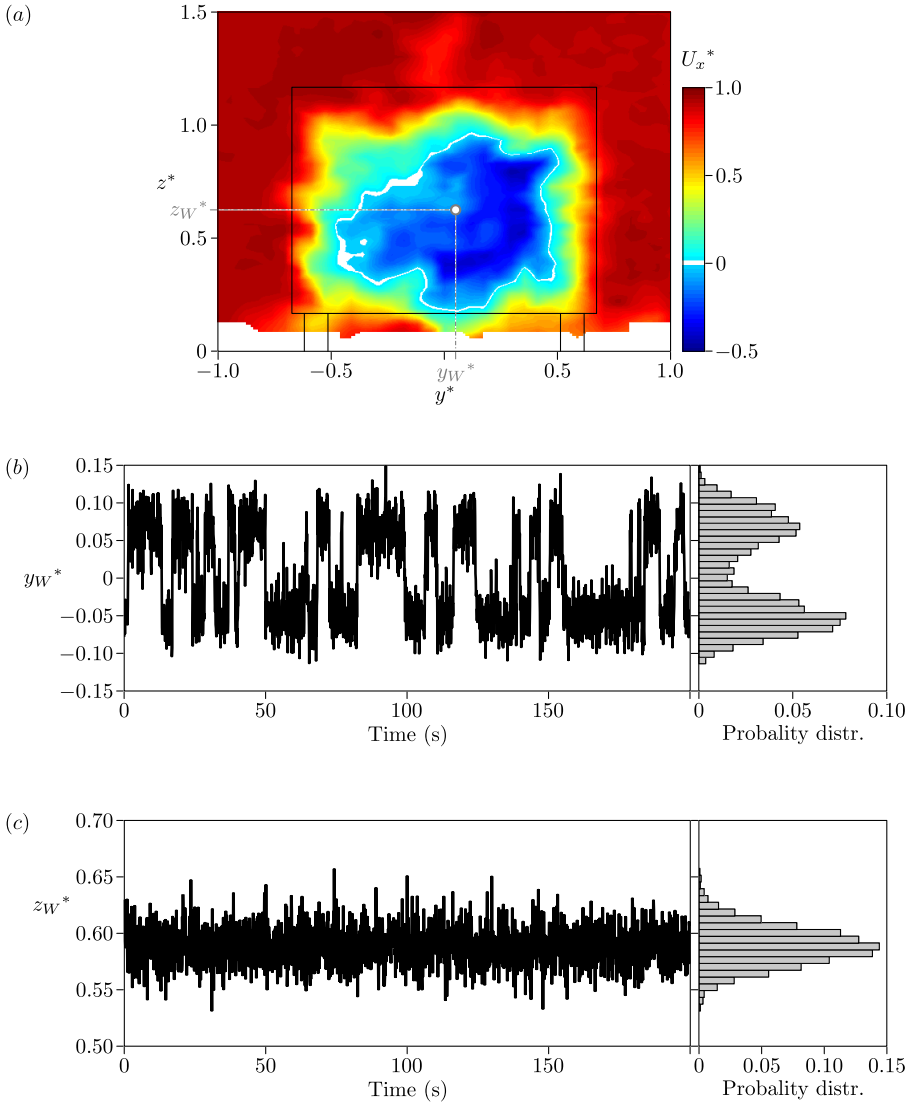

Figure 5.11. (a) Sample snapshot of streamwise velocity in the plane $x^* = 1.0$; ◯, barycenter of momentum deficiency located at ${y_W}^* = 0.043$ and ${z_W}^* = 0.575$. (b) Time evolution of the barycenter of momentum deficiency in the y direction and associated probability distribution. (c) Same as (b) in the z direction.

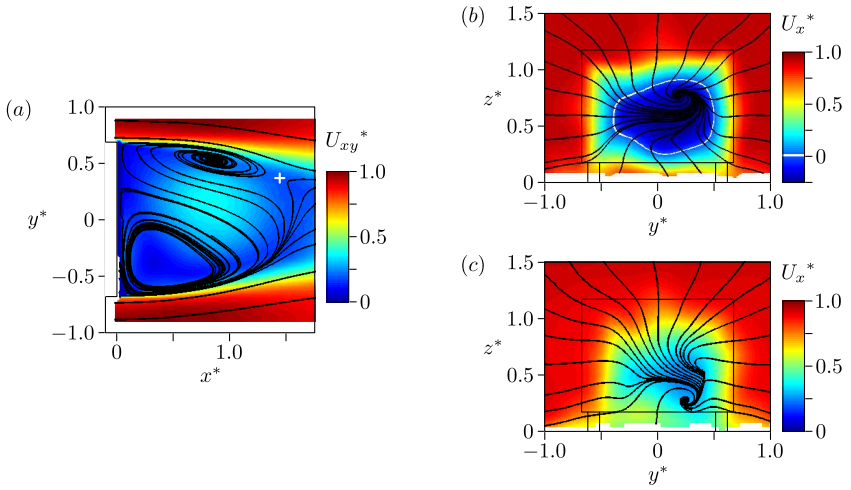

Figure 5.12. Velocities corresponding to state #P in the planes $z^* = 0.6$ (a), $x^* = 1.0$ (b) and $x^* = 2.0$ (c). The cross locates the saddle point.

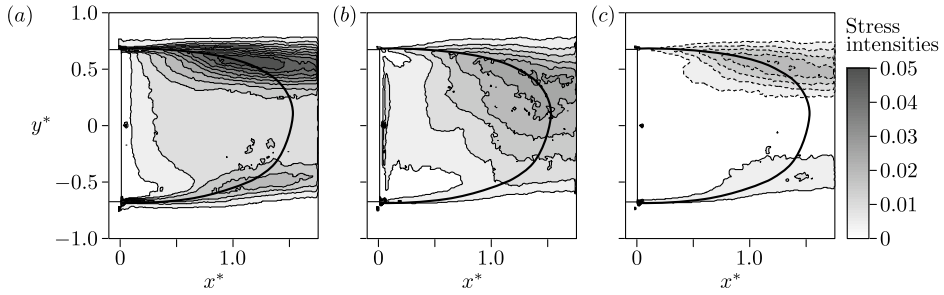

Figure 5.13. Contours of Reynolds stresses in the plane $z^* = 0.6$ of the wake in the state #P: $\langle {u'_x}^{*2} \rangle$, (a); $\langle {u'_y}^{*2} \rangle$, (b); $\langle {u'_x}^* {u'_y}^* \rangle$, (c). The continuous and dashed lines are respectively positive and negative values; the contour interval is 0.005; the contour 0 is not plotted. The thick black line locates the separatrix of the mean flow of the state #P.

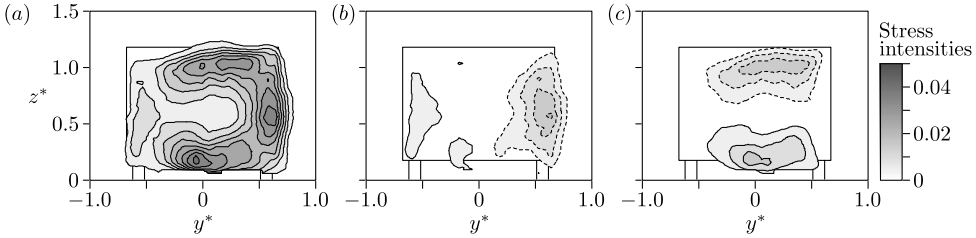

Figure 5.14. Contours of Reynolds stresses in the plane $x^* = 1.0$ of the wake in the state #P: $\langle {u'_x}^{*2} \rangle$, (a); $\langle {u'_x}^* {u'_y}^* \rangle$, (b); $\langle {u'_x}^* {u'_z}^* \rangle$, (c). The continuous and dashed lines are respectively positive and negative values; the contour interval is 0.005; the contour 0 is not plotted.

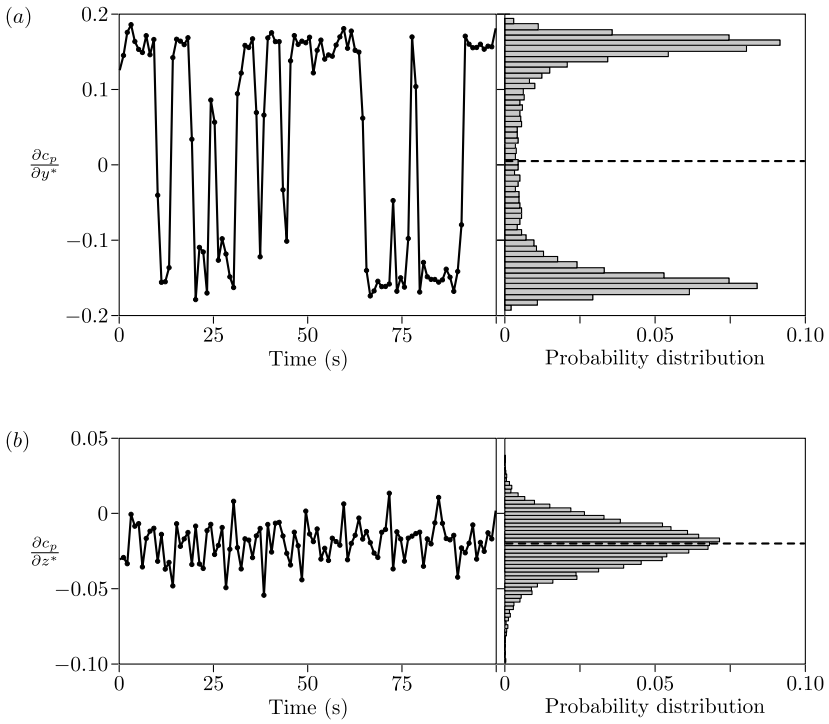

Figure 5.15. Sample time evolution and probability distribution of the base pressure gradient in the y direction (a) and in the z direction (b); the dashed lines locate the mean values.

in $C_p \in [-0.24, -0.12]$ and presents much larger variations than the results displayed in figure 5.4(c). It is then important to note that the view of a toric recirculation organization is not pertinent since it does not reflect the topology of the asymmetric flow.

Besides, the asymmetric distributions of pressure presented in figure 5.16(a) are associated with lateral forces that counterbalance in average. The pressure forces of the asymmetric states in the y direction are evaluated at $C_{yp} = \pm 0.021$ with a poor precision of 0.015. This force corresponds to the difference of the pressure on the side of the body for $-1 < x^* < 0$; it is associated with the wake asymmetry visible in figure 5.12(c). This difference in the streamwise pressure gradients for $-1 < x^* < 0$ induces distinct boundary layer characteristics on the sides of the geometry.

The boundary layer velocities presented in figure 5.5(b) can equally be analyzed regarding the bi-stability. An example of velocity signal in the boundary layer is displayed in figure 5.17(a). As in figure 5.10(b), a bistable behavior seems present but is not directly visible in the probability distribution. When the same velocity signal is filtered using an average filter over windows of 0.5 s (see figure 5.17b), the probability distribution shows two peaks corresponding to the two topologies #P and #N[3]. For each point in the boundary layer profile, this method allows the separation of the two states. Therefore, conditional averaging gives access to the boundary layer profiles of each state (see figure 5.18). The characteristic thicknesses of the boundary layers are similar for the two states; they are measured at 0.024 for the faster profile and 0.026 for the slower one with a precision of 0.003. The profiles of velocity fluctuations indicate that, whatever the current state, the

[3]The conditions of existence of one or two peaks in the PDF are studied in appendix D.

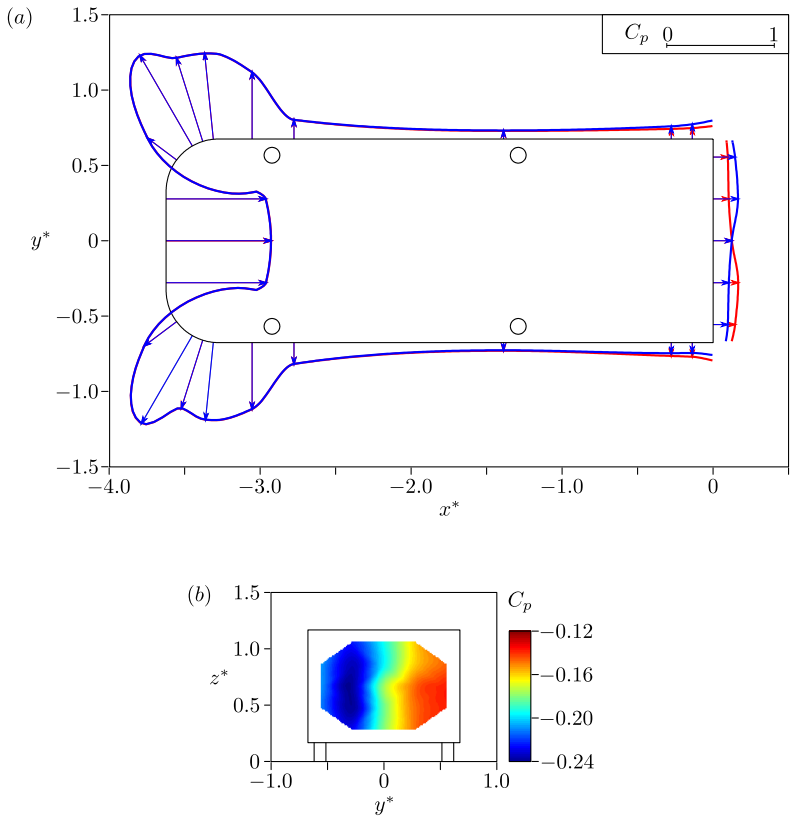

Figure 5.16. (a) Pressure distribution of the states #N (blue line) and #P (red line) on the body in the plane $z^* = 0.67$. The arrows locate the pressure taps. (b) Pressure distribution of the state #P on the base.

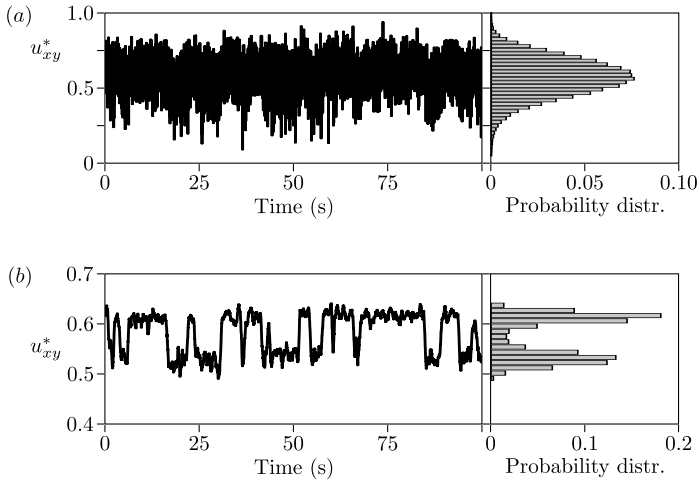

Figure 5.17. Sample time evolution of the velocity in the lateral boundary layer at the trailing edge and associated probability distribution: raw measurement (a) and filtered signal using an averaging filter over a window of 0.5 s (b).

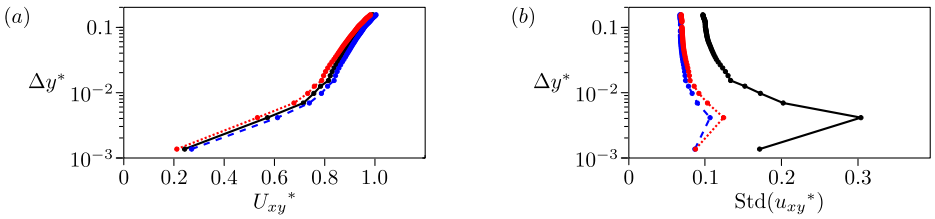

Figure 5.18. Mean (a) and fluctuating (b) velocity profiles of the boundary layers from the middle of the side face ($y^* > 0$) at $x^* = 0$: continuous black line, symmetric mean flow; dashed blue line, state #N; dotted red line, state #P. Δy is the gap between the probe and the surface.

$\mathbb{P}(\mathcal{S}_t = \#\mathrm{P}) = 0.514$	$\mathbb{P}(\mathcal{S}_t = \#\mathrm{N}) = 0.486$
$\mathbb{P}(\mathcal{S}_t = \#\mathrm{P} \vert \mathcal{S}_{t-1} = \#\mathrm{P}) = 0.816$	$\mathbb{P}(\mathcal{S}_t = \#\mathrm{N} \vert \mathcal{S}_{t-1} = \#\mathrm{N}) = 0.806$

Table 5.3. Probabilities of states #P and #N depending on the previous states. $\mathbb{P}(\mathrm{A}|\mathrm{B})$ is the conditional probability of A, given B; the events are considered at 1 Hz; the precision is better than 0.01.

two boundary layers are turbulent. This confirms that the bi-stability is neither associated with an intermittent boundary separation on the forebody nor dependent on its laminar or turbulent regime at the trailing edge. The difference in the levels of velocity fluctuations between the mean symmetric flow and the asymmetric states in figure 5.18(b) is due to the contribution of the bi-stability: part of the fluctuations are ascribed to the difference in average velocities between the two states (see figure 5.18a).

Now that the bistable behavior is evidenced and the asymmetric states are characterized, the associated dynamics are considered.

Random topology shifts

The topology shifts between the state #P and #N are analyzed from the evaluation of the base pressure gradient in the y direction at 1 Hz over 10^4 s (see figure 5.15a). The state of the flow at the instant t, obtained from the sign of $\partial c_p/\partial y^*$, is denoted by $\mathcal{S}_t \in \{\#\mathrm{P}, \#\mathrm{N}\}$. The states #P and #N are equiprobable (see table 5.3), the shifts seem random and appear in average after $T_S = 5.3$ s. Note that $T_S U_0/H \sim 1500$ so that the bistable dynamics have a time scale that is three orders of magnitude larger than the typical time scale of the wake (H/U_0). Thus, the normalization using U_0 and H seems inappropriate and the following analyses are left in their respective units.

To detail these statistics, the time between two successive shifts is studied. The distribution follows an exponential law consistent with independent evolutions of the states. Indeed, let $\mathbb{P}_{\mathrm{shift}} = \mathbb{P}(\mathcal{S}_t \neq \mathcal{S}_{t-1})$ be the probability to shift between two successive measurements, *i.e.* the rate of shift per second, independent of the instant t. The results listed in table 5.3 give $\mathbb{P}_{\mathrm{shift}} = 0.189$ with

$$\begin{aligned} \mathbb{P}_{\mathrm{shift}} \quad = \quad & \mathbb{P}(\mathcal{S}_t = \#\mathrm{N})\,\mathbb{P}(\mathcal{S}_t = \#\mathrm{P} \vert \mathcal{S}_{t-1} = \#\mathrm{N}) \\ & + \mathbb{P}(\mathcal{S}_t = \#\mathrm{P})\,\mathbb{P}(\mathcal{S}_t = \#\mathrm{N} \vert \mathcal{S}_{t-1} = \#\mathrm{P}). \end{aligned} \tag{5.5}$$

In case of independent topology shifts, the probability of remaining exactly k seconds

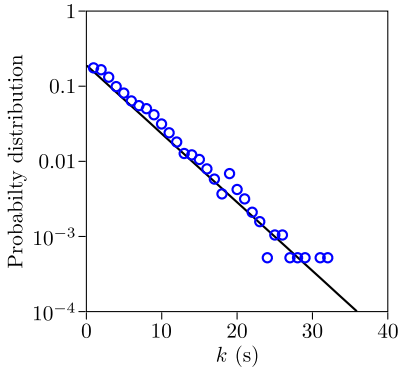

Figure 5.19. Probability distribution of remaining exactly k seconds in the same state: ◯, experimental data; —, theoretical law given in equation (5.7).

in the same state is then given by

$$\mathbb{P}(S_{k+1} \neq S_i, \forall i \in \{1..k\}) = \mathbb{P}_{\text{shift}}\ (1 - \mathbb{P}_{\text{shift}})^k. \tag{5.6}$$

So the probability distribution of remaining exactly k seconds in the same state follows

$$\mathbb{P}(S_{k+1} \neq S_i, \forall i \in \{1..k\}) = 0.189 \times 0.811^k. \tag{5.7}$$

In figure 5.19, the experimental data are in good agreement with the model given in equation (5.7). It confirms that the shifts between the topologies #P and #N are random and independent, *i.e.* the succession of states #P and #N behaves like a stationary Markov chain. This point is also consistent with the autopower spectra at B plotted in figure 5.10(a): the repartition of energy for frequencies under 1 Hz follows a power law with an exponent close to -2 expected for such random evolutions (see section D.2.2).

To improve the understanding of this bistable behavior, the impact of the free-stream velocity on the dynamics is now detailed.

Effect of the free-flow velocity

By changing the flow velocity, the bi-stability is observed in this facility at Reynolds numbers from 4.6 10^4 to 1.2 10^5. For each Reynolds number, the probability distribution of the base pressure gradient in the y direction presents two preferred positions as in figure 5.15(a). The states #P and #N always correspond to similar values of $\partial c_p/\partial y^* \approx \pm 0.17$. This indicates that the two topologies #P and #N are identical in this range of Reynolds numbers. Besides, it is observed that $\mathbb{P}_{\text{shift}}$, which is the rate of shift at 1 Hz, increases with the velocity, *i.e.* the mean time between shifts diminishes while the velocity increases (see figure 5.20). The precision also increases with the velocity since the ratio signal by noise is proportional to ${U_0}^2$ in the measurements of pressure gradients. It remains limited at moderate velocities and the experimental setup is not appropriate for further quantitative investigation of the dependence on U_0.

The randomness of the shifts and the absence of spontaneous topology shift in the laminar experiments in chapter 4 tend to identify the activity of the large-scale structures of turbulence as one of the main ingredients of the switch from one asymmetric state to the other.

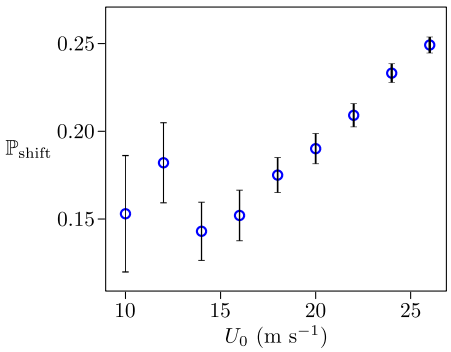

Figure 5.20. Probability to shift $\mathbb{P}_{\text{shift}}$ obtained from pressure measurements at 1 Hz as a function of free-stream velocity.

The observed asymmetric wake seems independent of the Reynolds number but in chapter 4, the presence of RSB regimes strongly relies on the ground proximity. So it appears important to investigate the effect of the ground clearance on the bi-stability.

Effect of the ground clearance

To explore the conditions of existence of the bi-stability, experiments are performed at different ground clearances $C^* \in [0; 0.50]$. For each ground clearance, the pressure on the base is recorded during 3 10^3 s; this allows the measurement of the base pressure gradients in the y direction which is an indicator of the wake asymmetry. For a given value of C, the probability distribution of $\partial c_p/\partial y^*$ indicates whether the wake has a bistable behavior or not: the bi-stability is characterized by two preferred asymmetric positions as in figure 5.15(a) whereas a stable wake is associated with a probability distribution concentrated around 0. The results are shown in figure 5.21; they must be interpreted for a constant value of C^*, the gray levels corresponding to PDF($\partial c_p/\partial y^*$) for this value of C^*. For example, the dashed line locates the reference case $C^* = 0.17$ for which the probability distribution of $\partial c_p/\partial y^*$ is given in figure 5.15(a).

- For $C^* < 0.07$, the PDF is centered on 0 and the most probable event is clearly $\partial c_p/\partial y^* = 0$. Hence, the wake is stable in the symmetric state.
- For $0.07 < C^* < 0.10$, the PDF remains centered on 0 but the peak gradually spreads: for $C^* = 0.10$, the probability density function is almost constant in the range $\partial c_p/\partial y^* \in [-0.10; 0.10]$. Thus, the wake is stable but it gradually loses its preference toward the centered state.
- For $C^* > 0.10$, the PDF presents two clear peaks centered around $\partial c_p/\partial y^* = \pm 0.17$ and these preferred values are independent of the ground clearance at first order. So the wake is bistable and the ground clearance has no effect on its degree of asymmetry.

As a result, the bistable behavior is strongly linked to the ground clearance: a critical value $C^* = 0.10$ is measured under which the bi-stability is suppressed. It may be associated with a change of topology related to a separation on the ground. Besides, the preference of the flow toward asymmetric states is obvious even far from the ground which indicates that the ground effect is not necessary to have preferred asymmetric positions[4].

[4]These points are thoroughly addressed in chapter 6.

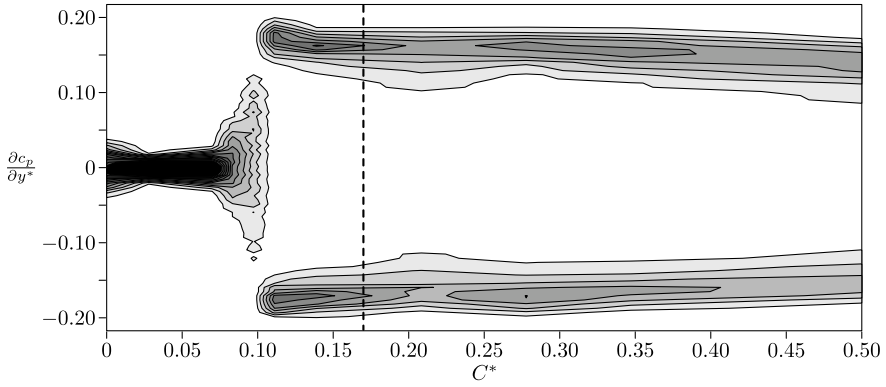

Figure 5.21. Probability density function of the base pressure gradient in the y direction as a function of the ground clearance C; the measurements are performed for $C^* = 0$, 0.03, 0.07, 0.08, 0.10, 0.11, 0.14, 0.21, 0.28, 0.35 and 0.50 with a precision of 0.005; the reference ground clearance is $C^* = 0.17$ (dashed line) and the corresponding histogram is given in figure 5.15(a); the contour interval is 2.

In addition to these long time evolutions ascribed to the bi-stability, figure 5.10 reports some unsteady global modes in the wake which are now considered.

5.3.2 Oscillating global modes

The autopower spectra at $A(2.5, 0, 0.9)$ and $B(2.5, 0.5, 0.6)$ reveal two peaks of energy at Strouhal numbers 0.127 and 0.174 (see figure 5.22a). These characteristic frequencies are denoted by f_{m1} and f_{m2} respectively and the Strouhal numbers are St_{Hm1} and St_{Hm2}. As in the experiments of Kiya & Abe (1999), depending on the hot-wire position, one or both frequencies can be measured. Figure 5.22(b) presents the probe positions A, A', B, B', C and C' in the plane $x^* = 2.5$ that are regularly used in the following.

To examine the envelops of these two modes, autopower spectra are first studied depending on the position of the hot-wire probe in the wake. The spectra in the plane $z^* = 0.6$ are shown in figure 5.23 for different streamwise positions. Only the St_{Hm1} mode is reported. Its activity is not significant in the mixing layers upstream of the end of the recirculation bubble, *i.e.* for $x^* < 1.5$. Downstream of $x^* = 1.5$, it is more energetic than the large-scale structures of turbulence and it is particularly clear at $x^* = 2.0$ and 2.5. The lack of symmetry in figures 5.23(a)–(b) is due to the asymmetric intrusion of the hot-wire probe (see figure 5.1) in a region where the flow is likely to be highly sensitive. The probe induces a predominance of the state #P presented in section 5.3.1 so the energy of the fluctuations of velocity is greater in the $y^* > 0$ region. The symmetry is recovered as soon as the probe is located downstream of $x^* = 2.0$. These results are in agreement with the experiments detailed in chapter 3 which indicate that the sensitivity of the wake orientation is concentrated upstream of the end of the recirculation bubble. Similarly, the results plotted in figure 5.24 show that only the St_{Hm2} mode is present in the plane of symmetry $y^* = 0$.

As a consequence, the two unsteady modes are reported in the autopower spectra downstream of the end of the recirculation bubble only. Nevertheless, it is important to note that these modes are global properties of the flow and they seem to affect the boundary layer detachment on the forebody. Indeed, the peak of energy at $\mathrm{St}_{Hm2} = 0.174$

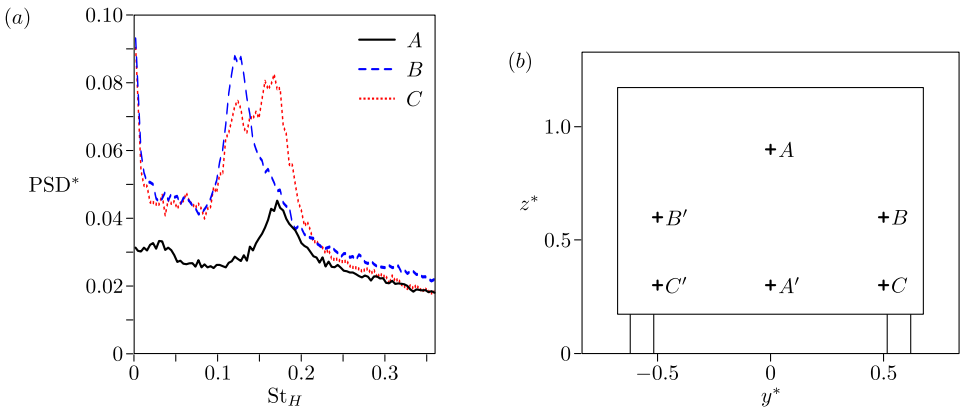

Figure 5.22. (a) Autopower spectra in the wake at $A(2.5, 0, 0.9)$ (continuous black line), $B(2.5, 0.5, 0.6)$ (dashed blue line) and $C(2.5, 0.5, 0.3)$ (dotted red line). (b) Locations of the hot-wire probe position A, A', B, B', C and C' in the cross-flow plane $x^* = 2.5$.

is also visible in the autopower spectrum of a hot-wire probe signal in the shear layer of the forebody separation, at least on the upper face (see figure 5.3c). This point is confirmed by the visualizations presented in figures 5.3(a)–(b); the shear presents low frequency dynamics in front of the rolling frequency of the shear layer: evolutions of the angle of separation, streamwise position of appearance of the rollings...

The three-dimensional repartition of these modes can also be characterized by the flying hot-wire probe. A criterion is used to detect the locations where these two frequencies are reported in the cross-flow planes $x^* = 1.5$, 2.5 and 4.0: it determines whether the mode at St_{Hmi}, with $i \in \{1, 2\}$, is present or not. This detection is based on the comparison between the average energy in the range $\mathrm{St}_H \in [\mathrm{St}_{Hmi} - 0.015; \mathrm{St}_{Hmi} + 0.015]$ and the average energy in $\mathrm{St}_H \in [0.040; 0.300]$. If the energy ratio is larger than 1.2 then the mode is marked. In figures 5.25, circles (crosses respectively) locate the positions of the hot-wire probe where the mode at St_{Hm1} (St_{Hm2} respectively) is detected. Nevertheless, it is worth noting a limitation of this criterion: as the energy of the mode at St_{Hm1} is generally larger than the other one, the criterion is less selective for the mode at St_{Hm1}.

The results in the plane $x^* = 1.5$ are displayed in figure 5.25(a); the mode at St_{Hm1} is mostly found in the lateral mixing layers whereas the one at St_{Hm2} is associated with the upper and lower mixing layers; both frequencies are obtained at the frontiers of these regions. Moving downstream at $x^* = 2.5$ (see figure 5.25b), the locations are similar, the main difference is the extension of the bottom region associated with St_{Hm2} in the y direction. Finally, in the plane $x^* = 4.0$, figure 5.25(c) indicates that the mode at St_{Hm1} stays downstream of the lateral mixing layers whereas the one at St_{Hm2} separates into three regions: one located downstream of the upper mixing layer, the two others are downstream of the bottom corners of the base. As previously mentioned, there is an adverse pressure gradient on the ground in the plane $y^* = 0$ so that the velocity is reduced in the plane of symmetry. Hence, the coherent structures emitted from the lower mixing layer are probably convected with the flow to the sides at $y^* \approx \pm 0.5$.

The structure of these modes is now considered through cross-correlations between two hot-wire probes at the different positions shown in figure 5.22(b). The coherence and phase, $r_{\mathcal{F}}$ and $\varphi_{\mathcal{F}}$ respectively, are defined in equation (A.4).

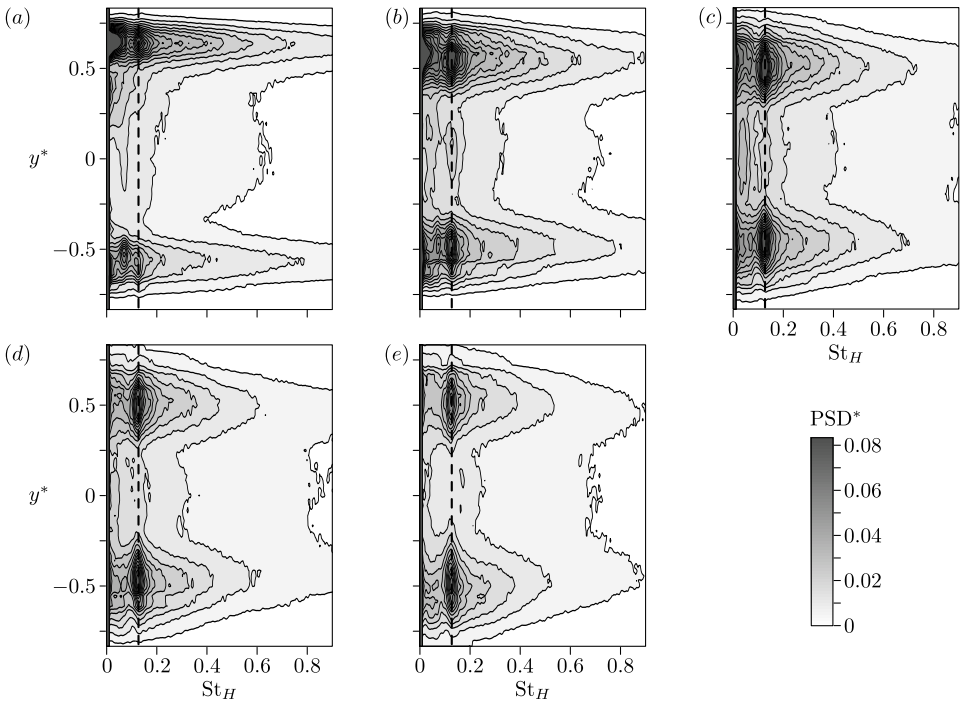

Figure 5.23. Autopower spectra in the plane $z^* = 0.6$ at $x^* = 1.0$ (a), $x^* = 1.5$ (b), $x^* = 2.0$ (c), $x^* = 2.5$ (d), $x^* = 3.0$ (e) for $y^* \in [-0.83, 0.83]$. The dashed line locates $\mathrm{St}_H = 0.127$.

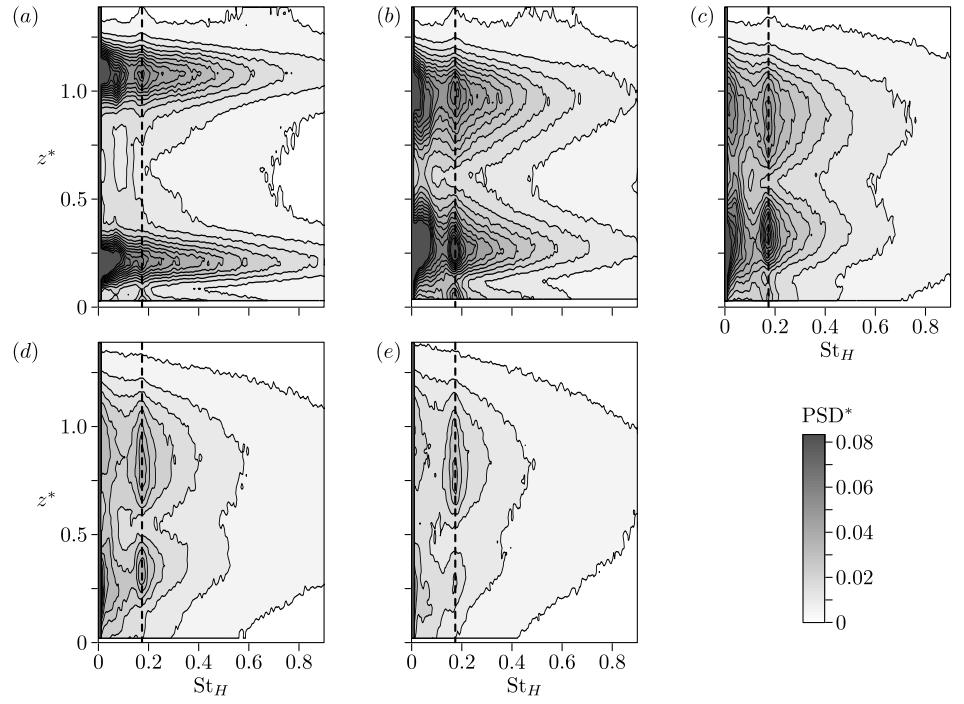

Figure 5.24. Autopower spectra in the plane $y^* = 0$ at $x^* = 1.0$ (a), $x^* = 1.5$ (b), $x^* = 2.0$ (c), $x^* = 2.5$ (d), $x^* = 3.0$ (e) for $z^* \in [0.03, 1.39]$. The dashed line locates $\mathrm{St}_H = 0.174$.

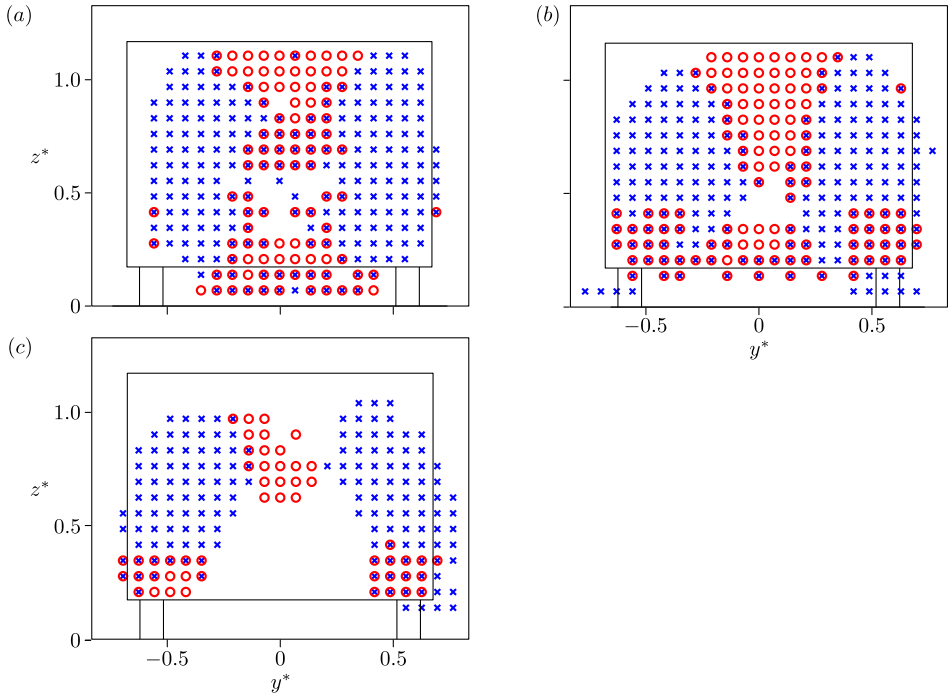

Figure 5.25. Locations where the modes are reported in the planes $x^* = 1.5$ (a), $x^* = 2.5$ (b) and $x^* = 4.0$ (c): $\times$, mode at $\mathrm{St}_{Hm1} = 0.127$; $\bigcirc$, mode at $\mathrm{St}_{Hm2} = 0.174$.

First, the velocity signals at $A(2.5, 0, 0.9)$ and $A'(2.5, 0, 0.3)$ are studied; the results can be seen in figure 5.26(a). The coherence is measured close to 0.5 at $\mathrm{St}_{Hm2} = 0.174$ with a phase shift of 0.75π. So, the periodic motion at St_{Hm2} results from an interaction of the upper and lower mixing layers. To understand the value of 0.75π, the phase shift at St_{Hm2} is analyzed varying the streamwise position of the lower hot-wire probe, denoted x_{probe}, while the upper probe stays at A. The results displayed in figure 5.27 show that the phase shift linearly depends on the distance $x_{\mathrm{probe}} - x_A$, the perfect phase opposition being found at $A''(2.1, 0, 0.3)$. As a consequence, the mode at St_{Hm2} consists in an oscillation of the wake in the z direction but the presence of the ground affects the phase so that the oscillation is not exactly in phase opposition.

Similar analysis can be made from the velocity signals at $B(2.5, 0.5, 0.6)$ and $B'(2.5, -0.5, 0.6)$. $r_{\mathcal{F}}(\mathrm{St}_{Hm1})$ reaches 0.65 and the corresponding phase is measured at π. Thus, the coherent motion associated with the lateral mixing layers consists in an oscillation of the wake in the y direction.

Finally, analyzing $r_{\mathcal{F}}$ and $\varphi_{\mathcal{F}}$ from the velocity measurements at $C(2.5, 0.5, 0.3)$ and $C'(2.5, -0.5, 0.3)$, the signals are found to have a coherence of 0.3 at the two mode frequencies. The signals are in phase opposition at St_{Hm1} and in phase at St_{Hm2}. Consequently, these values confirm the superposition of oscillations of the wake in the y direction at $\mathrm{St}_{Hm1} = 0.127$ and in the z direction at $\mathrm{St}_{Hm2} = 0.174$.

When these frequencies are normalized respectively by the height and width of the body, the corresponding Strouhal numbers are $\mathrm{St}_{Wm1} = 0.167$ and $\mathrm{St}_{Hm2} = 0.174$. These results must be compared to the analyses of Kiya & Abe (1999) concerning the global modes in the wake of elliptical and rectangular cross-flow plates. They prove that two modes associated with the interactions of opposite mixing layers coexist. The frequencies roughly rely on the

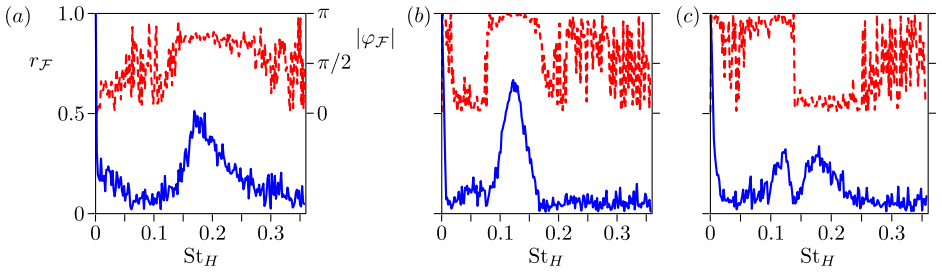

Figure 5.26. Modulus $r_{\mathcal{F}}$ (continuous blue line, left scale) and phase $\varphi_{\mathcal{F}}$ (dashed red line, right scale) of the coherence of velocity signals measured at $A(2.5, 0, 0.9)$ and $A'(2.5, 0, 0.3)$ (a), $B(2.5, 0.5, 0.6)$ and $B'(2.5, -0.5, 0.6)$ (b), $C(2.5, 0.5, 0.3)$ and $C'(2.5, -0.5, 0.3)$ (c). For clarity, the probe positions are displayed in figure 5.22(b).

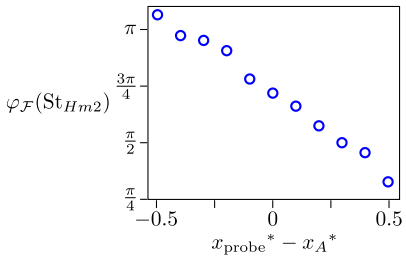

Figure 5.27. Phase $\varphi_{\mathcal{F}}(\mathrm{St}_{Hm2} = 0.174)$ of the coherence of velocity signals measured at $A(2.5, 0, 0.9)$ and $(x_{\mathrm{probe}}, 0, 0.3)$.

distance between the shear layers even if no universal Strouhal number can be found. Kiya & Abe (1999) also indicate that a larger energy is measured in the high frequency mode, *i.e.* the one corresponding to the interaction of the closer shear layers. The main difference with their experiments is the presence of the ground that limits the periodic oscillations in the z direction as mentioned in the literature (Ruiz *et al.*, 2009; Khalighi *et al.*, 2012). So the ground proximity explains the phase shift between the upper and lower part of the wake at St_{Hm2} and also its reduced energy even if the height of the body is smaller than its width.

5.4 Synthesis

From the observations of the natural flow in sections 5.2 and 5.3, a probable structure of the instantaneous flow is given in section 5.4.1. Then, the different drag sources in the wake are discussed in section 5.4.2.

5.4.1 Structure of the instantaneous wake

The coherent wake dynamics detailed in sections 5.3 are the superposition of three different phenomena:

- the bi-stability in the y direction associated with a random wake orientation;
- the interaction of the lateral shear layers inducing periodic oscillations of the wake in the y direction;
- the interaction of the upper and lower shear layers inducing periodic oscillations of the wake in the z direction.

The bistable behavior has a long time evolution in front of the oscillating global modes: an asymmetric state (#P or #N) persists in average for hundreds of global mode periods. To be pertinent, the organization of the coherent structures at St_{Hm1} and St_{Hm2} must be analyzed for a fixed asymmetric state. In the following, the case of the wake in the state #P is considered; a spatial organization of the coherent oscillations of the wake is suggested from the asymmetric conditional statistics of the flow (see section 5.3.1) and also from the visualizations of the laminar wake in chapter 4.

The oscillating global mode in the z direction is in phase opposition at the end of the recirculation region but the phase shift measured between two velocity signals downstream of the upper and lower mixing layers gradually evolves. Indeed, $\varphi_{\mathcal{F}}(\mathrm{St}_{Hm2})$ is measured at 0.95π, 0.75π and 0.65π for $x^* = 2.0$, 2.5 and 3.0 respectively. Such an evolution of the phase shift is certainly associated with the difference in the convecting velocities between the upper and lower parts of the wake due to the ground proximity. This point is clearly visible in figure 4.2(b) when the wake is in the transient unsteady symmetric regime. A structure of alternative vortex loops from the upper and lower parts of the recirculation region is probable but there is no reason for them to have similar intensities.

Besides, the confrontation of the Reynolds shear stresses in the upper and lower mixing layers for the mean flow and for the state #P (see figures 5.9c and 5.14c respectively) indicates that this unsteady global mode is only slightly affected by the bi-stability: at first sight, its structure is independent of the asymmetric state #P or #N. An interpretation of the spatial structure of this periodic oscillation in the z direction is given in figure 5.28(a).

On the other hand, the wake oscillation in the y direction remains in phase opposition in the wake but it is strongly affected by the selection of the asymmetric state. Figures 5.14(a)–(b) show that the fluctuations of velocity are concentrated on one side of the recirculation region. So a structure of parallel loops is expected, oriented toward the $y^* > 0$ regions ($y^* < 0$ respectively) when the wake is fixed in the asymmetric state #P (#N respectively). Nevertheless, this point could not be clearly evidenced because of the high difficulty to separate these structures from the z oscillations in the spatial domain. A sketch of this mode is suggested in figure 5.28(b).

The organization of the wake is a combination of these two oscillating global modes. It is impossible to present a global sketch as the associated frequencies are different. A

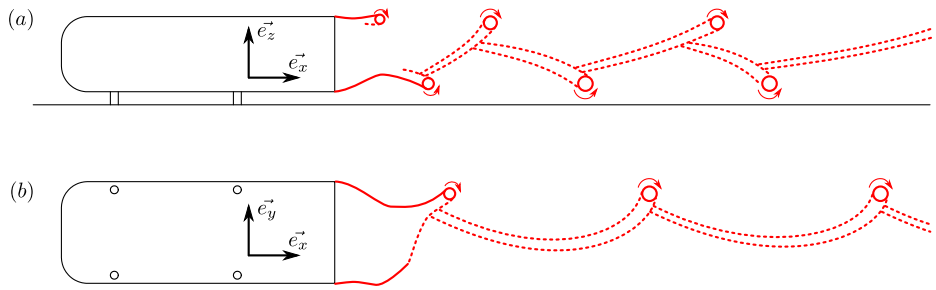

Figure 5.28. Sketch of the structure of the oscillating global modes in the z direction (a) and in the y direction (b) while the wake is in the state #P.

certain continuity between the vortices is presumed but such dynamics would necessarily be source of vortex dislocations.

Finally, these results can be confronted to the wake descriptions reported in the literature. First, the vertical wake oscillation is likely to be the one reported by Khalighi *et al.* (2012) at $\mathrm{St}_H = 0.17$ downstream of the recirculation region with a peak of energy particularly clear when the probe is in the plane of symmetry. Second, in the numerical simulations of Bayraktar *et al.* (2001), the peaks of energy observed in the autopower spectra of the cross-flow forces might be associated with similar dynamics even if the Strouhal numbers do not correspond to the present results. On the contrary, the low frequency pumping mode was not observed here and these results prove that an interpretation of interactions between the upper and the lower part of the toric recirculation structure is not sustainable: a toric topology of the wake is not consistent with the time-scale of a coherent motion at $\mathrm{St}_H \sim 0.07$.

Now that the structure of the flow is detailed, the different drag sources are considered in section 5.4.2.

5.4.2 Identification of the drag sources

From these experiments, some issues on the drag sources can be addressed: the contributions of the oscillating modes and of the bi-stability are discussed successively.

Impact of the oscillating global modes

The results presented in section 5.3.2 reveal coherent oscillations of the wake in both the y and z directions. However, contrary to the bidimensional configurations, the autopower spectra show that the energy associated with these modes is small in front of the turbulent activity of the mixing layers. For example, in the autopower spectra at A and B presented in figure 5.22(a), the increase of energy associated with the peaks at St_{Hm1} and St_{Hm2} are measured respectively at 7% and 3% of the total energy. For comparison, in the turbulent wake past a circular cylinder at similar Reynolds numbers, the contributions of the coherent and incoherent velocity fluctuations to the Reynolds stresses are equivalent (Cantwell & Coles, 1983; Balachandar *et al.*, 1997). Furthermore, the energy of the coherent oscillations is particularly small around the separatrix of the recirculation bubble (see figures 5.23a and 5.24a). As a consequence, the contribution of these oscillating modes to the physics of the recirculation bubble is certainly not sufficient to affect the drag significantly.

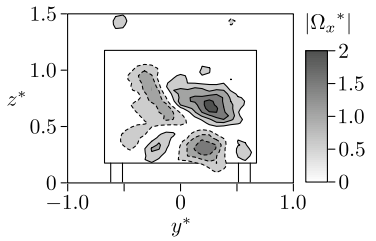

Figure 5.29. Contours of streamwise vorticity in the plane $x^* = 2.0$ for the state #P. The continuous and dashed lines are respectively positive and negative values; the contour interval is 0.5; the contour 0 is not plotted.

Impact of the bi-stability

Because of the bi-stability, the instantaneous wake is off the reflectional plane of symmetry. An aerodynamic force is present in the y direction while the flow is in the state #P or #N but it counterbalances in average due to the equipresence of the two states. Nevertheless, the mean drag corresponds to the drag of the asymmetric states which is likely to be enhanced by this side force. Indeed, part of the drag is induced by the cross-flow forces and is linked to the pair of vortices visible in the streamwise vorticity map presented in figure 5.29. These phenomena of induced drag are well known in aeronautics but also in the car industry (see section 1.2.4). For comparison, the normalized circulation of one vortex in the plane $x^* = 2.0$ is estimated around ± 0.2 in the present asymmetric case while the data from Lienhart & Becker (2003) give ± 0.8 in the plane $x^* = 1.7$ for the 25° Ahmed configuration. The intensity of the pair of streamwise vortices is smaller but it remains non-negligible.

For the asymmetric states, the forces F_y and F_z may be intuited from the orientation of the pair of streamwise vortices in figure 5.12(c) but the streamlines in the mean symmetric flow in figure 5.2(d) marks the influence of the lift force exclusively. So, the effect of the unsteady side force is only measured in the mean symmetric flow through the wake width and the Reynolds stresses[5]. This point is particularly clear comparing the global and conditional statistics in figures 5.8(b) and 5.13(b): the maximum of $\langle {u'_y}^2 \rangle$ is measured respectively inside and outside the recirculation region in the plane $z^* = 0.6$. As a result, it seems that the mean force but also its fluctuations must be taken into account to analyze induced drag phenomena in three-dimensional flows; additional remarks on this point are given in chapter 7.

[5]Part of the fluctuations of velocity are related to the differences in the mean velocities of the states #P and #N.

5.5 Concluding remarks

The flow around the squareback Ahmed geometry is characterized at $\mathrm{Re}_H = 9.2\ 10^4$. First, a boundary layer detachment occurs on the four faces of the forebody due to a high adverse pressure gradient; then, a massive recirculation responsible for a dominant part of the drag is reported on the base. The equilibrium of the wake in the z direction is slightly affected by the presence of the ground so the low pressure region in the wake, superimposed on the time-averaged recirculation structures, preserves a toric shape. However, it is important to be clear in the interpretation of the toric organization of the recirculation region: it is a long time-averaged vision and it does not reflect the topology of the flow because the wake presents a bistable behavior. The recirculation region has two preferred reflectional symmetry breaking positions leading to the statistical symmetric wake, the succession of these asymmetric states being random. This behavior results in an unsteady side forcing which must be responsible for part of the drag.

In addition, the interactions of the opposed shear layers induce oscillations of the wake at Strouhal numbers close to 0.17 when normalized by their respective gap. Nonetheless, these modes are not particularly energetic and only represent a negligible part of the Reynolds stresses around the recirculation region. So, their impact on the base pressure is certainly small.

These results evidence different traps in the study of such bistable flows. First, a particular attention must be paid to the instrumentation of the experiment. The common technique consisting in reducing the number of sensors given the symmetries of a geometry may induce significant errors. A residual asymmetry in the setup or a limited time of measurement necessarily results in asymmetric data. Indeed, the equipresence of the asymmetric states #P and #N is highly dependent on the quality of the reflectional symmetry of the setup and the statistical symmetry is obtained only after a duration far larger than the characteristic time between the shifts. Now, if the data are recorded on only half of the geometry, it is impossible to get accurate measurements of base pressure. On the other hand, in the framework of numerical simulations, a limited physical time of calculation may prevent the flow from reaching an asymmetric state which can lead to unstable or transient wake solutions.

More generally, such bistable behaviors may be an important characteristic of turbulent wakes. It is observed in the wake past different three-dimensional geometries but the circumstances of existence still need to be clarified. This is the objective of chapter 6. In addition, the sensitivity of the flow to local disturbances is studied in chapter 7 providing quantitative information on the contribution of such asymmetries to the drag.

Chapter 6

Domains of appearance of the cross-flow instabilities

Most of these results are published in Grandemange *et al.* (2013*a*).

This chapter aims at clarifying the conditions of existence of the bistable behavior observed in chapter 5 in the wake of a parallelepiped body. A parametric study explores the influences of the aspect ratio of the base (height/width) and of the ground clearance.

Abstract

In the previous chapter, the Ahmed geometry is bistable in the y direction but only for large ground clearances. Hence, it is useful to define the domains of existence of such behaviors in the turbulent wakes past parallelepiped bodies in wall proximity. Various aspect ratios $H/W \in [0.51, 1.63]$ and ground clearances $C/W \in [0, 1.00]$ are explored at $\mathrm{Re}_W = 4.5\ 10^4$. It is found that the near wake often presents antisymmetric instabilities that can be either in the lateral direction (parallel to the wall) or in the vertical direction (normal to the wall). The instantaneous wake has preferred states with high degrees of asymmetry; in some configurations, bistable behaviors are found as topology shifts occur after long time scales $T_l \sim 10^3 W/U_0$. These instabilities vanish for sufficiently small values of ground clearance ($C^* < 0.08$) when a detachment on the ground appears. However, the wall proximity does not necessarily stabilize the wake in the plane of symmetry since the flow still presents an instability in the lateral direction for $C^* < 0.03$ and $H^* < 0.65$. A general criterion for the existence of the instabilities is deduced from the parametric study in the domain (H^*, C^*) together with symmetry considerations. When these instabilities develop in the wake, the flow becomes highly sensitive to slight perturbations of the setup; such observations motivate the sensitivity analyses that are detailed in the following chapter.

Contents

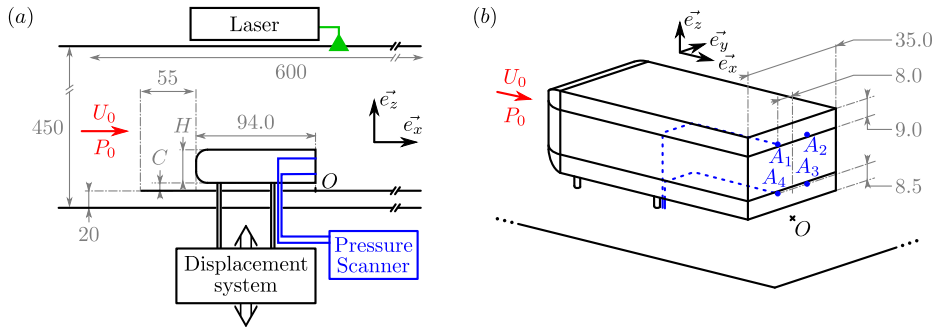

Figure 6.1. (a) Experimental setup of the model in the wind tunnel. (b) Scheme of the body. O sets the origin of the coordinate system; the blue dots on the base locate the pressure taps; for clarity, only the pressure tubings from the taps A_1 and A_4 are displayed. The dimensions are given in mm.

6.1 Experimental setup

Geometry

The wind tunnel is a closed-loop facility blowing at $U_0 = 20$ m s^{-1}. The homogeneity of the velocity over the test section is 0.2% and the turbulence intensity is 0.5%. The bluff bodies are designed from the squareback model used in the experiments of Ahmed *et al.* (1984). The geometry is placed in wall proximity with a plate up-raised from the floor of the tunnel as presented in figure 6.1(a). The coordinate system is defined as x in the streamwise direction, z normal to the ground and y forming a direct trihedral. The origin O of the coordinate system is in the reflectional plane of symmetry on the ground at the position of the base in the x direction. The boundary layer develops on the ground plate from the streamlined leading edge 55 mm upstream of the forebody; its thickness based on 99% of the free-flow velocity at $x = -94.0$ mm when the geometry is removed from the tunnel are $\delta_{0.99} = 3.80 \pm 0.05$ mm; the displacement and momentum thicknesses are $\delta_1 = 0.64 \pm 0.03$ mm and $\delta_2 = 0.45 \pm 0.01$ mm respectively.

The geometry is detailed in figure 6.1(b); the length L and width W of the geometry are 94.0 mm and 35.0 mm respectively, the supports are cylindrical with a diameter of 3.0 mm. The radius of the rounding of the forebody is 9.0 mm. The body is made of several blocs: one lower part and one upper part of 9.0 mm height each plus intermediate blocs of variable height so that the total height H of the body can be adjusted between 18.0 mm and 57.0 mm by steps of 1.0 mm. The ground clearance C of the geometry is accurately set between 0 mm and 35.0 mm with a precision better than 0.1 mm using a Micro-controle motion controller.

The Reynolds number based on the width W of the base is $\mathrm{Re}_W = U_0 W/\nu = 4.5\ 10^4$. Note that, for this chapter only, the width W is used to build the non-dimensional values.

Pressure measurements

The pressure on the body is measured at four locations on the base using a Scanivalve DSA 3217/16 px device. The taps are denoted by A_i with $i \in \{1, 2, 3, 4\}$ (see figure 6.1b); their positions on the base are defined by y_{A_i} and z_{A_i} with $i \in \{1, 2, 3, 4\}$. The taps are holes of 0.8 mm in diameters pierced at $y_{A_2} = y_{A_3} = -y_{A_1} = -y_{A_4} = \Delta_y/2$ with $\Delta_y = 16.0$ mm, $z_{A_3} = z_{A_4} = C + \Delta_z/2$ and $z_{A_1} = z_{A_2} = C + H - \Delta_z/2$ with $\Delta_z = 17.0$ mm. They are

connected to the measurement device by four tubes of 0.8 mm diameter and 0.5 m long going through the geometry and then through the ground just behind the rear supports to minimize their effects on the flow.

The pressure is recorded at 5 Hz with a precision better than 2 Pa which corresponds to 8 10^{-3} in terms of pressure coefficient.

The base pressure denoted C_{pb} is obtained using the mean value of the four pressure taps. In additions, the degree of asymmetry of the recirculation region in the y and z directions is quantified by the pressure gradients. Using the formalism introduced in appendix A, c_p is the measurement of the pressure coefficient averaged over a window of 0.2 s; it is abusively called *instantaneous pressure coefficient* in the following in opposition to $C_p = \langle c_p \rangle$ which is the long time averaged value. The sampling frequency at 5 Hz allows to measure the *instantaneous gradients of base pressure* in the y and z directions, denoted $\partial c_p/\partial y^*$ and $\partial c_p/\partial z^*$ respectively. These gradients are evaluated as

$$\frac{\partial c_p}{\partial y^*} = \frac{[c_p(A_2) + c_p(A_3)]/2 - [c_p(A_1) + c_p(A_4)]/2}{\Delta_y/W}, \tag{6.1}$$

and

$$\frac{\partial c_p}{\partial z^*} = \frac{[c_p(A_1) + c_p(A_2)]/2 - [(c_p(A_3) + c_p(A_4)]/2}{(H - \Delta_z)/W}. \tag{6.2}$$

In chapters 3 and 5, this method is proved to be a relevant topology indicator as soon as the averaging time (here 0.2 s) is small in comparison to the characteristic time of the bi-stability. The precision of the instantaneous measurement of the pressure gradient relies on the pressure but also on the gap between the sensors. The accuracy is constant and better than 2 10^{-2} in the y direction. On the contrary, in the z direction, it is 8 $10^{-3}W/(H-\Delta_z)$; the results are no longer considered for $H^* < 0.67$ when the precision becomes worse than 4 10^{-2}.

Velocity measurements

Particle image velocimetry (PIV) is used to obtain the velocity field in the plane $y^* = 0$ for different configurations. The system is comprised of a New Wave Solo PIV laser and a Lavision CCD camera (1600 px $\times$ 1400 px). The laser is located on the top of the test section and the CCD camera is outside of the flow. Each acquisition records 200 image pairs at a rate of 8 Hz. The software Davis 7.2 is used to calculate the velocity fields. The vector calculations use interrogation windows of 16 px $\times$ 16 px which correspond to 0.9 mm $\times$ 0.9 mm in the plane $y^* = 0$.

6.2 Evidence of the y and z instabilities

The experimental setup presents two geometrical parameters: the normalized ground clearance denoted $C^* = C/W$ and the aspect ratio of the base $H^* = H/W$. First, in section 6.2.1, the results concerning the fixed aspect ratio of the reference Ahmed geometry for $H^* = 0.74$ are presented varying C^*. Then, section 6.2.2 is devoted to the analysis of the case $H^* = 1/0.74 = 1.34$. Finally, the data are considered in the whole domain (C^*, H^*) in section 6.2.3.

6.2.1 Ahmed reference case: $H/W = 0.74$

This section studies the aspect ratio $H/W = 0.74$ corresponding to the reference Ahmed geometry. The impact of the ground proximity on the flow topology and on the base pressure are first presented. Then, the bistable behavior in the y direction evidenced in chapter 5 is considered.

Ground effect

To depict the influence of the ground proximity, several PIV measurements in the near wake of the geometry are presented in the left column of figures 6.2 and 6.3 for different values of ground clearance C. For $C^* < 0.04$, viscous effects are dominant under the geometry and limit the underbody flow. As a result, the topology corresponds to the flow past a three-dimensional backward facing step (see figures 6.2*a*–*c*). A separation at the top edge and a reattachment on the wall are observed in the plane $y^* = 0$, they are denoted by S_b and R_g respectively. In average, the recirculation organization certainly forms an arch parallel to the base like downstream of a wall-mounted cube (Martinuzzi & Tropea, 1993; Depardon, 2006), the signature of this structure being denoted by #1 in the plane $y^* = 0$.

For moderate ground clearances $C^* \in [0.04, 0.09]$, the momentum of the underbody flow gradually increases as it becomes less influenced by viscous effects (see figures 6.2*c*–*e* and 6.3*a*–*b*). A second recirculation structure, denoted #2, appears due to a separation at the bottom edge of the base. After this separation S_b, the underbody flow is curved toward the top of the base and reattaches on it at R_b. In association with this bottom edge separation, there is stagnation point, denoted S_g, corresponding to the detachment of the ground boundary layer. When the ground clearance increases in the range $C^* \in [0.6, 0.9]$, the recirculation structure #2 progressively extends, pushing the structure #1 downstream and toward the ground, while it reveals the separation point S_g on the ground. The underbody flow is now concentrated into a jet with a strong curvature and enough energy to reach the mixing layer developing from the upper edge of the base. This forms a third structure denoted #3 (see figure 6.2*e*). Progressively, the recirculation structure #1 vanishes on the ground and disappears at $x^* = 1.2$ for $C^* = 0.09$.

Eventually, for $C^* \geq 0.09$, the underbody flow has enough momentum to prevent the boundary layer from separating on the ground (see figures 6.3*c*–*e*) at least from a time averaged point of view; it is very likely that intermittent separation occurs up to $C^* \approx 0.10$. The recirculation bubble gradually reaches an organization with a recirculating flow strictly oriented in the x direction as in chapter 5.

The experimental setup also allows the simultaneous analysis of the PIV measurements and the levels of base pressure; the sample measurements given in figures 6.2 and 6.3 show strong evolutions of both C_{pb} and the length of the recirculation region, denoted L_r, depending on the value of C^*. These dependences on C^* are discussed in section 6.3.2.

In parallel, the flow dynamics for large ground clearances, typically for $C^* > 0.1$, report bistable behaviors of the recirculation region; they are analyzed in the following section.

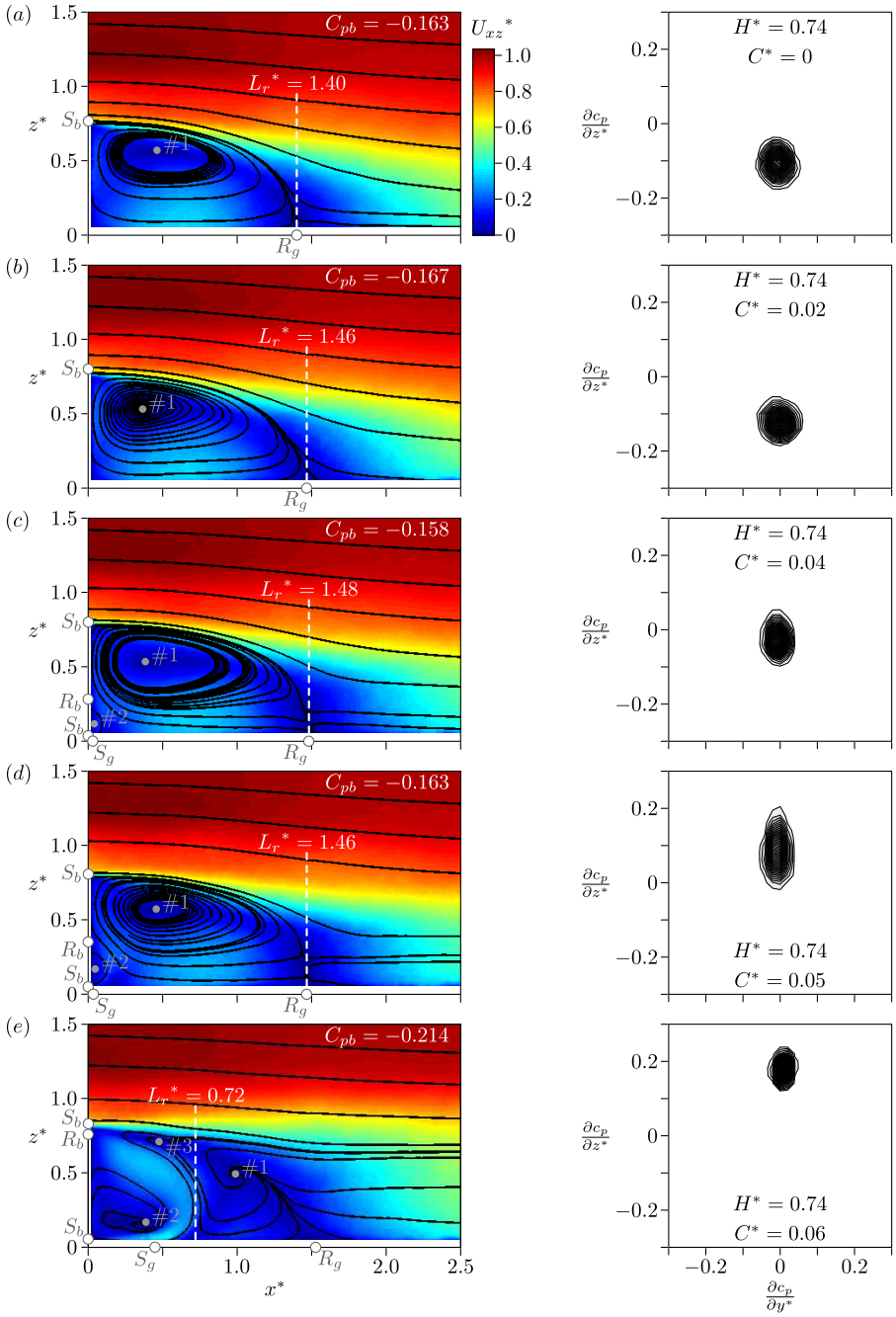

Figure 6.2. Velocity fields from PIV measurements in the plane $y^* = 0$ (left) and associated probability density functions of base pressure gradients (right) for $H^* = 0.74$ and various ground clearances: $C^* = 0$, (a); $C^* = 0.02$, (b); $C^* = 0.04$, (c); $C^* = 0.05$, (d); $C^* = 0.06$, (e). The positions of the separation and reattachment points, denoted S_b, S_g, R_b and R_g, are precisely determined from the velocity fields. The contour interval of the PDF is 10.

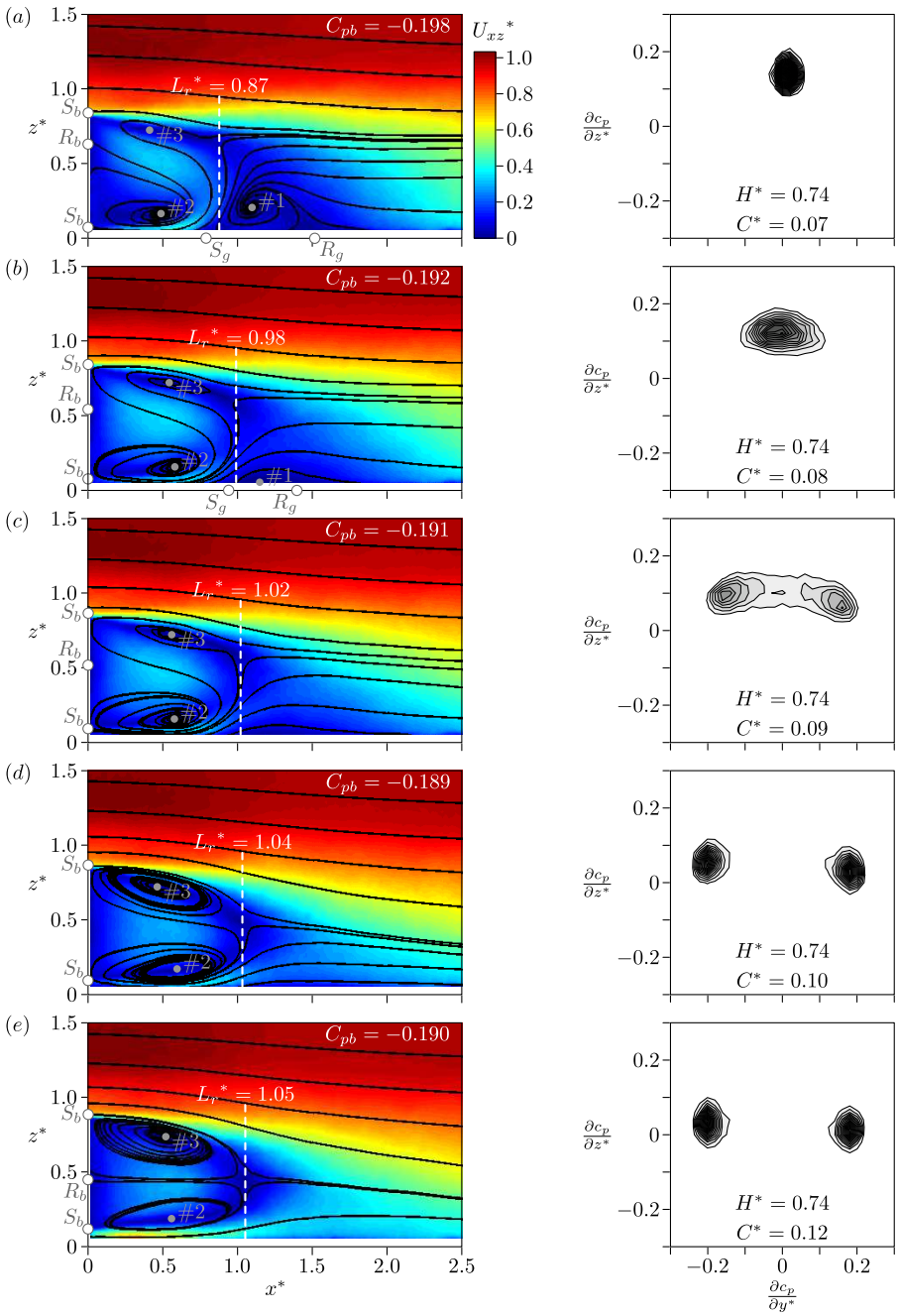

Figure 6.3. Same as figure 6.2 for larger ground clearances: $C^* = 0.07$, (a); $C^* = 0.08$, (b); $C^* = 0.09$, (c); $C^* = 0.10$, (d); $C^* = 0.12$, (e).

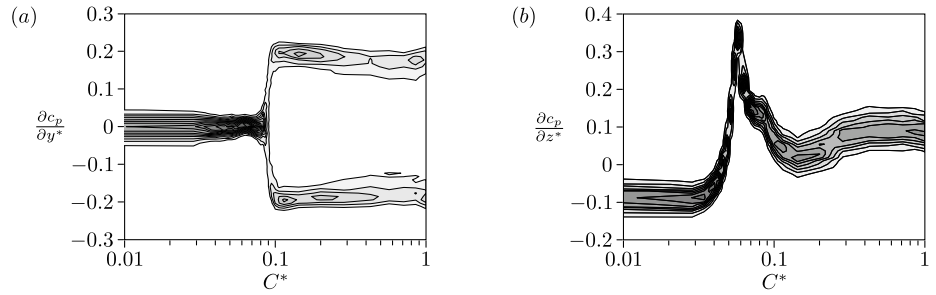

Figure 6.4. Probability density functions of the base pressure gradient in the y direction (a) and in the z direction (b) as a function of the ground clearance C^* for $H^* = 0.74$; the contour interval is 2.

Bi-stability as a function of the ground clearance

To study the bistable properties of the flow, the statistics of the *instantaneous values of base pressure*[1] are considered. The joint probability density functions of the two base pressure gradients corresponding to the PIV measurements are presented in the right column of figures 6.2 and 6.3.

For $C^* \leq 0.08$, there is only one maximum in the joint PDF; it is centered on $\partial c_p/\partial y^* = 0$ and the value of $\partial c_p/\partial z^*$ is linked to the intensity and proximity to the base of the structures #1, #2 and #3. For example, the case $C^* = 0.07$ (see figure 6.3a) presents a stable state at $\partial C_p/\partial y^* = 0$ and $\partial C_p/\partial z^* = 0.14$ which corresponds to the asymmetry of the recirculation region in the z direction. The difference of intensity between the structures #2 and #3 can be estimated by the diagonal orientation of the recirculating flow: $U_z \sim -U_x > 0$ in the middle of the recirculation region.

For $C^* > 0.08$, the joint PDF of the base pressure gradients present two maxima which are the signature of the bistable behavior (see figures 6.3c–e): the wake presents two preferred states with opposite values of $\partial c_p/\partial y^*$ for identical values of $\partial c_p/\partial z^*$. The states associated with positive and negative values of $\partial c_p/\partial y^*$ are denoted by #Py and #Ny respectively. The mean flow preserves the symmetry of the setup due to the equiprobability of the states #Py and #Ny. For $C^* = 0.12$, the mean recirculating flow oriented along the x direction is consistent with the value of $\partial C_p/\partial z^* = 0.02 \approx 0$. As the two states #P$y$ and #Ny are symmetrical to each other referring to the plane $y^* = 0$, they are expected to present the same drag. This point is verified experimentally since the levels of base pressure are measured at $C_{pb}(\#\mathrm{P}y) = -0.190$ and $C_{pb}(\#\mathrm{N}y) = -0.189$ for the case $C^* = 0.12$ after conditional averaging.

The probability density functions of the base pressure gradient in the y and z direction, PDF($\partial c_p/\partial y^*$) and PDF($\partial c_p/\partial z^*$), are plotted against the ground clearance in figures 6.4(a) and 6.4(b) respectively. The statistics in the y direction are identical to the one presented in chapter 5 (see figure 5.21): a bistable behavior is reported as soon as the ground clearance is large enough, the critical value being $C^* = 0.08$ in this setup. For comparison, a similar critical value of 0.07 is reported in chapter 5 while the experiments are conducted in a different facility. In parallel, the base pressure gradient in the z direction only presents one preferred value of $\partial c_p/\partial z^*$ for all the ground clearances. It shows sharp variations depending on C^*, especially for $C^* \in [0.03, 0.08]$. As previously depicted in the comments

[1] The pressure is recorded at 5 Hz and averaged over 0.2 s windows.

on the left columns of figures 6.2 and 6.3, these evolutions are related to the organization of the recirculation region and to the underbody flow momentum: they are associated with the transition from a backward facing step topology to a usual wake topology of vehicles, without ground detachment.

Once the bistable behavior is reported in the y direction, $\partial C_p/\partial z^*$ is measured less dependent on the ground clearance: $\partial C_p/\partial z^* \in [0, 0.1]$. This indicates that the ground proximity has only a limited impact on the near wake. One might expect $\partial C_p/\partial z^* = 0$ for large values of C^* but the presence of the supports under the geometry may still introduce an asymmetry in the z direction. When the geometry is out of the wall influence (typically $C^* > 0.3$), the stable state of the wake is associated with $\partial C_p/\partial z^* \approx 0.1$; thus it is expected to present slight asymmetries between the structures #2 and #3 as it is the case for $C^* = 0.09$ in figure 6.3(c). So, the *rather symmetric* organization of the recirculation bubble in the vertical direction observed for $C^* \approx 0.12$ with $\partial C_p/\partial z^* \approx 0$ is likely to be ascribed to a ground effect that counterbalances the asymmetry introduced by the supports of the geometry.

The full description of the two states #Py and #Ny observed for $C^* > 0.08$ is provided in chapter 5 using conditional averaging.

6.2.2 Case $H/W = 1.34$

The aspect ratio $H/W = 1.34$ is now studied for different ground clearances. This particular value of H^* corresponds to $W/H = 0.74$ so that it is the inverse of the aspect ratio of the Ahmed geometry. The effect of the ground clearance on the PDF of the base pressure gradients in the cross-flow directions is shown in figure 6.5. Figure 6.5(a) indicates that, for all the ground clearances, the base pressure gradient in the y direction is stable for $\partial c_p/\partial y^* = 0$. Thus, the symmetric wake is always stable in a centered state.

On the contrary, PDF($\partial c_p/\partial z^*$) in figure 6.5($b$) presents strong differences compared to the case $H^* = 0.74$ for $C^* > 0.05$ (see figure 6.4b). Indeed, for small values of C, the evolutions are identical: a plateau is measured at $\partial C_p/\partial z^* \approx -0.08$ when $C^* < 0.03$ followed by a sharp increase in the range $C^* \in [0.03, 0.05]$. But, while $\partial C_p/\partial z^*$ keeps increasing to 0.33 for $C^* = 0.06$ in the case $H^* = 0.74$, it saturates at 0.13 for the aspect ratio $H^* = 1.34$. Then, for $C^* \geq 0.06$, figure 6.4(b) shows that $\partial C_p/\partial z^*$ decreases to stabilize between 0 and 0.1 for $H^* = 0.74$ whereas for $H^* = 1.34$, figure 6.5(b) points out that only two preferred values of $\partial C_p/\partial z^*$ are reported (0.13 and -0.09) with bistable behaviors in the z direction for some values of C^*.

The particular case $C^* = 0.10$ presents two peaks in the joint PDF of the base pressure gradients centered on $\partial c_p/\partial y^* \approx 0$ and $\partial c_p/\partial z^* \approx -0.09$ and 0.13 (see figure 6.6). As a result, two states are evidenced; the one centered on $\partial c_p/\partial y^* \approx 0$ and $\partial c_p/\partial z^* \approx -0.09$ is denoted by #Nz while the other one, centered on $\partial c_p/\partial y^* \approx 0$ and $\partial c_p/\partial z^* \approx 0.13$, is denoted by #P$z$. The mean velocity field of this z bistable case is displayed in figure 6.6(a); note that there is only saddle point at the end of the recirculation bubble. Hence, the presence of two saddle points is not a necessary condition of such bistable behaviors.

Using conditional averaging as in chapter 5, it is possible to separate these two states in the 200 instantaneous velocity fields. Since the base pressure gradient is related to a diagonal recirculating flow (see chapters 3 and 5), the two states are expected to present differences in the orientation of the recirculating flow. As in chapter 2, the integral value

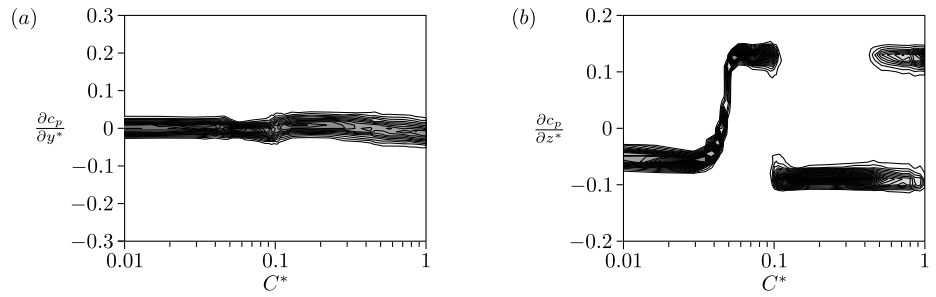

Figure 6.5. Probability density functions of the base pressure gradient in the y direction (a) and in the z direction (b) as a function of the ground clearance C^* for $H^* = 1.34$; the contour interval is 2.

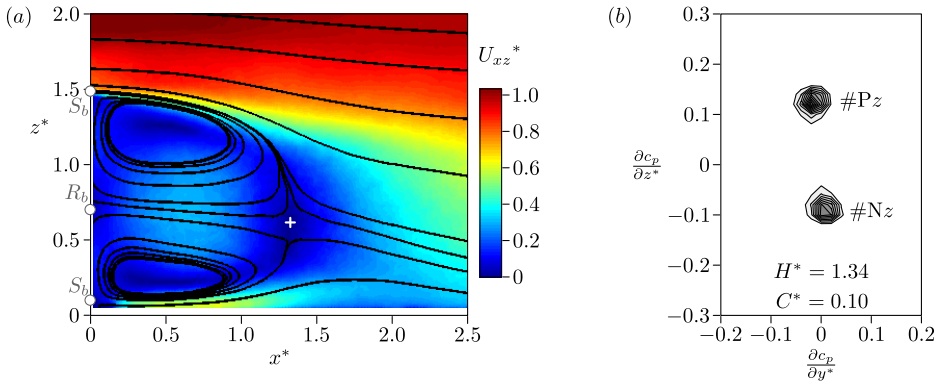

Figure 6.6. Mean velocity field from PIV in the plane $y^* = 0$ (a) and associated probability density function of base pressure gradients (b) for $H^* = 1.34$ and $C^* = 0.10$; the contour interval is 10. The cross locates the saddle point. S_b and R_b are the positions of the separation and reattachment points on the base.

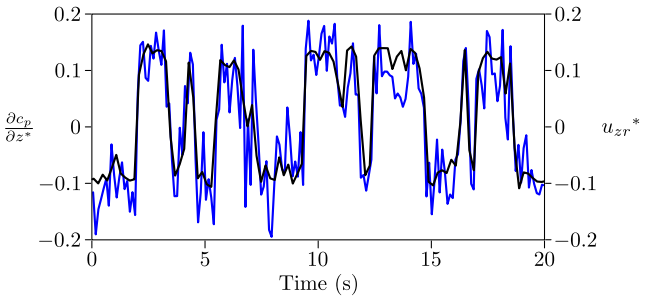

Figure 6.7. Time evolutions of $\partial c_p/\partial z^*$ (black line, left scale) and of ${u_{zr}}^*$ (blue line, right scale) for $H^* = 1.34$ and $C^* = 0.10$.

u_{zr} is used; it is defined by

$$ {u_{zr}}^* = \int_{x^*=0.2}^{1.2} \int_{z^*=0.2}^{1.2} {u_z}^*(x^*, z^*)\, \mathrm{d}x^* \mathrm{d}z^*. \tag{6.3} $$

It estimates the average velocity in the z direction in the recirculation bubble. Simultaneous time evolutions of u_{zr} and of $\partial c_p/\partial z^*$ are presented in figure 6.7. Over the 20 s of the measurement, the correlation between these two quantities reaches 0.86: ${u_{zr}}^* > 0$ when $\partial c_p/\partial z^* > 0$ and reciprocally, ${u_{zr}}^* < 0$ when $\partial c_p/\partial z^* < 0$. Thus, each state can be obtained from conditional averaging, one with ${u_{zr}}^* > 0$ which correspond to the state #Pz and the other with ${U_{zr}}^* < 0$ associated with the state #Nz.

The mean velocity fields obtained after conditional averaging are presented in figure 6.8. By construction of the conditional averaging, the orientation of the recirculating flow is different for the two states. The organization of the recirculation region is consistent with the base pressure gradients observed in the z direction: ${u_{zr}}^* > 0$ and the lower recirculation structure is closer to the base than the upper one for the state #Pz. This results in the positive value of $\partial C_p/\partial z^*$ and reciprocally for the state #Nz.

In contrast to the states #Py and #Ny observed in section 6.2.1, there is no symmetry between the states #Pz and #Nz (see figure 6.8). So the two states may present distinct fluid forces. Indeed, the velocity fields suggest very different lift whether the wake is in the state #Nz or in the state #Pz. The drag may also be different[2] as the base pressure are measured at $C_{pb}(\#\mathrm{P}z) = -0.212$ and $C_{pb}(\#\mathrm{N}z) = -0.200$. The state #P$z$ is therefore expected to have a larger drag than the state #Nz.

For $C^* > 0.06$, figure 6.5(b) evidences that $\partial c_p/\partial z^*$ is measured either around 0.13 or around -0.09 with bistable configurations for $C^* = 0.1$ and $C^* \in [0.5, 1.0]$; for the other values of C^*, only one of the two states is observed in the wake. The topology associated with each value of $\partial c_p/\partial z^*$ (at 0.13 or -0.09) must correspond to two different orientations of the recirculating flow; so the corresponding topologies are expected to present a near wake organization similar to the one presented in figures 6.8(a)–(b).

Now that the base pressure statistics are detailed for the two aspect ratios $H^* = 0.74$ and $H^* = 1.34$, section 6.2.3 considers the data in the whole domain (C^*, H^*).

[2]The drag is directly connected to the base pressure but in these experiments, the pressure is measured only at four locations and there are strong gradients. Hence, the estimation of the base pressure suffers from the lack of spatial resolution.

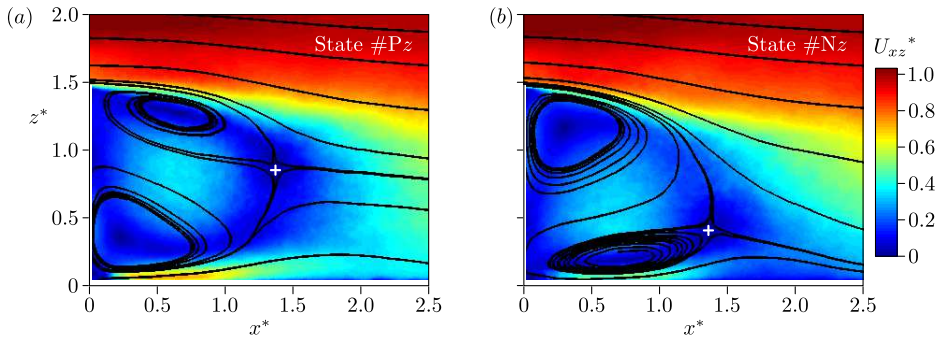

Figure 6.8. Velocity fields in the plane $y^* = 0$ for $H^* = 1.34$ and $C^* = 0.10$ after conditional averaging to extract the state #Pz for ${u_{zr}}^* > 0$ (a) and the state #Nz for ${u_{zr}}^* < 0$ (b). The crosses locate the saddle points.

6.2.3 Base pressure statistics in the domain (C^*, H^*)

In sections. 6.2.1 and 6.2.2, the development of antisymmetric instabilities are observed in the y and z directions respectively. In some configurations, the coexistence of two preferred asymmetric topologies of the wake leads to bistable wakes. Both the ground clearance and the aspect ratio of the base have a critical impact on these phenomena; so further experiments are performed to explore the range $H^* \in [0.51, 1.63]$ by steps of 0.06 while the effect of the ground clearance are considered for $C^* \in [0, 1.00]$.

First, the average value of the base pressure is considered. In figure 6.9, C_{pb} is plotted in the domain (C^*, H^*). As observed in section 6.2.1, there are important evolutions of the mean base pressure: it ranges from -0.14 to -0.24. The best drag configurations correspond to the low values of H^* with $C^* < 0.05$. The high drag cases correspond to the values $C^* \approx 0.06$ when the wake is in transition from a backward facing step topology to a wake topology without ground detachment. This characteristic value of $C^* \approx 0.06$ is independent of H^* at first order. For $C^* > 0.10$, the base pressure is measured approximately constant around -0.20 with a slight decrease as H^* increases.

To evaluate the domains of existence of the instabilities in the y and z directions, global quantities are needed. In the y direction, the natural indicator is the absolute value of the instantaneous pressure gradient in the y direction: $\langle|\partial c_p/\partial y^*|\rangle$. This quantity is plotted in the domain (C^*, H^*) in figure 6.10(a). Bistable wakes are characterized by large values of $\langle|\partial c_p/\partial y^*|\rangle$, typically greater than 0.10, while stable centered wakes are associated with low values of $\langle|\partial c_p/\partial y^*|\rangle$, less than 0.05. The case $H^* = 0.74$ presented in section 6.2.1 is stable up to $C^* = 0.10$ and bistable for $C^* > 0.10$. The case $H^* = 1.34$ presented in section 6.2.2 remains stable in the y direction for all the values of C^*. Two zones of y bi-stability are identified; they are associated with $0.60 \pm 0.02 < H^* < 0.90 \pm 0.05$ for $C^* > 0.08$ and $H^* < 0.65 \pm 0.02$ for $C^* < 0.03$. This latter range corresponds to three-dimensional backward facing step configurations. It is consistent with the results of Herry *et al.* (2011) reporting a similar bi-stability downstream of a double three-dimensional backward facing step.

Similarly, the instability in the z direction is evaluated using $\langle|\partial c_p/\partial z^*|\rangle$. However, its interpretation is more ambiguous since both the ground proximity and the z instability

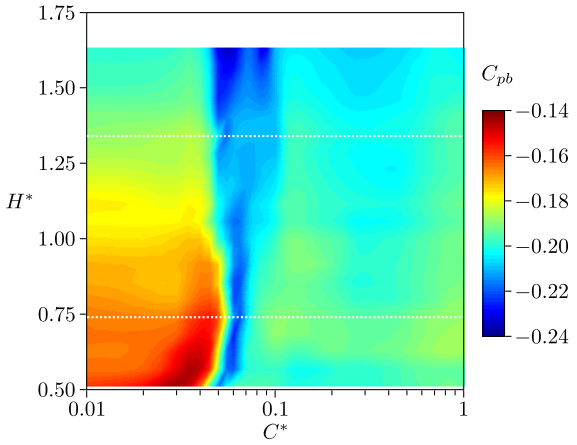

Figure 6.9. Base pressure in the domain (C^*, H^*). The dotted lines locate $H^* = 0.74$ and $H^* = 1.34$.

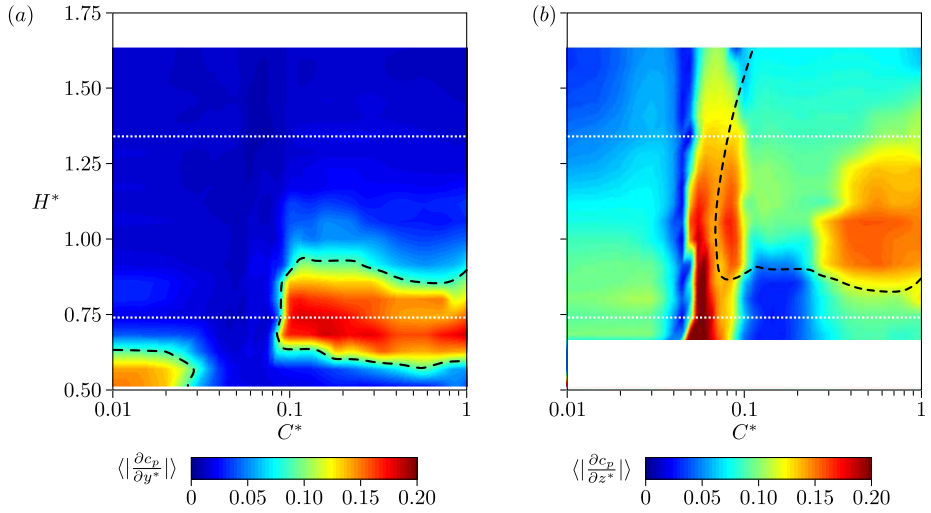

Figure 6.10. Quantitative asymmetry of the base pressure distribution in the y direction (a) and in the z direction (b) in the domain (C^*, H^*). The dashed lines limit the domains of the instability in the y direction (a) and in the z direction (b). The dotted lines locate $H^* = 0.74$ and $H^* = 1.34$.

of the recirculation bubble are responsible for a pressure gradient in the z direction. A second difficulty is that, once the instability appears, the wake is very likely to be trapped in one of the two states as depicted in section 6.2.2. The map of $\langle|\partial c_p/\partial z^*|\rangle$ in the domain (C^*, H^*) is presented in figure 6.10(b); the values for $H^* < 0.67$ are not considered as the gap separating the taps of the upper and lower part of the base is not sufficient to preserve the precision in the evaluation of $\partial c_p/\partial z^*$ (see section 6.1). Most of the configurations, even far from the wall, induce significant asymmetries in the z direction: in most of the domain, $\langle|\partial c_p/\partial z^*|\rangle > 0.10$. A systematic analysis of PDF($\partial c_p/\partial z^*$) enables to delimit the domain of appearance of the instability in the z direction (similar to the one presented in section 6.2.2). This region is marked by the dashed line in figure 6.10(b), roughly for $H^* > 0.85 \pm 0.05$ and $C^* > 0.07 \pm 0.01$.

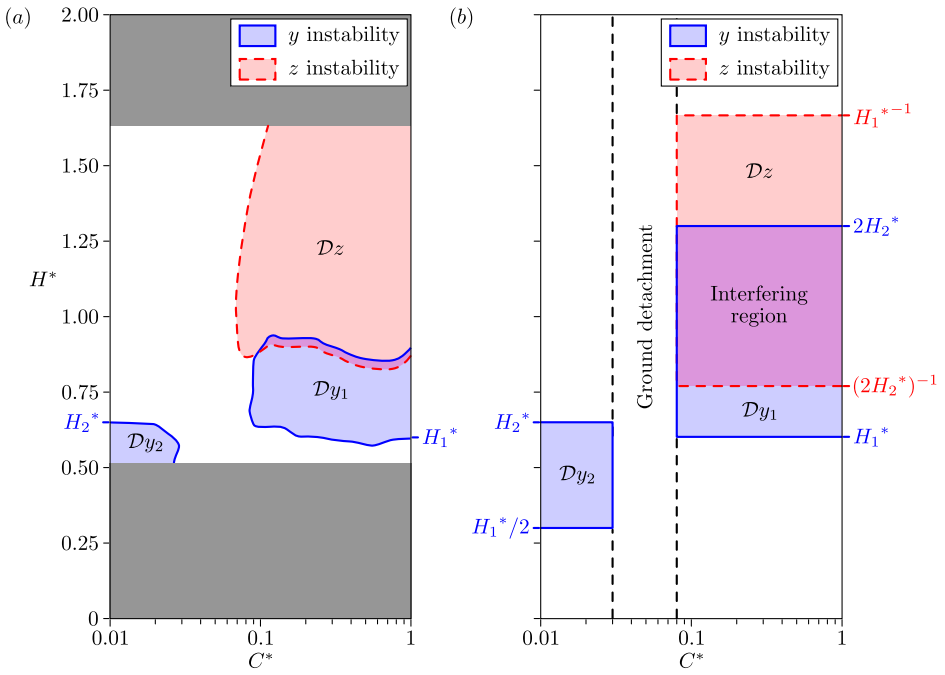

Figure 6.11. Domains of development of the instabilities measured from the experiments (a) and predicted by the model (b). The limits ${H_1}^*$ and ${H_2}^*$ of the model are reported from the experiments, the other limits are deduced from symmetry considerations only.

6.3 Synthesis

The domains of existence of the instabilities in the y and z directions are now discussed in section 6.3.1 while section 6.3.2 is devoted to the mean base pressure evolutions in the field (C^*, H^*).

6.3.1 Domains of existence of the y and z instabilities

The goal of this section is to deduce a general criterion defining the domains of existence of the instabilities in the y and z directions presented in section 6.2. A synthesis of the domains obtained from the experiments is provided in figure 6.11(a); the following depicts the construction of the limits presented in figure 6.11(b).

One can start by analyzing these domains as a function of the ground clearance. Figure 6.11(a) indicates that the instabilities can occur either for $C^* < 0.03$ or for $C^* > 0.08$. Referring to figure 6.2, the underbody flow is nil for the low ground clearances ($C^* < 0.03$) due to dominant viscous effects. For the large ground clearances, the flow around the body retrieves a certain symmetry (see figure 6.3e) with respect to the plane $z^* = C^* + H^*/2$ located at the mid-height of the body. Now, in these ranges $C^* < 0.03$ and $C^* > 0.08$, the domains of appearance of the instabilities do not depend much on C^* (see figure 6.11a); this tends to indicate that the low values of C^* are equivalent to the extreme case $C^* = 0$ while the large values of C^* are similar to the case without ground. As a consequence, the general criterion presented in figure 6.11(b) separates the range of C^* into three regions: $C^* < 0.03$ assumed equivalent to $C^* = 0$, $0.03 < C^* < 0.08$ with a ground detachment preventing the

development of both instabilities and $C^* > 0.08$ equivalent to a configuration without wall influence.

Therefore, the ground clearance has a stabilizing effect on the instabilities for $0.03 < C^* < 0.08$ when a detachment is present on the ground. For practical reasons and further comparisons with other studies, it is worth mentioning the corresponding critical range of Reynolds numbers of the underbody flow, *i.e.* based on C and U_0: this gives $\mathrm{Re}_C < 1350$ when the underbody flow is almost nil, $\mathrm{Re}_C > 3600$ when there is no detachment on the ground[3].

Now, addressing the effect of base aspect ratio H^*, the instability in the lateral direction leading to the y bi-stability is first discussed. This behavior is characterized by the coexistence of two states of the wake, switching randomly between the right hand side and the left hand side of the body (see chapter 5).

For the large values of C^*, one can see in figure 6.11(a) that the domain of y bi-stability, denoted $\mathcal{D}y_1$, corresponds to the range of aspect ratios $0.60 \pm 0.02 < H^* < 0.90 \pm 0.05$. The inferior limit at 0.60 ± 0.02, denoted ${H_1}^*$, is ascribed to a pure transition from a stable symmetric flow to a bistable flow whereas the superior limit seems less clear since both the y and z instabilities interfere.

For the low values of C^*, assumed equivalent to $C^* = 0$, the experiments report bistable behaviors in the y direction when $H^* < 0.65 \pm 0.02$; the corresponding domain is denoted $\mathcal{D}y_2$ in figure 6.11(a). The superior limit at 0.65 ± 0.02 equally corresponds to a pure transition from a stable symmetric flow to a bistable wake; it is denoted ${H_2}^*$. Now, for these low ground clearances, the flow can be regarded as a symmetric flow with respect to the plane $z^* = 0$ that is produced by a virtual body of double height out of wall influence. Indeed, using the inviscid theory for large Reynolds number flows, the wall boundary condition is equivalent to a mirror condition; a sketch of such equivalent flows is given in figure 6.12. This interpretation introduces a clear interdependence between the domains $\mathcal{D}y_1$ and $\mathcal{D}y_2$. The reasoning is the following: if a body of aspect ratio $2H^*$ is bistable out of wall influence, *i.e.* within domain $\mathcal{D}y_1$, then the bi-stability is very likely to be also found for a body of aspect ratio H^* at $C^* = 0$, *i.e.* within the domain $\mathcal{D}y_2$; and the reverse is true. Consequently, the superior limit to the domain $\mathcal{D}y_1$ can be defined at $2{H_2}^* = 1.30 \pm 0.04$ and the inferior limit to the domain $\mathcal{D}y_2$ at ${H_1}^*/2 = 0.30 \pm 0.01$.

Furthermore, the mirror condition of the inviscid flow theory is applied on the instantaneous flow. So, this only allows symmetric flow perturbations referring to the plane $z^* = 0$. Since the mirror condition still permits the bi-stability in the domain $\mathcal{D}y_2$, the perturbations related to the y instability must be of symmetric nature in the z direction while they are obviously antisymmetric in the y direction. Assuming that the y and z instability results from the same physics, the instability in one direction cannot coexists with the instability in the other direction due to incompatible characteristics of the associated perturbations. Thus, it is very likely that the instability in one direction takes the advantage on the other which extinguishes. Such interferences between the y and z instabilities may explain why the superior limit of the domain $\mathcal{D}y_1$ at $2{H_2}^* = 1.30 \pm 0.04$ is far larger than the frontier observed experimentally at 0.90 ± 0.05.

Finally, the instability in the vertical direction is considered. Two states of the flow can be observed; they correspond to wakes oriented either toward the top or the bottom of the body base. For some configurations, the wake is bistable switching randomly between the two states. Contrary to the bi-stability in the y direction which is related to a reflectional

[3]These thresholds are larger than the ones observed experimentally in the laminar regime in chapter 4 but the experiments are performed in two very different facilities.

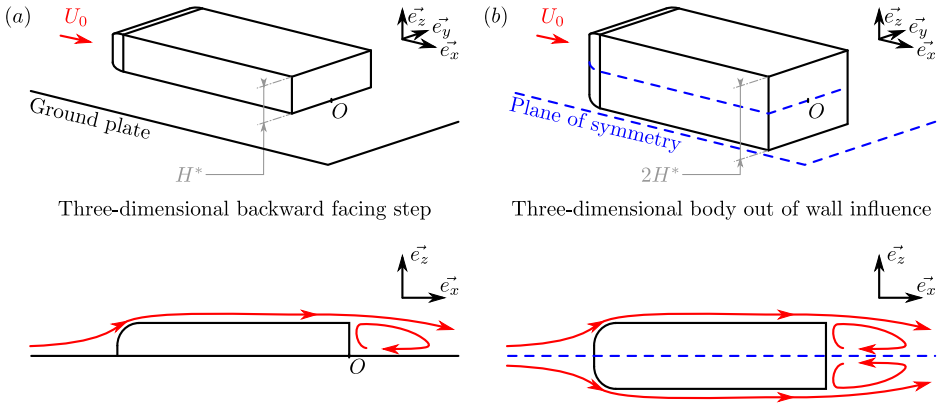

Figure 6.12. Equivalent configurations using the inviscid flow theory: three-dimensional backward facing step (a) and three-dimensional symmetric body out of wall influence (b).

symmetry breaking (RSB) of the flow around the body, for the z instability there is not, in a strict sense, any associated reflectional symmetry (RS) of the geometry because of the ground. The RS around the bluff body may be restored in two cases.

- For the low values of C^*, the flow around the virtual body is symmetric but RSB is impossible due to the mirror symmetry introduced by the proximity of the ground. This is consistent with the experiments.
- For the large values of C^*, the wall effect is limited and, neglecting the support influence, the configuration is almost equivalent to the flow without ground. This restores the RS of the geometry and in that case, the RSB of the flow becomes possible.

The range of aspect ratios associated with the z instability can be deduced from the one obtained for the y instability by symmetry considerations. Making use of the symmetry of rotation by $\pi/2$ around the longitudinal axis of the body out of the wall influence, $H^* = H/W$ becomes $1/H^*$ and y to $-z$. Hence, the range of the y instability of the domain $\mathcal{D}y_1$ for ${H_1}^* < H^* < 2{H_2}^*$ is equivalent to the range of the z instability in the domain $\mathcal{D}z$ that is defined as $(2{H_2}^*)^{-1} < H^* < {{H_1}^*}^{-1}$, *i.e.* $0.77 \pm 0.03 < H^* < 1.67 \pm 0.05$. This prediction is in agreement with the experimental findings presented in figure 6.11(a).

As a result, an interfering region $\mathcal{D}y_1 \bigcap \mathcal{D}z$, *i.e.* $0.77 \pm 0.03 < H^* < 1.30 \pm 0.04$ is evidenced where the instability in one direction takes the advantage on the other. Out of wall influence, one may expect the dominant instability to be the one associated with the larger dimension of the base, *i.e.* the y direction for $H^* < 1$ and the z direction for $H^* > 1$. Nevertheless, residual asymmetries in the z direction may modify this balance of power; the presence of the four cylindrical supports could explain why the z instability predominates as soon as $H^* > 0.90 \pm 0.05$.

Now that a general criterion defining the domains of instability in the cross-flow directions is provided, the mean levels of base pressure are considered in section 6.3.2.

6.3.2 Mean base pressure *vs.* H^* and C^*

The detailed study of the aspect ratio $H^* = 0.74$ presented in figures 6.2 and 6.3 shows that both the mean base pressure C_{pb} and the recirculation length L_r strongly depend on the

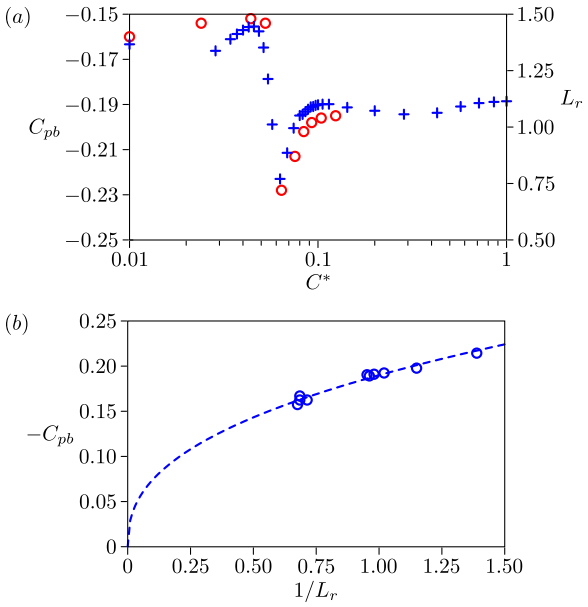

Figure 6.13. (a) Base pressure (+, left scale) and recirculation length (◯, right scale) as a function of the ground clearance C^* for the case $H^* = 0.74$. (b) Base pressure level as a function of the recirculation length for the case $H^* = 0.74$ for different values of C^*: ◯, experimental data; ---, best power fit: $C_{pb} = -0.19({L_r}^*)^{-0.41}$.

ground clearance C^*; these evolutions are presented in figure 6.13(a). First, for $C^* < 0.04$ when the topology corresponds to the flow past a three-dimensional backward facing step, the recirculation bubble extents up to $x^* \approx 1.5$ and the base pressure is measured close to $C_{pb} \approx -0.16$. Then, when the underbody flow becomes more energetic, for $C^* \in [0.06, 0.09]$, two different recirculation bubbles can be distinguished: one on the base (comprised of structures #2 and #3) and one on the ground (structure #1). Only the recirculation structure close to the base is considered in the calculation of L_r as shown in figure 6.2(e). For these values of C^*, the recirculation length is smaller (${L_r}^* < 1.0$) and it strongly depends on the ground clearance. In parallel, the base pressure decreases to values $C_{pb} < -0.22$ (see figure 6.13a) with a clear correlation to the recirculation length. Eventually, for $C^* \geq 0.09$, both the recirculation length and the base pressure stabilize at ${L_r}^* \approx 1.0$ and $C_{pb} \approx -0.19$ respectively.

For massive separation at the rear-end of a body, base pressure is proved to be a reliable indicator of the drag of bidimensional bodies (Roshko, 1993). For large Reynolds number flows, the curvature of the high velocity flow is source of pressure evolutions because of the associated centripetal acceleration. For a given geometry varying the ground clearance, one can use the length of the recirculation bubble L_r as an estimator of the global curvature of the flow in the near wake. This analysis is confirmed by the excellent correlation between L_r and C_{pb} presented in figure 6.13(a) and their power-law relationships displayed in figure 6.13(b).

The map of the base pressure presented in figure 6.9 reflects the consequences of the modification of both the aspect ratio H^* and ground clearance C^* on the drag. The domain can be separated into three regions: roughly $C^* < 0.05$, $C^* \approx 0.06$ and $C^* > 0.1$.

The first zone corresponds to the cases $C^* < 0.05$ when there is almost no underbody flow which leads to topologies of three-dimensional backward facing steps. These configurations are low drag cases, especially for the low values of H^*, with large recirculation lengths. In the limit case of the bidimensional backward facing step, *i.e.* $H^* \ll 1$, at large Reynolds numbers, the ratio H/L_r quantifying the global curvature of the flow is constant (Armaly *et al.*, 1983). This points out that the base pressure does not depend on H. In the present experiments, this might be the case for sufficiently small H^*. However, as H^* is increased, three-dimensional effects related to the sides of the geometry must gradually limit the recirculation length to a saturated size proportional to W. This saturation effect of L_r when H is increased should lead to a decrease of base pressure which is actually the observed tendency in figure 6.9.

The second region is related to low levels of base pressure, *i.e.* high drag, in a vertical stripe centered around $C^* \approx 0.06$. It corresponds to the situation displayed in figure 6.2(e) where the underbody flow is concentrated into an energetic jet[4] detaching from the ground at R_g and returning back to the top of the base with strong curvature. Interestingly, the drag increase for $C^* \approx 0.06$ does not depend on H^*. So, for these ground clearances, the curvature of the jet is constant at first order so that L_r should scale as H at least within the observed range $0.51 < H^* < 1.63$.

Finally, the third zone is associated with large values of ground clearances ($C^* > 0.1$). The top and bottom shear layers become similar (see figure 6.3e) and the influence of the ground clearance on the flow seems negligible. Hence, the variations in base pressure should be ascribed to the transitions from bidimensional flows when $H^* \gg 1$ and $H^* \ll 1$ to a three-dimensional flow for $H^* \sim 1$. Experimentally, a slight base pressure reduction is observed for extreme values of H^* in agreement with this transition trend. The drag increases when the flow gradually becomes bidimensional as reported by Wang *et al.* (2012) and references therein.

[4]The velocity of the jet is close to $0.5U_0$.

6.4 Concluding remarks

The experimental investigation of the wake past parallelepiped bodies with various aspect ratios H^* and ground clearances C^* identifies three different regimes depending on the ground clearance.

- For $C^* < 0.05$, viscous effects prevent the development of the underbody flow and the geometry behaves like a three-dimensional backward facing step.
- For $0.05 < C^* < 0.10$, the underbody flow gradually becomes more energetic but separates on the ground; it forms a curved jet that reattaches on the top of the base. These configurations are associated with low levels of base pressure, *i.e.* high drag.
- Finally, for $C^* > 0.10$, the underbody flow has enough momentum to prevent the separation on the ground. The effect of the wall is less visible on the near wake organization since the top and bottom shear layer developing from the base are similar.

Besides, when there is only a limited wall influence, typically for $C^* > 0.1$, an instability develops in the y direction for the aspect ratios in the range $0.60 \pm 0.02 < H^* < 1.30 \pm 0.04$. Symmetrically, by rotation of the body, an instability in the z direction is observed for $0.77 \pm 0.03 < H^* < 1.67 \pm 0.05$. These instabilities result in antisymmetric perturbations of the opposed shears in the considered direction and can lead to a wake bi-stability. The orientation of the antisymmetry, left or right for the y instability and top or bottom for the z instability, is highly sensitive to the symmetries of the setup: a residual yaw angle or wall effect is very likely to trap the wake in one of the two states.

Out of the interfering range $0.77 \pm 0.03 < H^* < 1.30 \pm 0.04$, the antisymmetry is reported in the opposed shears detaching from the smallest sides so that the y and z instability are dominant for $H^* < 1$ and $H^* > 1$ respectively. Within the interfering range, instabilities from both the smallest and the largest sides can occur. The frontier at $H^* = 1$ is not observed: the z instability predominates the y one as soon as $H^* > 0.90 \pm 0.05$, possibly because of residual asymmetries in the setup.

The suppression of these instabilities is possible by forcing symmetric perturbations. For example, when the body is placed on a wall (or equivalently using a splitter plate), the flow asymmetries in the direction normal to the wall are not possible and only the instability parallel to the wall can subsist. These symmetry considerations justify that the bi-stability in the y direction is equally reported for $C^* < 0.03$, *i.e.* for three-dimensional backward facing step configurations, in the range $0.30 \pm 0.01 < H^* < 0.65 \pm 0.02$.

The definition of the domains of appearance of such cross-flow instabilities are of fundamental importance for the understanding of three-dimensional wakes. One may observe some slight evolutions of the frontiers depending on the Reynolds number or the length of the body due to modifications of the boundary layers at the trailing edge. Nevertheless, at first order, these domains are very likely to be independent of these parameters as the reflectional symmetry breaking states in the case of the squareback Ahmed geometry is already observed at $\mathrm{Re}_H = 340$ (see chapter 4).

More generally, these experiments show that the cases of reflectional symmetry breaking found in the literature are not isolated configurations and are likely to result from the development of similar instabilities. Besides, such a high sensitivity of the organization of the near wake should be considered to design ground vehicles from cars to buses. Such phenomena affect the force intensities: the side or lift force depending on the geometry, but

also the drag. A quantification of the drag ascribed to such bistable behavior is provided through the control studies that are presented in chapter 7.

Chapter 7

Sensitivity analyses of the bistable wake

Most of these results are submitted to *Journal of Fluid Mechanics*.

This chapter explores the sensitivity of the wake past the squareback Ahmed geometry[1]. The objective is to clarify how a local disturbance affects the global properties of the flow with a particular focus on the natural bi-stability.

Abstract

The sensitivity of the flow around the reference Ahmed geometry is now investigated experimentally at Reynolds number 9.2 10^4. Vertical and horizontal control cylinders are used to disturb the natural flow which is the superposition of two reflectional symmetry breaking states (see chapter 5). When the perturbation breaks the symmetry of the setup, it can select one of the two asymmetric topologies so that a mean side force is reported. On the other hand, when the reflectional symmetry is preserved, some positions of horizontal and vertical control cylinders alter the natural bi-stability of the flow which may result in drag reduction. In addition, it is found that the horizontal perturbation affects the lift especially when the top and bottom mixing layers are disturbed. The ability of the disturbances to suppress the bistable behavior is discussed and, introducing a formalism of induced drag, a quantification of the impact of the cross-flow forces on the drag is suggested. In particular, the results point out a quadratic dependence between the drag and the lift that is thoroughly studied in chapter 8.

Contents

[1] The detailed study of the natural wake is provided in chapter 5.

7.1 Experimental setup

The experimental facility and the model are identical to the ones used in chapter 5. This section only details the differences with the setup presented in section 5.1.

A scheme of the setup is visible in figure 7.1. As in chapter 3, the sensitivity analysis is based on the experimental work of Parezanović & Cadot (2012) in a bi-dimensional configuration. In this previous study, the flow is found sensitive when the control cylinder disturbs the shear layers. Given the parallelepiped shape of the present geometry and the shear layer interactions reported in the natural wake (see chapter 5), the direct extension of the work of Parezanović & Cadot (2012) consists in disturbing the lateral mixing layers or the top and bottom ones. Hence, it appears suitable to use small vertical and horizontal control cylinders placed around the afterbody as displayed in figure 7.1. Their lengths are logically equal to the height or to the width of the body (see figures 7.1*c–d*).

Besides, in Parezanović & Cadot (2012), two different rod sizes are used; they correspond to $0.04D$ and $0.12D$ which should be compared to the initial thickness of the shear layer of $0.05D$, D being the main cylinder diameter. It is found that the smaller control cylinder can be considered as a disturbance while the larger one induces important modifications of the main flow features. Thus, the perturbation assumption remains relevant as soon as the control rod is smaller than the disturbed shears. In the present configuration, the diameter of the cylinders is $d = 4$ mm, *i.e.* $d/D = 5.6\%$. This cylinder diameter correspond to a compromise between the perturbation assumption and the amplitude of the measurable effect on the flow. As the initial thickness of the shear is of order of $0.03H$ (see chapter 5), the cylinders may be too big to be considered as local disturbance in the very near wake. Nevertheless, as soon as $x > 0.2H$, the shear layers of the natural flow are larger than $0.05H$ and the perturbation assumption becomes sustainable.

The vertical rod is moved in the x and y directions whereas the horizontal one is moved in the x and z directions; their positions are denoted by (x_C, y_C) and (x_C, z_C) respectively. The disturbance location is controlled by a three-dimensional displacement system made up of three Newport (M-)MTM long travel consoles and controlled by the Newport Motion Controller ESP301; the precision of the robots is better than 0.1 mm. The disturbances are automatically displaced over a matrix by steps of $\Delta_x = 3$ mm in the streamwise direction and of $\Delta_y = \Delta_z = 1$ mm in the cross-flow directions, *i.e.* ${\Delta_x}^* = 0.042$ and ${\Delta_y}^* = {\Delta_z}^* = 0.014$. The explored domains are $({x_C}^*, {y_C}^*) \in [0.04, 1.67] \times [-0.97, 0.97]$ and $({x_C}^*, {z_C}^*) \in [-1.00, 1.67] \times [0.04, 1.69]$. As a result, the full exploration of the wake by one disturbance typically needs more than 120 positions in the cross-flow direction and 50 in the x direction.

The cylinders are held by 0.5 mm steel wires oriented along y (one wire for the horizontal cylinder and two wires for the vertical one) in such a way that they are aligned with the base of the body. The supporting wires are sufficiently stretched to have vibration amplitudes that are small in front of d. Besides, tests with only the 0.5 mm wires have been performed to verify that their influence is at least one order of magnitude smaller that the one of the main control cylinders.

The construction of sensitivity maps are based on global quantities of the flow but it is crucial to distinguish two different approaches in this work.

- First, the construction of the sensitivity maps corresponds to a statistical approach. They are obtained after the systematic displacement of the disturbance in the wake and, for each position, the data is recorded for 60 s. This is too short to obtain converged values of mean and standard deviation, especially considering the long time dynamics of the bi-stability. These 60 s are limited by the total duration of an experiment which already lasts for two days. As a result, these sensitivity maps are

only relevant as a whole and the accuracy of the associated data is visible through the dispersion of points in the scatter plots presented in the following.

- In addition, some precise control cylinder positions are studied with a particular attention in sections 7.2.1 and 7.2.2. They are associated with converged measurements, performed over 500 s. The accuracy of the data is identical to the natural case detailed in chapter 5.

Contrary to the experiments of chapter 5, the balance measurements are not used. As the sensitivity analyses need a continuous blowing of the wind tunnel for two days, there is an important daily drift of the balance signal, essentially due to temperature variations. Moreover, preliminary tests have shown that the balance-based and pressure-based sensitivity maps present identical trends: they contain the same information. As a result, the forces are estimated from the pressure measurements only.

The wake analyses are based on pressure and PIV measurements (see section 5.1). The only difference lies in the number of snapshots of the PIV: it is limited to 500 image pairs in this chapter. From these velocity fields, the length of the recirculation region L_r is obtained as the maximal streamwise position of the dividing streamlines of the recirculation bubble. Note that the plane at $z^* = 0.6$ correspond to the z coordinate of the closure of the natural recirculation bubble (see chapter 5). Hence, both planes at $y^* = 0$ and $z^* = 0.6$ allow the measurement of L_r.

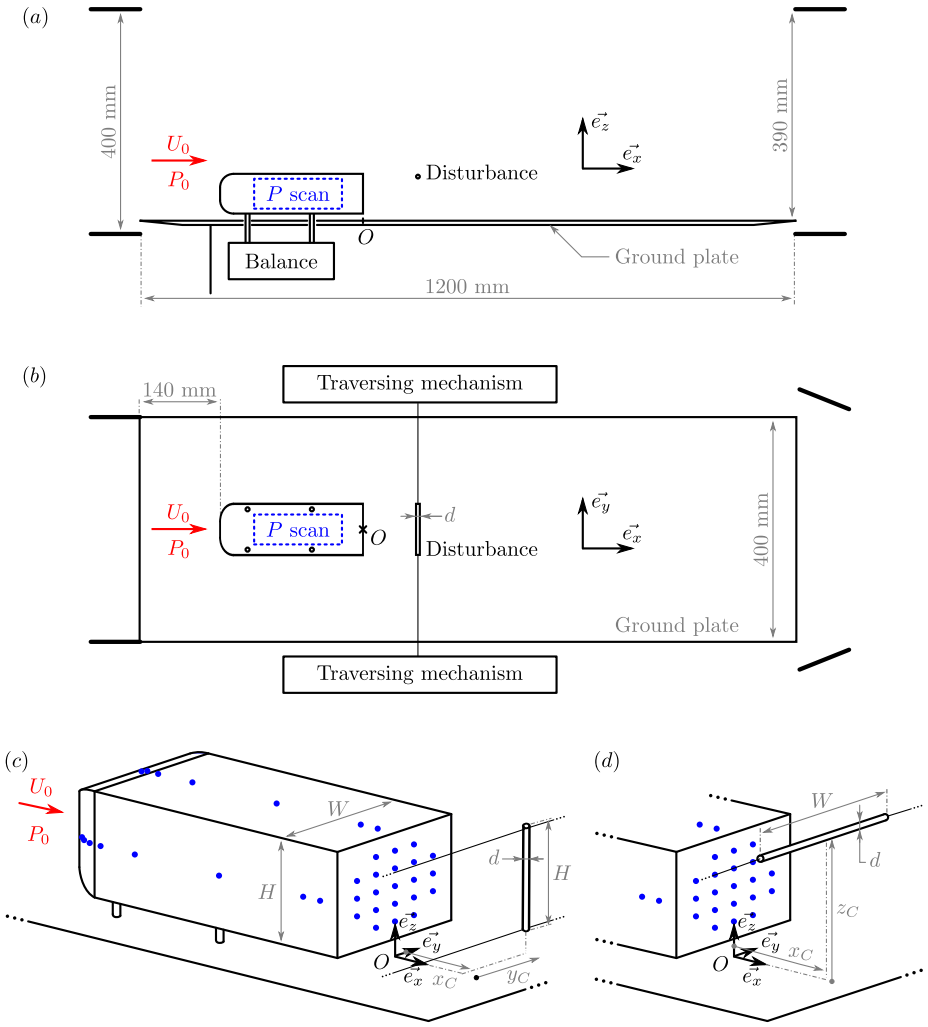

Figure 7.1. Experimental setup: side view (a), top view (b) and perspective view (c,d) disturbed by a vertical control cylinder (c) and an horizontal control cylinder (a), (b) and (d); gray dots are pressure taps, they are distributed symmetrically referring to the planes $y^* = 0$ and $z^* = 0.67$ (mid-height of the body); O sets the origin of the coordinate system.

7.2 Experimental sensitivity to local disturbances

The natural flow is presented in chapter 5. The wake presents two preferred reflectional symmetry breaking positions; each asymmetric state is associated with a diagonal recirculating flow and a base pressure gradient in the y direction: $\partial C_p/\partial y^* = \pm 0.17$. The states are denoted #P and #N for the positive and negative gradients respectively. The succession of the states is random and the equiprobability of the two asymmetric topologies leads to a symmetric mean flow; the bi-stability is characterized by the presence of two maxima in the probability distribution of $\partial c_p/\partial y^*$, centered on ± 0.17.

The sensitivity of the aerodynamic forces and of the bi-stability to a steady disturbance is studied in sections 7.2.1 and 7.2.2 through the displacement of the vertical and horizontal control cylinders in the wake.

7.2.1 Vertical control cylinder

The analyses of the effect of the vertical control cylinder are separated into three sections. First, four characteristic positions are studied through the impact on the flow and on the converged pressure statistics. Then, the sensitivity maps for all the disturbance positions are presented and the third paragraph addresses the dependences between global quantities of the wake.

Sample positions of vertical cylinder

The analysis of four cylinder positions is performed through PIV and pressure measurements. The corresponding velocity fields and statistics of $\partial c_p/\partial y^*$ are given in figure 7.2 while the relevant quantities are listed in table 7.1.

The equiprobability of the states #P and #N relies on the symmetry of the setup. As soon as the vertical control cylinder is out of the plane of symmetry, *i.e.* ${y_C}^* \neq 0$, there is no reason for the flow to be symmetric. Figures 7.2(a)–(b) present the mean velocities in the plane $z^* = 0.6$ and the base pressure statistics for the cylinder positions V_a $({x_C}^* = 0.29, {y_C}^* = -0.60)$ and V_b $({x_C}^* = 0.79, {y_C}^* = -0.40)$.

For the position V_a, the state #N of the flow is selected (see figure 7.2a): the wake is clearly oriented toward the domain $y^* < 0$; the mean diagonal recirculating flow corresponds to the presence of a single peak in the probability distribution of the base pressure gradient $\partial c_p/\partial y^*$ centered on -0.16 ± 0.01. On the contrary, figure 7.2(b) shows that the state #P is dominant for the position V_b: the wake is oriented toward the domain $y^* > 0$, the diagonal recirculating flow is associated with the maximum in the probability distribution of $\partial c_p/\partial y^*$ centered on 0.16 ± 0.01.

As a result, when ${y_C}^* \neq 0$, the vertical disturbance can select one asymmetric state; the selected state depends not only on the sign of ${y_C}^*$ but also on the streamwise position ${x_C}^*$ of the disturbance. Besides, the base pressure and the pressure drag measured for these cylinder positions are very similar to the natural case indicating that there is no drag evolution: the main effect of the disturbance is the selection of one asymmetric state (see table 7.1).

Two other positions of vertical control cylinder are presented in figures 7.2(c)–(d): V_c $({x_C}^* = 0.71, {y_C}^* = 0)$ and V_d $({x_C}^* = 1.37, {y_C}^* = 0)$. These positions preserve the reflectional symmetry of the setup so the flow is symmetric.

For V_c, there is no clear asymmetric peak in the probability distribution of $\partial c_p/\partial y^*$ (see figure 7.2c) so the bistable behavior of the flow is altered. This configuration is associated

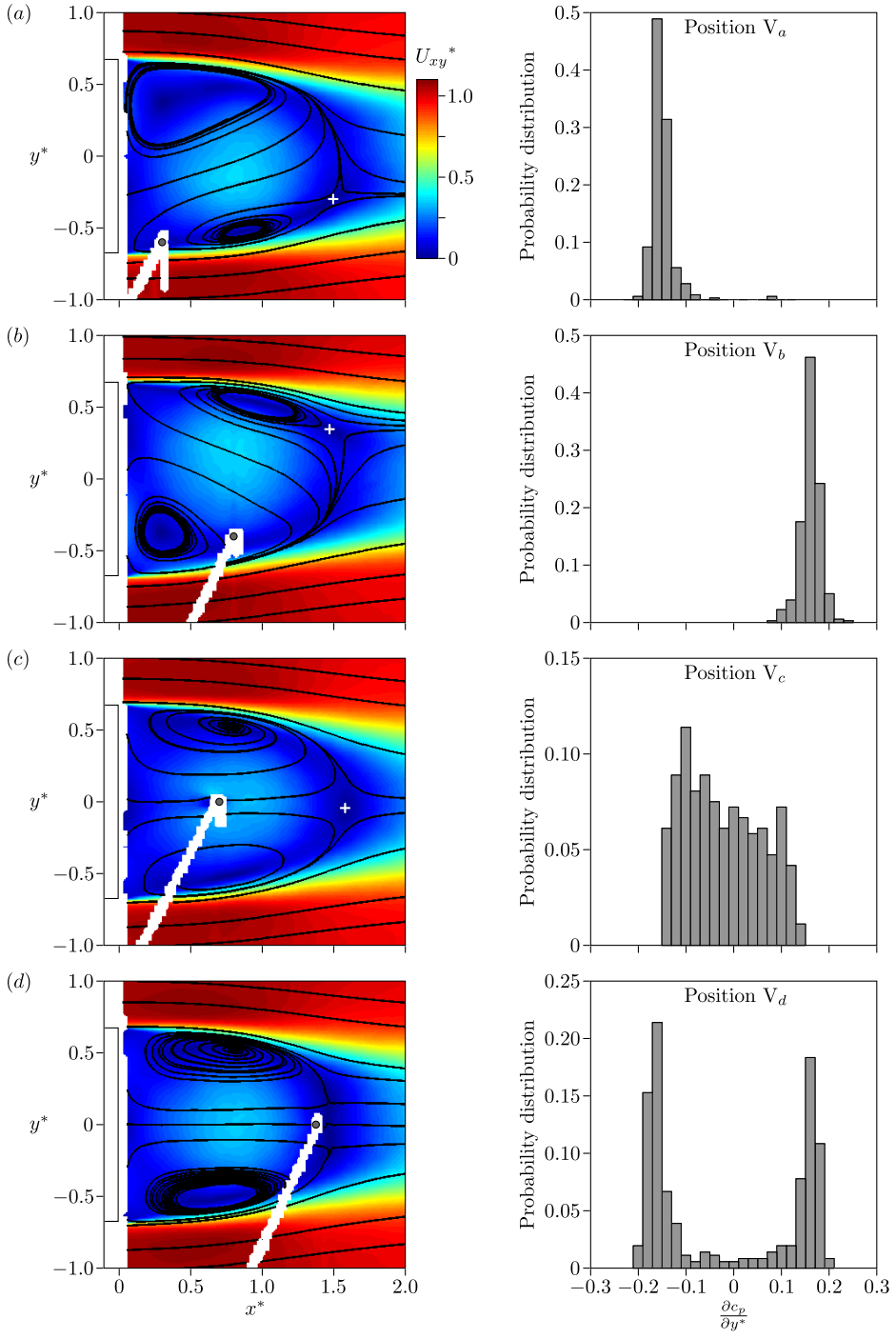

Figure 7.2. Velocity fields in the plane $z^* = 0.6$ (left) and probability distributions of the base pressure gradient in the y direction (right) for different positions of the vertical control cylinder: V_a for ${x_C}^* = 0.29$ and ${y_C}^* = -0.60$, (a); V_b for ${x_C}^* = 0.79$ and ${y_C}^* = -0.40$, (b); V_c for ${x_C}^* = 0.71$ and ${y_C}^* = 0$, (c); V_d for ${x_C}^* = 1.37$ and ${y_C}^* = 0$, (d). The crosses locate the saddle points.

$x_C{}^*$	$y_C{}^*$	$\partial C_p/\partial y^*$	Std($\partial c_p/\partial y^*$)	C_{xp}	C_{yp}	C_{zp}	C_{pb}	$L_r{}^*$
Natural		0.01	0.15	0.206	0.00	−0.08	−0.185	1.47
0.29	−0.60	−0.15	0.03	0.206	0.02	−0.08	−0.188	1.52
0.79	−0.40	0.16	0.02	0.205	−0.02	−0.09	−0.186	1.53
0.71	0	−0.02	0.08	0.194	0.00	−0.08	−0.175	1.57
1.37	0	−0.01	0.15	0.205	0.00	−0.09	−0.186	1.46
Accuracy		±0.01	±0.01	±0.005	±0.01	±0.01	±0.003	±0.01

Table 7.1. Global properties of the natural and disturbed wakes for four different positions of the vertical control cylinder.

with base pressure recovery and a drag reduction of 5.8% while an increase in the recirculation length is observed. On the other hand, for V_d, the perturbation has no significant effect on the flow. The base pressure is equal to the natural value and the two peaks in the probability distribution of $\partial c_p/\partial y^*$ are recovered: the two states #P and #N coexist.

Eventually, the lift measured for the four configurations is very close to the natural value (see table 7.1). Thus, the vertical control cylinder does not seem to affect the pressure distributions on the upper and lower faces of the body.

Now, the control cylinder is systematically displaced in the wake. At each position, the global parameters listed in table 7.1 can be measured to the build sensitivity maps that are presented in the next paragraph.

Sensitivity maps

It is now proved that the asymmetric disturbance introduced by the vertical control cylinder affects the cohabitation of the two asymmetric states. To evaluate the degree of asymmetry generated by the vertical disturbance, the mean base pressure gradient at $y^* = 0$ is measured for all the cylinder positions explored (see section 7.1 for definition of the displacement matrix). Figure 7.3(a) presents the sensitivity map of $\partial C_p/\partial y^*$ which is a symmetry indicator of the recirculation bubble. For $y_C{}^* \neq 0$, the control cylinder almost always selects a wake orientation depending on its position in both the x and y directions. On the contrary, as soon as the symmetry of the geometry is preserved, *i.e.* $y_C{}^* = 0$, the flow retrieves its reflectional symmetry in average with $\partial C_p/\partial y^* \approx 0$.

A second indicator of the flow symmetry is the mean side force which can be estimated from the pressure taps on the lateral faces of the geometry. From these measurements, it is observed that the asymmetric pressure distributions on the base are associated with a force in the y direction (see figure 7.3b). In most of the control cylinder positions where $|\partial C_p/\partial y^*| > 0.1$, a value of $C_{yp} \approx \pm 0.02$ is measured which corresponds to the side force of the asymmetric states #P and #N of the natural wake. Eventually, wherever $\partial C_p/\partial y^* \approx 0$, C_{yp} is equally measured close to 0 which confirms the symmetry of the pressure distribution around the whole geometry.

In order to study the impact of the disturbance on the bi-stability, an indicator independent of the repartition of the two asymmetric states is needed. When the flow is symmetric in average but spontaneously asymmetric because of the bi-stability, the superposition of the two asymmetric states induces important variations of $\partial c_p/\partial y^*$: typically for equiprobable states, Std($\partial c_p/\partial y^*$) ≈ 0.16 while $\partial C_p/\partial y^* \approx 0$. On the contrary, when the flow is locked in one of the asymmetric states: Std($\partial c_p/\partial y^*$) ≈ 0 while $\partial C_p/\partial y^* \approx \pm 0.16$. Hence, the

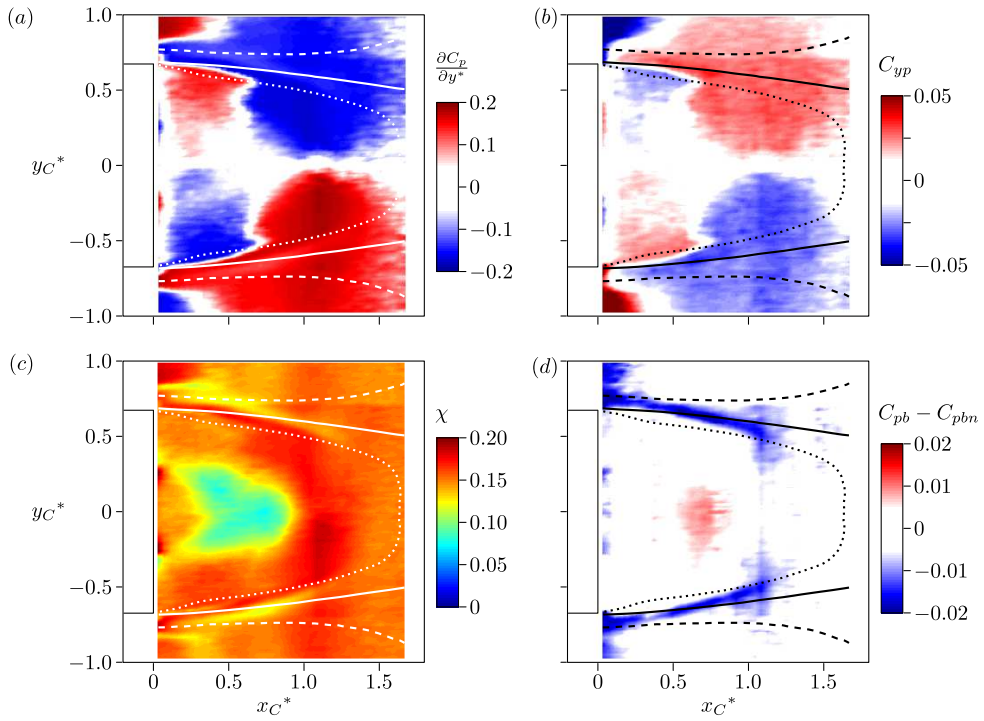

Figure 7.3. Effect of the vertical control cylinder on the pressure on the body: $\partial C_p/\partial y^*$ at $y^* = 0$, (a); C_{yp}, (b); χ, (c); C_{pb}, (d). The thick lines are velocity contours of the natural flow: $\cdots$, ${U_x}^* = 0.1$; —, 0.5; - - -, 0.9.

root mean square of the gradient, denoted χ, is used to quantify the degree of asymmetry.

$$\chi = \sqrt{\langle \left(\frac{\partial c_p}{\partial y^*}\right)^2 \rangle} = \sqrt{\frac{\partial C_p}{\partial y^*}^2 + \mathrm{Std}\left(\frac{\partial c_p}{\partial y^*}\right)^2}. \tag{7.1}$$

The measurement of χ for all the vertical control cylinder positions leads to the sensitivity map shown in figure 7.3(c). For most of the locations, χ is close to 0.16. This indicates that either the flow is bistable (for $\partial C_p/\partial y^* \approx 0$) or the asymmetry in the y direction is at least equal to that of states #P and #N. The exceptions are measured in the center of the recirculation bubble, for ${x_C}^* \approx 0.6$ and ${y_C}^* \approx 0$. For such positions, the diminution of χ indicates that the bistable behavior is suppressed like for the configuration V_c (see figure 7.2c) and, as previously mentioned, these cylinder positions achieve base pressure recovery.

The sensitivity map of C_{pb} is given in figure 7.3(d). Increases in C_{pb} are concentrated around the center of the recirculation region where the symmetry of the flow is preserved and the bi-stability is suppressed. The detailed results associated with the optimal position V_c are provided in the previous paragraph. On the other hand, when the lateral mixing layers are disturbed, the base pressure tends to decrease. For the other control cylinder positions, C_{pb} is measured close to the natural value of $C_{pbn} = -0.185$.

The sensitivity maps presented in figure 7.3 show that the different quantities are correlated; these dependences are now studied.

Correlations between the global quantities of the wake

Before going further, it is important to remind that the disturbance approximation is not sustainable when the cylinder is larger than the local shear or when it is close to a surface. Hence, the data for ${x_C}^* < 0.2$ are ignored in the next section, *i.e.* the correlations between the global quantities are limited to the domain $({x_C}^*, {y_C}^*) \in [0.21, 1.67] \times [-0.97, 0.97]$.

In figures 7.3(a,b), an obvious correlation is found between the base pressure gradient $\partial C_p/\partial y^*$ and the mean side force C_{yp}. The relationship between these two parameters is presented in the scatter plot in figure 7.4(a): each point corresponds to one position of vertical cylinder and the data globally follow a linear dependence. It is worth mentioning that, by definition, the evaluation of C_{yp} is performed using exclusively the pressure taps on the sides and on the forebody whereas $\partial C_p/\partial y^*$ is defined only from the pressure measurements on the base. As a result, the two quantities rely on independent pressure data. One can conclude that the base pressure gradient in the y direction contains the information of the circulation associated with the side force on the geometry.

In equation (7.1), the degree of asymmetry χ is the sum of two terms containing the mean asymmetry of the base pressure $\partial C_p/\partial y^*$ and its fluctuations $\mathrm{Std}(\partial c_p/\partial y^*)$. In figure 7.4($b$) are presented correlations between these mean and fluctuating contributions. Most of the data are observed on the circle centered on 0 of radius 0.16 ± 0.01, *i.e.* for $\chi \approx 0.16$. All the configurations on that circle are wakes with different proportions of each state. This scatter plot confirms that χ is a relevant parameter to quantify the asymmetry of the near wake.

Now, some data are not located on that circle but at a reduced level of χ. These points correspond to the cylinder positions close to V_c, in the center of the recirculation region (see figures 7.2c and 7.3c). As mentioned previously, these points are associated with base pressure recovery and then drag reduction (see figure 7.3d).

The scatter plot of χ *vs.* C_{pb} is visible in figure 7.5(a). There is a high density of points close to the natural levels at $\chi \approx 0.16$ and $C_{pb} \approx -0.185$. Some data report significant

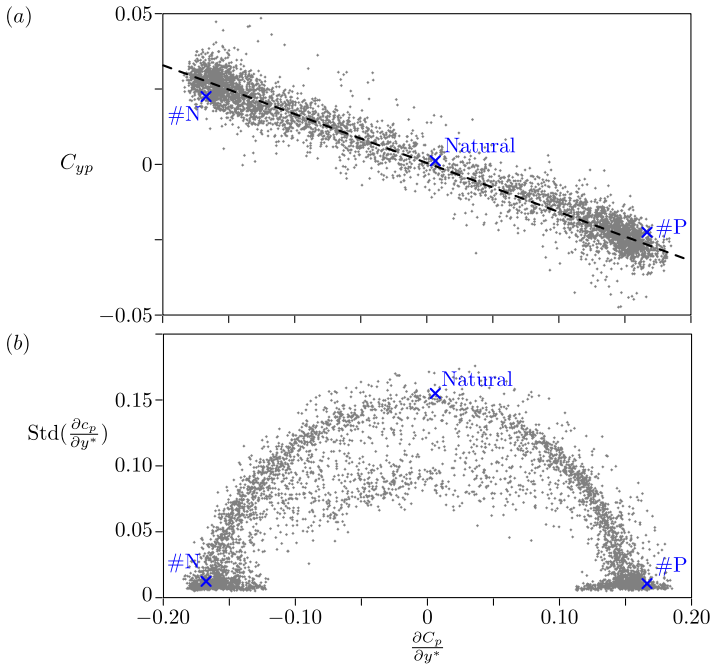

Figure 7.4. Scatter plots of C_{yp} *vs.* $\partial C_p/\partial y^*$ (a) and of $\mathrm{Std}(\partial c_p/\partial y^*)$ *vs.* $\partial C_p/\partial y^*$ (b) for the vertical cylinder positions ${x_C}^* > 0.2$. The dashed line is the linear fit $C_{yp} = -0.16\,\partial C_p/\partial y^*$. The crosses are the natural values.

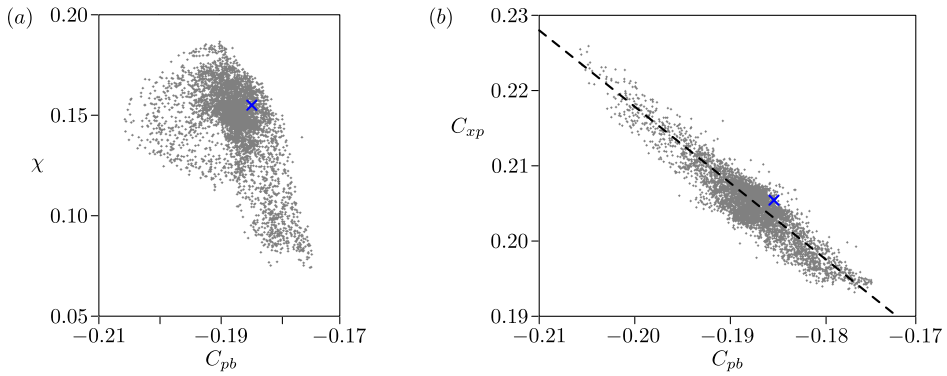

Figure 7.5. Scatter plots of χ *vs.* C_{pb} (a) and of C_{xp} *vs.* C_{pb} (b) for the vertical cylinder positions ${x_C}^* > 0.2$. The dashed line is the linear law $C_{xp} = -C_{pb} + 0.018$ (not a fit). The crosses are the natural values.

base pressure decrease ($C_{pb} < -0.19$) for $\chi = 0.15 \pm 0.03$: they are associated with the disturbance of the lateral mixing layers. Nevertheless, for $C_{pb} > -0.19$, it is clear that there is a correlation between the two quantities: the optimal base pressure recovery corresponds to the minimum level of asymmetry of the recirculation region.

Eventually, in the present experiments, the average level of base pressure is considered as a drag indicator. Indeed, there is a strong dependence between the level of base pressure and the pressure drag as visible in the scatter plot in figure 7.5(b). It is important to say that the evaluation of the pressure drag uses all the taps on the base so that there is, by construction, a certain correlation between these two quantities. Having said that, the affine dependence between C_{xp} and C_{pb} with a slope -1 proves that the disturbance does not affect the pressure distribution on the forebody: the total pressure drag is the sum of the contribution of the forebody which is constant at first order and of the base which depends on the control cylinder position.

As a result, the flow presents an important sensitivity to the vertical disturbance principally due to its natural bi-stability. Now, the sensitivity towards the horizontal control cylinder, which preserves the symmetry of the setup, is presented in section 7.2.2.

7.2.2 Horizontal control cylinder

As in section 7.2.1, the analyses of the effect of the horizontal control cylinder are separated into three sections. Four characteristic disturbance positions are first considered. Then, the sensitivity maps are presented; they are followed by the analyses of the correlation between the global quantities of the flow.

Sample positions of horizontal cylinder

The converged velocity and pressure measurements are given in figure 7.6 and in table 7.2 for four characteristic positions of the horizontal cylinder.

For H_a ($x_C{}^* = 0.37, z_C{}^* = 1.17$) and H_b ($x_C{}^* = 0.58, z_C{}^* = 0.25$), the cylinder is located in the inner shear layers developing from the upper and lower faces of the geometry respectively. The associated velocity fields are presented in figures 7.6(a,b). First, for H_a, the top – bottom organization of the recirculation region is significantly modified in comparison to the natural case which is consistent with the negative value of $\partial C_p/\partial z^*$ (see table 7.2). On the other hand, the flow modifications for H_b are almost undetectable and $\partial C_p/\partial z^*$ is close to the natural value. However, in both case, there is an increase in the recirculation lengths and a suppression of the bi-stability. There is only one preferred position centered on 0 visible in the probability distribution of $\partial c_p/\partial y^*$ with $\chi \approx 0.07$. In parallel, it is measured that these positions achieve base pressure recovery and up to 6.3% reduction of pressure drag.

The data for the control cylinder at H_c ($x_C{}^* = 0.71, z_C{}^* = 0.21$) are presented in figure 7.6(c). At this location, the cylinder is in the outer shear layer coming from the bottom face of the geometry. It generates a vertical jet by deviating flow from the mixing layer to the center of the recirculation region. The organization of the near wake is strongly modified. A curved jet develops from the control cylinder and reaches the top of the base. It is associated with the large pressure gradient in the z direction: $\partial C_p/\partial z^* = 0.16$. This cylinder position is a high drag case ($C_{pb} = -0.212$) which is ascribed to the strong curvature of the jet and the reduced recirculation length. Note that only the recirculating structure close to the base is considered to define the recirculation length L_r (see chapter 6).

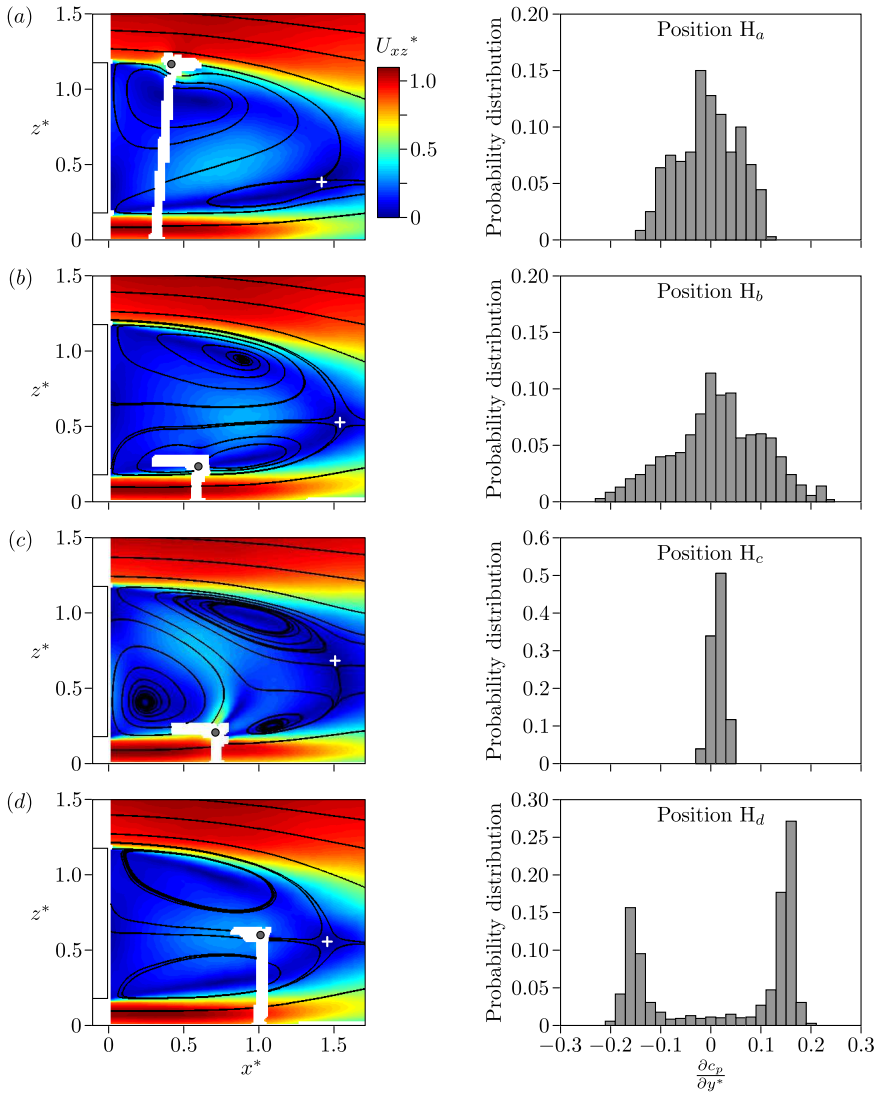

Figure 7.6. Velocity fields in the plane $y^* = 0$ (left) and probability distributions of the base pressure gradient in the y direction (right) for different positions of the horizontal control cylinder: H_a for ${x_C}^* = 0.37$ and ${z_C}^* = 1.17$, (a); H_b for ${x_C}^* = 0.58$ and ${z_C}^* = 0.25$, (b); H_c for ${x_C}^* = 0.71$ and ${z_C}^* = 0.21$, (c); H_d for ${x_C}^* = 1.00$ and ${z_C}^* = 0.60$, (d). The crosses locate the saddle points.

${x_C}^*$	${z_C}^*$	$\partial C_p/\partial z^*$	χ	C_{xp}	C_{zp}	C_{pb}	${L_r}^*$
Natural		−0.02	0.15	0.206	−0.08	−0.185	1.47
0.37	1.17	−0.08	0.06	0.193	−0.06	−0.172	1.54
0.58	0.25	−0.01	0.07	0.196	−0.09	−0.175	1.54
0.71	0.21	0.16	0.01	0.234	−0.14	−0.212	0.86
1.00	0.60	0.01	0.14	0.206	−0.08	−0.188	1.45
Accuracy		±0.01	±0.01	±0.005	±0.01	±0.003	±0.01

Table 7.2. Global properties of the natural and disturbed wakes for four different positions of the horizontal control cylinder.

For this cylinder position, the probability distribution of $\partial c_p/\partial y^*$ shows that the wake is clearly stable in the centered state.

Finally, the position H_d ($x_C{}^* = 1.00, z_C{}^* = 0.60$) is presented in figure 7.6(d) when the control cylinder is out of the shear layers in the middle of the recirculation region. One can observe that the corresponding data are highly similar to the one of the natural wake. The bi-stability of the wake is clearly observable and all the global properties listed in table 7.2 are similar to the natural ones.

The systematic study of the effects of the control cylinder on these global quantities are now presented when the disturbance is displaced in the wake.

Sensitivity maps

For each position of horizontal control cylinder, the pressure distribution on the base and the forces on the geometry are considered through the measurement of $\partial C_p/\partial z^*$, χ, C_{zp} and C_{pb}. As the perturbation preserves the reflectional symmetry of the setup, the mean side force and $\partial C_p/\partial y^*$ remain nil for all the disturbance positions.

The sensitivity map of $\partial C_p/\partial z^*$ is presented in figure 7.7(a). The results confirm the trends observed in the previous paragraph. There are significant modifications of the pressure gradient when the control cylinder is in the shear layers: $\partial C_p/\partial z^* > 0$ in the lower one while $\partial C_p/\partial z^* < 0$ in the upper one. Elsewhere, the gradient is close to 0 like in the natural case. It is worth noting that this map strongly differs from the one presented in figure 7.3(a) due to the absence of bi-stability in the z direction.

Figure 7.7(b) presents the lift modifications $C_{zp} - C_{zpn}$ for all the cylinder positions, C_{zpn} being the natural lift coefficient. The perturbation of the top and bottom mixing layers induces significant variations: the lift is increased for cylinder in the upper shear while it is reduced in the lower one.

The sensitivity map of χ is presented in figure 7.7(c). When the cylinder is located in the shear layers, $\chi < 0.1$ so the bi-stability is suppressed as in figures 7.6(a,b,c). Everywhere else, the measurement of $\chi \approx 0.16$ is associated with the cohabitation of the asymmetric states: as for H_d (see figure 7.6d), the wake is bistable.

Eventually, the sensitivity map of C_{pb} is presented in figure 7.7(d). For $x_C{}^* > 0$, the base pressure is increased up to 6% when the control cylinder acts on the inner part of the mixing layers in the near wake. However, the lower mixing layer is particularly sensitive as the optimal position is H_b but if the disturbance is moved to H_c, which is only slightly below, then the base pressure is strongly reduced. The other region of base pressure recovery is measured on the top face especially for $x_C{}^* < -0.5$. Nevertheless, C_{pb} does not take into account the proper drag of the disturbance. When the cylinder is in a high momentum stream, an additional drag is expected so the base pressure recovery related to the positions $x_C{}^* < -0.5$ are certainly not cases of global drag reduction.

As in the case of the vertical cylinder in section 7.2.1, the sensitivity maps visible in figure 7.7 are correlated; these dependences are now presented.

Correlations between the global quantities of the wake

Scatter plots of the data associated with $(x_C{}^*, z_C{}^*) \in [0.21, 1.67] \times [0.15, 1.30]$ are now presented in figure 7.8 to study the correlations between the global quantities visible in figure 7.7. Note that, as in section 7.2.1, the considered domain is cleared of the uncertainty regions ascribed to local effects of the cylinder and unsustainable disturbance assumption.

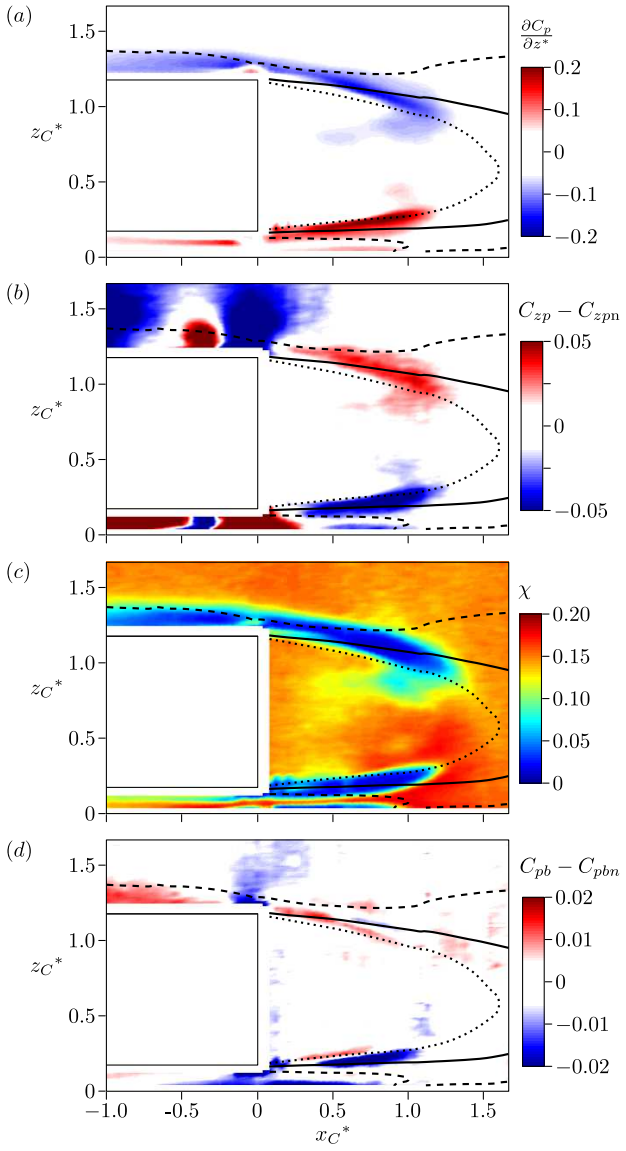

Figure 7.7. Effect of the horizontal control cylinder on the pressure on the body: $\partial C_p/\partial z^*$, (a); C_{zp}, (b); χ, (c); C_{pb}, (d). Thick lines are U_x contours of the natural flow: $\cdots$, ${U_x}^* = 0.1$; —, 0.5; - - -, 0.9.

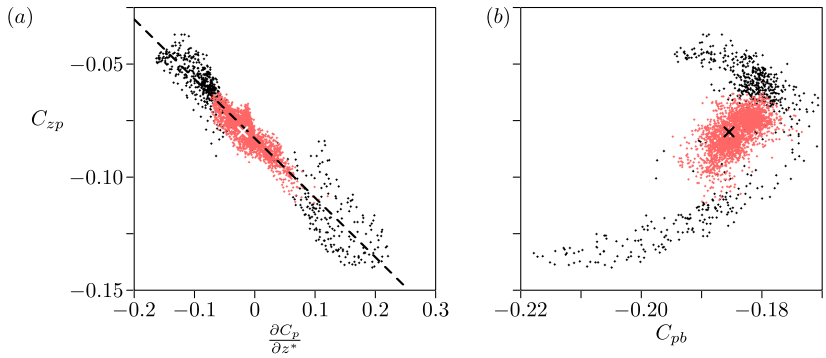

Figure 7.8. Scatter plots of C_{zp} *vs.* $\partial C_p/\partial z^*$ (a) and of C_{zp} *vs.* C_{pb} (b) for the horizontal cylinder positions $({x_C}^*, {z_C}^*) \in [0.21, 1.67] \times [0.15, 1.3]$: black, $\chi < 0.1$; red, $\chi > 0.1$. The dashed line is the linear fit $C_{zp} = -0.083 - 0.26\,\partial C_p/\partial y^*$. The cross is the natural value.

First, an affine dependence between $\partial C_p/\partial z^*$ and C_{zp} is found (see figure 7.8a). The data superimpose on the fit

$$C_{zp} = -0.083 - 0.26\,\frac{\partial C_p}{\partial z^*}. \tag{7.2}$$

Contrary to the dependence between the side force and the pressure gradient in the y direction presented in figure 7.4(a), a negative lift coefficient is obtained for $\partial C_p/\partial z^* = 0$; this point may be ascribed to the ground proximity. As a consequence, the pressure gradient in the z direction reproduces the modifications of the lift but the presence of the ground introduces an offset.

The relationship between C_{xp} and C_{zp} is studied depending on the value of χ. In figure 7.8, degrees of asymmetry χ larger than 0.1 in red are associated with bistable flows while the data with $\chi < 0.1$ in black correspond to flows without bi-stability. Figure 7.8(b) shows that the bistable data are concentrated around the natural point. On the contrary, the stable data are measured in a wide range of base pressure ($C_{pb} \in [-0.22, -0.17]$) presenting a parabolic-like dependence towards the lift coefficient. The positions of base pressure recovery are associated with C_{zp} close to the natural value whereas the base pressure decreases are reported for significant lift modifications and then important recirculation asymmetries in the z direction (large values of $|\partial C_p/\partial z^*|$). These latter cases often correspond to the creation of a curved jet into the recirculation region as visible in figure 7.6(c). More generally, the scatter plot in figure 7.8(b) confirms that the domain of drag reduction associated with the horizontal control cylinder is limited and only correspond to few precise configurations. Hence, this drag reduction domain is less robust than the one observed in section 7.2.1 with a vertical disturbance.

7.3 Synthesis

After presenting the probable mechanisms leading to the suppression of the bi-stability in section 7.3.1, the dependencies between the drag and the cross-flow forces are analyzed in section 7.3.2. Then, section 7.3.3 quantifies the drag ascribed to the bi-stability and discusses more generally about the suppression of the symmetry breaking modes as a control strategy for drag reduction of three-dimensional bluff body.

7.3.1 Suppression of the bi-stability

In section 7.2, it is found that the natural bistable behavior of the wake is suppressed by the control cylinders in two different cases:

- for the vertical cylinder in the center of the recirculation, *i.e.* near the case V_c;
- for the horizontal cylinder in the top and bottom mixing layers like the configurations H_a, H_b and H_c.

The mechanisms responsible for the suppression of the bi-stability for these configurations may be detailed from the results of chapter 6. Indeed, this experimental work evidences that the y instability (responsible for the bi-stability) corresponds to antisymmetric perturbations in the y directions and to symmetric ones in the z directions.

From this statement, one can interpret the vertical cylinder in the plane $y^* = 0$ as a symmetric forcing of the flow, maybe due to the boundary condition imposing ${u_y}^* = 0$ on its surface. However, from figure 7.3(c), it is clear that the receptivity of the flow is not uniform in the plane $y^* = 0$: for example, forcing the symmetry at the end of the recirculation bubble is useless (see configuration V_d).

On the other hand, the horizontal cylinder in the top and bottom shear layers is likely to introduce an asymmetry in the z direction, preventing the development of the y instability. This interpretation is confirmed by the comparison of figures 7.6(a, c) to figure 7.6(d). As a result, in these cases, the suppression of the bi-stability seems associated with a breaking of the relative top – bottom symmetry of the recirculation bubble observed in the natural wake.

7.3.2 Drag of the disturbed wakes

The dependences between the drag and the cross-flow forces are now considered through the effects of the vertical and horizontal disturbances. Finally, a synthesis is provided in a third step.

Drag due to forces in the y direction

In section 7.2.1, it is shown that the vertical disturbance generates modifications of drag and side force while the modifications of lift are negligible. Thus, the data obtained using the vertical disturbance are relevant to study the dependences between the side force and the drag. To do so, two different domains of disturbance positions are considered:

- the domain $\mathcal{D}_1$ for $({x_C}^*, {y_C}^*) \in [1.08, 1.46] \times [-0.21, 0.21]$;
- the domain $\mathcal{D}_2$ for $({x_C}^*, {y_C}^*) \in [0.70, 0.87] \times [-0.49, 0.49]$.

These two domains are presented in figures 7.9(a,b) which are parts of the sensitivity maps of C_{yp} and χ (extracted from figures 7.3b,c). In both domains, when the disturbance goes

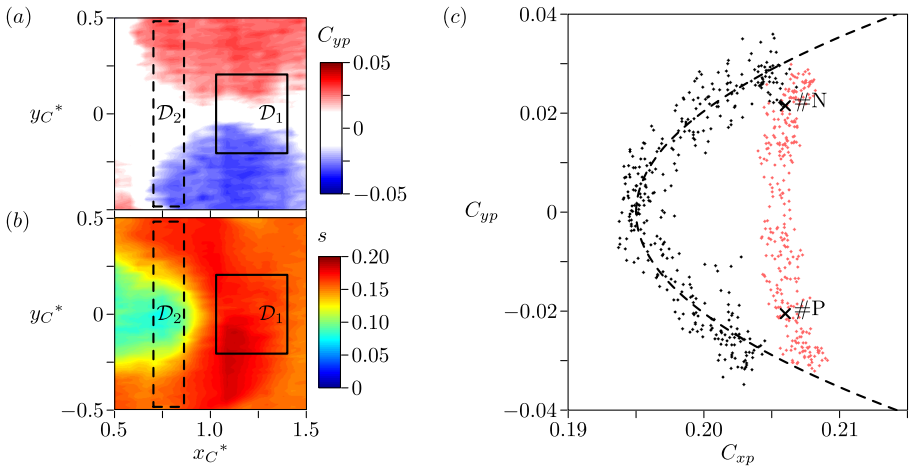

Figure 7.9. (a,b) Domains of vertical control cylinder positioned in the sensitivity maps of C_{yp} and χ: —, $\mathcal{D}_1$; ---, $\mathcal{D}_2$. (c) C_{yp} *vs.* C_{xp} for vertical control cylinder positions in the domains $\mathcal{D}_1$ (red) and $\mathcal{D}_2$ (black); ×, natural values of the asymmetric states; ---, 2$^{\text{nd}}$ order polynomial fit.

from the negative to the positive values of $y_C{}^*$, the wake goes from a mean side force of about -0.025 to $+0.025$ which are imputed to state #P and #N respectively. The difference between both domains lies in the degree of asymmetry χ for $y_C{}^* \approx 0$. In the domain $\mathcal{D}_1$, χ is constant at first order; the position $y_C{}^*$ of the cylinder selects the proportion of the states #P and #N. The equiprobability is obtained for $y_C{}^* = 0$ so that the wake is clearly bistable for $y_C{}^* \approx 0$ (like V_d in figure 7.2d). On the contrary, in the domain $\mathcal{D}_2$, the degree of asymmetry χ diminishes continuously as the mean lateral force tends to 0 and the wake bi-stability is suppressed for $y_C{}^* \approx 0$ (like V_c in figure 7.2c).

The correlation between C_{yp} and C_{xp} is revealed in the scatter plot in figure 7.9(c). Depending on the domain ($\mathcal{D}_1$ or $\mathcal{D}_2$), two different drag *vs.* side force behaviors are observed. First, in the domain $\mathcal{D}_1$ (red dots), the drag is measured constant at $C_{xp} = C_{xpn} \pm 0.002$ and independent of the side force in the whole range of C_{yp}. On the other hand, the drag from the domain $\mathcal{D}_2$ (black dots) depends on the side force; the minimum of drag is measured for $C_{yp} \approx 0$ and progressively increases with $|C_{yp}|$ leading to a parabolic dependence. As a result, an additional drag proportional to ${C_{yp}}^2$ seems ascribed to the side force for control cylinders in the domain $\mathcal{D}_2$; this drag contribution is denoted by C^y_{xp}.

The fact that such a quadratic dependence is not observed in the domain $\mathcal{D}_1$ can be explained as follows. When located in the domain $\mathcal{D}_1$, the disturbance gradually modifies the repartition between the states #P and #N so that all the values of the lateral force between -0.025 and 0.025 are explored. However, the side force is always close to the level of the current asymmetric states, *i.e.* $|c_{yp}| \approx 0.025$. Thus, if the presence of a side force generates an additional drag, an alternating side force even nil in average must equally produce additional drag.

The mean square of the lateral force $\langle {c_{yp}}^2 \rangle$ measures both the steady and unsteady contribution in the y direction. The scatter plot in figure 7.10 shows a linear correlation between C_{xp} and $\langle {c_{yp}}^2 \rangle$, confirming the previous analysis. Indeed, the data associated with both the domain $\mathcal{D}_1$ and $\mathcal{D}_2$ now follow the same trend that can be fitted by the affine law:

$$C_{xp} = 20 \langle c_{yp} \rangle^2 + 0.18. \tag{7.3}$$

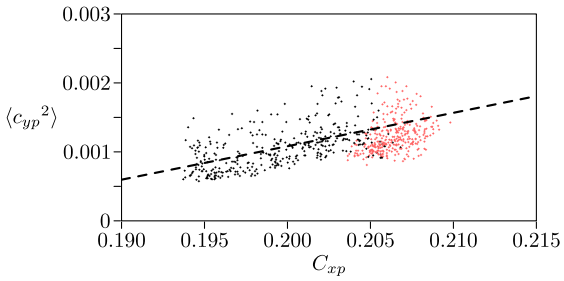

Figure 7.10. Scatter plot of C_{xp} *vs.* $\langle {c_{yp}}^2 \rangle$ for vertical control cylinder positions in the domains $\mathcal{D}_1$ (red) and $\mathcal{D}_2$ (black); ---, affine fit.

Consequently, the quantification of the total pressure drag C_{xp} contains an additional contribution of the side force denoted C_{xp}^y which must take into account both the mean side force and its fluctuations:

$$C_{xp} - C_{xp1} = C_{xp}^y = a_y \langle {c_{yp}}^2 \rangle = a_y \left[C_{yp}^2 + \mathrm{Std}(c_{yp})^2 \right], \tag{7.4}$$

with $a_y \approx 20$. C_{xp1} is the pressure drag that can be achieved for a steady nil side force.

At this stage, it is important to mention that the measurement of $\langle {c_{yp}}^2 \rangle$ suffers from a lack of accuracy partially because the statistics are not fully converged. This is visible through the dispersion of the data along the vertical axis in figure 7.10. Hence, the value of $\langle {c_{yp}}^2 \rangle$ tends to be overestimated, independently of C_{xp}. So, a non-negligible part of $\langle {c_{yp}}^2 \rangle$ is not responsible for induced drag; in other words, C_{xp1} in equation (7.4) can not be evaluated at 0.18 as it would be expected from the fit (7.3). However, this does not affect the following analyses since only the slope of the affine fit (7.3) is used.

Drag due to forces in the z direction

The drag *vs.* lift dependence is now considered using the data presented in section 7.2.2, when the wake is disturbed by the horizontal control cylinder at $({x_C}^*, {z_C}^*) \in [0.21, 1.67] \times [0.15, 1.30]$ (data plotted in figure 7.8). In this domain, the data present evolutions of lift but also of side force since there are stable and bistable cases. To get rid of the additional drag introduced by the fluctuations of side force (see previous paragraph) and obtain the drag evolutions ascribed to the lift only, one may subtract the term $C_{xp}^y = 20 \langle {c_{yp}}^2 \rangle$. Even if this term certainly overestimates the drag ascribed to the side force, it should not alter the drag *vs.* lift dependence: the important point is that the overestimation is independent of C_{zp}.

In figure 7.11 are plotted the dependence between $(C_{xp} - C_{xp}^y)$ and C_{zp}. Contrary to the scatter plot in figure 7.8(b), the data now present a global coherence: both the stable and bistable data superimpose on the same master curve. The dependence can be approximated by the 2$^{\mathrm{nd}}$ order polynomial fit

$$C_{xp} - C_{xp}^y = C_{xp0} + C_{xp}^z, \tag{7.5}$$

with

$$C_{xp}^z = a_z (C_{zp} - C_{zp0})^2 \tag{7.6}$$

and $a_z = 9.9$, $C_{zp0} = -0.079$. As a result, C_{xp0} corresponds to the minimal value of drag that can be achieved for a stable wake with optimal cross-flow forces but its accurate evaluation is impossible using the fit (7.5) due to the overestimation of C_{xp}^y. In parallel, it

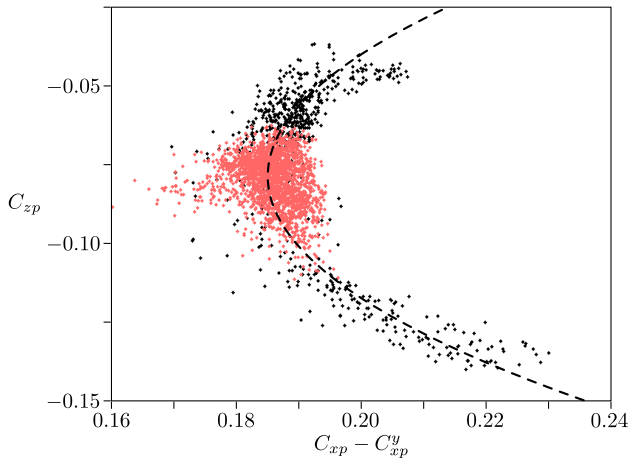

Figure 7.11. Dependence between $C_{xp} - C_{xp}^{y}$ and ${c_{zp}}^2$ for horizontal control cylinder positions $({x_C}^*, {z_C}^*) \in [0.21, 1.67] \times [0.15, 1.30]$ sorted on the value of χ: red, $\chi > 0.10$; black, $\chi < 0.10$; ---, 2^{nd} order polynomial fit.

is observed that $C_{zp0} \neq 0$: the optimal drag point does not correspond to the minimum of ${C_{zp}}^2$ contrary to what is found for the force in the y direction. It seems rather to be related to the best homogeneity of the base pressure distribution: $\partial C_p / \partial z^* \approx 0$ for $C_{zp0} \approx -0.08$.

Now that the influence of each of the cross-flow forces on pressure drag are characterized, a synthesis is presented with a confrontation to notions of induced drag for lifting airfoils.

Interpretation of the drag contributions

The quadratic dependencies between drag and side forces presented in the two previous paragraphs are reminiscent of the notions of induced drag commonly used in aeronautics (Batchelor, 2002). For an airfoil of lift coefficient C_L, the total drag coefficient C_D is usually separated into a parasitic drag and an induced drag (which is part of the pressure drag) that relies on three-dimensional effects. This term of induced drag is associated with the lift which can also be ascribed to the pair of counter-rotating vortices downstream of the wingtips. Denoting C_{D0} and C_{Di} the coefficients associated with the parasitic and the induced drag respectively, the total drag coefficient verifies:

$$C_D = C_{D0} + C_{Di}, \tag{7.7}$$

with

$$C_{Di} = \alpha_L {C_L}^2 \tag{7.8}$$

and α_L depending on the geometry of the wing and more precisely, on the force distribution along the span.

In the framework of car aerodynamics, the results of Ahmed *et al.* (1984) demonstrates the critical impact of the three-dimensional flow structures on the drag. For afterbody slant angles $\phi \in [13°, 25°]$, an increase of drag associated with the development of an intense pair of counter-rotating vortices is reported (Beaudoin *et al.*, 2004). Exploring the effect of flaps mounted on the afterbody in the 25° case, Beaudoin & Aider (2008) prove the strong correlation between the drag, the lift and the pair of counter-rotating vortices.

The theory of induced drag in relation (7.8) can be extended to the analysis of the aerodynamic forces in a road vehicle configuration considering the lift force but also the side

force. Moreover, both the steady and unsteady side force must be taken into account due to the bistable behavior. Now, there is no apparent reason for considering the fluctuations of forces from bi-stability only. Even if it could not be evidenced in this work, the fluctuations of cross-flow forces related to oscillating global modes and to turbulent activity (at least at large scales) may logically be added, in both the y and z directions. As a consequence, the following expression for the pressure drag is suggested:

$$C_{xp} = C_{xp0} + C_{xpi}, \tag{7.9}$$

with

$$C_{xpi} = \alpha_y \langle {c_{yp}}^2 \rangle + \alpha_z \langle (c_{zp} - C_{zp0})^2 \rangle. \tag{7.10}$$

This expression (7.10) relies on three parameters: α_y, α_z and C_{zp0}. As previously mentioned, C_{zp0} is certainly an offset due to the presence of the ground and hence it is likely to rely on the precise configuration of the vehicle such as the ground clearance. However, this optimal lift correspond to the best homogeneity of the base pressure in the z direction (see figure 7.8*a*) which could be a general rule. On the other hand, extending the interpretation of α_L in aeronautics, the coefficients α_y and α_z are expected to depend on the force distribution in the y and z directions. In the present experiment, α_y is thought to be close to a_y because $a_y = 20$ is obtained in equation (7.3) from the sensitivity analysis in the domains $\mathcal{D}_1$ and $\mathcal{D}_2$ only. There, the cylinder is out of the lateral shear layers and it only controls the natural circulation around the geometry. So $C^y_{xp} = 20\langle {c_{yp}}^2 \rangle$ is the drag induced by the natural lateral fluctuations of the wake (including bi-stability), independently of the control cylinder. On the contrary, it is clear that the horizontal cylinder produces a lift on the body, especially when it is located in the mixing layers. Consequently, the measurement of a_z in equation (7.6) is associated with the system comprised of the main geometry and the disturbance while α_z is related to the main geometry only. In other words, one expects $\alpha_z \neq a_z$.

7.3.3 Stabilization of the symmetric state as a control strategy

An estimation of the additional drag due to the bi-stability of the natural wake can be provided by the sensitivity analysis. $\langle {c_{yp}}^2 \rangle$ is measured at 9.0 10^{-4}, 8.8 10^{-4} and 8.9 10^{-4} for the states #P, #N and the mean symmetric flow respectively; these values give an average of $C^y_{xp} = 0.018$. However, the direct application of equation (7.3) with $C^y_{xp} = 20\langle {c_{yp}}^2 \rangle$ may over-estimate the contribution of the bi-stability so $C^y_{xp} < 0.018$. Now, an inferior limit can be obtained from the results on the natural flow (see chapter 5). Using a conditional averaging technique, the side force is measured at $|C_{yp}| = 0.021$ for both mirror states. Hence, it is obtained that $C^y_{xp} > 20{C_{yp}}^2 \approx 0.008$ and this inferior bound is free from the over-estimation of $\langle {c_{yp}}^2 \rangle$. As a conclusion, the drag related to the bi-stability is estimated between 0.008 and 0.018, *i.e.* between 4% and 9% of the total pressure drag.

In chapter 4, it is found that the origin of the bi-stability is ascribed to a pitchfork bifurcation of the laminar wake. For Re > 340, the steady symmetric flow disappears and the wake solutions are two mirror steady asymmetric states. At large Reynolds numbers, turbulent fluctuations allow the exploration of the two solutions but the symmetric flow is never observable in a strict sense. The effect of the vertical cylinder placed at the center of the recirculating bubble (see figure 7.2*c*) might be interpreted as a control of the reminiscences of the steady reflectional symmetry breaking mode, which renders the symmetry of the wake.

Now, steady pitchfork bifurcations are common feature of three-dimensional flows; for instance Pier (2008) evidences that for a sphere, the loss of axisymmetry is a source of

additional drag. Hence, the stabilization of this steady symmetric regime offers a relevant control strategy for drag reduction of three-dimensional bluff bodies, even at large Reynolds numbers.

7.4 Concluding remarks

Using horizontal and vertical perturbations, the sensitivity analyses of the separated flow past the squareback Ahmed geometry reveal the receptive zones of the wake. First, a disturbance that breaks the reflectional symmetry of the setup selects one of the two asymmetric states depending on both the streamwise and lateral positions of the perturbation. Besides, the receptive region of the bi-stability to a steady symmetric forcing is found in the center of the recirculation region. These positions of vertical cylinder lead to a stable centered wake with an increased recirculation length and a base pressure recovery. Moreover, the sensitivity maps obtained with a vertical control cylinder show strong similitude with the ones presented in chapter 3. Thus, the bi-stability of these two geometries is very likely to result from the same physics. Given the generality of these bistable phenomena (see chapter 6), the high receptivity of the center of the recirculation to a symmetric forcing may be a widespread characteristic of three-dimensional separated flows.

On the other hand, the sensitivity maps obtained with the horizontal control cylinder indicate that the receptivity is concentrated in the upper and lower shear layers. Significant lift modification are reported, especially when the control cylinder generates a jet from the high momentum flow to the recirculation region. Such a wake asymmetry in the z direction is likely to prevent the development of the y instability responsible for the bi-stability which results, in some cases, in drag reduction.

From these sensitivity analyses, correlations between the drag and the cross-flow forces are identified. Extending the formalism induced drag in aeronautics, a quantification of the impact of the cross-flow forces on the pressure drag is suggested. It is found that both the steady and unsteady cross-flow forces must be taken into account. The optimal point in terms of induced drag is obtained for a steady force at $C_{yp} = 0$ and $C_{zp} = -0.08$. The fact that the optimal lift is negative should be ascribed to the ground proximity and may differ from an experiment to another; however, these forces correspond to the best uniformity in the base pressure distribution which is very likely to be a general result.

As a consequence, it is confirmed that the bi-stability of the natural flow is responsible for part of the drag, estimated between 4% to 9% of the total pressure drag. This evaluation quantifies the potential of drag reduction on the Ahmed geometry by using control devices able to force a centered wake that is steady at long time-scales.

More generally, one can wonder if the drag dependence on the fluctuations of cross-flow forces stands for non-bistable wakes at high Reynolds number. This question may motivate future studies which could lead to the definition of new strategies of drag reduction.

These dependences between the drag and the cross-flow forces are now studied by additional experiments of flow orientation at the base separation in chapter 8.

Chapter 8

Flow deviation at the top and bottom of the base

Most of these results are published in Grandemange *et al.* (2013*c*).

This chapter clarifies the link between the angles of the flow separations at the trailing edge, the wake topologies and the aerodynamic forces. In particular, it gives an interpretation of the quadratic dependence between the drag and the lift that is reported in chapter 7.

Abstract

The dependences between the drag and the cross-flow forces evidenced previously is highly used in the developments of vehicles. By orientating of the flow at the trailing edge, the manufacturers set empirically the angles of the flow separations on the rear of the vehicle to reach the drag optimum. Using flaps at the end of the top and bottom faces of the Ahmed geometry at $\mathrm{Re}_H = 7.4\ 10^5$, a parametric study regarding their orientations is performed from pressure and force measurements as well as particle image velocimetry. When the orientation of the bottom flap is fixed, the variations of the top slant angle indicate a quadratic dependence of drag *vs.* lift. This relationship presents self-similarities for all the angles of bottom flap. It is furthermore observed that the lift is an affine function of both angles and the drag is a second order polynomial containing a coupling term between the two flap orientations. The evolution of the drag, depending on both angles is discussed. The contributions of the wake size, of the lift induced drag and of the local drag induced by the inclination of the flaps are identified. As a logical progression of this work, these drag sources are considered at industrial scales in the next chapter.

Contents

8.1 Experimental setup

The studied bluff body is the squareback model used in Ahmed *et al.* (1984). The total length of the body is $L = 1044$ mm, the height H and width W of the base are 288 mm and 389 mm respectively. The four supports are cylindrical with a diameter of 30 mm and the ground clearance is set at 50 mm in order to match the reference experiments. The body is placed in the PSA in-house wind tunnel (see Gohlke *et al.*, 2007, for a description of the facility). This open-loop wind tunnel has a 6 m long test section and a rectangular cross-section 2.1 m high and 5.2 m wide. The turbulence intensity is 1.3%. The body is placed on an up-raised plate as depicted in figure 8.1(a). The boundary layer that develops on this plate (without the body) is turbulent and its thickness is $\delta_{99} = 24 \pm 1$ mm at 1.0 m downstream of the NACA leading edge. The free-flow velocity is $U_0 = 40$ m s^{-1} and the Reynolds number based on the height of the geometry is $\mathrm{Re}_H = U_0 H/\nu = 7.4\ 10^5$.

The flow around the Ahmed body is controlled by two flaps mounted downstream of the top and bottom faces of the model as depicted in figure 8.1(b). The streamwise length of the flaps is 50 mm, their cross-flow length matches the width of the geometry and their thickness is 2 mm. The slant angles can be controlled in the range $(\phi_T, \phi_B) \in [-12°, 17°] \times [-17°, 12°]$; these ranges remain reasonably small to keep the flow attached on the flaps in all the configurations. The inclinations of the flaps are set with a precision better than 1°. The different combinations of angles are presented in figure 8.1(c).

The drag and the lift are obtained using an aerodynamic balance placed under the elevated floor and attached to the four body supports. The body supports go through the elevated floor without any contact so that only the fluid force exerted on the Ahmed body is measured. Reference force measurements are performed before and after each blowing to check the reliability. Each measurement consists in five samples of 60 s at the frequency of 50 Hz. The accuracy of C_x and C_z in the conditions of the experiments is 0.001 and 0.002 respectively.

The static pressure on the body is measured at 47 locations through 0.8 mm diameter holes pierced around the geometry in the reflectional plane of symmetry. The pressure is obtained using a 64 port HD miniature pressure scanner and a SCANdaq 8000 interface; the measurement is based on the time-averaged value obtained with one sample of 60 s; the precision is better than 4 Pa. To locate the taps in the plane $y^* = 0$, the curvilinear abscissa s is used; its origin is taken in the middle of the base and goes positive on the top face.

In addition, wake analyses are made from PIV measurements. The system is able to perform stereoscopic PIV to obtain the three components of the velocity in a plane. It is comprised of a Quantal Big Sky Laser (dual pulse Nd:YAG) placed above the model as depicted in figure 8.1 and two Dantec CCD cameras (FlowSense MkII, 4 Mpx). The setup acquires image pairs at a rate of 10 Hz; each acquisition records 400 image pairs per camera. The flow is seeded by droplets of olive oil. The interrogation window size for the cross-correlation processing of the image pairs is 32 px $\times$ 32 px; the corresponding spatial resolution is 2% of the body height. The mean velocities are taken into account only when more than 80% of the 400 measurements are valid vectors. Note that the flaps are transparent; this allows velocity measurements close to the base.

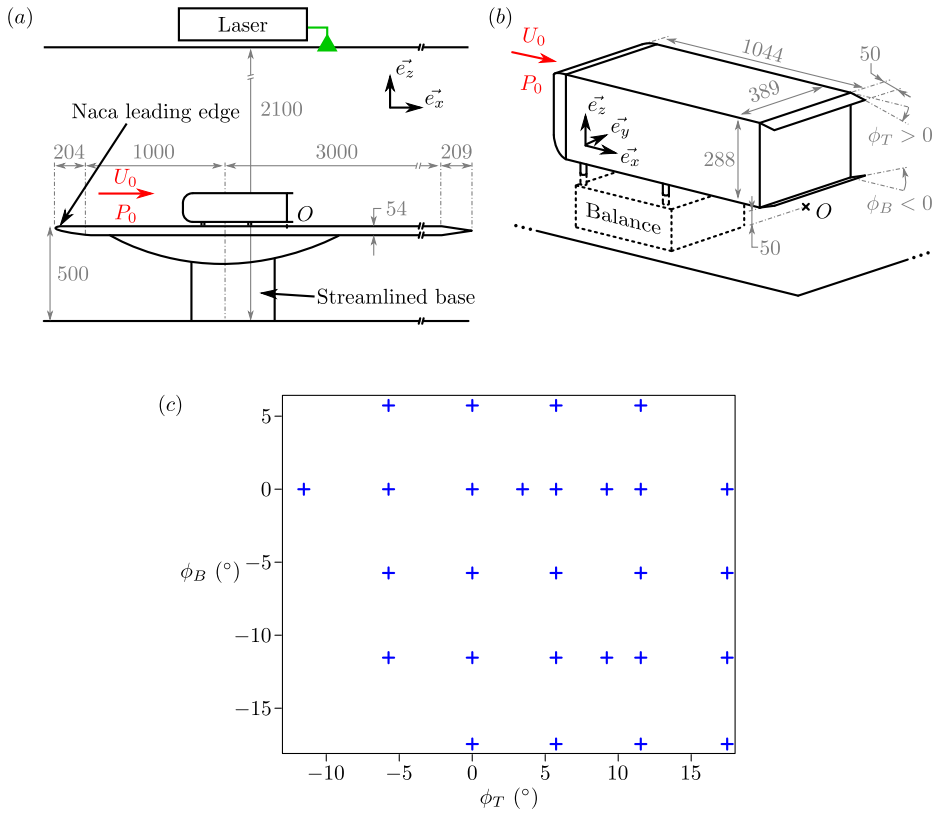

Figure 8.1. (a)–(b) Experimental setup of the model; the dimensions are in mm; O sets the origin of the coordinate system; the dihedral angles ϕ_T and ϕ_B are displayed positive and negative respectively. (c) Couples of slant angles (ϕ_T, ϕ_B) studied.

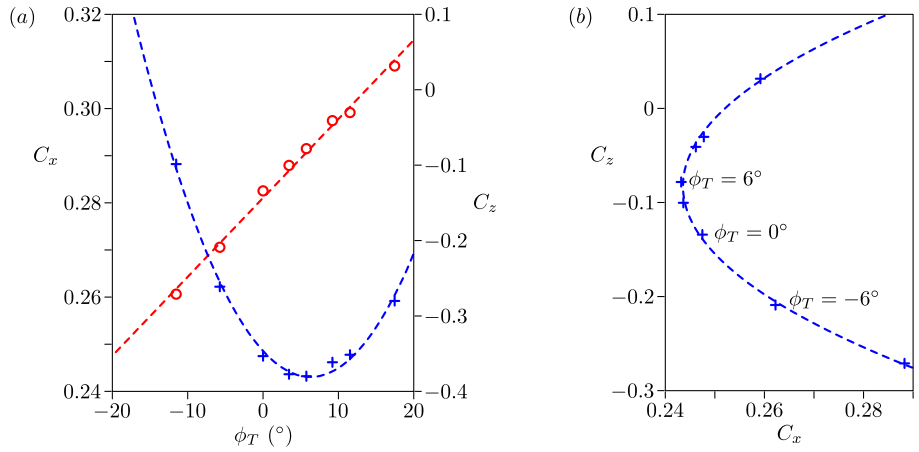

Figure 8.2. (a) Drag (+) and lift (◯) as a function of the top slant angle ϕ_T for $\phi_B = 0°$; ---, 1st and 2nd order polynomial fits of drag and lift respectively. (b) Drag *vs.* lift as a parametric function of the top slant angle ϕ_T for $\phi_B = 0°$: +, experimental data; ---, 2nd order polynomial fit.

8.2 Evidence of a drag optimum

In this section, the force measurements, the pressure levels on the body and the flow topologies are depicted varying the top and bottom slant angles. First, the effect of the orientation of the top flap ϕ_T in the case $\phi_B = 0°$ is considered in section 8.2.1. Then, the analyses are extended to the different bottom angles in section 8.2.2. Finally, the drag and the lift are presented in the bidimensional domain (ϕ_T, ϕ_B) in section 8.2.3.

8.2.1 Study of the cases $\phi_B = 0°$

The inclination of the bottom flap is fixed at $\phi_B = 0°$. The results of the drag and lift coefficients associated with the different top flap angles are presented in figure 8.2(a). As reported by Littlewood & Passmore (2010), the lift is an affine function of the inclination of the top flap. It can be fitted by

$$C_z = 0.600\,\phi_T - 0.143, \tag{8.1}$$

with ϕ_T in radians.

On the other hand, the drag presents a minimum for $\phi_T = 6°$ with a 1.8% reduction in comparison to the case $(\phi_T, \phi_B) = (0°, 0°)$. The experimental data follows a 2nd order polynomial fit given by

$$C_x = 0.243 + 0.457\,(\phi_T - 0.110)^2, \tag{8.2}$$

with ϕ_T in radians.

Similar parabolic-like dependences toward ϕ_T for the drag are presented in the experiments of Ahmed *et al.* (1984) and Littlewood & Passmore (2010). From these results, a clear quadratic dependence between the drag and the lift is reported. The relationship plotted in figure 8.2(b) is given by

$$C_x = 0.244 + 1.242\,(C_z + 0.083)^2. \tag{8.3}$$

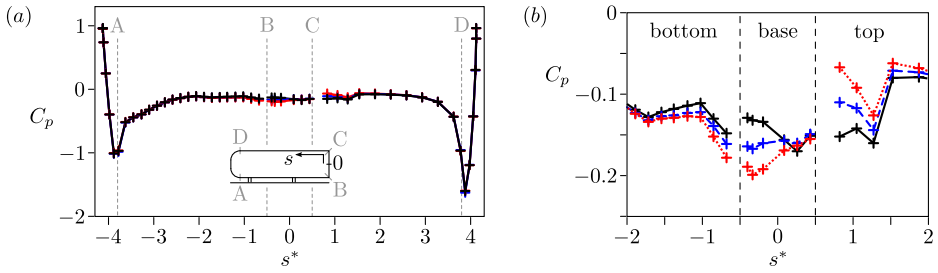

Figure 8.3. Pressure distribution in the plane $y^* = 0$ around the whole geometry (a) and focused on the afterbody (b) for $\phi_B = 0°$ and different ϕ_T: —, $\phi_T = 6°$; ---, $\phi_T = 0°$; $\cdots$, $\phi_T = -6°$.

These force evolutions correspond to modifications of the pressure distribution on the model which are presented in figure 8.3. As visble in the global pressure distribution in figure 8.3(a), the effect of the flaps on the pressure is limited to the afterbody, these local effects being displayed in figure 8.3(b). The angle ϕ_T significantly affects the pressure on the top face before separation as well as the base pressure distribution. Slight variations in the pressure levels on the bottom face are also observed. These pressure levels are consistent with the measurements of drag and lift presented in figure 8.2.

The velocity measurements in the plane $y^* = 0$ are presented in figure 8.4 for the three configurations studied in figure 8.3: $\phi_T = 6°$, $0°$ and $-6°$ with $\phi_B = 0°$. The direct consequence of manipulating the separation angle of the top dividing streamline is to modify the vertical size of the recirculation region (vertical distance between the two dividing streamlines). The case in figure 8.4(a) has the lower drag and the wake is narrower while the case in figure 8.4(c) the wake is thicker and the drag higher. This effect can be quantified by measuring the height of the recirculation bubble at $x^* = 0.5$, it is reduced by 3% in the configuration of figure 8.4(a) and increased by 4% in the case of figure 8.4(c) compared to that of the aligned flaps configuration in figure 8.4(b).

The orientation of the backward flow in the middle of the recirculation region, *i.e.* at $x^* \approx 0.8$ and $z^* \approx 0.6$, is equally changed which may be confronted to the base pressure gradient in the z direction visible in figure 8.3(b). The lowest pressure on the base is measured at the opposite side of the mean backward flow: for example, the flow presented in figure 8.4(a) presents a backward flow oriented toward the ground and the base pressure gradient in the z direction is negative (see figure 8.3b). Such a correlation between the asymmetry of the recirculating flow and the base pressure gradient is equally observed in the previous chapters. The direction of the backward flow is also related to the relative position of the saddle point at the end of the recirculation bubble: it is centered for $\phi_T = 0°$ whereas it goes close to the upper recirculation structure for $\phi_T = -6°$ and to the lower one for $\phi_T = 6°$. The optimal drag configuration for $\phi_B = 0°$ is measured at $\phi_T = 6°$, the velocities and pressure measurements show that this case does not correspond to the best top – bottom symmetry of the recirculation region: the saddle point at the end of the recirculation closure is obviously off-centered (see figure 8.4a) and the base pressure gradient in the z direction is negative (see figure 8.3b) in comparison to the case $\phi_T = 0°$.

The influence of the bottom flap angle on the previous results is now considered in section 8.2.2.

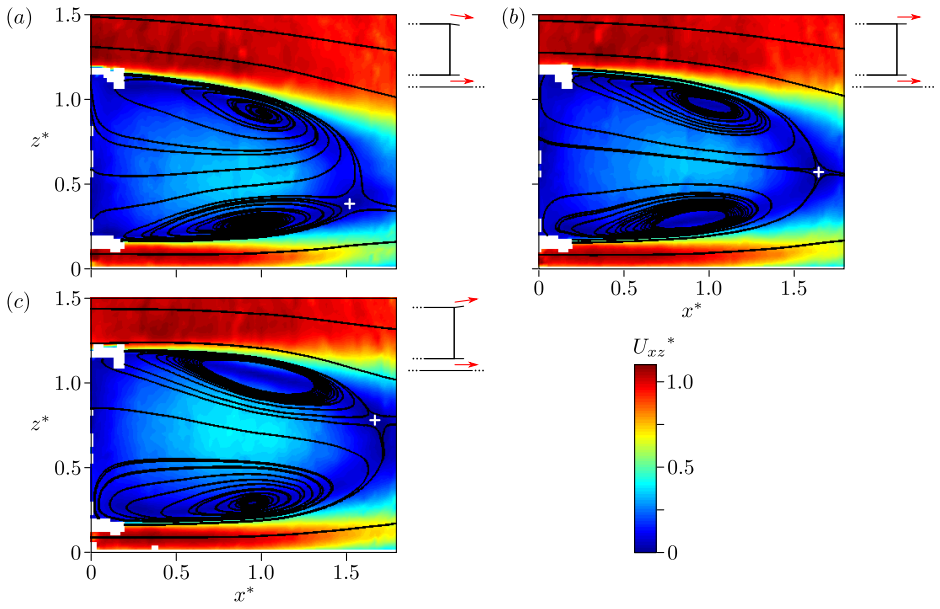

Figure 8.4. Velocity measurements in the plane $y^* = 0$ for $\phi_T = 6°$ (a), $\phi_T = 0°$ (b) and $\phi_T = -6°$ (c) with $\phi_B = 0°$; the crosses locate the saddle points. Due to the laser sheet diffusion and the reflections on the transparent flaps, the measurements are missing in their vicinity.

8.2.2 Study varying ϕ_T for different ϕ_B

By varying the top flap angle ϕ_T, the dependences between the lift and the drag for different angles ϕ_B are plotted in figure 8.5. For each value of ϕ_B, a quadratic relationship is found between C_x and C_z; the results are similar to the case $\phi_B = 0°$ presented in section 8.2.1. Thus, as expressed in equation (8.3), the data varying ϕ_B at constant ϕ_T follows

$$C_x = C_{x0} + \alpha\,(C_z - C_{z0})^2, \tag{8.4}$$

C_{x0}, C_{z0} and α being the three parameters defining each 2$^{\text{nd}}$ order polynomial fit.

Figure 8.6 presents the data centered on their respective value of C_{x0} and C_{z0}. For all the values of ϕ_B, the data superimpose well on the master curve

$$C_x - C_{x0} = \alpha\,(C_z - C_{z0})^2, \tag{8.5}$$

with $\alpha = 1.25$. Therefore, the curves visible in figure 8.5 are self-similar and α is independent of the angle of the bottom flap ϕ_B. So, the relationship between the lift and the drag are perfectly defined from the two parameters C_{x0} and C_{z0}. Besides, it is observed that the optimal angle of the top flap ϕ_T is a function of the bottom angle ϕ_B. This indicates that the optimal drag configuration results from a coupling between the two angles and not from independent optimization regarding ϕ_T and ϕ_B.

The drag and the lift of each optimum (C_{x0} and C_{z0}) are now studied for the different values of ϕ_B. Figure 8.7(a) displays the dependence between ϕ_B and C_{z0}. The optimal lift linearly depends on the bottom slant angle according to

$$C_{z0} = 0.580\,\phi_B - 0.079, \tag{8.6}$$

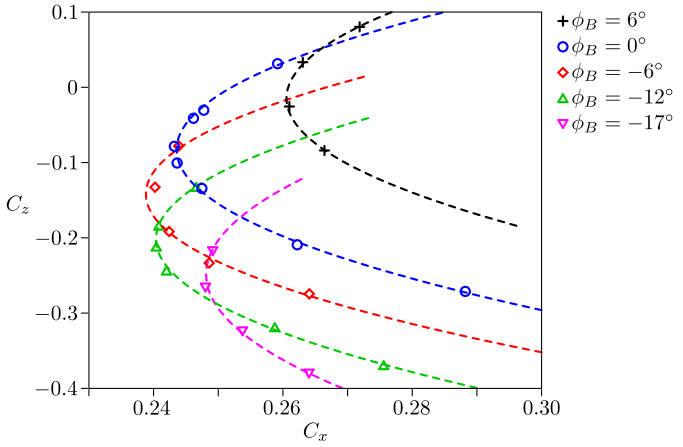

Figure 8.5. Drag *vs.* lift as a function of the top angle ϕ_T for different ϕ_B: +, $\phi_B = 6°$; ◯, $\phi_B = 0°$; ⋄, $\phi_B = -6°$; △, $\phi_B = -12°$; ▽, $\phi_B = -17°$; ---, 2nd order polynomial fits.

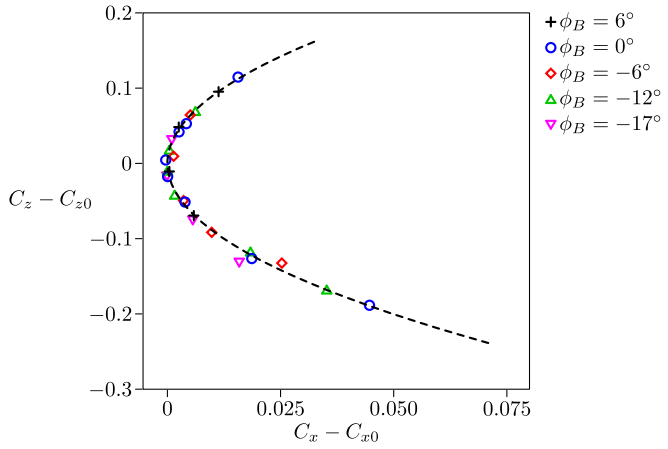

Figure 8.6. Drag *vs.* lift for different values of ϕ_B centered on their respective value of C_{x0} and C_{z0}: +, $\phi_B = 6°$; ◯, $\phi_B = 0°$; ⋄, $\phi_B = -6°$; △, $\phi_B = -12°$; ▽, $\phi_B = -17°$; ---, 2nd order polynomial fit of all the centered data.

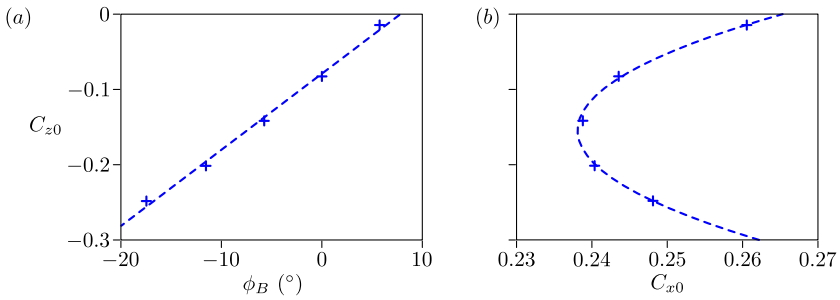

Figure 8.7. (a) C_{z0} as a function of the bottom slant angle ϕ_B: +, experimental data; ---, 1st order polynomial fit. (b) C_{x0} *vs.* C_{z0} as a function of the bottom angle ϕ_B: +, experimental data; ---, 2nd order polynomial fit.

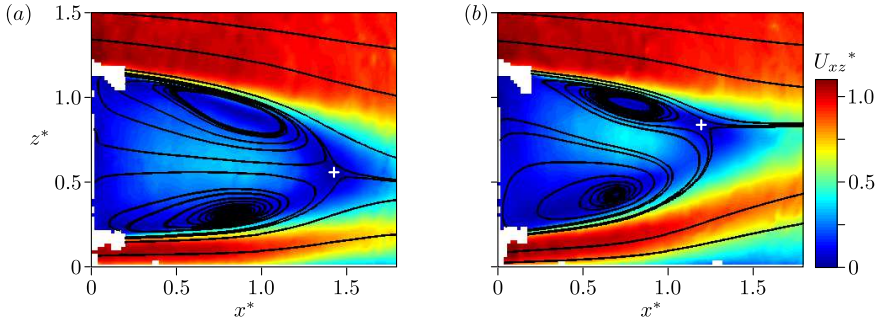

Figure 8.8. Velocity measurements in the plane $y^* = 0$ for $\phi_T = 12°$ and $\phi_B = -6°$ (a, lower drag configuration) and for $\phi_T = 12°$ and $\phi_B = -17°$ (b); the crosses locate the saddle points.

with ϕ_B in radians.

On the other hand, the optimal drag C_{x0} presents a quadratic evolution referring to C_{z0} given by

$$C_{x0} - C_{x\,\mathrm{opt}} = \alpha_{\mathrm{opt}}\,(C_{z0} - C_{z\,\mathrm{opt}})^2, \tag{8.7}$$

with $\alpha_{\mathrm{opt}} = 1.14$, $C_{x\,\mathrm{opt}} = 0.238$ and $C_{z\,\mathrm{opt}} = -0.155$. This latter relationship can be seen in figure 8.7(b). So, $C_{x\,\mathrm{opt}}$ is the optimal drag point considering both parameters ϕ_T and ϕ_B while $C_{z\,\mathrm{opt}}$ is the corresponding lift. This optimal configuration is expected for the flap angles $\phi_{T\,\mathrm{opt}} = 9.2°$ and $\phi_{B\,\mathrm{opt}} = -7.4°$.

Experimentally, the best configuration in terms of drag is obtained for the case ($\phi_T = 12°, \phi_B = -6°$) with $C_x = 0.240$ and $C_z = -0.133$. The associated drag and the corresponding flap angles are fairly close to $C_{x\,\mathrm{opt}}$ and to ($\phi_{T\,\mathrm{opt}}, \phi_{B\,\mathrm{opt}}$) given the precision of the force measurement and the limited resolution of the parameters ϕ_T and ϕ_B (see figure 8.1c). The corresponding velocity field is presented in figure 8.8(a). The mean backward flow is mostly oriented along x and the saddle point is centered in the z direction at the end of the recirculation. The wake height at $x^* = 0.5$ is reduced by 9% in comparison to the one associated with the case $\phi_T = \phi_B = 0°$ presented in figure 8.4(b).

However, it is worth noting that the mean wake topology in the plane $y^* = 0$ is not sufficient to understand the drag evolutions. Indeed, the case $\phi_T = 12°$ and $\phi_B = -17°$

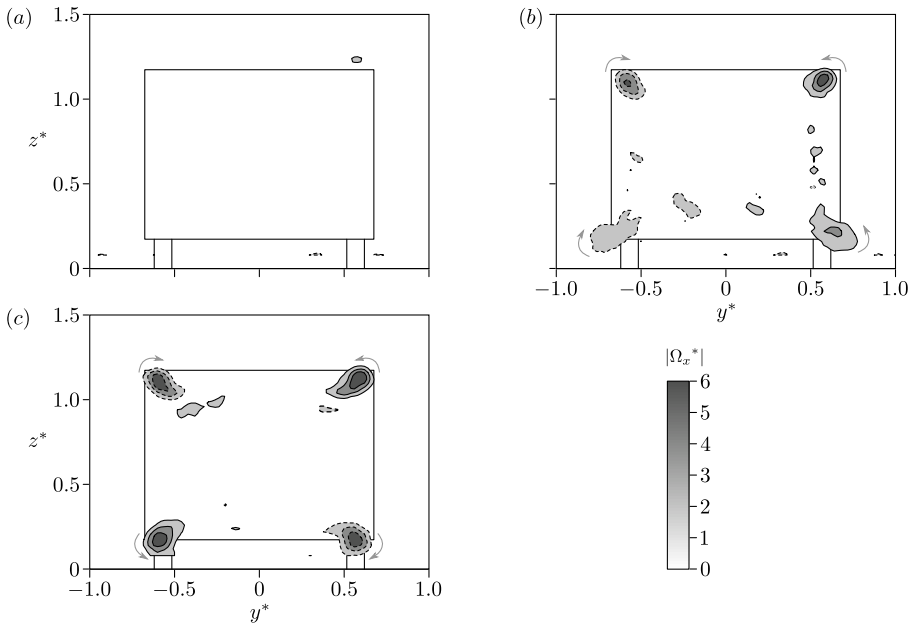

Figure 8.9. Contours of streamwise vorticity $\Omega_x{}^*$ in the plane $x^* = 0.6$: $\phi_T = 0°$ and $\phi_B = 0°$, (a); $\phi_T = 12°$ and $\phi_B = 6°$, (b); $\phi_T = 12°$ and $\phi_B = -12°$, (c). The continuous and dashed lines are respectively positive and negative values; the contour interval is 2; the contour 0 is not plotted.

has an even thinner wake[1] (see figure 8.8*b*) but it still presents a larger drag coefficient ($C_x = 0.248$) than the case ($\phi_T = 12°, \phi_B = -6°$).

The inclination of the top (bottom respectively) flap certainly lead to pressure differences between the top (bottom respectively) face and the side faces upstream of the base (see figure 8.3*b*). As a result, streamwise vortices are likely to develop from the lateral edges of the flaps. Such structures, already suggested by Littlewood & Passmore (2010) must be responsible for a part of the drag and might play a significant role in the drag optimization using such flaps.

To evidence this point, the contours of streamwise vorticity in the plane $x^* = 0.6$ are presented in figure 8.9 for different configurations: ($\phi_T = 0°, \phi_B = 0°$), ($\phi_T = 12°, \phi_B = 6°$) and ($\phi_T = 12°, \phi_B = -12°$). In the case $\phi_T = \phi_B = 0°$ presented in figure 8.9(a), there are no observable vortices; however, as soon as the flaps are inclined, intense vortices are measured in the near wake downstream of the side edges of the flaps (see figures 8.9*b*–*c*); the sign of the vorticity depends on the flap orientation. When the signs of ϕ_T and ϕ_B are identical, the vortices from each side of the model ($y^* > 0$ or $y^* < 0$) are co-rotating (see figure 8.9*b*) whereas, when the signs of the flap angles are different, the vortices are counter-rotating (see figure 8.9*c*).

8.2.3 Study in the domain (ϕ_T, ϕ_B)

To go further in the analyses, the measurements of lift and drag are considered in the bidimensional domain (ϕ_T, ϕ_B). The experimental lift as a function of the angles ϕ_T and

[1]This is the optimal top angle for $\phi_B = -17°$.

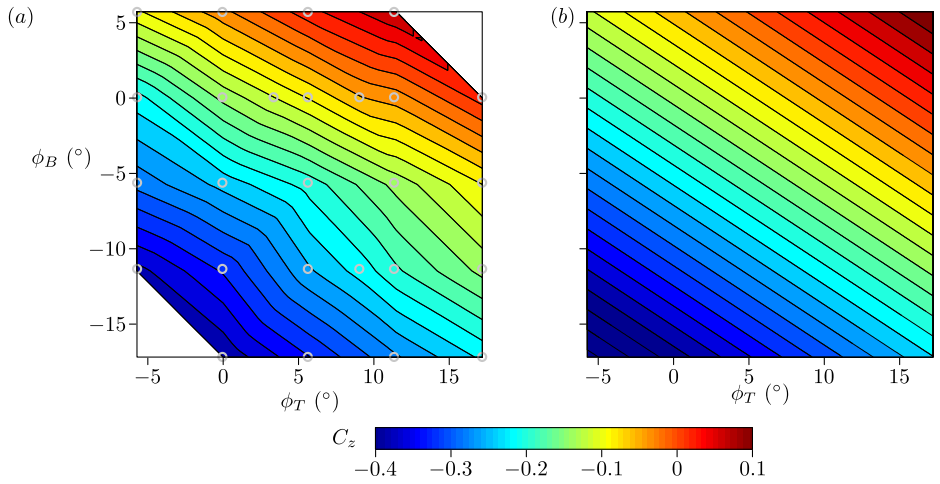

Figure 8.10. Lift depending on ϕ_T and ϕ_B: experimental data (a) and affine fit given in equation (8.8) (b). The contour interval is 0.02.

ϕ_B is displayed in figure 8.10(a). The affine dependence on the top slant angle, depicted in figure 8.2 for the case $\phi_B = 0°$, is confirmed for all the values of ϕ_B. Besides, figure 8.10(a) proves that the lift is equally an affine function of ϕ_B for all the values of ϕ_T. Thus, it can be fitted by

$$C_z = -0.135 + 0.566\,\phi_T + 0.858\,\phi_B, \tag{8.8}$$

with ϕ_T and ϕ_B in radians. This affine fit is plotted in figure 8.10(b).

Similarly, the drag measurements in the domain (ϕ_T, ϕ_B) are plotted in figure 8.11(a). The data confirm the presence of the minimal drag configuration for $\phi_T \approx 10°$ and $\phi_B \approx -10°$ presented in section 8.2.2. In addition, the quadratic evolution of the drag regarding ϕ_T (see section 8.2.1) is recovered and a similar dependence toward ϕ_B is observed. Now, the results detailed in section 8.2.2, in particular equations (8.4) and (8.7), lead to the drag expression

$$C_x = C_{x\,\mathrm{opt}} + \alpha\,(C_z - C_{z0})^2 + \alpha_{\mathrm{opt}}\,(C_{z0} - C_{z\,\mathrm{opt}})^2. \tag{8.9}$$

Since the dependences of C_z and C_{z0} toward ϕ_B and ϕ_T are given in equations (8.6) and (8.8), the drag coefficient is obtained as a function of the top and bottom angles only. The result is displayed in figure 8.11(b); it gives

$$\begin{aligned} C_x \;=\; & 0.248 \\ & - 0.079\,\phi_T + 0.062\,\phi_B \\ & + 0.400\,{\phi_T}^2 + 0.480\,{\phi_B}^2 \\ & + 0.393\,\phi_T\,\phi_B. \end{aligned} \tag{8.10}$$

with ϕ_B and ϕ_T in radians. All of the drag trends observed in the experiments are found in equation (8.10). Besides, it is worth noting that the minimum of drag is not particularly sensitive to the angles ϕ_T and ϕ_B: a low value of drag, close to $C_{x\,\mathrm{opt}}$, can be obtained in a reasonably wide range of parameters around $(\phi_{T\,\mathrm{opt}}, \phi_{B\,\mathrm{opt}})$. Finally, the term proportional to $\phi_T\,\phi_B$ in equation (8.10) corresponds to the coupling effect of the top and bottom slant

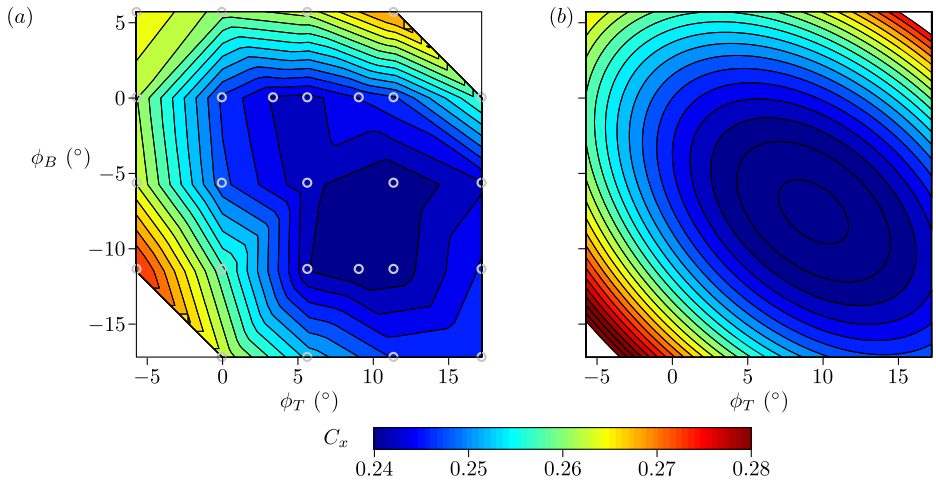

Figure 8.11. Drag depending on ϕ_T and ϕ_B: experimental data (a) and law given in equation (8.10) (b). The contour interval is 0.002.

angles. This might be related to the fact that the inclination of the top flap leads to slight variations of pressure on the bottom face as evidenced in figure 8.3(b). So it may alter the effect of the bottom flap; reciprocally, the orientation of the bottom flap is likely to affect the influence of the top one.

Now that the dependences of the drag and the lift on the two flap orientations are presented, the mechanisms responsible for the selection of these forces are discussed in section 8.3.

8.3 Identification of the drag contributions

As mentioned in section 8.2.2, the height of the separated region is modified by the inclination of the flaps. For a given two dimensional bluff body, one would expect the drag to diminish as the height of the separation is reduced. This is equivalent to the bluffness effect presented in section 1.2.2 where the bluffness is defined as the ratio of the separation width to the body size. Hence, the rule *the more bluff the body, the larger the drag* is not relevant anymore due to three-dimensional effects.

The quadratic relationship between the drag and the lift observed in figure 8.5 is reminiscent of the trends obtained through sensitivity analyses in chapter 7. In the present case, the additional drag contribution due to the flaps can be explicitly introduced by rewriting equation (8.10) as

$$\begin{aligned} C_x &= C_{xn} \\ &\quad - 0.079\,\phi_T + 0.062\,\phi_B && \mathcal{C}_1 \\ &\quad + 0.405\,(C_z - C_{zn})^2 && \mathcal{C}_2 \\ &\quad + 0.270\,{\phi_T}^2 + 0.182\,{\phi_B}^2. && \mathcal{C}_3 \end{aligned} \tag{8.11}$$

where $C_{xn} = 0.248$ and $C_{zn} = -0.135$ are respectively the drag and the lift of the case $\phi_T = \phi_B = 0°$ and C_z follows the affine function defined in equation (8.8). So, the three terms $\mathcal{C}_1$, $\mathcal{C}_2$ and $\mathcal{C}_3$ account for the total drag contribution of the flaps. This expression suggests the following decomposition: a linear contribution $\mathcal{C}_1$, an additional induced drag $\mathcal{C}_2$ due to the lift introduced by the flaps[2] and a quadratic contribution $\mathcal{C}_3$. These three terms are plotted in figure 8.12 for the case of a fixed bottom flap at the optimal angle $\phi_{B\,\mathrm{opt}} = -7.4°$ and a variable top flap angle ϕ_T. When the top angle increases from $-20°$, the height of the separated region decreases gradually as illustrated in figure 8.4. In a pure bidimensional context, this would have led to a monotonous drag decrease since the bluffness is continuously reduced. The term $\mathcal{C}_1$ captures this trend; it should be interpreted as a bidimensional contribution of the separated region to the drag introduced by the flaps.

The additional drag having three-dimensional origin are described by $\mathcal{C}_2$ and $\mathcal{C}_3$. Basically, they are associated to three-dimensional separations producing pairs of longitudinal vortices in the wake. Their properties mainly result from the lift distribution on the geometry. In the case $\phi_T = \phi_B = 0°$, a negative lift is observed but the vorticity field in figure 8.9(a) does not reveal the corresponding longitudinal vortices. The reason may be that they are hardly detectable because the lift is produced by a small pressure difference between the bottom surface and top surface of the body separated by the body height. So the corresponding pressure gradient is weak which induces large vortices, typically of the size of the base, with low intensities. On the contrary, when a flap is inclined, the lift is due to a variation of pressure concentrated on a region of the scale of the flap. This intense pressure gradient on the sharp edges produces concentrated vortices as observed in figure 8.9(b)–(c). In terms of drag quantification, the difference between equation (8.11) and the expression of induced drag used in aeronautics is the contribution $\mathcal{C}_3$. This third term corresponds to an induced drag introduced in the vicinity of the flap edges. Due to the lifting property of the inclined flap, local three-dimensional separations occur on both edges of the top and bottom flaps. The two longitudinal vortices released on the same side of the Ahmed body (from the top and bottom flaps) can cancel out after merging in the far wake. Thus, they are not necessarily associated with lift and they cannot be taken into

[2]This contribution contains the coupling term $0.393\phi_T\phi_B$ of equation (8.10).

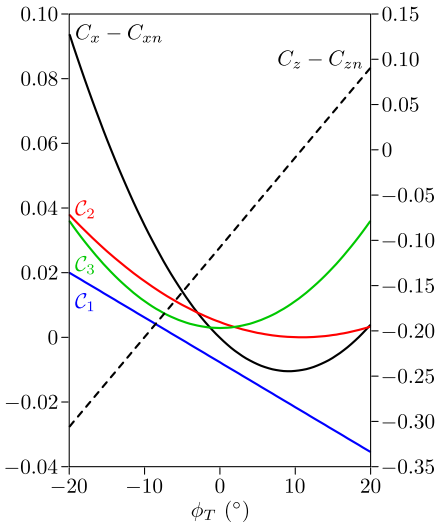

Figure 8.12. Drag decomposition $C_x - C_{xn} = \mathcal{C}_1 + \mathcal{C}_2 + \mathcal{C}_3$ as defined in equation (8.11) (continuous lines, left scale) and lift (dashed line, right scale) for the configurations with fixed $\phi_B = \phi_{B\,\mathrm{opt}} = -7.4°$ and varying ϕ_T.

account in $\mathcal{C}_2$. In other word, one may have four intense vortices, sources of part of the drag ($\mathcal{C}_3 > 0$), without any lift-induced drag at all ($\mathcal{C}_2 = 0$) equivalently to a system of two airfoils with opposite angles of attack.

The existence of a drag optimum by adjusting ϕ_B and ϕ_T might be understood as follows. In figure 8.12, the drag optimum is obtained for $\phi_T = 9.2°$. From that optimal configuration, the decrease of the bluffness (in order reduce $\mathcal{C}_1$) by increasing ϕ_T intensifies the longitudinal vortices produced by the top flap while the term $\mathcal{C}_2$ is constant at first order[3]; this results in a drag increase. On the other hand, decreasing ϕ_T, in order to reduce the induced drag due to the top flap from the optimal configuration, produces a thickening of the separated region so that the drag increases.

Eventually, to give a global view of these different drag sources, sketches interpreting the flow topology of two configurations are presented in figure 8.13. The configuration for $\phi_T = \phi_B = 0°$ in figure 8.13(a) has a thick separated region at the rear of the body. The optimal configuration (figure 8.13b) has a much thinner recirculation region. This thinning is responsible of the substantial drag reduction compared to that of the natural configuration. Nevertheless, the inclination of both flaps creates two pairs of intense longitudinal vortices which are sources of additional drag.

[3]The evolutions $\mathcal{C}_2$ are negligible for $\phi_T \approx 9.2°$ in front of the ones of $\mathcal{C}_1$ and $\mathcal{C}_3$ (see figure 8.12).

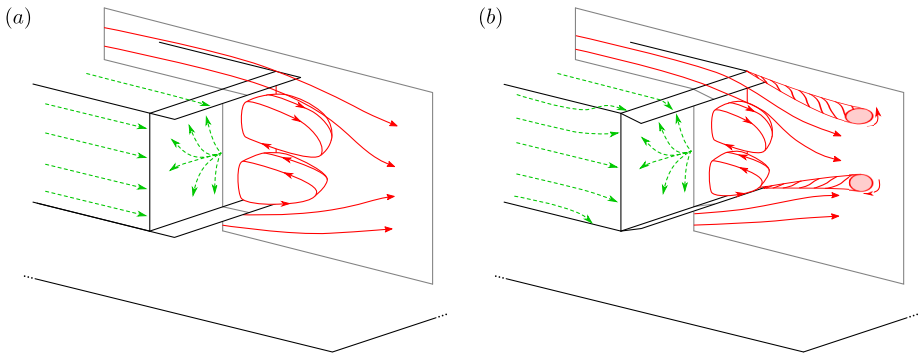

Figure 8.13. Sketch of the flow topologies for the configuration $\phi_T = \phi_B = 0°$ (a) and for the optimal drag configuration (b).

8.4 Concluding remarks

The inclination of two small flaps downstream of the top and bottom faces of the square-back Ahmed geometry is proved to affect the drag, the lift as well as the flow topology. When the bottom flap is fixed, the lift and the drag are respectively 1^{st} and 2^{nd} order polynomial functions of the top flap angle. This leads to a quadratic dependence between the drag and the lift. Such a drag *vs.* lift relationship is self similar for five different angles of bottom flap. In the bidimensional domain (ϕ_T, ϕ_B), the lift is in good agreement with an affine function of ϕ_T and ϕ_B. On the other hand, the drag can be expressed by a second order polynomial of ϕ_T and ϕ_B plus a term proportional to $\phi_T\,\phi_B$. This coupling term shows that the optimal top slant angle relies on the bottom flap orientation and the minimum of drag cannot be achieved from independent optimization on the two slant angles.

From these results, a classification of three drag sources is suggested. First, the linear term quantifies the interest of having a thin wake to limit the pressure drag from the base. A second term corresponds to a notion of induced drag directly linked to the lift force introduced by the flaps. However, these two drag contributors are not sufficient to explain the whole drag and a contribution associated with the local development of streamwise vortices from the side edges of the flaps is identified.

The presence of terms of induced drag points out the interest of having a certain axisymmetry in the recirculation region, at both global and local scales. As in chapter 7, the benefits of having a global top – bottom symmetry is evidenced by the quadratic dependence between the drag and the lift. In parallel, these experiments prove that part of the drag may also be related to local phenomena such as the formation of concentrated streamwise vortices.

Before studying the flow past real vehicles in part III, similar experiments are now considered at industrial scales in chapter 9.

Chapter 9

From laboratory to industrial scales

Confidential until December 2018

Part III

Road vehicle geometries

Chapter 10

Characterization of the flow over real vehicles

Most of these results are published in Grandemange *et al.* (2014). The experiments are performed in the context of the CNRT R2A[1].

This chapter aims at clarifying the flow around two different vehicles with a blunt rear-end: a commercial van and a compact crossover. It describes the flow separations and the global mode dynamics in the wake of these cars. In parallel, general characteristics of vehicle wakes are presented in appendix B using cavitation techniques.

Abstract

Using the same industrial wind tunnel as in chapter 9, two different cars with blunt afterbodies are now studied at a Reynolds number of 4 10^6. The boundary layers and the pressure distribution around the body are first characterized. Then, the wake is investigated through pressure and velocity measurements. Similar properties are obtained for both vehicles; in particular the lowest pressure on the afterbody is reported on the lower part of the base. In parallel, hot-wire anemometry is used to depict the dynamics of the flow. The detached shear layer from the roof behaves as a free shear flow whereas the flow from the underbody rather corresponds to an homogeneous shear flow. Additionally, periodic dynamics are reported in the wake of one vehicle; they are associated with an antisymmetric coupling of the lateral mixing layers. Hence, these results improve the general comprehension of vehicle wakes before the approach of flow control presented in chapter 11.

Contents

[1] http://www.cnrtr2a.asso.fr

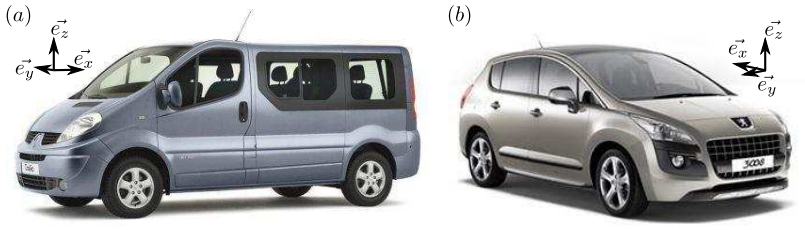

Figure 10.1. Pictures of the vehicles: Renault Trafic (a) and Peugeot 3008 (b).

10.1 Experimental setup

The flows past two different vehicles with blunt afterbodies are investigated: a Renault Trafic and a Peugeot 3008 (see figure 10.1). The first geometry is a commercial vehicle so its cubic afterbody is related to its function. The originality of its shape is the small hump at the junction between the windshield and the roof, just above the heads of the front passengers. The second vehicle has also a blunt afterbody but its general shape is more streamlined, in particular regarding the inclination of the roof.

As in chapter 9, the experiments are performed in the full-scale aeroacoustic wind tunnel of the GIE S2A[2] at Montigny-Le-Bretonneux (see Waudby-Smith *et al.*, 2004, for description of the tunnel). The test section is a 3/4 open jet with a cross-section of 24 m^2. Four wheel spinners and a central rotating belt enable to operate under road conditions. The inlet and moving belt velocities are set at 33.3 m s^{-1}. The Reynolds number based on the height of the vehicles is close to 4 10^6.

The coordinate system is defined as $\vec{e_x}$ oriented along the free-flow direction, $\vec{e_z}$ in the vertical direction and $\vec{e_y}$ forming a direct coordinate system. The origin is set on the floor in the middle of the vehicles in the y direction and at the maximum x coordinate of the vehicle. Δi is the algebraic distance in the i direction to a given reference point as the separation from the roof or a surface.

The pressure distributions on the vehicles are obtained using parietal pressure taps. In the flow, a 18 hole probe mounted on a three-axis robot gives the mean velocities U_x, U_y and U_z as well as the static pressure. Automatic displacements record these data in iso-x, iso-y or iso-z planes.

The displacement system can also support a hot-wire probe system. The velocity u_{xz} is measured with a time resolution better than 1 kHz wherever wanted around the vehicles. Velocity signals are recorded during several minutes and power spectra are time averaged over windows of 1 s or 10 s depending on the signal duration.

[2]http://www.soufflerie2a.com/en

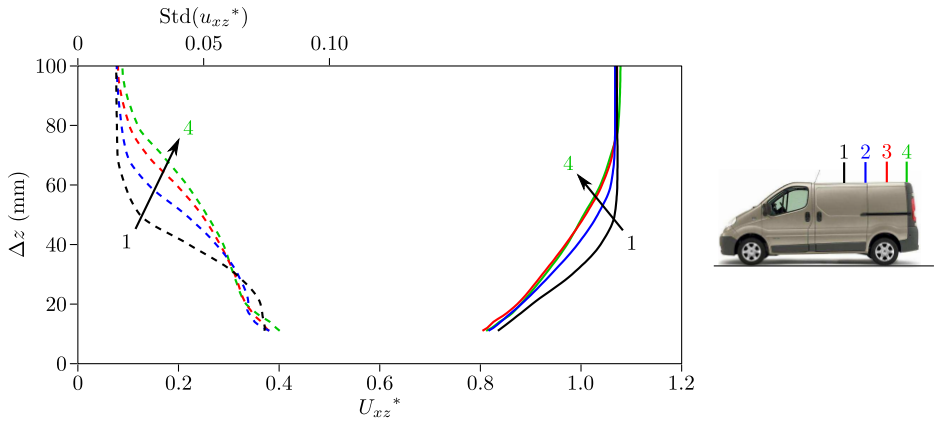

Figure 10.2. Mean (continuous lines) and fluctuating (dashed lines) velocity profiles of the boundary layer on the roof of the Renault Trafic in the plane $y = 0$ m: $\Delta x = -1.5$ m, black lines; $\Delta x = -1.0$ m, blue lines; $\Delta x = -0.5$ m, red lines; $\Delta x = -0.15$ m, green lines. Δx and Δz are the algebraic distances to the roof end and to the roof surface respectively.

	Renault Trafic			Peugeot 3008		
Δx (mm)	$\delta_{0.99}$ (mm)	δ_1 (mm)	δ_2 (mm)	$\delta_{0.99}$ (mm)	δ_1 (mm)	δ_2 (mm)
-1500	46 ± 0.5	9.5 ± 0.2	5.3 ± 0.2	–	–	–
-1000	58 ± 0.5	11.0 ± 0.2	6.4 ± 0.2	32 ± 0.5	7.3 ± 0.2	3.4 ± 0.2
-500	69 ± 0.5	12.2 ± 0.2	7.4 ± 0.2	47 ± 0.5	8.7 ± 0.2	4.6 ± 0.2
-150	74 ± 0.5	12.6 ± 0.2	7.7 ± 0.2	–	–	–
-50	–	–	–	73 ± 0.5	13.6 ± 0.2	7.8 ± 0.2

Table 10.1. Boundary layer thicknesses on the roof of the Renault Trafic and on the Peugeot 3008 in the plane $y = 0$ m and $y = 0.12$ m respectively: $\delta_{0.99}$, thickness based on 99% of free-stream velocity; δ_1, displacement thickness; δ_2, momentum thickness.

10.2 Wall boundary layers

The boundary layers are characterized using the hot-wire probe mounted on the displacement system. Four profiles on the roof in the plane $y = 0$ m are presented in figure 10.2 at 0.15, 0.5, 1.0 and 1.5 m upstream of the end of the roof of the Renault Trafic. The corresponding results on the Peugeot 3008 are plotted in figure 10.3. The characteristic thicknesses are listed in table 10.1; the data close to the wall, that are missing to calculate δ_1 and δ_2, are estimated from cubic interpolation adding the point ${U_{xz}}^* = 0$ at $\Delta z = 0$ m. To avoid the proper wake of the antenna on the Peugeot 3008, the measurements are systematically performed in the plane $y = 0.12$ m rather than at $y = 0$ m.

The boundary layers just upstream of the roof separation have very similar characteristic thicknesses ($\delta_{0.99} \approx 70$ mm) but the associated evolutions are distinct. The boundary layer has a linear growth on the Renault Trafic while it grows much faster on roof of the Peugeot 3008. This is certainly due to the difference in the roof inclinations: the Renault Trafic has an horizontal roof whereas the Peugeot 3008 presents a streamlined shape inducing an adverse pressure gradient along the roof. There may also be a role of the roof roughness of the Renault Trafic since it is made of corrugated metal.

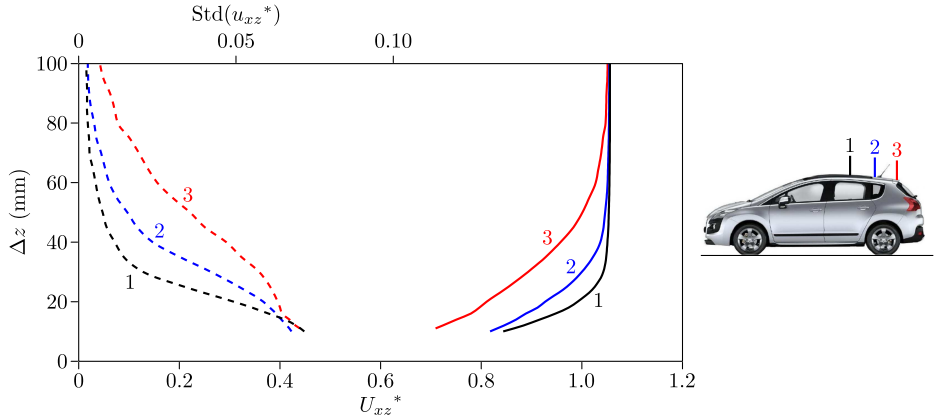

Figure 10.3. Mean (continuous lines) and fluctuating (dashed lines) velocity profiles of the boundary layer on the roof of the Peugeot 3008 in the plane $y = 0.12$ m: $\Delta x = -1.0$ m, black lines; $\Delta x = -0.5$ m, blue lines; $\Delta x = -0.05$ m, red lines. Δx and Δz are the algebraic distances to the roof end and to the roof surface respectively.

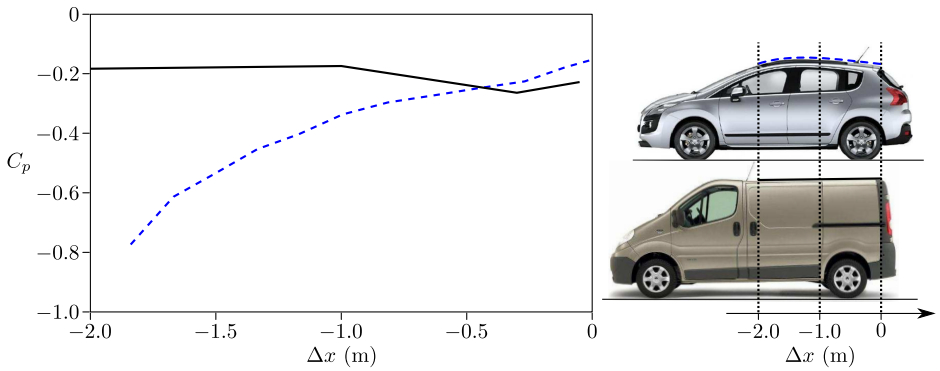

Figure 10.4. Static pressure on the roof of the Renault Trafic (continuous line) and of the Peugeot 3008 (dashed line). Δx is the algebraic distance to the roof end.

The distributions of static pressure on the roof are shown in figure 10.4 for both vehicles. On the Renault Trafic, the static pressure is constant in the range -2 m $< \Delta x < -1$ m. Then, there is a decrease followed by an increase of pressure just before the massive separation at the roof end. This evolution is probably related to the chamfered shape of the roof end as discussed in chapters 8 and 9. A similar evolution is observed on the sides of this commercial vehicle[3]. On the contrary, there is a regular increase of pressure from the windshield to the roof end on the Peugeot 3008. The inclination of the roof leads to a decrease of velocity in the potential flow which results in pressure recovery.

Now that the flow characteristics upstream of the afterbody separation are presented, section 10.3.1 is devoted to the study of the near wake.

[3]The associated measurements are not presented here.

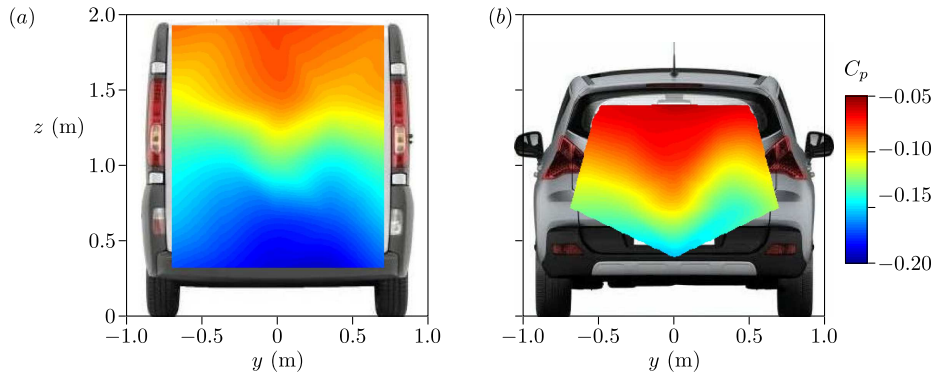

Figure 10.5. Static pressure on the base of the Renault Trafic (a) and of the Peugeot 3008 (b).

10.3 Mean properties of the near wake

10.3.1 Base pressure

Parietal pressure sensors are placed on the rear part of the vehicles to get the pressure distribution displayed in figure 10.5. The pressure levels on the two vehicles have a similar repartition. The average levels are slightly larger on the base of the Peugeot 3008 than on the one of the Renault Trafic. This is consistent with the fact that the flow separates with a higher pressure in the Peugeot 3008 due to the roof shape (see figure 10.4). Measurement are almost independent of y whereas there are important gradients in the z direction ($\partial c_p/\partial z^* \approx 0.15$). The pressure in the upper region of the base is close to -0.05, there is a continuous decrease of pressure up to almost -0.20 at the lower part of the base.

These low values may result from the underbody roughness and from the ground presence. They also remind the development of the z instability in the wake of parallelepiped bodies in chapter 6. To argue on this point, distributions of pressure and velocities in the recirculating flow are now considered in section 10.3.2.

10.3.2 Recirculation region

The wake topologies are obtained in the planes $y = 0$ m and $x = 1.0$ m for the Renault Trafic and in the planes $y = 0.12$ m and $x = 0.5$ m for the Peugeot 3008.

The distributions of pressure in the iso-y planes are shown in figure 10.6. The low pressure regions close to the base are clearly visible. As expected from the pressure measurements on the base of the vehicles, the pressure levels in the recirculation region strongly depend on z. Further downstream, the pressure coefficient increases to reach positive values after the recirculation closure as past simplified geometries.

The associated flow velocities in the iso-y planes are presented in figure 10.7. On both vehicles, the pressure gradient in the z direction is associated with a diagonal recirculating flow. In average, the recirculation bubble is fed by the flow coming from the underbody. This point is confirmed by the streamlines in the cross-flow planes in figure 10.8: inside the recirculating flow marked by the iso-contour ${U_x}^* = 0$, the streamlines in the planes iso-x are vertical, *i.e.* $U_y \ll U_z$. In addition, the contours of U_x preserves roughly the shape of the base. The main difference lies in the reduced height of the wake of the Peugeot 3008

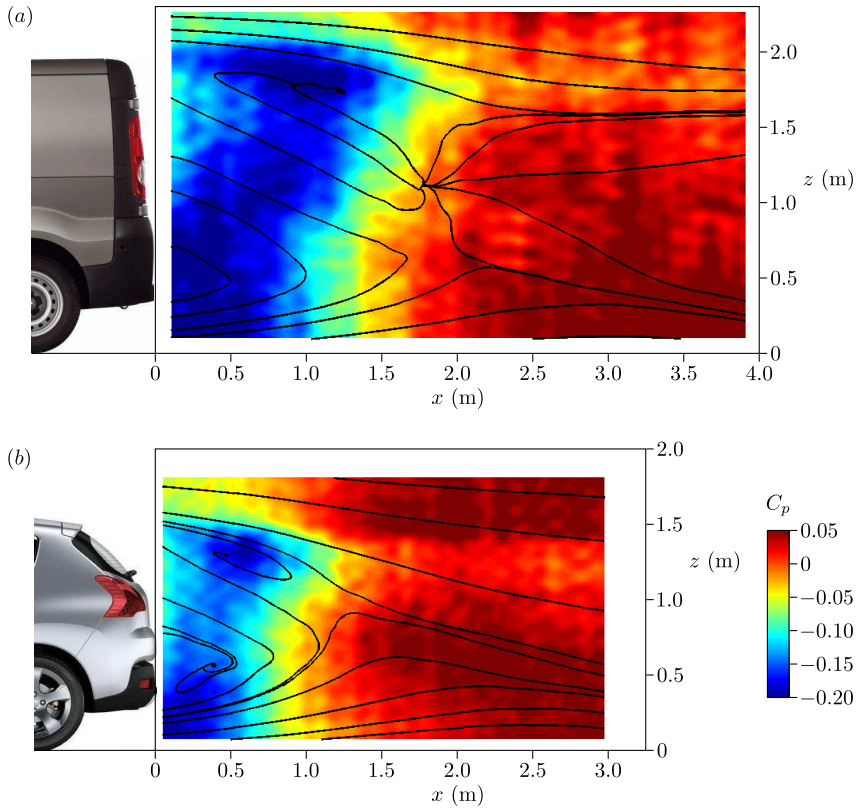

Figure 10.6. Static pressure and streamlines in the wake of the Renault Trafic in the plane $y = 0$ m (a) and of the Peugeot 3008 in the plane $y = 0.12$ m (b).

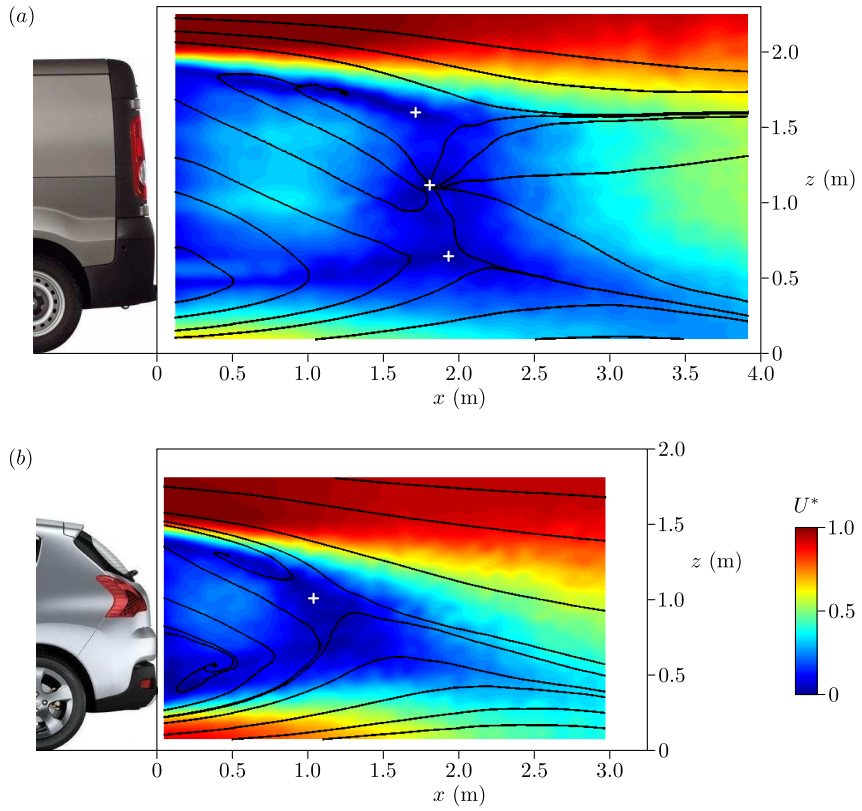

Figure 10.7. Velocity in the wake of the Renault Trafic in the plane $y = 0$ m (a) and of the Peugeot 3008 in the plane $y = 0.12$ m (b). The crosses locate the stagnation points.

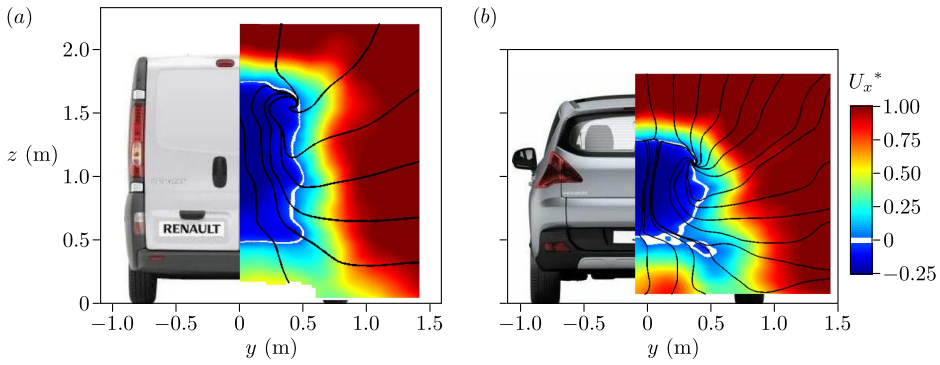

Figure 10.8. Velocity in the wake of the Renault Trafic in the plane $x = 1$ m (a) and of the Peugeot 3008 in the plane $x = 0.5$ m (b).

as the flow separates with an approximate angle of 8° referring to the streamwise direction due to the inclination of the roof (compare figures 10.8*a* and 10.8*b*). On the contrary, the separations occur rather aligned to the streamwise direction on the side and bottom faces of the Peugeot 3008 and on the four faces of the Renault Trafic.

Only half cross-flow planes are presented but the result is not expected to be perfectly symmetric since the vehicles do not strictly respect the reflectional symmetry of plane $y = 0$ m: air cooling of the engine, underbody roughness... In addition, even if not observed during these experiments, cases of reflectional symmetry breaking may appear as presented in parts I and II. Moreover, it is interesting to note the three stagnation points at $x \approx 1.8$ m downstream of the Renault Trafic in figure 10.7(a). There are two saddle points at $z = 0.65$ m and 1.55 m and one source point at $z = 1.1$ m, whereas the Peugeot 3008 has classically one saddle point at $x = 1.1$ m and $z = 1$ m (see figure 10.7b). The former wake organization might correspond to a bistable behavior in the z direction as presented in chapter 6. However, such a phenomenon is not identified here and the presence of the two saddle points may rather rely on the intrusion of the probe mounted on the displacement system.

10.3.3 Mixing layer developments

In order to characterize the differences in the flow coming from the roof and the underbody, hot-wire measurements are performed in the top and bottom mixing layers. Velocity profiles at different streamwise positions are measured and the location of the mixing layer is marked in the z direction by the contours z_α defined as

$$U_{xz}(x, z_\alpha) = \alpha\, U_0. \tag{10.1}$$

As in section 1.2.1, the size of the mixing layer δ_m is deduced as

$$\delta_m = |z_{0.9} - z_{0.1}|. \tag{10.2}$$

At a given x, the position of the maximum of the velocity fluctuations is denoted by z_{rms} and verifies

$$\mathrm{Std}\left(U_{xz}(x, z_{rms})\right) = \max_z \left(\mathrm{Std}\left[U_{xz}(x, z)\right]\right). \tag{10.3}$$

First, the mixing layer downstream of the roof is considered. In figure 10.9, its growth is almost linear at least up to 1 m downstream of the separation. The growth rate $\mathrm{d}\delta_m/\mathrm{d}x$ is respectively measured at 0.14 and 0.12 for the upper mixing layer of the Renault Trafic and of the Peugeot 3008. This linear growth is a characteristic of free shear turbulent flows (Champagne *et al.*, 1976; Dimotakis, 1991) where the growth rate depends on the state of the flow at the separation and usually ranges between 0.1 and 0.2. The second common characteristic with turbulent free shear flows is that the mixing layer spreads preferentially into the low velocity region (Pope, 2000). In figure 10.9 the contour of $z_{0.9}$ is roughly parallel to the potential flow, *i.e.* along the x direction on the Renault Trafic and slightly oriented due to the inclination of the roof on the Peugeot 3008. Past approximately 0.2 m downstream of the separation from the roof, the contour $z_{0.5}$ is located right between $z_{0.1}$ and $z_{0.9}$ so that the vorticity, initially concentrated near the wall, spreads rapidly to reach

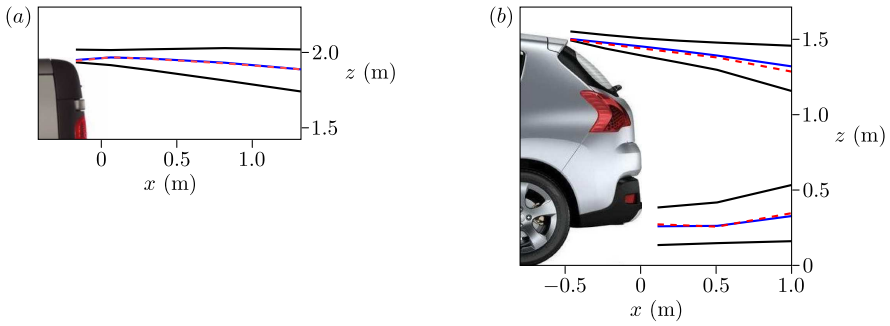

Figure 10.9. Positions of the contours $z_{0.1}$ and $z_{0.9}$ (back lines), $z_{0.5}$ (blue lines) and z_{rms} (dashed red lines) in the mixing layers of the Renault Trafic (a) and of the Peugeot 3008 (b).

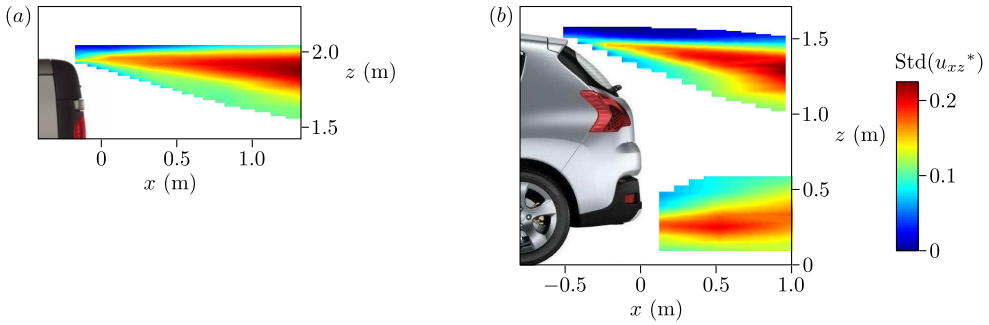

Figure 10.10. Velocity fluctuations in the mixing layers of the Renault Trafic (a) and of the Peugeot 3008 (b).

a symmetric distribution along the mixing layer. It is observed that the curves of z_{rms} and $z_{0.5}$ are superimposed so that the activity of the mixing layer is maximal in the middle of the shear layer. This point is clarified by the spatial distribution of the velocity fluctuations plotted in figure 10.10.

Similar measurements are performed in the mixing layer from the underbody of the Peugeot 3008. The size of the mixing layer is close to the ground clearance partially due to the underbody roughness and to the evacuation of the flow from the engine cooling. The growth is not linear but the expansion remains oriented toward the recirculation region. The mixing layer activity is equally centered on $z_{0.5}$ and the intensity of the velocity fluctuations is slightly lower than the one measured in the upper mixing layer. In the wake of the Renault Trafic, figure 10.7(a) points out that the velocity is reduced right downstream of the underbody and that vorticity is homogeneous over the ground clearance.

The autopower spectra of the velocity signals in the upper mixing layers at z_{rms} are presented in figure 10.11 for different streamwise positions. They all show an almost constant distribution of energy corresponding to the large-scale structures of turbulence below a characteristic frequency $f_{LS/I}$ (10 Hz to 50 Hz depending on x). Then, the distribution of energy decreases with a $-5/3$ power law as expected by the Kolmogorov theory for the inertial range of an homogeneous and isotropic turbulence.

Studying the evolution in the streamwise direction, the results in figure 10.11 show that

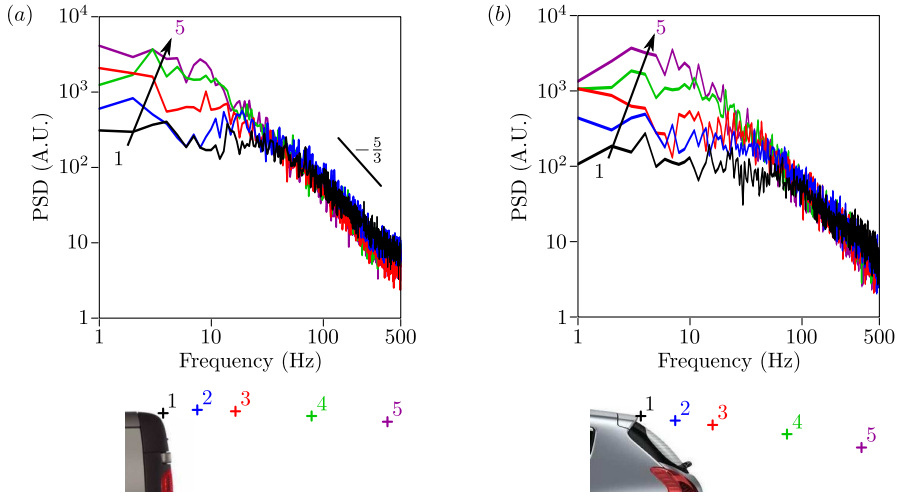

Figure 10.11. Autopower spectra in the mixing layer from the roof of the Renault Trafic (a) and of the Peugeot 3008 (b) at the maximum of fluctuating velocities at $\Delta x = 0.02$ m (black line), $\Delta x = 0.25$ m (blue line), $\Delta x = 0.5$ m (red line), $\Delta x = 1.0$ m (green line) and $\Delta x = 1.5$ m (purple line). Δx is the algebraic distances to the roof end.

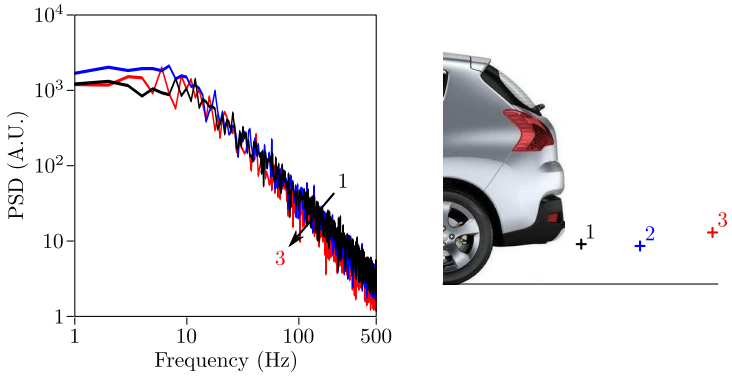

Figure 10.12. Autopower spectra in the mixing layer from the underbody of the Peugeot 3008 at the maximum of fluctuating velocities at $x = 0.1$ m (black line), $x = 0.5$ m (blue line) and $x = 1.0$ m (red line).

the characteristic frequency of the spectra $f_{LS/I}$, separating the large scales and the inertial ranges, decreases as x increases. This indicates that this frequency is based on the local thickness of the mixing layer: $f_{LS/I} \sim U_0/\delta_m$ which is also a characteristics of free shear turbulent flows (Hussain & Zaman, 1985).

The autopower spectra from the bottom mixing layer visible in figure 10.12 present the exact same repartition of energy but the characteristic frequency $f_{LS/I} \approx 10$ Hz is now independent of x. Then, the size and activity of the mixing layer right downstream of the underbody is similar to the one from the roof but at 1 m downstream of the separation. In parallel, these two regions where the mixing layers become unstructured correspond to the locations where the pressure is minimal in the wake (see figure 10.6).

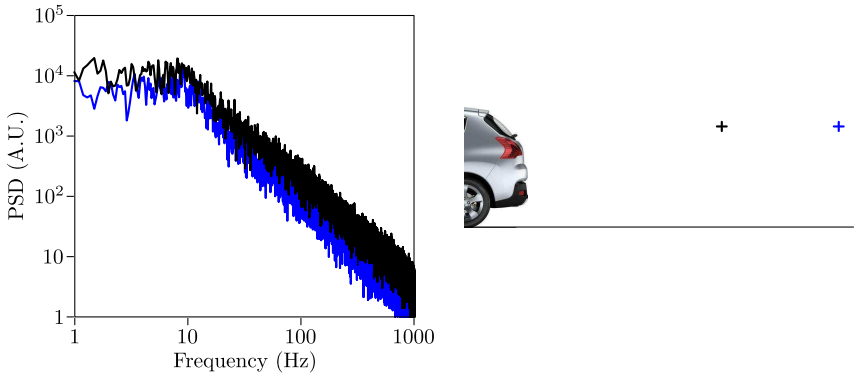

Figure 10.13. Autopower spectra in the wake of the Peugeot 3008 at $x = 2.5$ m, $y = 0$ m and $z = 1.3$ m (black line) and at $x = 4.0$ m, $y = 0$ m and $z = 1.3$ m (blue line).

10.4 Periodic dynamics of the wake

The presence of a synchronized dynamics, *i.e.* oscillating global modes, is now studied in the wake of these two vehicles.
In the flow over the Peugeot 3008, no peak of energy is reported in the spectral repartition of energy. Wherever the probe is located, the results are similar to the ones presented in figure 10.13. As for spectra in the mixing layer detailed in section 10.3.3, there is a characteristic frequency $f_{LS/I} \approx 10$ Hz at the inception of the inertial range of turbulence. Note that $f_{LS/I}$ is always measured around 10 Hz except in the near wake mixing layers as presented in figure 10.11(b). Hence, this value of 10 Hz appears to be the frequency associated with the large-scale structures of turbulence of the whole wake.

On the contrary, in the flow past the Renault Trafic, some periodic motions of the wake are reported. Indeed, the autopower spectra of the velocity signals at $x = 4.0$ m, $y = \pm 0.3$ m and $z = 1.0$ m present peaks of energy at $f_m = 4$ Hz (see figure 10.14a). To detail the structure of this mode, cross-correlations between these two simultaneous signals are performed. They show that the coherence reaches 0.7 at 4 Hz and corresponds to an antisymmetric mode in the y direction since the signals are in phase opposition at this frequency. Only 0.6 m separate the probes, which could seem small compared to the vehicle width, but this corresponds to the wake width at this streamwise location. Once normalized by W, f_m corresponds to a Strouhal number of $\mathrm{St}_{Wm} = fW/U_0 \approx 0.2$.

Autopower spectra even much closer to the base at ($x = 0.4$ m, $y = 0.7$ m, $z = 1.8$ m) and ($x = 0.4$ m, $y = -0.7$ m, $z = 1.8$ m) report the same periodic structure at $f_m = 4$ Hz with a coherence close to 0.5 in phase opposition (see figure 10.15). Thus, f_m being constant in space, this peak of energy corresponds to a global phenomenon. However, it is not reported everywhere in the wake. For example, the autopower spectra and the cross-correlation analyzes performed at $x = 2$ m could easily measure a lateral or a vertical oscillation of the wake at the end of the recirculation; nevertheless, they do not report any significant coherent motion (see figures 10.16 and 10.17). In figure 10.16(a), a slight increase of energy is measured around f_m at $x = 2.0$ m, $y = 0$ m and $z = 1.8$ m but it is not as clear as in figures 10.14 and 10.15. As a result, this mode seems to develop from the interaction of the lateral mixing layers mostly from the upper part of the vehicle. Then, it persists downstream and is particularly visible at $x = 4$ m which corresponds to two times the

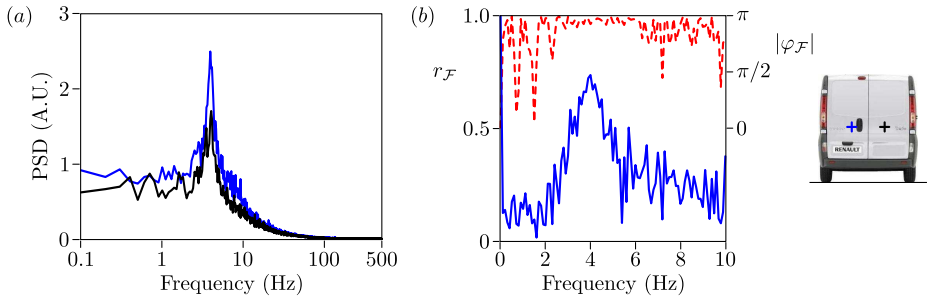

Figure 10.14. (a) Autopower spectra in the lateral mixing layers from the Renault Trafic at ($x = 4.0$ m, $y = 0.3$ m, $z = 1.0$ m) (black line) and at ($x = 4.0$ m, $y = -0.3$ m, $z = 1.0$ m) (blue line). (b) Correlation (left scale, continuous line) and phase (right scale, dashed line) between the two velocity signals.

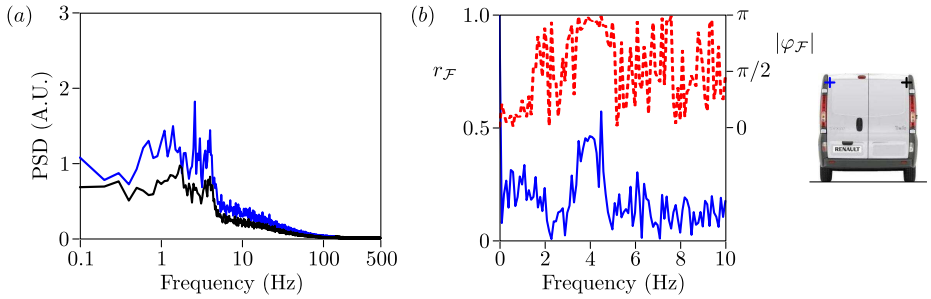

Figure 10.15. (a) Autopower spectra in the lateral mixing layers from the Renault Trafic at ($x = 0.4$ m, $y = 0.7$ m, $z = 1.8$ m) (black line) and at ($x = 0.4$ m, $y = -0.7$ m, $z = 1.8$ m) (blue line). (b) Correlation (left scale, continuous line) and phase (right scale, dashed line) between the two velocity signals.

characteristic width or height of the vehicle. The exploration of the envelop of this mode in the wake is very difficult to achieve since the resolution of the activity at 4 Hz requires spectral analyses over windows of 10 s. In addition, to get converged distribution of energy, the averaging denoted $\langle ... \rangle_{\mathcal{W}}$ needs to be performed over a sufficient number of windows so that each velocity signal is recorded over at least 500 s which is an important cost regarding the use of this industrial wind tunnel.

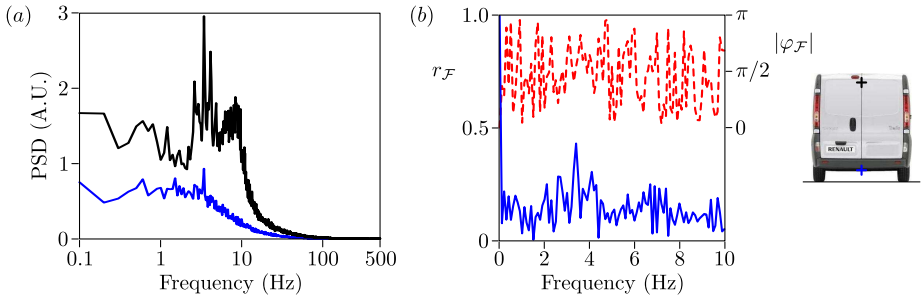

Figure 10.16. (*a*) Autopower spectra in the top and bottom mixing layers from the Renault Trafic at ($x = 2.0$ m, $y = 0$ m, $z = 1.8$ m) (black line) and at ($x = 2.0$ m, $y = 0$ m, $z = 0.2$ m) (blue line). (*b*) Correlation (left scale, continuous line) and phase (right scale, dashed line) between the two velocity signals.

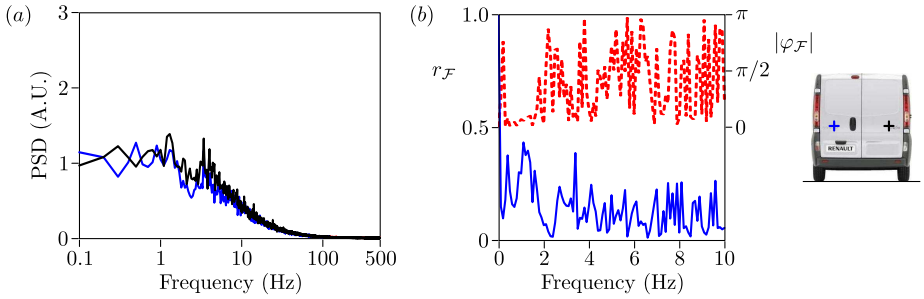

Figure 10.17. (*a*) Autopower spectra in the lateral mixing layers from the Renault Trafic at ($x = 2.0$ m, $y = 0.5$ m, $z = 1.0$ m) (black line) and at ($x = 2.0$ m, $y = -0.5$ m, $z = 1.0$ m) (blue line). (*b*) Correlation (left scale, continuous line) and phase (right scale, dashed line) between the two velocity signals.

10.5 Concluding remarks

The flow around two different blunt vehicles is characterized at Reynolds number $4\ 10^6$. First, the development of the boundary layers on the roof is depicted; it depends on the inclination of the roof that drives the pressure gradient along the vehicle. Then, a massive recirculation responsible for a large part of the drag is reported on the base. The mean recirculating flow is highly dependent on the z direction, in particular the low pressure region is located close to the bottom part of the base whereas it has a reduced impact on the pressure on the top part. This may be explained by the differences between the upper and lower mixing layers: the upper one presents the characteristics of free shear flows in opposition to the mixing layer from the underbody. The spectral analyses also indicate the presence of a lateral oscillation of the wake but only past the Renault Trafic. However, this mode is not particularly energetic so its impact on the base pressure is certainly limited.

These experiments confirm some trends observed past simplified geometries. First, they provide examples of the benefits of the the control of the flow orientation at the afterbody separations. Then, they evidence that the correlation between the direction of the mean recirculating flow and the base pressure gradients still persists in real vehicle wakes. Finally, the hot-wire measurements prove that the large-scale periodic oscillations of the wake are negligible phenomena of the recirculation dynamics; so, their control does not seem to be a relevant lever of drag reduction.

As a consequence, these results may be used as a reference to orient the work on automotive drag reduction toward the control of the underbody flow in order to move the low pressure structure further downstream. A second control strategy could consist in reducing the growth rate of the mixing layer that should lead to base pressure recovery and increased recirculation length.

Now, leaving these drag reductions strategies for future work, some of the experiments of flow control presented past simplified geometries in parts I and II are extended to real vehicles in the next chapter.

Chapter 11

Bistable behaviors in vehicle wakes

Confidential until December 2018

Chapter 12

General synthesis and perspectives

This chapter concludes this thesis with a general synthesis. The main results exposed in parts I, II and III are discussed with a broader view. Then, some perspectives for future work are exposed with a particular focus on drag reduction strategies.

Abstract

The previous experiments analyze the wakes past different geometries, by increasing the complexity from axisymmetric bodies to real road vehicles. In addition, the dynamics of the flow over the squareback Ahmed geometry is considered over a large range of Reynolds numbers: from $\mathrm{Re}_H = 3.0\ 10^2$ to $2.5\ 10^6$. Whatever the complexity of the geometry, cross-flow instabilities are likely to develop in its turbulent wake; they appear to be reminiscences of the bifurcations that occur in the laminar regime. They are found for a wide range of geometrical parameters which extends the scope of this work beyond the study of road vehicle wakes. In addition, some periodic wake oscillations are reported. Nevertheless, they are far less energetic than past bidimensional bodies, so they are expected to have a negligible impact on drag. These unsteady global modes seem to weaken when either the Reynolds number or the complexity of the geometry increases. The study of these phenomena, combined with sensitivity analyses to small perturbations, places the minimization of the instantaneous wake asymmetries as a relevant strategy for drag reduction.

Contents

12.1 Development of stationary modes

One of the fundamental results of the present work is the description of stationary cross-flow instabilities in three-dimensional wakes. In laminar configurations, the amplification of the non-linearities with the Reynolds number leads to the appearance of stationary symmetry breaking regimes. Then, as the Reynolds number increases and the turbulence develops in the flow, the average topology is expected to restore the symmetries of the geometries in a statistical sense (Frisch, 1996).

All the presented results are consistent with this property of fully developed turbulence since the long time-averaged wakes in the turbulent regime always present the symmetries of the setup: axisymmetry in the cases of the sphere and the disk, $y^* = 0$ reflectional symmetry in the case of parallelepiped bodies[1]. However, traces of the symmetry breaking that occurs in the laminar regime persist at very high Reynolds numbers; the symmetries of the geometry are restored in the turbulent regime after the exploration of the different symmetry breaking positions. The sensitivity experiments show that a slight perturbation of the symmetry can lead to a clear preference towards one of the states. Consequently, even for a fully developed turbulence, the mean flow can be disproportionately asymmetric because of some residual asymmetries of the geometry.

A surprising property of this behavior lies in the time scale during which the flow remains in the same symmetry breaking state. Typically, the mean time of shift is two or three orders of magnitude larger than H/U_0 which is the characteristic time of the flow. The mechanisms responsible for such a long time evolution of the topology are still unclear and would benefit of additional experiments. Nevertheless, the randomness of the dynamics may be interpreted by a role of the rare but energetic large-scale structures of turbulence.

A general bifurcation scheme of the y instability is suggested in figure 12.1 through energy considerations: figures 12.1(a)–(b) show typical evolutions of ${y_W}^*$, the wake position in the y direction, and of the energy of the flow fluctuations as the Reynolds number increases. Figure 12.1(c) presents a three-dimensional representation. At very low Reynolds numbers, the wake is steady and symmetric; then, for $\mathrm{Re} > \mathrm{Re}_1$, a steady bifurcation leads to a permanent asymmetric state. In terms of energy, the disappearance of the centered state corresponds to a maximum of energy at ${y_W}^* = 0$; this forms a potential barrier of energy of amplitude $\mathcal{E}_{PB}$. In other words, Re_1 marks a transition: for $\mathrm{Re} < \mathrm{Re}_1$, the energy $\mathcal{E}$ against ${y_W}^*$ follows a U-shaped distribution with a stable state at ${y_W}^* = 0$ whereas for $\mathrm{Re} > \mathrm{Re}_1$, $\mathcal{E}({y_W}^*)$ presents W-shaped distribution with two off-centered stable states (see figure 12.1c). The flow being stationary, only the position ${y_W}^*$ located by the thick black lines are admissible. Then, for $\mathrm{Re} > \mathrm{Re}_2$, unsteady global modes are reported; they induce oscillations of ${y_W}^*$ around the asymmetric stables states (green admissible zones in figures 12.1a and 12.1c). However their energy, denoted $\mathcal{E}_{UGM}$, remains limited and may not be large enough to overcome the potential barrier at the center[2]. As soon as the transition to turbulence occurs at Re^T, a turbulent energy denoted $\mathcal{E}_T$ adds to $\mathcal{E}_{UGM}$. So, there may be a threshold of Reynolds number, denoted Re^B, over which

$$\mathcal{E}_T + \mathcal{E}_{UGM} > \mathcal{E}_{PB}.$$

Therefore, ${y_W}^* = 0$ becomes an admissible position of the instantaneous wake and now, the total energy is sufficient to allow topology shifts, at certain moments depending on available

[1] In the case of real vehicle wakes, the air cooling system and the underbody details introduce asymmetries in the y direction that may affect the reflectional symmetry of the mean flow.

[2] This is consistent with the absence of topology shift reported during the laminar experiments in chapter 4.

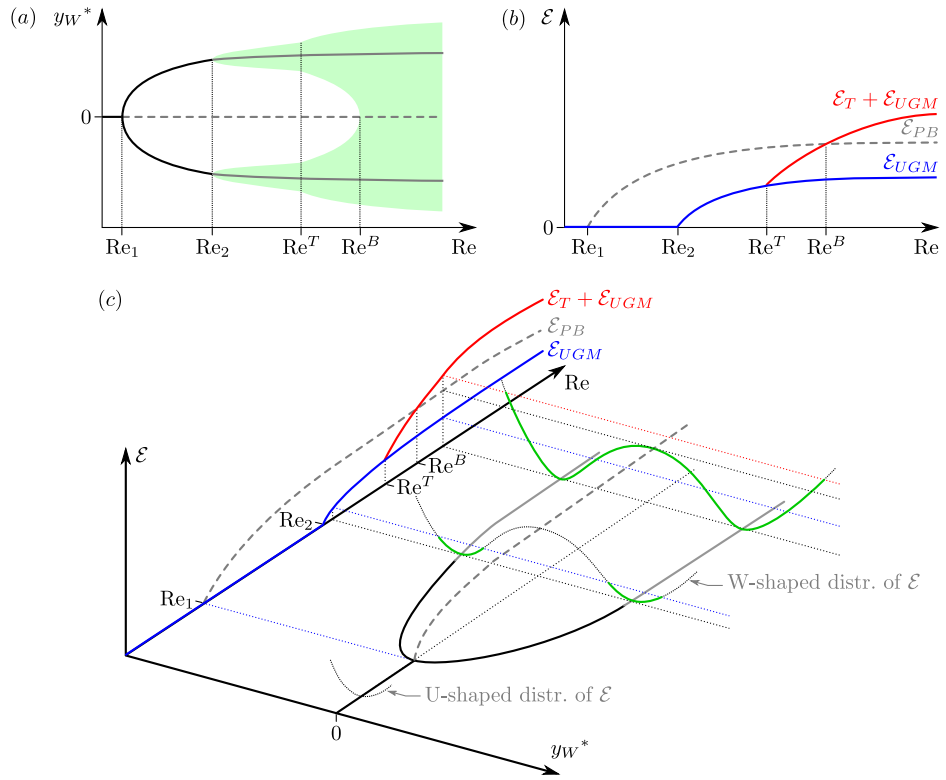

Figure 12.1. Bifurcation scheme of the y instability: bifurcation scenario in the domain (Re, y_{W^*}) (a), energy of the fluctuations as a function of Re (b) and three-dimensional representation (c). The black and gray lines are steady and unsteady regimes respectively, the continuous and dashed lines are stable and unstable regimes respectively. The green zones are admissible positions of the instantaneous wake given the available energy $\mathcal{E}_T + \mathcal{E}_{UGM}$ at the considered Reynolds number.

instantaneous energy. Consequently, for $\mathrm{Re} > \mathrm{Re}^B$, the bistable dynamics may be observed in the wake, the dynamics of the topology shifts being dependent on the turbulent activity.

At this stage, it is important to note that this interpretation of the y bi-stability is based on energy considerations and the important point is the comparison between $\mathcal{E}_{PB}$ and $\mathcal{E}_T + \mathcal{E}_{UGM}$. The trends plotted in figure 12.1(c) are certainly not realistic but the physical analyses are still sustainable. For example, $\mathcal{E}_T + \mathcal{E}_{UGM}$ is related to the energy of the flow so it is strongly linked to the transfers of momentum from the geometry to the fluid and necessarily to the drag of the body; thus, there is probably no change of slope at Re^T in the curve $\mathcal{E}_T + \mathcal{E}_{UGM}$.

The existence of these symmetry breaking states and the associated long time evolutions are of crucial interest in the study of three-dimensional turbulent wakes. As mentioned in the conclusions of chapter 5, it has strong consequences for both experimental and numerical work. A particular attention must be paid to the duration of the acquisition and the spatial distribution of the sensors in experiments. On the other hand, a limited time simulation or basic turbulence modeling could lead to significant errors in the evaluation of the mean flow.

Finally, these experiments show that the bistable phenomena are not isolated cases in

three-dimensional turbulent wakes; they are reported past basic bodies up to industrial geometries. It could be interesting to extend the domains of appearance of these cross-flow instabilities to other geometries such as elliptical shapes. Furthermore, it is found that cross-flow instabilities appear in the wake of a wall mounted three-dimensional geometry (see region $\mathcal{D}y_2$ in figure 6.11*a*) so it may equally develop in free-surface flows. Hence, it could be of critical interest in the naval industry for the hull wakes. Additional studies may provide useful data exploring the impact of the geometry of the submerged part of the ship and the dependence on the Froude number. In these experiments the development of the instabilities are independent of the free-stream velocity but it might not be the case once the gravity effects are no more negligible. As a consequence, it could be interesting to evaluate how much these instabilities are sensitive to the deformation of the free surface.

Now, before addressing the drag related to the development of these cross-flow instabilities in section 12.3, section 12.2 gives a synthesis of the periodic wake motions.

12.2 Dynamics of the oscillating modes

The second widespread phenomenon observed in these experiments is the development of unsteady global modes. In particular, the dependences on both the Reynolds number past a given geometry and the complexity of the geometry can be considered from these different studies. Note that these discussions are ascribed to fixed flow separations: the possible drag-crisis transitions are not taken into account.

On the Reynolds number

The results obtained in the sphere wake give a first insight of the impact of an increase in Reynolds number on the periodic dynamics of the wake. Autopower spectra presented in figure 2.8 for different Reynolds numbers point out a gradual attenuation of the mode activity from $\mathrm{Re}_D = 1.4\ 10^4$ to $5.3\ 10^4$.

Then, in part II, the wake past the Ahmed reference geometry is considered over a very wide range of Reynolds numbers: from $\mathrm{Re}_H = 3.0\ 10^2$ to $2.5\ 10^6$, *i.e.* over four orders of magnitude. At very low Reynolds numbers, the viscous effects prevent the development of unsteady modes but over $\mathrm{Re}_H = 340$ the wake starts oscillating in the vertical direction[3] as visible in figure 4.2(*b*). In such a wake, the periodic motion is clear and the energy of the flow fluctuations in the spectral domain is expected to concentrate at the shedding frequency. This implies that the oscillating global mode is highly coherent at low Reynolds numbers. When the wake becomes turbulent, the wake oscillation in the vertical direction is still reported but with a reduced level of coherence (see chapter 5).

As a consequence, for a given geometry, it seems that the larger the Reynolds number, the less the oscillating global modes contribute to the energy of the fluctuations in the flow.

This experimental fact might be interpreted as follows. The development of the instabilities associated with the oscillating global modes is closely related to the distribution of vorticity in the flow. Now, the turbulent structures of the scale of the shear layer may alter the orientation of the vorticity. As there is no production of vorticity after detachment, the turbulent activity redistributes the instantaneous vorticity from its initial direction to the two others. Indeed, it is well-known that turbulence produces vortices aligned to the local stretching direction in the fluid. These dynamics certainly lead to a gradual decrease of the mean vorticity in the shear layers during its convection. Thus, an increase in the turbulent activity in the early shear layers is likely to lead to a diminution of the spatial coherence of the vorticity and so to less energetic unsteady modes.

In parallel, this observation helps understand why the unsteady modes past three-dimensional geometries are generally less energetic than the ones past bidimensional bodies. Indeed, the vorticity emitted at the base separation of a three-dimensional afterbody naturally presents a lower spatial coherence. In the case of the Ahmed geometry for example, the characteristic length of the spatial coherence (H for the lateral shear layers, W for the upper and lower ones) is only of the order of the distance between the facing mixing layers.

Such an analysis naturally leads to the study of the effect of an increase in complexity of the geometries that is now detailed.

[3]The corresponding topology is not the stable solution but this does not affect the following analyses.

On the complexity of the geometries

The global mode dynamics are studied in three-dimensional wakes from basic axisymmetric configurations to real vehicle shapes. Before considering the spatial structure of the modes, it is worth noting that the increase in complexity of the geometry necessarily alters the spatial coherence of the vorticity at separation. Therefore, as discussed in the previous section, it is very likely to reduce the intensity of the unsteady global modes.

The experiments presented in part I and II depict the evolution of the structures of the unsteady global modes from the well-known case of the shedding past axisymmetric bodies to the shedding past bodies of various aspect ratios and wall effects.

The aspect ratio of the base appears essential in the spatial organization of the unsteady global modes. For axisymmetric geometries, the periodic motions are associated with the shedding of hairpin-shaped vortex loops. However, as soon as the aspect ratio of the base is not equal to 1, two different frequencies are reported in the wake and the spatial organization of the corresponding structures becomes more complex. In the case of the Ahmed reference geometry, each frequency corresponds to a coherent motion in one cross-flow direction (see figure 5.28). The combination of the two modes is very likely to form a wake dynamics that could appear chaotic in the time domain (see figure 4.2*d*). In addition, the localization of the global mode activity may depend on the development of the stationary cross-flow instabilities discussed in section 12.1. So, quantitative studies in the laminar regime could be of valuable interest for the comprehension of the flow dynamics. In particular, it might be useful to study the interactions between two modes of different frequencies f_1 and f_2. For example, if $f_1 \sim f_2$, then nonlinear interactions between the modes may lead to the appearance of a very low frequency dynamics at $|f_1 - f_2|/2$. This could be an explanation of the pumping mode that is sometimes reported in the literature at the end of the recirculation bubble.

In parallel, the presence of the ground seems to have a stabilizing effect on the development of the unsteady global modes as shown in figure 4.6: as the ground clearance diminishes, the threshold of appearance of the unsteady regimes is increased. As in the experiments of Ruiz *et al.* (2009), the wall proximity seems to reduce the intensity of the mode in the direction normal to the wall (compare the amplitude of the peaks at $\mathrm{St}_H = 0.127$ and 0.174 in figure 5.22*a*). A gradual evolution of the phase shift between the structures shed from the upper and lower parts of the wake is equally reported because the vortex loops are convected at different speeds. Furthermore, in presence of a z instability in the wake, the flow orientation is highly dependent on the ground clearance (see figure 6.5*b*). Consequently, the spatial organization of the unsteady global mode in the z direction, when one is present, is expected to present a strong dependence on the ground clearance.

As a conclusion, it appears that future work studying the structures of the unsteady global modes, even in the laminar regime, could provide valuable information for the understanding of the periodic wake dynamics.

12.3 Flow control for drag reduction

The general description of both steady and unsteady global modes given in sections 12.1 and 12.2 allows to address issues on the pressure drag ascribed to the wake. For a fixed orientation of the flow at separation, *i.e.* for a given bluffness, the base pressure is linked to the recirculation length: the longer the recirculation bubble, the higher the base pressure and the lower the drag. Therefore, the development of efficient strategies for drag reduction relies on the preliminary identification of the mechanisms responsible for the closure of the recirculation bubble.

Contrary to bidimensional flows (Parezanović & Cadot, 2012), the presence of unsteady global modes is not identified as an essential parameter for the recirculation length, especially for complex three-dimensional geometries at high Reynolds numbers. An argumentation is presented in section 5.4.2, it is based on the fact that the unsteady modes in three-dimensional wakes are weak and their energy is reported only downstream of the recirculation region.

On the other hand, the experimental results evidence quadratic dependences between the drag and the cross-flow forces, *i.e.* large-scale pressure gradients on the sides of the geometry; such phenomena are reminiscent of the notions of induced drag which are widely used in aeronautics. In addition, the drag is proved to be increased by the formation of small-scale streamwise vortices related to local pressure gradients (see chapters 8 and 9). Consequently, the uniformity of the pressure distribution on the afterbody, in proximity of the flow separations and on the base, is thought to play a significant role in the selection of the mean base pressure.

Thus, these observations place the development of cross-flow instabilities as relevant contributors to the pressure drag. In particular, the sensitivity analyses performed past simplified geometries in chapters 3 and 7 show that the suppression of these instabilities limits the intensity of the cross-flow forces, which systematically leads to base pressure recovery.

Now, the connections between the geometry, the lift force, the base pressure gradients and the drag are still to be clarified. For example, the turbulent wakes of the sphere and the disk (in chapter 2 and appendix C respectively) show similar degrees of asymmetry in the instantaneous wake whereas there is, theoretically, no pressure lift in the disk case[4]. Hence, the analysis of the instantaneous cross-flow forces might not be a universal criterion for the development of future strategies for drag reduction. Furthermore, in ground proximity, the comparison of the drag evolutions ascribed to a base pressure gradient and to a cross-flow force remains to be detailed. For example, in the control experiments past the Ahmed geometry, the optimal drag configuration is found for a nil pressure gradient in the vertical direction but for a non-nil lift (see chapter 7). Hence, there might be some influence of the forebody shape on the optimal lift; it could be interesting to analyze these phenomena for other ground clearances and also for a simplified vehicle with a A-pillar.

In terms of flow control strategies, the long time dynamics pave the way to the implementation of both open-loop and closed-loop active techniques. The use of movable flaps, synthetic jets or any control device improving the uniformity of the instantaneous pressure distribution on the afterbody, is very likely to achieve drag reduction.

Such drag reduction strategies are likely to be complementary to the work devoted the

[4]In the limit case of an infinitely thin disk, the pressure distribution on the surface can only produce drag.

control of the mixing layer growth. Even if not considered in these experiments, the fluid entrainment by the mixing layer is also believed to be a dominant ingredient of the closure of the recirculation region. For example, high frequency excitations of the turbulent mixing layers past vehicles is likely to provide drag reductions (Greenblatt & Wygnanski, 2000; Parezanović *et al.*, 2013).

Part IV

Appendices

Appendix A

General concepts of fluid mechanics

This appendix introduces the formalism and the general notions of fluid mechanics that are used in this work. In particular, it depicts the dependence between the fluid force and the fields of pressure and velocity.

Abstract

For any quantity $a(x, y, z, t)$, $A(x, y, z) = \langle a(x, y, z, t) \rangle$ is the time-averaged value of a and a^* is the non-dimensional value of a. Considering the flow around a bluff body, one can identify three different regions: the potential flow (irrotational and inviscid), the wall boundary layer (rotational and viscid) and the wake (rotational and inviscid). The characteristics of these different regions are responsible for the fields of velocity and pressure in the proximity of the geometry. So, they are closely related to the fluid force that applies on the body, this force being separated into friction and pressure contributions. In the case of a bluff body at high Reynolds numbers, most of the force results from the pressure effects. In particular, the low pressure on the afterbody is responsible for dominant part of the drag. This fluid force is directly connected to the pressure and velocity gradients on the surface but it can also be estimated from pressure and velocity measurements downstream of the geometry.

Contents

A.1 Notations

The uniform displacement of a body in a fluid at rest is studied in the reference frame of the geometry; so the body is considered facing an incompressible Newtonian fluid flow of density ρ and free-stream velocity U_0. The static pressure of the free-flow is denoted by P_0.

The coordinate system is defined as $\vec{e_x}$ in the streamwise direction, $\vec{e_z}$ in the vertical direction (normal to the ground when one is present) and $\vec{e_y}$ forming a direct trihedral. The velocity at the instant t and at the position (x, y, z) is defined as $\vec{u} = u_x\vec{e_x} + u_y\vec{e_y} + u_z\vec{e_z}$; $u_{ij} = \sqrt{{u_i}^2 + {u_j}^2}$ is the amplitude of velocity at the considered point in the plane $(\vec{e_i}, \vec{e_j})$. When specified, the notation of implicit sum is used; for example $\vec{u} = u_i\vec{e_i}$ with $i \in \{x, y, z\}$. The vorticity is $\vec{\omega} = \vec{\mathrm{rot}}(\vec{u})$ and the pressure in the fluid is denoted by p. For any quantity a, A (or $\langle a \rangle$) and $\mathrm{Std}(a)$ refer to the average value and the standard deviation respectively; $a' = a - A$ is the fluctuating part of a. When $\vec{a}$ is a vector, a denotes its modulus: $a = \|\vec{a}\|$.

A characteristic dimension of the geometry (D in this appendix), the density ρ and the velocity U_0 are used to obtain non-dimensional values marked by an asterisk. For example, the normalized mean streamwise vorticity is

$$ {\Omega_x}^* = \vec{\mathrm{rot}}(\vec{u}) \cdot \vec{e_x} D/U_0 = \Omega_x D/U_0. $$

Exceptions are made for the pressure, the forces and the frequencies. The normalized pressure coefficient is denoted by c_p and defined as

$$ c_p = \frac{p - P_0}{\frac{1}{2}\rho {U_0}^2}. \tag{A.1} $$

Note that the mean pressure coefficient is $C_p = \langle c_p \rangle$. The notations of the fluid forces are presented in section A.3; the normalized frequency is the Strouhal number defined as

$$ \mathrm{St}_D = \frac{fD}{U_0}. \tag{A.2} $$

When spectral analyses are performed on a fluid measurement, the time evolution of the signal is recorded at a fixed position during several minutes and spectra are averaged over windows, the window duration being 1 s, 2 s or 10 s. This averaging is denoted by $\langle ... \rangle_{\mathcal{W}}$. $\xi_{\mathcal{F}}(f)$ standing for the Fourier transform of a function ξ evaluated at the frequency f and $\overline{\xi}(f)$ for its complex conjugate, the power spectral density (PSD) is calculated from the signal $a(t)$ as defined in equation (A.3); autopower spectra are obtained with a resolution of 0.1, 0.5 or 1 Hz.

$$ \mathrm{PSD}(f) = \langle a_{\mathcal{F}}(f)\ \overline{a_{\mathcal{F}}}(f) \rangle_{\mathcal{W}}. \tag{A.3} $$

Cross-correlations between two signals at different locations can also be performed: the coherence $r_{\mathcal{F}}$ and phase $\varphi_{\mathcal{F}}$ between two signals $a(t)$ and $b(t)$ are the modulus and the argument of γ defined in equation (A.4).

$$ \gamma(f) = \frac{\langle a_{\mathcal{F}}(f)\ \overline{b_{\mathcal{F}}}(f) \rangle_{\mathcal{W}}}{\sqrt{\langle |a_{\mathcal{F}}(f)|^2 \rangle_{\mathcal{W}} \langle |b_{\mathcal{F}}(f)|^2 \rangle_{\mathcal{W}}}} = r_{\mathcal{F}}(f) e^{i\varphi_{\mathcal{F}}(f)}. \tag{A.4} $$

In terms of statistics, $\mathbb{P}(\mathrm{E})$ refers to the probability of an event E. The probability density function of a random variable X is denoted by PDF and the expected value of X is $\mathbb{E}(\mathrm{X})$.

A.2 Flow regions around the geometry

After normalization by D and U_0, the Navier-Stokes equations for an incompressible Newtonian fluid in absence of external forces[1] are the mass conservation

$$\mathrm{div}^* \left(\vec{u^*}\right) = 0 \tag{A.5}$$

and the momentum conservation

$$\frac{\mathrm{d}\vec{u^*}}{\mathrm{d}t^*} = -\frac{1}{2}\,\vec{\mathrm{grad}}^*\, c_p + \frac{1}{\mathrm{Re}_D}\,\vec{\mathrm{div}}^* \left(\underline{\underline{\mathrm{grad}}}^*\, \vec{u^*} +^t \underline{\underline{\mathrm{grad}}}^*\, \vec{u^*}\right), \tag{A.6}$$

the Reynolds number being defined by

$$\mathrm{Re}_D = \frac{\rho U_0 D}{\mu} = \frac{U_0 D}{\nu}, \tag{A.7}$$

where μ and $\nu = \mu/\rho$ are the dynamic and kinematic viscosity of the fluid respectively. The Reynolds number compares the inertial effects to the viscous ones in the fluid.

When averaged in time, equation (A.6) gives in the i direction

$$U_j{}^* \frac{\partial U_i{}^*}{\partial j^*} = -\frac{1}{2}\,\frac{\partial c_p}{\partial i^*} + \frac{1}{\mathrm{Re}_D}\,\frac{\partial^2 U_i{}^*}{\partial j^* \partial j^*} + \frac{\partial \langle -u_i'{}^* u_j'{}^* \rangle}{\partial j^*}, \tag{A.8}$$

using the notation of implicit sum on $j^* \in \{x^*, y^*, z^*\}$. The terms $\langle -u_i'{}^* u_j'{}^* \rangle$ related to the fluctuations of velocity are the Reynolds stresses.

Two different flow regimes are distinguished. In the laminar regime, usually for low Reynolds numbers, the fluid behavior depends mostly on the viscous effects and the particles move along regular trajectories. On the contrary, in the turbulent regime, for large Reynolds numbers typically, the inertial effects are dominant and the path of the fluid particles is characterized by irregular and incoherent motions. For moderate Reynolds number flows, transitions may occur from the laminar regime to the turbulent one.

Most of the following studies address high Reynolds number flows around bluff bodies, typically $\mathrm{Re}_D > 10^4$. Then, equation (A.6) simplifies as

$$2\frac{\mathrm{d}\vec{u^*}}{\mathrm{d}t^*} \approx -\vec{\mathrm{grad}}^*\, c_p, \tag{A.9}$$

which means that the local acceleration of the fluid is defined by the pressure gradients. A streamwise pressure gradient is linked to increases or decreases of fluid momentum while a cross-flow pressure gradient is associated with curvature of the fluid trajectories.

For such high Reynolds number flows, one can define different regions around the geometry as presented in figure A.1: the potential flow region, the wall boundary layer and the wake.

Potential flow

In figure A.1, the potential flow is comprised of the whole fluid domain apart from the boundary layer and the wake. In this region, the flow can be assumed inviscid and irrotational: $\vec{\omega^*} = 0$. The velocities can be deduced from a potential ψ; in other words, it exists a scalar quantity verifying $\vec{u^*} = \vec{\mathrm{grad}}^*\, \psi$.

[1] The gravity effects are neglected.

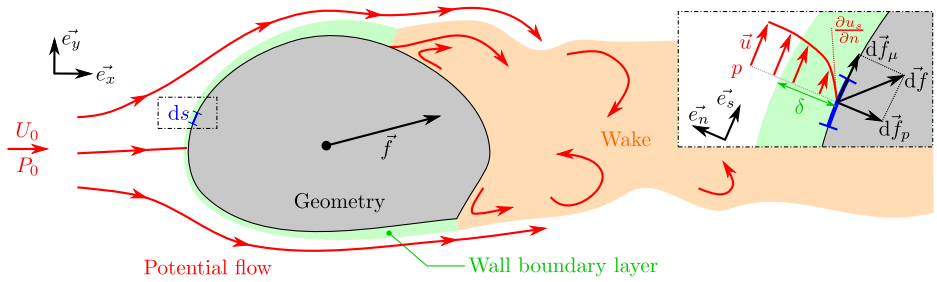

Figure A.1. Scheme of the instantaneous flow around a bluff body and definition of the notations. For simplification, the scheme is bidimensional.

The potential flow theory allows the calculation of analytical flow solutions around basic bidimensional bodies such as wing profiles (Kirchhoff, 1869; Riabouchinsky, 1921) but this method is poorly adapted to the study of bluff body flows.

The pressure and velocity fields verify Bernoulli's law: $c_p + u^{*2}$ is constant along a streamline; in the following configurations, the uniform inlet flow condition $(\vec{U_0}, P_0)$ lead to

$$c_p + u^{*2} = 1 \tag{A.10}$$

in the whole potential flow region.

Another interesting characteristic of the inviscid theory is that a stream surface is equivalent to a solid interface. As a consequence, when the fluid is assumed inviscid, a wall can be seen as a mirror condition on the instantaneous flow.

The inviscid hypothesis of the potential flow domain is no more sustainable close to the geometry, in the wall boundary layer.

Wall boundary layer and flow separation

The boundary condition on the geometry imposes $\vec{u} = \vec{0}$ on the surface of the geometry which is denoted by $\mathcal{S}_{\text{body}}$. This condition affects the velocities in the proximity of the body surface; the corresponding region is the boundary layer, its characteristic length is denoted by δ (see figure A.1). A detailed analysis of boundary layers can be found in Schlichting & Gersten (2000). The following remarks only remind the principal notions that are used in this work.

A small element ds of the surface $\mathcal{S}_{\text{body}}$ is considered. Its normal $\vec{e_n}$ is oriented inside the fluid domain. The directions parallel to the elementary surface are denoted by $\vec{e_{s_1}}$ and $\vec{e_{s_2}}$; s_1, s_2 and n denote the positions in the local coordinate system $(\vec{e_{s_1}}, \vec{e_{s_2}}, \vec{e_n})$. u_{s_1}, u_{s_2} and u_n are the velocity components in this local reference frame. For simplification, the characteristics of boundary layers are given using a bidimensional view of a stationary flow; so the notations merge the axes $\vec{e_{s_1}}$ and $\vec{e_{s_2}}$ in $\vec{e_s}$.

From the velocity U_{s_0} of the fluid outside the boundary layer, *i.e.* $U_{s_0} = U_s(n = \delta)$, different thicknesses are used to characterize the velocity profile in the boundary layer:

- the boundary layer thickness based on 99% of U_{s_0}, denoted $\delta_{0.99}$, verifying

$$U_s(\delta_{0.99}) = 0.99\, U_{s_0}, \tag{A.11}$$

- the displacement thickness

$$\delta_1 = \int_{n=0}^{\delta} \left(1 - \frac{U_s}{U_{s_0}}\right) \, \mathrm{d}n, \tag{A.12}$$

- the momentum thickness

$$\delta_2 = \int_{n=0}^{\delta} \frac{U_s}{U_{s_0}} \left(1 - \frac{U_s}{U_{s_0}}\right) \, \mathrm{d}n. \tag{A.13}$$

The shape factor of the boundary layer H_{12} is defined as

$$H_{12} = \delta_1/\delta_2. \tag{A.14}$$

This parameter gives information on the distribution of the kinetic energy in the boundary layer: the smaller the value of H_{12}, the more energetic the flow close to the wall. It can be used as an indicator of the laminar or turbulent state of the boundary layer under no streamwise pressure gradient ($\partial C_p/\partial s^* = 0$): $H_{12} \approx 2.6$ for a laminar boundary layer (Blasius profile) while $H_{12} \approx 1.4$ for a turbulent one.

The boundary layer evolves along the surface by viscous or turbulent diffusion depending on its regime; in absence of streamwise pressure gradient, the growth rate verifies $\mathrm{d}\delta/\mathrm{d}s \sim {\mathrm{Re}_s}^{-0.5}$ for a laminar boundary layer whereas $\mathrm{d}\delta/\mathrm{d}s$ is roughly constant for a turbulent one. Hence, a turbulent boundary layer has usually a larger growth rate than a laminar one.

When equation (A.8) is considered at large Reynold number ($\mathrm{Re}_\delta = U_{s_0}\delta/\nu \gg 1$) and under boundary layer assumptions ($U_n \ll U_s$ and $\partial/\partial n \gg \partial/\partial s$), the dominant terms in the n direction gives

$$\frac{\partial C_p}{\partial n^*} + 2\frac{\partial \langle {u'_n}^{*2} \rangle}{\partial n^*} = 0. \tag{A.15}$$

As a consequence, by integration in the n direction, equation (A.15) points out that $C_p + 2\langle {u'_n}^{*2} \rangle$ is constant across the boundary layer. As $\langle {u'_n}^{*2} \rangle = 0$ on $\mathcal{S}_{\mathrm{body}}$, the pressure on the geometry is equal to the pressure in the potential flow, so it is directly connected to the velocity of the potential flow.

Now, if equation (A.8) is studied in the s direction on the wall ($n^* = 0$) then at first order, the equilibrium is

$$-\frac{1}{2}\frac{\partial C_p}{\partial s^*} + \frac{1}{\mathrm{Re}_\delta}\frac{\partial^2 {U_s}^*}{\partial {n^*}^2} - \frac{\partial \langle -{u'_s}^* {u'_n}^* \rangle}{\partial n^*} = 0. \tag{A.16}$$

In particular, equation (A.16) shows that the pressure gradient in the s direction $\partial C_p/\partial s$, which relies on the velocity of the potential flow, affects both the curvature velocity profile and the Reynolds stresses in the close proximity of the wall. The following trends can be stated.

- The larger the pressure gradient, the larger the shape factor H_{12}.
- An adverse pressure gradient in the s direction makes the boundary layer thicker and more turbulent; on the contrary, a favorable pressure gradient makes the boundary layer thinner and reduces its turbulent activity.

- A strong pressure gradient in the s direction can induce a change of sign of U_s. This introduces the notions of flow separation and reattachment. The points of separation and reattachment are defined as the position s for which

$$\left.\frac{\partial {U_s}^*}{\partial n^*}\right|_{n^*=0} = 0. \tag{A.17}$$

  Note that these definitions of separation and reattachment can be extended to the instantaneous flow.

Examples of flow separations are presented in the scheme in figure A.1 at the frontier between the wall boundary layer and the wake. At the separation from the bottom part of the geometry, a strong and localized pressure gradient is introduced by a sharp edge on the body. This results in a fixed point of separation. On the contrary, the detachment on the top part of the geometry is related to a progressive slow down of the potential flow, *i.e.* a progressive adverse pressure gradient. These configurations often result in fluctuating points of separation.

Now, the shape factor H_{12} can be used to estimate whether the flow is close to separation or not: for a boundary layer facing an adverse pressure gradient, separation usually occurs for $H_{12} \approx 3$ (Simpson, 1989). Hence, a turbulent boundary layer is more resistant to an adverse pressure gradient than a laminar one. Further details on boundary layer separations can also be found in Simpson (1989) and references therein.

Wake past the geometry

When the flow detaches from the geometry, the vorticity initially concentrated in the boundary layer is convected downstream of the separation, in the wake. In this region, the flow is out of the viscous influence of the wall so the inviscid hypothesis is sustainable at high Reynolds numbers. However, contrary to the potential flow, the wake is not irrotational and the dynamics of the vorticity plays a significant role on the flow (Saffman, 1992).

First, it is worths noting the analogy between rotational inviscid flows and electromagnetism after substitution of the magnetic field by the velocity field and the current density by the vorticity. For example, one can deduce the velocity field from the distribution of vorticity using the Biot-Savart law.

Furthermore, by taking the divergence of equation (A.6), the pressure is linked to the vorticity as

$$\Delta^* c_p = {\omega^*}^2 - {\varsigma^*}^2, \tag{A.18}$$

with $\Delta^* c_p = \partial^2 c_p/(\partial i^* \partial i^*)$ and ${\varsigma^*}^2 = \frac{1}{2}\left(\frac{\partial {u_i}^*}{\partial j^*} + \frac{\partial {u_j}^*}{\partial i^*}\right)^2$, using implicit sums on $(i^*, j^*) \in \{x^*, y^*, z^*\}^2$.

Consequently, in the instantaneous wake, the mimina of pressure are located in regions dominated by vorticity.

Bibliographical details on the wakes past different geometries are given in section 1.2. Now, an overview of the fluid forces that apply on the geometry is presented in section A.3.

A.3 Fluid forces on the geometry

The fluid force that applies on a body at an instant t is denoted by $\vec{f} = f_x\vec{e_x} + f_y\vec{e_y} + f_z\vec{e_z}$; it results from integration on the geometry:

$$\vec{f} = \iint_{\text{Body}} \mathrm{d}\vec{f}\ \mathrm{d}s, \tag{A.19}$$

with $\mathrm{d}\vec{f}$ the local fluid force on the elementary surface $\mathrm{d}s$.

The local fluid force $\mathrm{d}\vec{f}$ can be decomposed as a sum of a pressure term $\mathrm{d}\vec{f}_p$, in the n direction, and a viscous term $\mathrm{d}\vec{f}_\mu$, parallel to the elementary surface (see figure A.1). These force contributions are linked to the fluid properties by

$$\mathrm{d}\vec{f}_p = -p\,\mathrm{d}s\,\vec{e_n}, \tag{A.20}$$

and

$$\mathrm{d}\vec{f}_\mu = \mu\left(\frac{\partial u_{s_1}}{\partial n}\vec{e_{s_1}} + \frac{\partial u_{s_2}}{\partial n}\vec{e_{s_2}}\right), \tag{A.21}$$

with μ the dynamic viscosity of the fluid, all the quantities being evaluated at $n = 0$. As a result, the total force is the sum of a pressure force $\vec{f_p}$ and a friction force $\vec{f_\mu}$, integrated on the body surface.

From these definitions, it is clear that the distribution of velocity in the boundary layers has a significant influence on the fluid forces. First, the velocity profile in the boundary layer has a strong effect on the friction drag through the gradient $\partial U_s/\partial n$. Furthermore, as previously stated, the momentum close to the wall is a first order parameter of the presence and position of flow separations. This can result in important modifications of pressure around the body.

The normalization of the fluid force is done by

$$c_i = \frac{f_i}{\frac{1}{2}\rho S {U_0}^2}, \tag{A.22}$$

with $i \in \{x, y, z\}$, S being the projected area of the geometry on a cross-flow plane. $C_i = \langle c_i \rangle$ is the mean force coefficient in the i direction; the normalized pressure and friction contributions are denoted by c_{ip} and $c_{i\mu}$ respectively.

To set the context of these experiments, it is useful to give some orders of magnitude of drag sources. The total drag is the sum of the pressure force on the forebody, the friction force on the sides and the pressure force on the afterbody. For bluff body flows at high Reynolds numbers, the dominant term is the pressure force on the afterbody as the flow separation on the base[2] is usually associated with low levels of pressure. The friction effects and the pressure distribution on the forebody have a limited contribution to the total drag, roughly 30% once cumulated.

Experimentally, the fluid force can be directly measured on the geometry using a strain balance; however, for some configurations, an alternative evaluation is done from the equilibrium of a volume of fluid $\mathcal{V}$ around the geometry.

The volume $\mathcal{V}$ is defined by a stream surface of the mean flow (see figure A.2). The closed contour of the volume denoted $\partial\mathcal{V}$ is made up of the interface $\mathcal{S}_{\text{body}}$ between the geometry and the fluid, a lateral stream surface $\mathcal{S}_{\text{lat}}$ and two cross-flow surfaces (normal to

[2]The base refers to the part of the afterbody where the flow is detached.

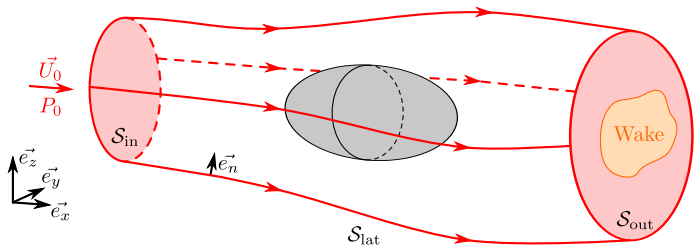

Figure A.2. Scheme of the fluid volume $\mathcal{V}$ around the geometry and its contour $\partial\mathcal{V} = \mathcal{S}_{\text{in}} \cup \mathcal{S}_{\text{lat}} \cup \mathcal{S}_{\text{out}} \cup \mathcal{S}_{\text{body}}$.

$\vec{e_x}$): the inlet $\mathcal{S}_{\text{in}}$ and the outlet $\mathcal{S}_{\text{out}}$. The cross-flow section $\mathcal{S}_{\text{out}}$ is chosen large enough to contain the wake of the geometry so that $\mathcal{S}_{\text{lat}}$ is in the potential flow. Finally, the inlet $\mathcal{S}_{\text{in}}$ is upstream enough to have constant flow conditions $(\vec{U_0}, P_0)$.

The area of the surface $\mathcal{S}_{\text{in}}$ is denoted by S_{in}, *idem* for $\mathcal{S}_{\text{lat}}$ and $\mathcal{S}_{\text{out}}$.

The equilibrium of the fluid in the domain $\mathcal{V}$ can be written

$$\iiint_{\Omega} \rho \frac{\mathrm{d}\vec{u}}{\mathrm{d}t} \,\mathrm{d}\Omega = -\iint_{\partial\Omega} p\,\vec{e_n} \,\mathrm{d}s + \iint_{\partial\Omega} \underline{\underline{\tau_v}}\,\vec{e_n} \,\mathrm{d}s, \tag{A.23}$$

with $\underline{\underline{\tau_v}} = \mu \left(\underline{\underline{\text{grad}}}\,\vec{u} + {}^t\underline{\underline{\text{grad}}}\,\vec{u}\right)$. Once averaged in time, equation (A.23) gives

$$\iint_{\partial\Omega} \rho \,\langle \vec{u}(\vec{u}\cdot\vec{e_n})\rangle \,\mathrm{d}s = -\iint_{\partial\Omega} P\,\vec{e_n} \,\mathrm{d}s + \iint_{\partial\Omega} \langle\underline{\underline{\tau_v}}\rangle\,\vec{e_n} \,\mathrm{d}s. \tag{A.24}$$

If $\mathcal{S}_{\text{out}}$ is large enough, the Reynolds stresses on $\mathcal{S}_{\text{lat}}$ can be neglected and additional simplifications are obtained. First, $\mathcal{S}_{\text{lat}}$ being a stream surface, $\vec{U}\cdot\vec{e_n}$ is nil on this part of $\partial\Omega$. As the following studies are devoted to high Reynolds number flows, the viscous effects on the external contour $\mathcal{S}_{\text{in}}\cup\mathcal{S}_{\text{lat}}\cup\mathcal{S}_{\text{out}}$ of $\mathcal{V}$ can be neglected. Under these conditions, equation (A.24) enables to express the fluid force on the body[3] as

$$\vec{F} = \rho\,{U_0}^2\,S_{\text{in}}\vec{e_x} - \iint_{\mathcal{S}_{\text{lat}}} (P-P_0)\,\vec{e_n} \,\mathrm{d}s - \iint_{\mathcal{S}_{\text{out}}} \left[\rho\langle u_x\,\vec{u}\rangle + (P-P_0)\,\vec{e_x}\right] \,\mathrm{d}s. \tag{A.25}$$

Now, the conservation of mass in the volume $\mathcal{V}$ gives

$$U_0\,S_{\text{in}} = \iint_{\mathcal{S}_{\text{out}}} U_x \,\mathrm{d}s. \tag{A.26}$$

So, when projected along $\vec{e_x}$ and normalized, equation (A.25) estimates the drag force on the geometry as

$$C_x = \iint_{\mathcal{S}_{\text{out}}} \left[2{U_x}^*\,(1-{U_x}^*) - 2\langle {u'_x}^{*2}\rangle - C_p\right] \frac{\mathrm{d}s}{S}. \tag{A.27}$$

In equation (A.27), the pressure term on $\mathcal{S}_{\text{lat}}$ is neglected as, when $\mathcal{S}_{\text{out}}$ is large enough, the pressure is close to the inlet level and the surface verifies $\vec{e_n}\cdot\vec{e_x} \approx 0$.

[3]The viscous effect are still considered on $\mathcal{S}_{\text{body}}$ so the friction force on the body is taken into account.

When projected along $\vec{e_y}$, after normalization, equation (A.25) gives

$$C_y = -\iint_{\mathcal{S}_{\text{out}}} 2\left[{U_x}^* {U_y}^* + \langle {u'_x}^* {u'_y}^* \rangle\right] \frac{\mathrm{d}s}{S} + \iint_{\mathcal{S}_{\text{lat}}} C_p \, \vec{e_n} \cdot \vec{e_y} \, \frac{\mathrm{d}s}{S}. \tag{A.28}$$

The result for C_z is identical after substitution of y by z.

As a result, using equations (A.27) and (A.28), the force coefficients are obtained from the measurements of pressure and velocities in the wake.

Additional details on the relationship between the measurements and fluid forces have been provided by Onorato *et al.* (1984) and by Ardonceau & Amani (1992) for road vehicle applications. Note that in the framework of car aerodynamics, it may be useful to decompose the cross-flow forces C_i, with $i \in \{y, z\}$ into front and rear contributions, denoted C_{if} and C_{ir} respectively: $C_i = C_{if} + C_{ir}$. These coefficients give the repartition of the cross-flow force on the front and rear axles of the vehicle.

Appendix B

Flow visualizations around vehicles using cavitation

Confidential until December 2018

Appendix C

Axisymmetry of the turbulent disk wake

This appendix studies the turbulent wake past a disk. The approach is identical to the one presented in chapter 2 for the sphere. The objectives are to clarify the statistics that lead to the axisymmetric wake and to detail the instantaneous topology of the natural flow. These experiments also quantify the wake asymmetry induced by an imperfection of the setup.

Abstract

The disk wake at $\mathrm{Re}_D = 1.8\ 10^4$ is axisymmetric in average with a periodic motion at $\mathrm{St}_D = 0.14$. As for the sphere, the analysis of the PIV snapshots in a cross-flow plane shows that the instantaneous wake explores all the azimuthal directions. Conditional averaging enables to extract the mean flow topology associated with one orientation; the obtained wake shows strong similarities with the unsteady planar symmetric flow reported in the laminar regime. Besides, the use of $m = 1$ azimuthal perturbations leads to modifications of the statistics: the wake presents one preferred orientation, toward the disturbance, and the larger the disturbance, the more the wake selects this orientation.

Contents

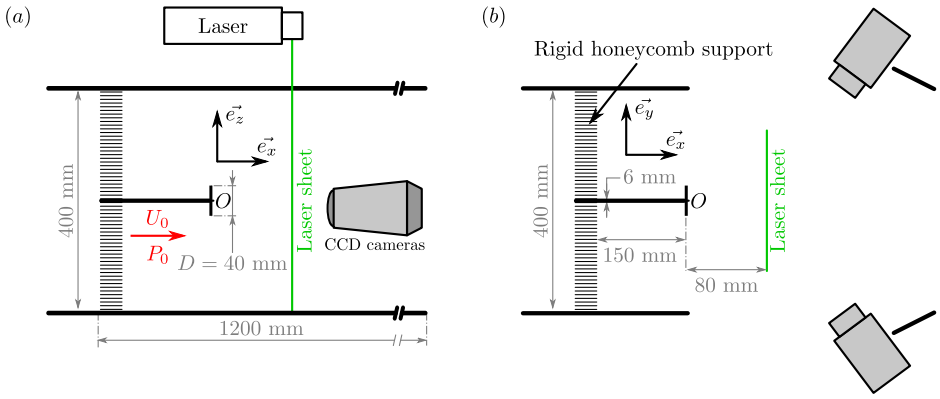

Figure C.1. Side view (a) and top view (b) of the experimental setup with the stereoscopic PIV system.

C.1 Experimental setup

The experimental setup is identical to the one used for the sphere in chapter 2; it is presented in figure C.1. Instead of the sphere, a disk of 4 mm thickness with a diameter $D = 40$ mm is placed in the middle of the test section. The free-flow velocity is increased to $U_0 = 6.9$ m s^{-1} in order to preserve a similar Reynolds number: $\mathrm{Re}_D = 1.8\ 10^4$.

The disk is designed with slots to accept azimuthal disturbances. The 100 mm length of the rods corresponds to $2.5D$ and the normalized diameters are $d^* = d/D \in \{0.03, 0.05, 0.10, 0.15\}$. Only the $m = 1$ azimuthal periodicity is considered in the following.

The measurements are based on PIV in the plane $y^* = 0$, stereoscopic PIV in the plane $x^* = 2.0$ and hot-wire probe signals. They are strictly identical to the ones presented in section 2.1.

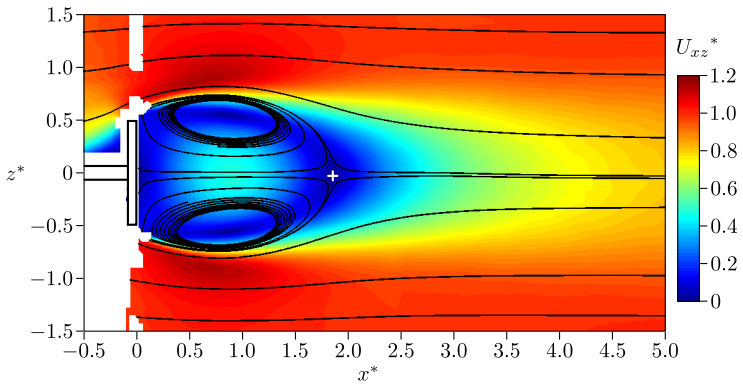

Figure C.2. Intensity of $U_{xz}{}^*$ in the plane $y^* = 0$; the white cross locates the saddle point.

RS	max (RS)	x^* (max (RS))	r^* (max (RS))
$\langle {u'_x}^{*2} \rangle$	0.085 ± 0.005	1.10 ± 0.02	0.69 ± 0.02
$\langle {u'_r}^{*2} \rangle$	0.075 ± 0.005	1.88 ± 0.02	0.08 ± 0.02
$-\langle {u'_x}^* {u'_r}^* \rangle$	0.040 ± 0.005	1.42 ± 0.02	0.58 ± 0.02

Table C.1. Maxima of the Reynolds stresses (RS) in the wake and their corresponding locations; the data are reported from PIV in the plane $y^* = 0$ where $u'_r = \pm u'_z$.

C.2 Natural mean flow

The mean properties of the natural flow are considered in the planes $y^* = 0$ and $x^* = 2.0$ respectively.

C.2.1 Velocities in the plane $y^* = 0$

The velocity field in the plane $y^* = 0$ is presented in figure C.2. The flow is symmetric referring to the plane $z^* = 0$. The recirculation region extends up to $x^* = 1.86$ with one saddle point at the end of the bubble. The maximum width of the wake is $D_r = 1.47$ at $x^* = 0.77$.

The statistics of the 2000 snapshots give the Reynolds stresses in the plane $y^* = 0$; they are visible in figure C.3. The distributions of the Reynolds stresses respect the symmetry of the setup; the maximal intensities are measured on the separatrix except for the normal cross-flow stress $\langle {u'_z}^2 \rangle = \langle {u'_r}^2 \rangle$ for which the maximum is slightly downstream of the recirculation bubble. The intensity and the position of the maxima are reported in table C.1.

C.2.2 Velocities in the plane $x^* = 2.0$

The mean streamwise and radial velocities in the plane $x^* = 2.0$ are given in figure C.4. As for the sphere in chapter 2, the axisymmetry of the mean flow is satisfactory. Besides, the distributions of velocities are very similar to the ones observed downstream of the sphere at equivalent streamwise positions, *i.e.* just downstream of the recirculation bubble (compare

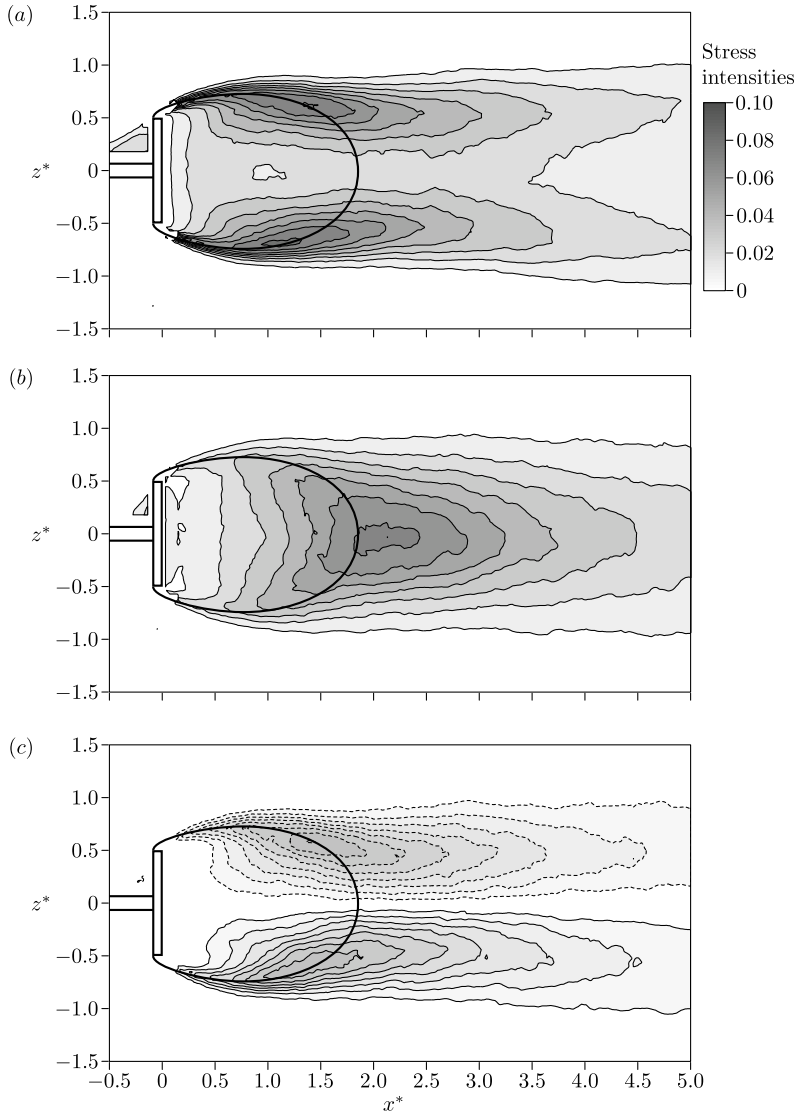

Figure C.3. Reynolds stresses in the plane $y^* = 0$: $\langle {u'_x}^{*2} \rangle$ (a), $\langle {u'_z}^{*2} \rangle = \langle {u'_r}^{*2} \rangle$ (b) and $\langle {u'_x}^* {u'_z}^* \rangle$ (c). The continuous and dashed lines are positive and negative values respectively; the contour intervals are 0.010 in (a)–(b) and 0.005 in (c), the contour 0 is not plotted. The thick black line is the separatrix of the mean recirculation bubble.

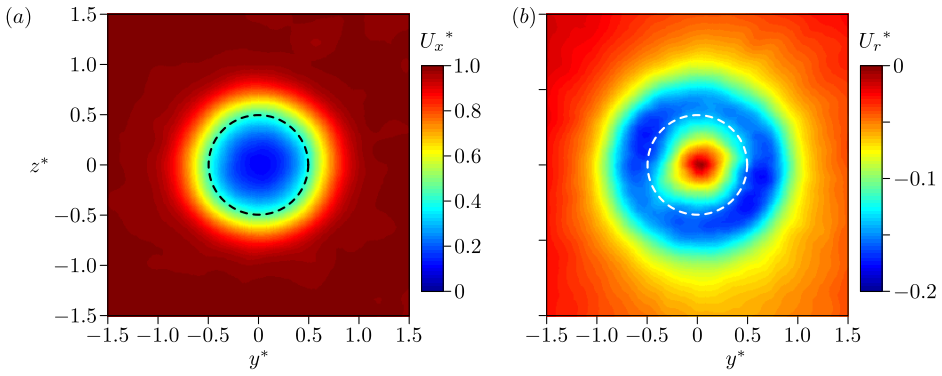

Figure C.4. Intensities of $U_x{}^*$ (a) and $U_r{}^*$ (b) in the plane $x^* = 2.0$; the dashed circle locates the disk.

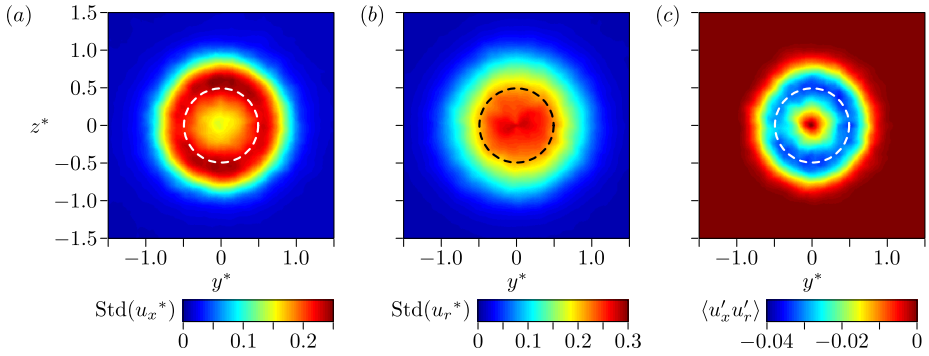

Figure C.5. Intensities of Std($u_x{}^*$) (a) and Std($u_r{}^*$) (b) and $\langle u_x'{}^* u_r'{}^* \rangle$ (c) in the plane $x^* = 2.0$; the dashed circle locates the disk.

to figure 2.4). The main difference lies in the cross-flow size of the wake due to the bluffness of the disk.

The fluctuations of velocities in the cross-flow plane $x^* = 2.0$ are presented in figure C.5. The axisymmetry is convincing and the distributions are very similar to the case of the sphere visible in figure 2.5. The maxima of the normal streamwise and shear stresses are located in the shear layers at $r^* \approx 0.6$ while the normal cross-flow stresses are concentrated around the axis of symmetry.

These maps of velocity allow the evaluation of the drag force using equation (A.27). As in the case of the sphere, the pressure contribution is neglected as a value of $C_p \approx 0$ is expected close to the end of the recirculation region[1]. The so-evaluated drag is $C_x = 1.21$ which remains consistent with the values reported in the literature between 1.1 and 1.2 (Hoerner, 1965; Tropea *et al.*, 2007).

The fluctuations of velocity in the wake are associated with the turbulent activity of the flow but also with the presence of oscillating global modes that are depicted in the next section.

[1]This point is evidenced in chapter 5 in figures 5.6(a)–(b): the mean pressure just downstream of the end of the recirculation bubble is close to the free-flow pressure for three-dimensional wakes.

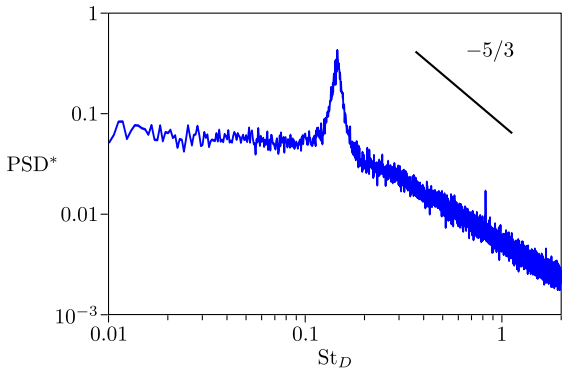

Figure C.6. Autopower spectrum of a hot-wire probe signal at $x^* = 2.00$, $y^* = 0$ and $z^* = 0.75$.

C.2.3 Periodic dynamics of the wake

The autopower spectrum of a hot-wire probe signal located downstream of the disk at $x^* = 2.00$, $y^* = 0$ and $z^* = 0.75$ is plotted in figure C.6. The distribution of energy presents a peak at $\mathrm{St}_D = 0.142$ which corresponds to the vortex shedding described in the literature. This antisymmetric global mode is usually reported at $\mathrm{St}_D = 0.135 \pm 0.05$ for equivalent Reynolds numbers (Berger *et al.*, 1990; Miau *et al.*, 1997; Ruiz *et al.*, 2009).

As for the sphere wake, the use of a flying probe enables to explore the spatial distribution of energy of this mode as well as the spectral repartition of the Reynolds stresses presented in figure C.3. The autopower spectra at $x^* = 0.5$, 1.0, 1.5, 2.0 and 2.5 are shown in figure C.7 for different z positions. The shedding process is reported downstream of the mixing layers. The corresponding peak of energy becomes particularly clear in front of the energy of the large-scale structures of turbulence when the probe is moved further downstream, typically for $x^* \geq 1.5$.

Besides, for $x^* = 2.5$, a significant energy of the velocity fluctuations is reported in figure C.7(e) around $z^* = 0$ at low frequencies, *i.e.* for $\mathrm{St}_D \lesssim 0.02$. At this location, the distributions of the Reynolds stresses in the plane $y^* = 0$ point out that the dominant term is $\langle {u'_r}^2 \rangle$ (see figure C.3). Hence, these low frequency dynamics are very likely to be related to fluctuations of the radial velocity. These effects might be the signature of long time evolutions of the azimuthal orientation of the instantaneous wake.

Finally, one can note slight asymmetries in figures C.7(a)–(b); they are due to the intrusiveness of the probe in the recirculation region where the wake is expected to be a highly sensitive (see chapters 3 and 7).

As a conclusion, the structure of the mean wake past the disk with this setup is consistent with the results reported in the literature. The topology of the instantaneous flow is now depicted in section C.3.

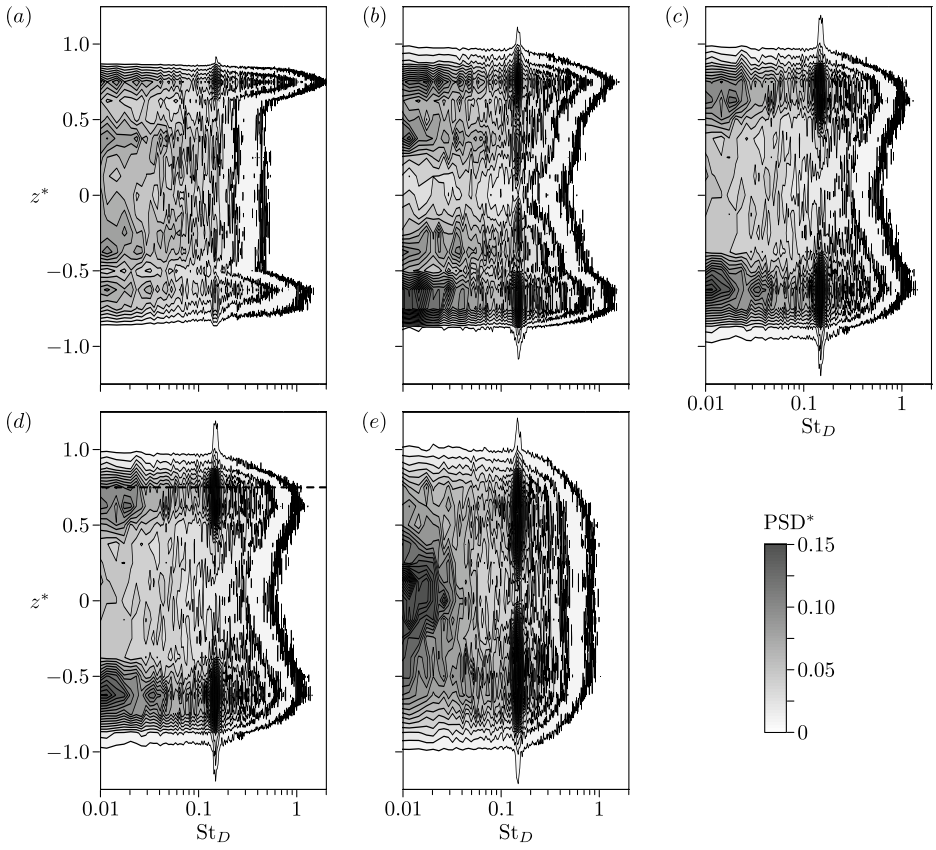

Figure C.7. Autopower spectra from hot-wire measurements in the plane $y^* = 0$ depending on z^* at $x^* = 0.5$ (a), $x^* = 1.0$ (b), $x^* = 1.5$ (c), $x^* = 2.0$ (d) and $x^* = 2.5$ (e). The contour interval is 0.01. The dashed line in (d) corresponds to the spectrum plotted in figure C.6.

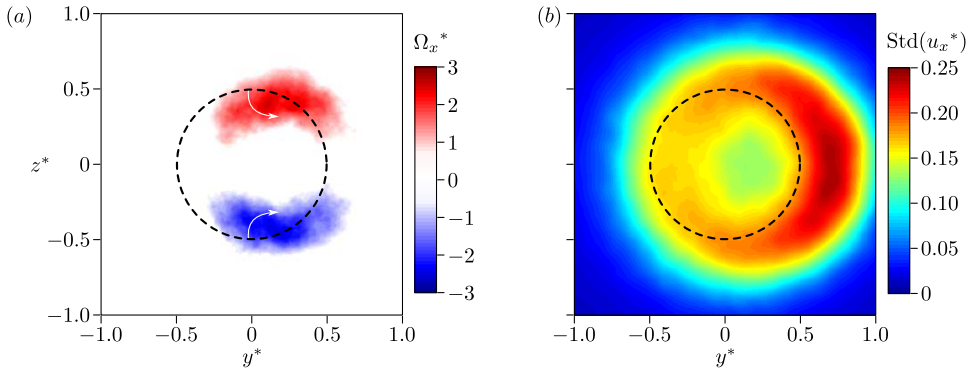

Figure C.8. Streamwise vorticity $\Omega_x{}^*$ (a) and fluctuations of streamwise velocity $\mathrm{Std}(u_x{}^*)$ (b) in the plane $x^* = 2.0$ for the natural flow when $\theta_W = 0$. The dashed circle locates the disk.

C.3 Statistics of the axisymmetry

The instantaneous topology of the natural wake is considered in section C.3.1 while section C.3.2 is devoted to the effects of $m = 1$ azimuthal disturbances.

C.3.1 Instantaneous topology of the natural flow

The PIV snapshots are processed in the exact same way as in chapter 2. The barycenter of momentum deficiency defined in equations (2.1) and (2.2) is used to study the statistics leading to the axisymmetric mean flow presented in the previous section. As for the sphere, the probability density functions of r_W and θ_W report that the instantaneous flow tend to be slightly off the axis of symmetry and all the azimuthal directions are explored with the same probability[2].

Conditional averaging allows the evaluation of the flow topology for a given azimuthal direction of the wake. By construction, the momentum deficiency is off-centered but the interesting points are the corresponding distributions of the mean streamwise vorticity $\Omega_x{}^*$ and of the fluctuations of streamwise velocity $\mathrm{Std}(u_x{}^*)$. They are presented in figure C.8 for the wake orientation $\theta_W = 0$. A topology similar to the case of the sphere is obtained: two counter-rotating vortices in the streamwise direction combined with a concentration of the fluctuations of velocity in the direction of the wake. One can remark that the shape of the vortices slightly differs between the disk in figure C.8(a) and the sphere in figure 2.10(a): the vortices have a bean shape past the disk whereas they are more elliptical in the sphere case. As for the sphere, this asymmetric flow topology for a given wake orientation is reminiscent of the shedding of parallel vortex loops observed in the laminar regime after the unsteady bifurcation (Szaltys *et al.*, 2012).

The asymmetric velocity field obtained for the wake orientation $\theta_W = 0$ is associated with a lift force estimated at $C_y = -0.26$. This lift force seems large and is certainly overestimated but it is difficult to find corresponding values in literature; to give a comparative

[2]The PDF are not presented here but the best $m = 1$ fit for $\mathrm{PDF}(\theta_W)$ is visible in figure C.9.

d^*	0	0.03	0.05	0.10	0.15
K	0.008	0.020	0.028	0.071	0.120

Table C.2. Amplitude of the $m = 1$ modulation in PDF(θ_W) for the different disturbance diameters d^*.

order of magnitude, the lift force is reported around 0.06 in laminar regime for a thick disk (Auguste *et al.*, 2010).

At this stage, it is interesting to note that the disk geometry implies that there is no pressure lift on the geometry and no friction drag. So, the lift force is measured from an asymmetric inertial flow but it is exclusively associated with viscous effects on the disk surface. In addition, the method used in the case of the sphere to obtain the flow topology in the plane $y^* = 0$ (see figure 2.14) does not work in the case of the disk. Indeed, the conditional averaging based on ${u_{zr}}^*$ does not allow to recover the asymmetries measured by stereo PIV in the plane $x^* = 2.0$.

Consequently, it appears difficult to interpret the instantaneous asymmetry of the flow in terms of force; in particular, the connections established in part II between the base pressure gradients, the wake asymmetries and the cross-flow forces do not seem to be valid in the disk case.

Having said that, these results show that the instantaneous wake still tends to be off the axis of symmetry; the axisymmetry of the mean flow results from the fact that the wake explores all the azimuths.

Now that the instantaneous topology is depicted, the effects of $m = 1$ azimuthal disturbances on the statistics of the axisymmetry are considered in section C.3.2.

C.3.2 Azimuthally disturbed flows

Cylinders of different diameters are placed on the disk in the direction $\theta = 0$. For each disturbance, stereoscopic PIV in the plane $x^* = 2.0$ leads to the probability density function of the wake orientation θ_W. All the results follow a $m = 1$ general trend that can be fitted by

$$K\cos(\theta_W) + \frac{1}{2\pi}. \tag{C.1}$$

The corresponding fits are presented in figure C.9. The first observation is that the wake is sensitive to the disturbance and the flow orientation is equal to that of the disturbance whatever the disturbance size. Contrary to the case of the sphere, there is no phase change when d^* is increased. It is also found that the larger the disturbance, the more the wake has a preferred orientation. In other words, the amplitude K defined in equation (C.1) increases with d^*: the results listed in table C.2 suggest a linear dependence between K and d^*.

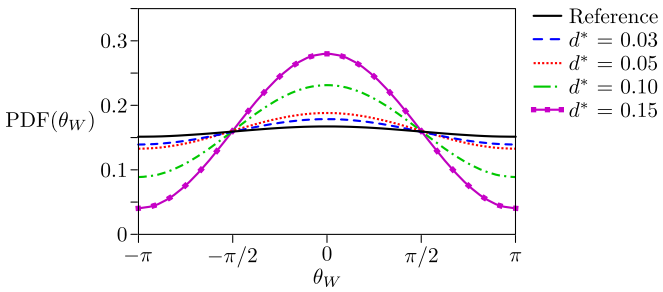

Figure C.9. Probability density functions of θ_W for the reference case and for the $m = 1$ configurations. The experimental data are not plotted, the presented curves are their best $m = 1$ periodic fits.

C.4 Concluding remarks

As for the sphere, the holding system consisting in fixing the disk downstream of an axis is relevant to generate a turbulent axisymmetric wake. The axisymmetry is statistical as the instantaneous wake tends to be off the axis of symmetry while it explores all the azimuths.

Conditional averaging gives the wake topology for a given orientation in the cross-flow plane $x^* = 2.0$. The resulting topology is reminiscent of unsteady planar symmetric flow in the laminar regime. However, the interpretations of the wake asymmetries in terms of force are not as clear as in parts I and part II because there is no possible cross-flow force in the disk case at large Reynolds numbers.

Finally, the use of $m = 1$ azimuthal perturbations evidences the high sensitivity of the statistical axisymmetry of the wake. The flow presents one most probable orientation toward the disturbance; its preference to this azimuthal direction is function of the amplitude of the disturbance.

Appendix D

Statistics of a bistable turbulent signal

This appendix provides some analytical characteristics of a bistable turbulent signal. It addresses necessary conditions for the presence of two peaks in the probability distribution and considers the expected autopower spectrum of such a signal.

Abstract

By modeling a bistable turbulent signal of pressure or velocity at a fixed location, an analytical study proves that the two peaks in the probability distribution are visible only if the fluctuations related to the turbulent activity are smaller than the ones related to the bistable behavior. If not, part of the turbulent fluctuations may be filtered as soon as the time scales are different. In the spectral domain, the signature of the bistable behavior in the autopower spectrum is a power-law distribution of energy of coefficient -2 at very low frequencies.

Contents

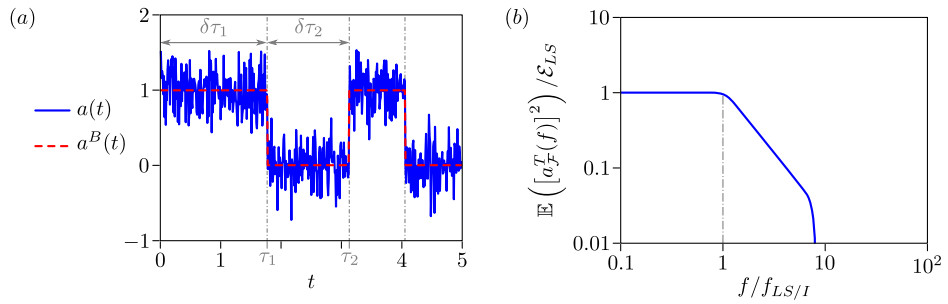

Figure D.1. (a) Example of modeled bistable signal $a(t)$ for $T_S = 5$ and $\sigma^T = 0.5$. (b) Expected autopower spectrum of the turbulent contribution a^T. The notation $\mathbb{E}(...)$ refers to the expected value defined in equation (D.5).

D.1 Definition of the signal

This section defines the signal $a(t)$, for $t \in \mathbb{R}^+$, modeling the pressure or velocity at a given position in a bistable turbulent flow. It can be written

$$a(t) = a^B(t) + a^T(t) \tag{D.1}$$

with independent functions a^B and a^T standing for the bistable and turbulent contributions respectively. In agreement with the physics measured in these experiments, the two terms are defined as follows.

The bistable part of the signal is assumed to be a piecewise constant function equal to 0 or 1 (see figure D.1a). $(\tau_k)_{k\in\mathbb{N}}$ is the sequence of the time of shifts initialized by $\tau_0 = 0$; $(\delta\tau_k)_{k\in\mathbb{N}^*}$ is the sequence of the time intervals between two successive shifts:

$$\delta\tau_k = \tau_k - \tau_{k-1} \text{ with } k \in \mathbb{N}^*. \tag{D.2}$$

The elements of the sequence $(\delta\tau_k)_{k\in\mathbb{N}^*}$ are independent. They are defined from an exponential probability distribution of parameter T_S, the mean time between two successive shifts. In other words, if $\delta\tau$ refers to the random variable of the elements of this sequence, then

$$\text{PDF}(\delta\tau = t) = \frac{1}{T_S}\mathrm{e}^{-t/T_S}. \tag{D.3}$$

The definition implies a shift at $t = 0$ and by convention, $u^B(0^+) = 1$. This is not restrictive as the probability to shift at an instant t is independent of the history.

In addition to this bistable term, $a(t)$ contains a random dynamics $a^T(t)$ that represents the turbulent activity. $a^T(t)$ is produced by a random variable following a normal law centered on 0 with a standard deviation σ^T:

$$\text{PDF}(a^T = y) = \frac{1}{\sigma^T\sqrt{2\pi}}\mathrm{e}^{-\frac{1}{2}\left(y/\sigma^T\right)^2}. \tag{D.4}$$

The time evolution of the signal $a^T(t)$ is defined from the statistics of its Fourier transform, denoted $a_{\mathcal{F}}^T(f)$. The expected autopower spectrum of the signal is presented in figure D.1(b). It presents a classic distribution of energy: at $f_{LS/I}$, there is the frontier between the large-scale structures of turbulence and the inertial range; then, a cutoff frequency marks the inception of the diffusion range. Hence, the PSD is constant at a level $\mathcal{E}_{LS}$ in the domain

$f < f_{LS/I}$ while it presents a power decay in the inertial range[1]. The following analyses do not depend on the possible peaks of energy related to unsteady global mode activity.

It is important to understand that such a definition of the autopower spectrum of a^T is statistical. It may be seen as the average value after successive independent experiments. If ${a_i}^T(t)$ refers to the turbulent signal of the i^{th} experiment, then $\mathbb{E}\left(\left[a^T_{\mathcal{F}}(f)\right]^2\right)$ is defined as

$$\mathbb{E}\left(\left[a^T_{\mathcal{F}}(f)\right]^2\right) = \lim_{n\to\infty}\left(\frac{1}{n}\sum_{i=1}^{n}\left[{a_i}^T_{\mathcal{F}}(f)\right]^2\right). \tag{D.5}$$

Finally, in agreement with the experimental results, it is assumed that $T_S \gg 1/f_{LS/I}$: the characteristic time of the bistable behavior is large in front of the characteristic time of turbulence.

[1] The Kolmogorov theory predicts a coefficient of the power decay $-5/3$ for an homogeneous and isotropic turbulence.

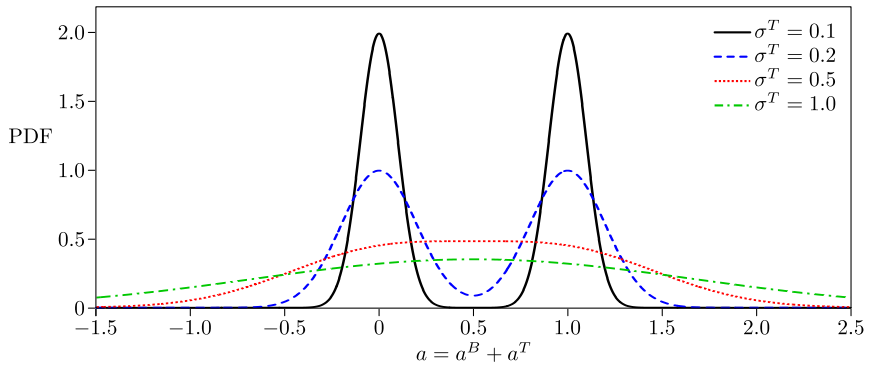

Figure D.2. PDF of the signal $a(t)$ for different fluctuations levels of the turbulent contribution: $\sigma^T = 0.1$, (a); $\sigma^T = 0.2$, (b); $\sigma^T = 0.5$, (c); $\sigma^T = 1.0$, (d).

D.2 Analytical results

The analytical study of the bistable turbulent signal defined in section D.1 is first performed to detail the conditions of existence of two peaks in the PDF of a. Then, the characteristics of the bi-stability in the power spectral analysis are considered in section D.2.2.

D.2.1 Peaks in the histograms

As a^B and a^T are independent, the probability distribution of $a = a^B + a^T$ can be deduced analytically by convolution of the two probability distributions. It can be expressed as

$$\mathrm{PDF}(a = y) = \frac{1}{2\sigma^T\sqrt{2\pi}}\left(\mathrm{e}^{-\frac{1}{2}(y/\sigma^T)^2} + \mathrm{e}^{-\frac{1}{2}[(y-1)/\sigma^T]^2}\right). \tag{D.6}$$

Examples of this PDF are presented in figure D.2 for different fluctuation levels σ^T of the turbulent contribution. Analytically, the presence of the two maxima in the PDF at $a = 0$ and $a = 1$ relies on the sign of

$$\left.\frac{\partial^2 \mathrm{PDF}}{\partial a^2}\right|_{a=0.5}, \tag{D.7}$$

defining whether $a = 0.5$ is a local maximum or minimum of the PDF. The term (D.7) is positive for $\sigma^T \leq 0.5$ and negative for $\sigma^T \geq 0.5$. As a result, the two peaks in the PDF are only visible if $\sigma^T \leq 0.5$. In the definition of the signal, the fluctuations related to the bistable behavior are $\mathrm{Std}(a^B) = 0.5$. Thus, the two peaks in the histogram of a bistable signal cannot be observed as soon as the fluctuations in the velocity signal are larger than fluctuations related to the bi-stability. Besides, it is worth noting that the result is similar when the fluctuations of a^T are ascribed to measurement uncertainty rather than to turbulent activity.

An experimental evidence of the influence of σ^T is visible in figure 5.17: the two peaks in the PDF of the velocity signal in the boundary layer are reported only after applying a low-pass filter to suppress part of the fluctuations related to the turbulent activity. Nevertheless, this method works because the bistable and the turbulent behaviors can be separated in the spectral domain.

D.2.2 Autopower spectrum

This section aims at characterizing the autopower spectrum of a bistable turbulent signal. The objective is to prove that the expected autopower spectrum follows a power law of coefficient -2 for $T_S f \ll 1$.

The expected Fourier transform of a is $a_{\mathcal{F}} = a^B_{\mathcal{F}} + a^T_{\mathcal{F}}$ so,

$$\begin{aligned}\mathbb{E}\left(\left[a_{\mathcal{F}}(f)\right]^2\right) &= \mathbb{E}\left(\left[a^T_{\mathcal{F}}(f) + a^B_{\mathcal{F}}(f)\right]^2\right) \\ &= \underbrace{\mathbb{E}\left(\left[a^T_{\mathcal{F}}(f)\right]^2\right)}_{P(f)} + \underbrace{\mathbb{E}\left(\left[a^B_{\mathcal{F}}(f)\right]^2\right)}_{Q(f)} + \underbrace{2\mathbb{E}\left(a^T_{\mathcal{F}}(f) a^B_{\mathcal{F}}(f)\right)}_{R(f)}. \end{aligned} \tag{D.8}$$

The term $P(f)$ is plotted in figure D.1(b); it is equal to $\mathcal{E}_{LS}$ as soon as $f < f_{LS/I}$, which is the case for $T_S f \ll 1$.

The terms $Q(f)$ and $R(f)$ can be studied through the analytical expression of a^B. It is a succession of positive and negative unit step functions that are offset in the time domain by the sequence $(\tau_k)_{k\in\mathbb{N}^*}$. Its Fourier transform can be expressed as

$$a^B_{\mathcal{F}}(f) = \frac{1}{f}\sum_{k\in\mathbb{N}} (-1)^k \mathrm{e}^{-\tau_k f}, \tag{D.9}$$

with $(\tau_k)_{k\in\mathbb{N}}$ the positive growing sequence of the times of shift.

It is easily obtained that the sequence

$$\left(\sum_{k<2l} (-1)^k \mathrm{e}^{-\tau_k f}\right)_{l\in\mathbb{N}}$$

is a decreasing sequence bounded from below while the sequence

$$\left(\sum_{k<2l+1} (-1)^k \mathrm{e}^{-\tau_k f}\right)_{l\in\mathbb{N}}$$

is a growing sequence bounded from above. One can conclude that these two sequences converge, necessarily to the same value $v(f)$; note that $v(f)$ depends on the sequence of the shifts.

From the particular statistics of the sequence $(\tau_k)_{k\in\mathbb{N}}$ defined in section D.1, one can prove[2] that

$$\mathbb{E}\left(e^{-\tau_k f}\right) = \left(\frac{1}{1+T_S}\right)^k, \tag{D.10}$$

with $\mathbb{E}(...)$ denoting the expected value. Thus, applying theorems of limit – sum and sum – sum inversions, it is found that

$$V(f) = \mathbb{E}\left(v(f)\right) = \frac{1+T_S f}{2+T_S f}. \tag{D.11}$$

As a result, the analytical expression of the expected Fourier transform is obtained as

$$\mathbb{E}\left(a^B_{\mathcal{F}}(f)\right) = \frac{1}{f}\frac{1+T_S f}{2+T_S f}. \tag{D.12}$$

[2]The mathematical induction is not detailed here.

Using a similar reasoning, one can study the term $Q(f) = \mathbb{E}\left(\left[a_{\mathcal{F}}^{B}(f)\right]^2\right)$. It can be expressed as

$$\mathbb{E}\left(\left[a_{\mathcal{F}}^{B}(f)\right]^2\right) = \frac{1}{f^2}V_2(f), \tag{D.13}$$

with

$$V_2(f) = \mathbb{E}\left(\left[\sum_{k\in\mathbb{N}}(-1)^k \mathrm{e}^{-\tau_k f}\right]^2\right). \tag{D.14}$$

Contrary to the calculus of $V(f)$ in equation (D.12), there is no simple expression for $V_2(f)$. The important characteristic is that it verifies

$$V(f)^2 < V_2(f) < 1, \tag{D.15}$$

which implies that

$$\frac{1}{4} < V_2(f) < 1. \tag{D.16}$$

So,

$$Q(f) = \mathbb{E}\left(\left[a_{\mathcal{F}}^{B}(f)\right]^2\right) \underset{T_S f \ll 0}{\sim} \frac{1}{f^2}. \tag{D.17}$$

The last term that must be evaluated in equation (D.8) is the coupling term

$$R(f) = 2\mathbb{E}\left(a_{\mathcal{F}}^{T}(f)a_{\mathcal{F}}^{B}(f)\right) = \lim_{n\to\infty} R_n(f), \tag{D.18}$$

with $R_n(f)$ defined as

$$R_n(f) = \frac{2}{n}\sum_{i=1}^{n} a_i{}_{\mathcal{F}}^{B}(f)a_i{}_{\mathcal{F}}^{T}(f). \tag{D.19}$$

Now, $|R_n(f)|$ can be bounded by above as

$$\begin{aligned} |R_n(f)| &\leq \frac{2}{n}\sum_{i=1}^{n}\left|a_i{}_{\mathcal{F}}^{T}(f)a_i{}_{\mathcal{F}}^{B}(f)\right| \\ &\leq \frac{2}{n}\sqrt{\sum_{i=1}^{n}\left|a_i{}_{\mathcal{F}}^{T}(f)\right|^2}\sqrt{\sum_{i=1}^{n}\left|a_i{}_{\mathcal{F}}^{B}(f)\right|^2}, \end{aligned} \tag{D.20}$$

making use of Hölder's inequality. Hence, using equation (D.12) and the definition of the turbulent power spectrum, a bounding from above of the term $R(f)$ is obtained as

$$|R(f)| \leq \frac{2}{f}\sqrt{\mathcal{E}_{LS}}, \tag{D.21}$$

which means that $R(f) \underset{T_S f \ll 1}{\ll} Q(f)$ in equation (D.8).

Consequently, as $P(f) \underset{T_S f \ll 1}{\ll} Q(f)$, it is proved that

$$\mathbb{E}\left(\left[a_{\mathcal{F}}(f)\right]^2\right) \underset{T_S f \ll 1}{\sim} Q(f) \underset{T_S f \ll 1}{\sim} \frac{1}{f^2}. \tag{D.22}$$

The power dependence of coefficient -2 in equation (D.22) explains the important energy measured in figure 5.10(a) for $f < 1$ Hz in the signal at B. Such a distribution of energy in the spectral domain may be an indicator of a bistable behavior at low frequency.

Bibliography

Abramson, P., Vukasinovic, B. & Glezer, A. 2011 Direct measurements of controlled aerodynamic forces on a wire-suspended axisymmetric body. *Experiments in Fluids* **50** (6), 1711–1725.

Achenbach, E. 1974 Vortex shedding from spheres. *Journal of Fluid Mechanics* **62** (02), 209–221.

Ahmed, S.R., Ramm, G. & Faitin, G. 1984 Some salient features of the time-averaged ground vehicle wake. *SAE Technical Paper Series* **840300**.

Aider, J.L., Beaudoin, J.F. & Wesfreid, J.E. 2010 Drag and lift reduction of a three-dimensional bluff body using active vortex generators. *Experiments in Fluids* **48** (5), 771–789.

Al-Garni, A.M. & Bernal, L.P. 2010 Experimental study of a pick-up truck near wake. *Journal of Wind Engineering and Industrial Aerodynamics* **98** (2), 100–112.

Apelt, C.J. & West, G.S. 1975 The effects of wake splitter plates on bluff body flow in the range 10^4 to 5 10^4. Part 2. *Journal of Fluid Mechanics* **71** (01), 145–160.

Apelt, C.J., West, G.S. & Szewczyk, A.A. 1973 The effects of wake splitter plates on the flow past a circular cylinder in the range from 10^4 to 5 10^4. *Journal of Fluid Mechanics* **61**, 187–198.

Arcas, D.R. & Redekopp, L.G. 2004 Aspects of wake vortex control through base blowing/suction. *Physics of Fluids* **16**, 452.

Ardonceau, P. & Amani, G. 1992 Remarks on the relation between lift induced drag and vortex drag. *European Journal of Mechanics, B/Fluids* **11** (4), 455–460.

Armaly, B.F., Durst, F., Pereira, J.C.F. & Schonung, B. 1983 Experimental and theoretical investigation of backward facing step flow. *Journal of Fluid Mechanics* **127** (473), 20.

Artana, G., Sosa, R., Moreau, E. & Touchard, G. 2003 Control of the near-wake flow around a circular cylinder with electrohydrodynamic actuators. *Experiments in Fluids* **35** (6), 580–588.

Auguste, F., Fabre, D. & Magnaudet, J. 2010 Bifurcations in the wake of a thick circular disk. *Theoretical and Computational Fluid Dynamics* **24** (1-4), 305–313.

Balachandar, S., Mittal, R. & Najjar, F.M. 1997 Properties of the mean recirculation region in the wakes of two-dimensional bluff bodies. *Journal of Fluid Mechanics* **351**, 167–199.

Batchelor, G.K. 2002 *An introduction to fluid dynamics*. Cambridge University Press.

Bayraktar, I., Landman, D. & Baysal, O. 2001 Experimental and computational investigation of Ahmed body for ground vehicle aerodynamics. *SAE Technical Paper Series* **2001-01-2742**.

Beaudoin, J.F. & Aider, J.L. 2008 Drag and lift reduction of a three-dimensional bluff body using flaps. *Experiments in Fluids* **44** (4), 491–501.

Beaudoin, J.F., Cadot, O., Aider, J.L., Gosse, K., Paranthoën, P., Hamelin, B., Tissier, M., Allano, D., Mutabazi, I., Gonzales, M. *et al.* 2004 Cavitation as a complementary tool for automotive aerodynamics. *Experiments in Fluids* **37** (5), 763–768.

Bell, J. & Mehta, R. 1990 Development of a two-stream mixing layer from tripped and untripped boundary layers. *AIAA Journal* **28** (12), 2034–2042.

Berger, E., Scholz, D. & Schumm, M. 1990 Coherent vortex structures in the wake of a sphere and a circular disk at rest and under forced vibrations. *Journal of Fluids and Structures* **4** (3), 231–257.

Bruneau, C.H., Creuse, E., Depeyras, D. & Gillieron, P. 2011 Active procedures to control the flow past the ahmed body with a 25° rear window. *International Journal of Aerodynamics* **1** (3), 299–317.

Cadot, O., Thiria, B. & Beaudoin, J.F. 2009 Passive drag control of a turbulent wake by local disturbances. In *IUTAM Symposium on Unsteady Separated Flows and their Control*, pp. 529–537. Springer.

Cantwell, B. & Coles, D. 1983 An experimental study of entrainment and transport in the turbulent near wake of a circular cylinder. *Journal of Fluid Mechanics* **136**, 321–374.

Champagne, F.H., Pao, Y.H. & Wygnanski, I.J. 1976 On the two-dimensional mixing region. *Journal of Fluid Mechanics* **74** (02), 209–250.

Chrust, M., Goujon-Durand, S. & Wesfreid, J.E. 2013 Loss of a fixed plane of symmetry in the wake of a sphere. *Journal of Fluids and Structures* **41**, 51–56.

Cooper, K.R. 1985 The effect of front-edge rounding and rear-edge shaping on the aerodynamic drag of bluff vehicles in ground proximity. *SAE Technical Paper Series* **850288**.

Dalton, C., Xu, Y. & Owen, J.C. 2001 The suppression of lift on a circular cylinder due to vortex shedding at moderate Reynolds numbers. *Journal of Fluids and Structures* **15** (3-4), 617–628.

Délery, J. 2013 *Three-dimensional separated flow topology: critical points, separation lines and vortical structures*. ISTE – John Wiley & Sons.

Depardon, S. 2006 *Analyse topologique d'écoulements complexes: utilisation de la vélocimétrie par imagerie de particules pour une approche quantitative*. PHD Thesis.

Dimotakis, P.E. 1991 Turbulent free shear layer mixing and combustion. *High Speed Flight Propulsion Systems* pp. 265–340.

Duell, E.G. & George, A.R. 1993 Measurements in the unsteady near wakes of ground vehicle bodies. *SAE Technical Paper Series* **930298**.

Duell, E.G. & George, A.R. 1999 Experimental study of a ground vehicle body unsteady near wake. *SAE transactions* **108** (6, part 1), 1589–1602.

Fabre, D., Auguste, F. & Magnaudet, J. 2008 Bifurcations and symmetry breaking in the wake of axisymmetric bodies. *Physics of Fluids* **20**, 051702.

Fourrié, G., Keirsbulck, L., Labraga, L. & Gilliéron, P. 2011 Bluff body drag reduction using a deflector. *Experiments in Fluids* **50** (2), 385–395.

Franck, G., Nigro, N., Storti, M. & d'Elia, J. 2009 Numerical simulation of the Ahmed vehicle model near-wake. *Latin American Applied Research* **39** (4).

Fransson, J.H.M., Talamelli, A., Brandt, L. & Cossu, C. 2006 Delaying transition to turbulence by a passive mechanism. *Physical Review Letters* **96** (6), 064501.

Frisch, U. 1996 *Turbulence*. Cambridge University Press.

Gerrard, J.H. 1966 The mechanics of the formation region of vortices behind bluff bodies. *Journal of Fluid Mechanics* **25** (02), 401–413.

Gilliéron, P. & Kourta, A. 2010 Aerodynamic drag reduction by vertical splitter plates. *Experiments in Fluids* **48** (1), 1–16.

Gohlke, M., Beaudoin, J.F., Amielh, M. & Anselmet, F. 2007 Experimental analysis of flow structures and forces on a three-dimensional bluff body in constant cross-wind. *Experiments in Fluids* **43** (4), 579–594.

Grandemange, M., Gohlke, M. & Cadot, O. 2012*a* Reflectional symmetry breaking of the separated flow over three-dimensional bluff bodies. *Physical Review E* **86**, 035302.

Grandemange, M., Gohlke, M. & Cadot, O. 2013*a* Bi-stability in the turbulent wake past parallelepiped bodies with various aspect ratios and wall effects. *Physics of Fluids* **25**, 095103.

Grandemange, M., Gohlke, M. & Cadot, O. 2013*b* Turbulent wake past a three-dimensional blunt body. Part 1. Global modes and bi-stability. *Journal of Fluid Mechanics* **722**, 51–84.

Grandemange, M., Mary, A., Gohlke, M. & Cadot, O. 2013*c* Effect on drag of the flow orientation at the base separation of a simplified blunt road vehicle. *Experiments in fluids* **54** (5), 1–10.

Grandemange, M., Parezanović, V., Gohlke, M. & Cadot, O. 2012*b* On experimental sensitivity analysis of the turbulent wake from an axisymmetric blunt trailing edge. *Physics of Fluids* **24**, 035106.

Grandemange, M., Ricot, D., Vartanian, C., Ruiz, T. & Cadot, O. 2014 Characterization of the flow past real road vehicles with blunt afterbodies. *International Journal of Aerodynamics* **4** (1/2), 24–42.

Greenblatt, D. & Wygnanski, I.J. 2000 The control of flow separation by periodic excitation. *Progress in Aerospace Sciences* **36** (7), 487–545.

Herry, B.B., Keirsbulck, L. & Paquet, J.B. 2011 Flow bi-stability downstream of three-dimensional double backward facing steps at zero-degree slideslip. *ASME Transactions Journal of Fluids Engineering* **133** (054501), 1–4.

Higuchi, H. 2005 Passive and active controls of three-dimensional wake of bluff body. *JSME International Journal Series B* **48** (2), 322–327.

Higuchi, H., Van Langen, P., Sawada, H. & Tinney, C.E. 2006 Axial flow over a blunt circular cylinder with and without shear layer reattachment. *Journal of Fluids and Structures* **22** (6), 949–959.

Hill, D.C. 1992 A theoretical approach for analyzing the restabilization of wakes. *NASA Technical Report* **103858**.

Ho, C.M. & Huerre, P. 1984 Perturbed free shear layers. *Annual Review of Fluid Mechanics* **16** (1), 365–422.

Hoerner, S.F. 1965 *Fluid-dynamic drag*. Hoerner fluid dynamics Brick Town, NJ.

Hucho, W.H. 1998 *Aerodynamics of road vehicles*. SAE International.

Hussain, A. & Zaman, K. 1985 An experimental study of organized motions in the turbulent plane mixing layer. *Journal of Fluid Mechanics* **159** (1), 85–104.

Hyun, K.T. & Chun, C.H. 2003 The wake flow control behind a circular cylinder using ion wind. *Experiments in Fluids* **35** (6), 541–552.

Inchul, K., Xin, G. & Hualei, C. 2008 Development of a rear spoiler of a new type for mini-vans. *International Journal of Vehicle Design* **48** (1), 114–131.

Irving Brown, Y.A., Windsor, S. & Gaylard, A.P. 2010 The effect of base bleed and rear cavities on the drag of an SUV. *SAE Technical Paper Series* **2010-01-0512**.

Jang, Y.I. & Lee, S.J. 2008 PIV analysis of near-wake behind a sphere at a subcritical Reynolds number. *Experiments in Fluids* **44** (6), 905–914.

Khalighi, B., Chen, K.H. & Laccarino, G. 2012 Unsteady aerodynamic flow investigation around a simplified squareback road vehicle with drag reduction devices. *Journal of Fluids Engineering* **134** (6).

Khalighi, B., Zhang, S., Koromilas, C., Balkanyi, S.R., Bernal, L.P., Iaccarino, G. & Moin, P. 2001 Experimental and computational study of unsteady wake flow behind a bluff body with a drag reduction device. *SAE Technical Paper Series* **2001-01-1042**.

Kirchhoff, G. 1869 *Advanced engineering mathematics*. John Wiley & Sons, New York, NY, USA.

Kiya, M. & Abe, Y. 1999 Turbulent elliptic wakes. *Journal of Fluids and Structures* **13** (7-8), 1041–1067.

Krajnović, S. & Davidson, L. 2005 Flow around a simplified car. Part 2. Understanding the flow. *Journal of Fluids Engineering* **127**, 919.

Lawson, N.J., Garry, K.P. & Faucompret, N. 2007 An investigation of the flow characteristics in the bootdeck region of a scale model notchback saloon vehicle. *Proceedings of the Institution of Mechanical Engineers - part D - Journal of Automobile Engineering* **221** (D6), 739–754.

Lee, J.Y., Paik, B.G. & Lee, S.J. 2009 PIV measurements of hull wake behind a container ship model with varying loading condition. *Ocean Engineering* **36** (5), 377–385.

Lienhart, H. & Becker, S. 2003 Flow and turbulence structure in the wake of a simplified car model. *SAE Transactions* **112** (6), 785–796.

Littlewood, R. & Passmore, M. 2010 The optimization of roof trailing edge geometry of a simple squareback. *SAE Technical Paper Series* **2010-01-0510**.

Littlewood, R.P. & Passmore, M.A. 2012 Aerodynamic drag reduction of a simplified squareback vehicle using steady blowing. *Experiments in Fluids* **53** (2), 1–11.

Luchini, P., Giannetti, F. & Pralits, J. 2009 Structural sensitivity of the finite-amplitude vortex shedding behind a circular cylinder. In *IUTAM Symposium on Unsteady Separated Flows and their Control*, pp. 151–160. Springer.

Magarvey, R.H. & Bishop, R.L. 1961 Transition ranges for three-dimensional wakes. *Canadian Journal of Physics* **39** (10), 1418–1422.

Mair, W.A. 1965 The effect of a rear-mounted disc on the drag of a blunt-based body of revolution. *Aeronautical Quarterly* **16**, 350–360.

Marquet, O., Sipp, D. & Jacquin, L. 2008 Sensitivity analysis and passive control of cylinder flow. *Journal of Fluid Mechanics* **615** (-1), 221–252.

Martinuzzi, R. & Tropea, C. 1993 The flow around surface-mounted prismatic obstacles placed in a fully developed channel flow. *Journal of Fluids Engineering* **115**, 85–85.

Meliga, P., Chomaz, J. & Sipp, D. 2009*a* Global mode interaction and pattern selection in the wake of a disk: a weakly nonlinear expansion. *Journal of Fluid Mechanics* **633**, 159–189.

Meliga, P., Chomaz, J.M. & Sipp, D. 2009*b* Unsteadiness in the wake of disks and spheres: instability, receptivity and control using direct and adjoint global stability analyses. *Journal of Fluids and Structures* **25** (4), 601–616.

Meliga, P., Pujals, G. & Serre, E. 2012 Sensitivity of two-dimensional turbulent flow past a D-shaped cylinder using global stability. *Physics of Fluids* **24** (6), 061701–061701.

Meliga, P., Sipp, D. & Chomaz, J.M. 2010 Open-loop control of compressible afterbody flows using adjoint methods. *Physics of Fluids* **22**, 054109.

Miau, J.J., Leu, T.S., Liu, T.W. & Chou, J.H. 1997 On vortex shedding behind a circular disk. *Experiments in Fluids* **23** (3), 225–233.

Michalke, A. 1965 On spatially growing disturbances in an inviscid shear layer. *Journal of Fluid Mechanics* **23** (3), 521–544.

Mittal, R. 1999 Planar symmetry in the unsteady wake of a sphere. *AIAA Journal* **37** (3), 388–390.

Mittal, R., Wilson, J.J. & Najjar, F.M. 2002 Symmetry properties of the transitional sphere wake. *AIAA journal* **40** (3), 579–582.

Morrison, J.F. & Qubain, A. 2009 Control of an axisymmetric turbulent wake by a pulsed jet. *Advances in Turbulence XII* pp. 225–228.

Munshi, S.R., Modi, V.J. & Yokomizo, T. 1997 Aerodynamics and dynamics of rectangular prisms with momentum injection. *Journal of Fluids and Structures* **11** (8), 873–892.

Nakamura, I. 1976 Steady wake behind a sphere. *Physics of Fluids* **19**, 5.

Nakamura, Y. 1996 Vortex shedding from bluff bodies with splitter plates. *Journal of Fluids and Structures* **10** (2), 147–158.

Onorato, M., Costelli, A.F. & Garrone, A. 1984 Drag measurement through wake analysis. *SAE Technical Paper Series* **840302**.

Ormières, D. & Provansal, M. 1999 Transition to turbulence in the wake of a sphere. *Physical Review Letters* **83** (1), 80–83.

Pao, H.P. & Kao, T.W. 1977 Vortex structure in the wake of a sphere. *Physics of Fluids* **20**, 187.

Parezanović, V. & Cadot, O. 2009 The impact of a local perturbation on global properties of a turbulent wake. *Physics of Fluids* **21**, 071701.

Parezanović, V. & Cadot, O. 2012 Experimental sensitivity analysis of the global properties of a two-dimensional turbulent wake. *Journal of Fluid Mechanics* **693**, 115–149.

Parezanović, V., Laurentie, J.C., Fourment, C., Cordier, L., Delville, J. & Noack, B.R. 2013 Open-loop control of a mixing layer by fluidic micro-jet actuators. In *48th International Symposium of Applied Aerodynamics*. 3AF.

Park, H., Lee, D., Jeon, W.P., Hahn, S., Kim, J., Kim, J., Choi, J. & Choi, H. 2006 Drag reduction in flow over a two-dimensional bluff body with a blunt trailing edge using a new passive device. *Journal of Fluid Mechanics* **563**, 389–414.

Pastoor, M., Henning, L., Noack, B.R., King, R. & Tadmor, G. 2008 Feedback shear layer control for bluff body drag reduction. *Journal of Fluid Mechanics* **608**, 161–196.

Pier, B. 2008 Local and global instabilities in the wake of a sphere. *Journal of Fluid Mechanics* **603**, 39–61.

Pope, S.B. 2000 *Turbulent flows*. Cambridge University Press.

Pujals, G., Depardon, S. & Cossu, C. 2010 Drag reduction of a three-dimensional bluff body using coherent streamwise streaks. *Experiments in Fluids* **49** (5), 1085–1094.

Ravelet, F., Marie, L., Chiffaudel, A. & Daviaud, F. 2004 Multistability and memory effect in a highly turbulent flow: experimental evidence for a global bifurcation. *Physical Review Letters* **93** (16).

Riabouchinsky, D. 1921 On steady fluid motions with free surfaces. *Proceedings of the London Mathematical Society* **2** (1), 206.

Roshko, A. 1954 On the drag and shedding frequencies of two-dimensional bluff bodies. *NACA Technical Note* **3169**.

Roshko, A. 1976 Structure of turbulent shear flows: a new look. *AIAA journal* **14** (10), 1349–1357.

Roshko, A. 1993 Perspectives on bluff body aerodynamics. *Journal of Wind Engineering and Industrial Aerodynamics* **49** (1-3), 79–100.

Rouméas, M., Gilliéron, P. & Kourta, A. 2009 Analysis and control of the near-wake flow over a squareback geometry. *Computers & Fluids* **38** (1), 60–70.

Ruiz, T., Sicot, C., Brizzi, L.E., Laumonier, J., Borée, J. & Gervais, Y. 2009 Unsteady near wake of a flat disk normal to a wall. *Experiments in Fluids* **47** (4), 637–653.

Saffman, P.G. 1992 *Vortex dynamics*. Cambridge University Press.

Sakamoto, H. & Haniu, H. 1990 A study on vortex shedding from spheres in a uniform flow. *Journal of Fluids Engineering* **112**, 386–392.

Sakamoto, H. & Haniu, H. 1994 Optimum suppression of fluid forces acting on a circular cylinder. *Journal of Fluids Engineering* **116** (2), 221–227.

Sakamoto, H., Haniu, H. & Tan, K. 1991 An optimum suppression of fluid forces by controlling a shear layer separated from a square prism. *Journal of Fluids Engineering* **113**, 183–189.

Schlichting, H. & Gersten, K. 2000 *Boundary layer theory*. Springer Verlag.

Schouveiler, L. & Provansal, M. 2002 Self-sustained oscillations in the wake of a sphere. *Physics of fluids* **14**, 3846.

Sevilla, A. & Martinez-Bazan, C. 2004 Vortex shedding in high Reynolds number axisymmetric bluff body wakes: local linear instability and global bleed control. *Physics of Fluids* **16**, 3460.

Simpson, R.L. 1989 Turbulent boundary-layer separation. *Annual Review of Fluid Mechanics* **21** (1), 205–232.

Spohn, A. & Gilliéron, P. 2002 Flow separations generated by a simplified geometry of an automotive vehicle. In *Congress IUTAM Symposium on Unsteady Separated Flows*.

Strykowski, P.J. & Sreenivasan, K.R. 1985 The control of transitional flows. In *AIAA Shear Flow Control Conference*.

Strykowski, P.J. & Sreenivasan, K.R. 1990 On the formation and suppression of vortex shedding at low Reynolds numbers. *Journal of Fluid Mechanics* **218**, 71–107.

Szaltys, P., Chrust, M., Przadka, A., Goujon-Durand, S., Tuckerman, L.S. & Wesfreid, J.E. 2012 Nonlinear evolution of instabilities behind spheres and disks. *Journal of Fluids and Structures* **28**, 483–487.

Taneda, S. 1978 Visual observations of the flow past a sphere at Reynolds numbers between 10^4 and 10^6. *Journal of Fluid Mechanics* **85** (01), 187–192.

Thiria, B., Goujon-Durand, S. & Wesfreid, J.E. 2006 The wake of a cylinder performing rotary oscillations. *Journal of Fluid Mechanics* **560**, 123–147.

Thompson, M.C., Leweke, T. & Provansal, M. 2001 Kinematics and dynamics of sphere wake transition. *Journal of Fluids and Structures* **15** (3-4), 575–585.

Tropea, C., Yarin, A.L. & Foss, J.F. 2007 *Springer handbook of experimental fluid mechanics*. Springer Verlag.

Tyagi, H., Liu, R., Ting, D.S.K. & Johnston, C.R. 2006 Measurement of wake properties of a sphere in free-stream turbulence. *Experimental Thermal and Fluid Science* **30** (6), 587–604.

Unal, M.F. & Rockwell, D. 1988 On vortex formation from a cylinder. Part 2. Control by splitter-plate interference. *Journal of Fluid Mechanics* **190**, 513–529.

Vilaplana, G., Grandemange, M., Gohlke, M. & Cadot, O. 2013 Experimental sensitivity analysis of the global mode of a sphere turbulent wake using steady disturbances. *Journal of Fluids and Structures* **41**, 119–126.

Wang, H.F., Zhou, Y. & Mi, J. 2012 Effects of aspect ratio on the drag of a wall-mounted finite-length cylinder in subcritical and critical regimes. *Experiments in Fluids* **53** (2), 1–14.

Wäschle, A. 2007 The influence of rotating wheels on vehicle aerodynamics. Numerical and experimental investigations. *SAE Technical Paper Series* **2007-01-0107**.

Wassen, E., Eichinger, S. & Thiele, F. 2010 Simulation of active drag reduction for a squareback vehicle. *Active Flow Control II* pp. 241–255.

Waudby-Smith, P., Bender, T. & Vigneron, R. 2004 The GIE S2A full-scale aeroacoustic wind tunnel. *SAE Technical Paper Series* **2004-01-0808**.

Weickgenannt, A. & Monkewitz, P.A. 2000 Control of vortex shedding in an axisymmetric bluff body wake. *European Journal of Mechanics-B/Fluids* **19** (5), 789–812.

Weiss, P.E. & Deck, S. 2011 Control of the antisymmetric mode ($m = 1$) for high Reynolds axisymmetric turbulent separating/reattaching flows. *Physics of Fluids* **23**, 095102.

Williamson, C.H.K. 1996 Vortex dynamics in the cylinder wake. *Annual review of fluid mechanics* **28** (1), 477–539.

Wu, T.Y.T. 1972 Cavity and wake flows. *Annual Review of Fluid Mechanics* **4** (1), 243–284.

Yun, G., Kim, D. & Choi, H. 2006 Vortical structures behind a sphere at subcritical Reynolds numbers. *Physics of Fluids* **18**, 015102.

Zdravkovich, M.M. 1997 *Flow around circular cylinders: fundamentals*. Oxford University Press.

Analysis and Control of Three-dimensional Turbulent Wakes: from Axisymmetric Bodies to Road Vehicles

Abstract: An experimental study of the turbulent wakes past different geometries is performed by increasing the complexity from axisymmetric bodies to road vehicles. Whatever the geometry is, two kinds of coherent wake motions are likely to be observed. First, at timescales of the order of $5H/U_0$, H and U_0 being the characteristic size and velocity of the flow respectively, the wake may generate periodic oscillations. These coherent motions are usually associated with the interaction of two facing shear layers of opposite vorticity. As the corresponding frequencies rely at first order on the distance between the shear layers, two distinct frequencies are reported when the afterbody has a cross-flow aspect ratio different than 1. These unsteady global modes seem to weaken when the Reynolds number and the complexity of the geometry increase. The second type of coherent motions corresponds to the development of stationary cross-flow instabilities. They are linked to the symmetry breaking modes observed in the laminar regime and their domains of appearance are defined from geometry considerations for parallelepiped bodies in ground proximity. These instabilities are responsible for strong asymmetries in the instantaneous flow and may generate bistable dynamics with a characteristic time scale of the order of $10^3 D/U_0$.

The study of these phenomena, combined with sensitivity analyses to steady perturbations, places the diminution of the cross-flow asymmetries of the instantaneous wake as a relevant strategy for drag reduction. In particular, it is found that both local and global pressure gradients on the sides of the body are source of streamwise vortices increasing the drag. Parabolic dependences between the drag and the cross-flow forces are reported, suggesting similarities with the mechanisms of induced drag that are well-known in aeronautics. Consequently, as they often generate significant wake asymmetries, the development of the cross-flow instabilities is identified as a drag contributor. On the contrary, the part of the drag ascribed to the periodic wake motions seems to be negligible, especially for complex geometries at high Reynolds number.

Keywords: Wakes · Instabilities · Flow control · Sensitivity analysis · Drag reduction